Thomas Gamse (editor)

Book of Abstracts

ERASMUS+ BIP ESS-HPT 2026

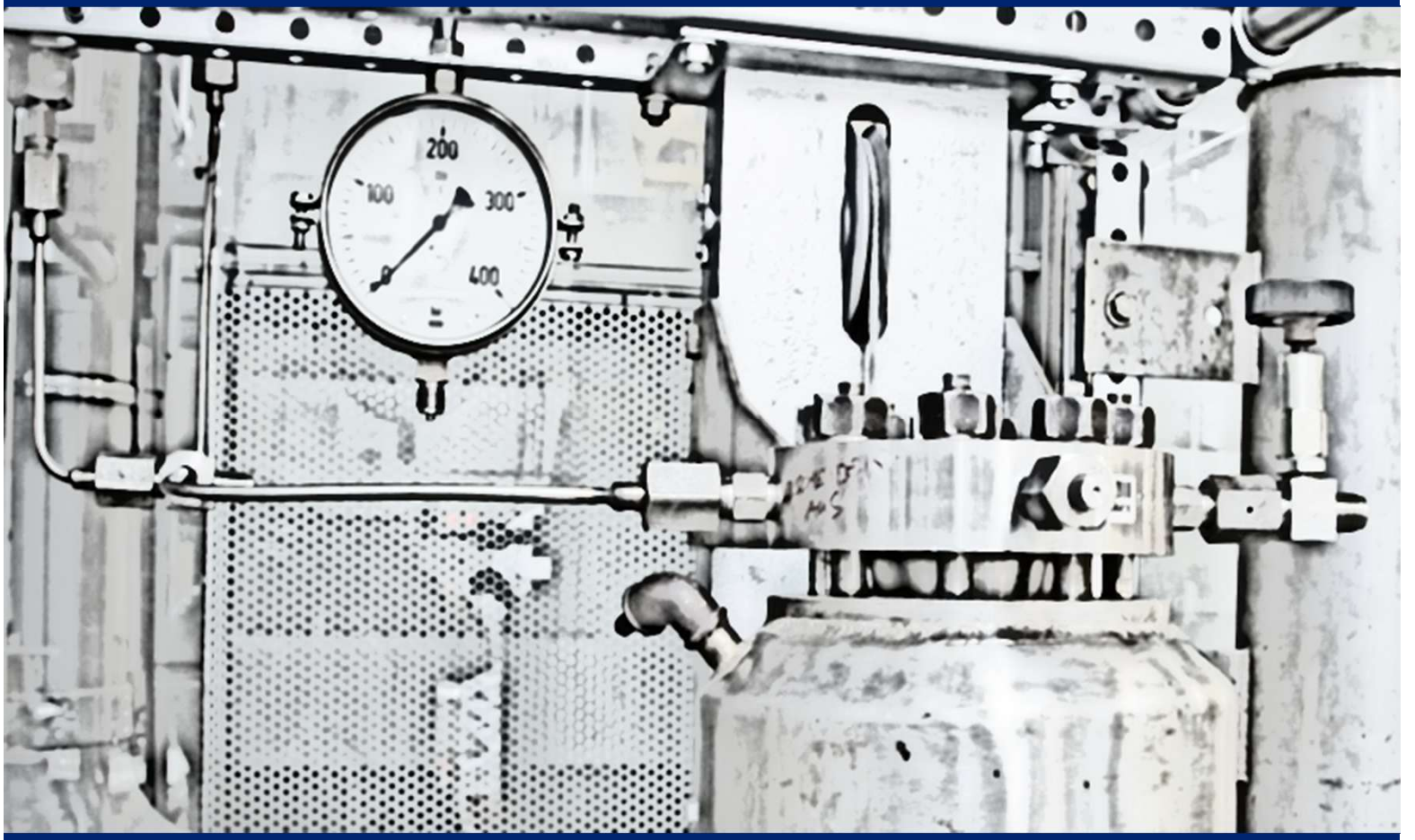

The European Summer School in
High Pressure Technology

5.7. – 18.7.2026

TU Graz
Graz University of Technology

Erasmus+

EFCE
European Federation of Chemical Engineering
Europäische Föderation für Chemie-Ingenieur-Wesen
Fédération Européenne de Génie Chimique

Imprint

Organisation: Thomas Gamse
Institute of Chemical Engineering and Environmental Technology
Graz University of Technology,
Inffeldgasse 25/C, 8010 Graz, Austria
Tel. +43 (0)316 873-7477
E-Mail: thomas.gamse@tugraz.at

Editor: Thomas Gamse
Layout: Thomas Gamse
Cover: Verlag der Technischen Universität Graz,
Thomas Gamse
Cover picture: Thomas Gamse

2026 Verlag der Technischen Universität Graz
Technikerstraße 4, 8010 Graz
verlag@tugraz.at
www.tugraz-verlag.at

ISBN (e-book) 978-3-99161-102-8

DOI 10.3217/978-3-99161-102-8

Book of Abstracts, ERASMUS+ BIP ESS-HPT 2026
"The European Summer School in High Pressure Technology"
5.7.-18.7.2026, Graz University of Technology

Preface

The European Summer School in High Pressure Technology (ESS-HPT) is the continuation of many years of high pressure intensive courses. The history of this very successful series of courses started in 1995, when the first intensive course took place in Monselice, Italy. Most of these Intensive Courses were supported by SOCRATES and later Life Long Learning, as shown in following overview:

SOCRATES IP "Current Trends in High Pressure Technology and Chemical Engineering"
- 1995 Monselice / Italy
- 1996 Nancy / France
- 1997 Erlangen / Germany

SOCRATES IP "High Pressure Technology in Process and Chemical Engineering"
- 1999 Abano Terme / Italy
- 2000 Valladolid / Spain
- 2001 Maribor / Slovenia and Graz / Austria

SOCRATES IP "High Pressure Chemical Engineering Processes: Basics and Applications"
- 2002 Graz / Austria and Maribor / Slovenia
- 2003 Budapest / Hungary
- 2004 Barcelona / Spain

SOCRATES IP "Basics, Developments, Research and Industrial Applications in High Pressure Chemical Engineering Processes"
- 2005 Prague / Czech Republic
- 2006 Lisbon / Portugal
- 2007 Albi / France

Life Long Learning IP "SCF- GSCE: Supercritical Fluids – Green Solvents in Chemical Engineering"
- 2008 Thessaloniki / Greece
- 2009 Istanbul / Turkey
- 2010 Budapest / Hungary

EFCE Intensive Course "High Pressure Technology - From Basics to Industrial Applications"
- 2011 Belgrade / Serbia

Life Long Learning IP "PIHPT: Process Intensification by High Pressure Technologies – Actual Strategies for Energy and Resources Conservation"
- 2012 Maribor / Slovenia and Graz / Austria
- 2013 Darmstadt / Germany
- 2014 Glasgow / Great Britain

Unfortunately, the financial support for these Intensive Programmes was cancelled in 2015 within ERASMUS+. The EFCE Working Party "High Pressure Technology" decided in September 2014 to go on with this course in the form of a Summer School named “The European Summer School in High Pressure Technology”. The ESS-HPT took place every year within the first 2 weeks of July at University of Maribor, Slovenia and Graz University of Technology, Austria.

EFCE ESS-HPT "The European Summer School in High Pressure Technology"

ESS-HPT 2015	Maribor / Slovenia and Graz / Austria
ESS-HPT 2016	Maribor / Slovenia and Graz / Austria
ESS-HPT 2017	Maribor / Slovenia and Graz / Austria
ESS-HPT 2018	Maribor / Slovenia and Graz / Austria
ESS-HPT 2019	Maribor / Slovenia and Graz / Austria
ESS-HPT 2021	Online Course, Graz / Austria
GEHPT and ESS-HPT 2022	Maribor / Slovenia and Graz / Austria

Since 2023 ESS-HPT is organised again as an ERASMUS+ Blended Intensive Programme (BIP). Unfortunately, there is no possibility to organise this summer school in two countries. So, the whole intensive programme takes place at Graz University of Technology.

ERASMUS+ BIP ESS-HPT 2023	Graz / Austria
ERASMUS+ BIP ESS-HPT 2024	Graz / Austria
ERASMUS+ BIP ESS-HPT 2025	Graz / Austria

This year ERASMUS+ BIP ESS-HPT 2026 will take place at Graz University of Technology in the period 5.7.2026 till 18.7.2026. Further this Summer School includes an Online Phase (20.7. till 21.8.2026) where students have to perform a project work based on the topics of the course.

All participants have to give an oral presentation and the abstracts of these presentations, which are peer-reviewed by the Members of the EFCE WP “High Pressure Technology”, are published in this book of abstracts.

The editor

Thomas Gamse
Organiser of ERASMUS+ BIP ESS-HPT 2026

Many thanks to our sponsors,

Erasmus+

NATEX Prozesstechnologie GesmbH,

INNOWELD-Metallverarbeitung GmbH

and Tourismusverband Stadt Graz.

Time Schedule

Oral Presentations Participants

	Monday, 6 July 2026		page
1	9:25 - 9:40	**J.Caputo,** A.Kilzer, M.Petermann Near-Critical Water Treatment of Natural and Synthetic Polymers	1
2	9:40 - 9:55	**G.Aturagaba**, M.I.Chinchilla, A.Martín, M.D.Bermejo Formate Separation from Hydrothermal CO_2 - Amine Mixtures Using Anion – Exchange Resins	6
3	9:55 - 10:10	**M.Grabowski** Three-Phase Drug Carriers for Periodontal Diseases Treatment	9

	Wednesday, 8 July 2026		page
4	20:30 - 20:45	**J.Geider,** T.Melchin, K.M.Zentel Modeling Monomer Phase Partitioning During Emulsion Polymerization of Vinyl Acetate	15
5	20:45 - 21:00	**J.Schäffer**, S.Grüner Molecular Modelling and Molecular Dynamic Studies of Water Vapour Adsorption on Silica Gel Surface Models with Varying Degrees of Condensation and Porosity of the Gel Matrix	20
6	21:00 - 21:15	**J.Joy** Liquid Hot Water Hydrolysis for the Extraction of β-Glucans from Industrial Residues	25
7	21:15 - 21:30	**S.Shahrtash** Carriers and Cocrystals for Carbamazepine Aqueous Solubility Enhancement	31
8	21:30 - 21:45	**M.Mladenović**, M.Milutinović, M.Rajilić-Stojanović Response Surface Optimization of Microwave-Assisted Extraction of Bioactive Compounds from Blueberry Leaves and Assessment of Their Functional Properties	37
9	21:45 - 22:00	**K.Gajšt**, K.Vasić, M.Primožič Magnetic Bacterial Nanocellulose Sphere Nanocomposites as Functional Adsorbents for Wastewater Treatment	44

HIGH-PRESSURE VESSELS

HIGH PRESSURE VESSELS FOR VARIOUS APPLICATIONS UP TO 3.000 BAR CAN BE DESIGNED, CALCULATED, FABRICATED AND TESTED BY INNOWELD. THE POSSIBILITIES OF USING A HIGH-PRESSURE VESSEL IS NUMBERLESS. CARRYING OUT REACTIONS, SEPARATING MEDIUMS AND STORING CHEMICALS ARE ONLY A FEW OF IT. FOR INNOWELD, THE INTEREST INCREASES PROPORTIONAL TO THE PRESSURE AND THE TEMPERATURE.

With our experience from engineering and welding pressure vessels with wall thicknesses up to nearly 250mm and combining them with weld overlays out of materials like nickel, nickel chromium alloys and stainless steels, we are always looking for individual solutions for our partners with individual requirements. The core business of Innoweld starts, whenever high temperature, high pressures and dangerous acids come together.

Beside this individual solutions, we are also manufacturing high pressure and high temperature vessels according to exact specifications from our clients. With best delivery times and our high flexibility during the execution of the project, we make sure that the high pressure vessel with the best quality is ready for installation during the next scheduled shutdown.

Furthermore, our focus is also on the economical side of the project. With our weight saving designs, we make sure that the vessels is not only from the technical, but also from the financial point of view

www.innoweld.at

Near-Critical Water Treatment of Natural and Synthetic Polymers

Jan Caputo, Andreas Kilzer, Marcus Petermann

Chair of Particle Technology, Ruhr-University Bochum, caputo@fvt.rub.de

Introduction

Water is one of the most versatile substances in nature and industry, serving as a heat transfer medium, reaction solvent, and process fluid in countless applications. Its unique properties are governed primarily by its molecular structure and by the formation of an extensive hydrogen-bond network. Under standard conditions, this network confers high solubility for polar and ionic substances such as inorganic salts, while limiting the dissolution of nonpolar or organic compounds. When temperature and pressure are elevated, the hydrogen-bond network progressively breaks down, causing the properties of water to change substantially. These changes are especially pronounced in the near-critical region (see Table 1 for the definition of the relevant states). Key properties such as density, dynamic viscosity, dielectric constant, and the ionic product vary by several orders of magnitude, resulting in markedly increased solubility for nonpolar and organic substances. Dissolved gases, including oxygen, become fully miscible with water under these conditions. [1]

Tab. 1.: Different states of water

	Abbreviation	Temperature [°C]	Pressure [MPa]
Nearcritical	NCW	$T > 300$	$p > p_{vap}$
Supercritical	SCW	$T > T_{crit}$	$p > p_{crit}$

The critical point of water is located at a temperature of 374 °C and a pressure of 22.1 MPa. In the supercritical state the distinction between liquid and gaseous phases ceases to exist. In this region, density and transport properties can be tuned by varying temperature and pressure alone, without the occurrence of a phase transition. Both liquid-like and gas-like states are accessible.

The adjustable properties of water in the near-critical state (NCW) open up a broad range of technical applications, including the total oxidation of wastewater and explosive residues, the gasification of biomass, and the synthesis and hydrolysis of organic

compounds. In the last case reaction pathways can be steered selectively towards desired products through targeted adjustment of temperature and pressure. [2]

The depolymerisation of biopolymers such as cellulose under near-critical conditions has been demonstrated in several studies. Using continuous reactor configurations, polymers like cellulose are broken down into the respective monomers in high yields (e.g. [3–5]). In addition to natural polymers, synthetic polymers such as polyethylene terephthalate (PET) have also been successfully depolymerised in NCW (e.g. [6-7]). These studies demonstrate the potential of near-critical treatment as an approach for chemical recycling and the valorisation of polymer-based waste streams.

Experimental

In this work a pseudo-continuous plant was designed and constructed on a laboratory scale to investigate the depolymerisation of both natural and synthetic polymers in near- and supercritical water. The plant is based on the Sudden Expansion Micro-Reactor (SEMR) principle [3], in which a preheated high-pressure water stream and an ambient-temperature polymer slurry are merged at a T-junction. A schematic diagram of the plant is shown in Fig. 1.

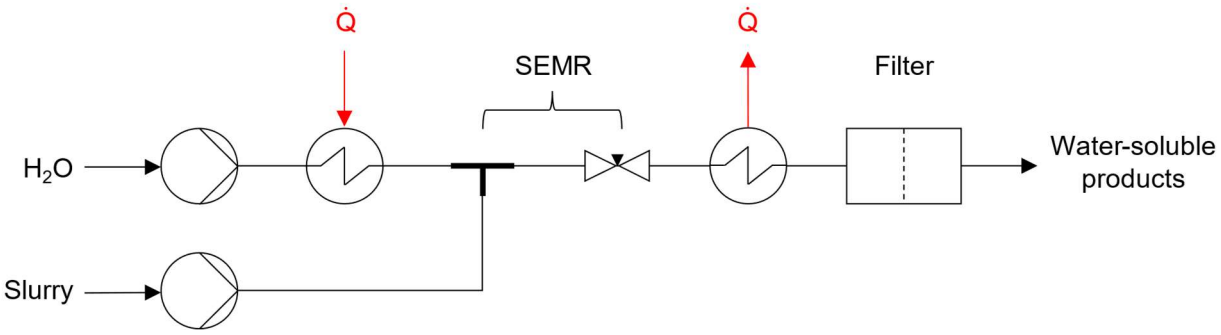

Fig. 1.: Schematic diagram of the laboratory plant

Two Teledyne ISCO syringe pumps (models 260D and 100DX) are used to feed both streams at controlled flow rates. Syringe pumps were selected because their design provides a near-pulsation-free flow: the piston advances at a precisely regulated, constant rate, ensuring that neither system pressure nor volumetric flow rate fluctuates over time.

At the mixing point, the slurry is heated instantaneously to the target reaction temperature without a temperature ramp. The enthalpy balance at the mixing point is described by Eq. (1) and can be used to calculate the mixing temperature using IAPWS-IF97 [8]. The mixing temperature can be adjusted by varying the individual stream temperatures and

their respective flow rates. Heating of the water stream is accomplished using a GC oven in combination with an additional electrical inline heater.

$$h_{mix} = \frac{\dot{m}_{sus} \cdot h_{sus} + \dot{m}_{ncw} \cdot h_{ncw}}{\dot{m}_{mix}} \quad (1)$$

The reactor residence time τ is defined by the reactor volume and the total flow rate at reaction conditions, as given in Eq. (2).

$$\tau = \frac{V_{reactor} \cdot \rho_{mix}}{\dot{m}_{mix}} \quad (2)$$

The reactor itself is assembled from interchangeable SS316 stainless-steel tube sections with an outer diameter of 1/8'' or 6 mm and lengths between 8 cm and 55 cm, enabling the reactor volume to be varied systematically. With the present configuration, residence times in the range of 0.5 s to 20 s are achievable.

At the reactor outlet, a micro-metering valve expands the product stream to ambient pressure. The sudden expansion causes the temperature to drop into the hydrothermal regime, thereby terminating all reactions instantaneously without requiring a separate quench-water stream, which would otherwise dilute the product. All components are fabricated from SS316 stainless steel. The plant is limited to a maximum allowable working pressure of 400 bar, enforced by two spring-loaded relief valves and a rupture disc. The laboratory setup is shown in Fig. 2.

Fig. 2.: Laboratory-scale SEMR plant.

Initial experiments were conducted with polyethylene glycol in two molecular-weight grades (PEG 3350 and PEG 12000). PEG was employed as a water-soluble model compound in a 5 wt.-% aqueous solution. Full solubility of PEG in water eliminates the need to pump a solid suspension, thereby substantially simplifying the initial

commissioning phase. Experiments were conducted at mixing temperatures of 350 °C and 400 °C, system pressures of 300 bar and 350 bar, and residence times between 0.1 s and 20 s. The water-to-feed flow-rate ratio was fixed at 4:1.

Gel-permeation chromatography (GPC; SECcurity HPLC system from PSS Polymer Standards Service GmbH, MCX-columns, 0.1 mol/L NaOH mobile phase) was employed to determine the molecular-weight distribution of PEG and its degradation products.

Regardless of molecular weight (PEG 3350 or PEG 12000) and reaction conditions, GPC analysis revealed total depolymerisation with ethylene glycol as the primary product. Further degradation to secondary products was observed at residence times exceeding 5 s. These findings indicate that PEG exhibits low thermal stability under near-critical conditions.

Summary

The present work demonstrates the broad technical potential of supercritical and near-critical water as a reaction medium for the treatment of various polymers. The variable properties of NCW (e.g. ionic product, transport properties) enable precise control over polymer degradation pathways and product distributions.

Central to the experimental approach is the Sudden Expansion Micro-Reactor, which affords precise control over residence time in the reactor. This enables control over the resulting product distribution and is essential for resolving depolymerisation kinetics observed in NCW.

Initial experiments showed total depolymerisation of PEG in NCW. Future work will extend the scope to chemically more complex substrates, including natural and synthetic polymers that require delivery as solid suspensions. Accordingly, the plant will be adapted to enable reliable pumping of heterogeneous slurries, opening the way towards systematic depolymerisation studies of various polymers under near- and supercritical water conditions.

References

[1] G. Brunner, *Hydrothermal and Supercritical Water Processes*, in *Supercritical Fluid Science and Technology*, vol. 5, E. Kiran, Ed. Amsterdam: Elsevier, 2014.

[2] A. Kruse, "Reaktionen in nah- und überkritischem Wasser," ["Reactions in near- and supercritical water,"] *Nachrichten – Forschungszentrum Karlsruhe*, vol. 33, pp. 59–70, 2001.

[3] D. A. Cantero, M. D. Bermejo, and M. J. Cocero, “High glucose selectivity in pressurized water hydrolysis of cellulose using ultra-fast reactors,” *Bioresource Technology*, vol. 135, pp. 697–703, 2013.

[4] M. Sasaki *et al.*, “Dissolution and hydrolysis of cellulose in subcritical and supercritical water,” *Industrial & Engineering Chemistry Research*, vol. 39, pp. 2883–2890, 2000.

[5] L. Tolonen, et al., “The swelling and dissolution of cellulose crystallites in subcritical and supercritical water,” *Cellulose*, vol. 20, pp. 2731–2744, 2013.

[6] M. Čolnik, Ž. Knez, M. Škerget, “Sub- and supercritical water for chemical recycling of polyethylene terephthalate waste,” *Chemical Engineering Science*, vol. 233, p. 116389, 2021.

[7] T. Adschiri *et al.*, “Recovery of terephthalic acid by decomposition of PET in supercritical water,” *Kagaku Kogaku Ronbunshu*, vol. 23, no. 4, 1997.

[8] H.-J. Kretzschmar and W. Wagner, *International Steam Tables: Properties of Water and Steam Based on the Industrial Formulation IAPWS-IF97*, 3rd ed. Berlin: Springer Vieweg, 2019.

Formate Separation from Hydrothermal CO_2 - Amine Mixtures Using Anion – Exchange Resins

Godwin Aturagaba, Maira I. Chinchilla, Ángel Martín, María D. Bermejo
Research Institute on Bioeconomy - BioEcoUVa, PressTech Group, Universidad de Valladolid, Dr. Mergelina s/n., Valladolid, 47011, Spain
Department of Chemical Engineering and Environmental Technology, Universidad de Valladolid, Dr. Mergelina s/n., Valladolid, 47011, Spain

Introduction

The capture and utilization of carbon dioxide (CO_2) is an important strategy for reducing greenhouse gas emissions while producing valuable chemicals. Aqueous amine solutions remain among the most established technologies for CO_2 capture. Among the aqueous amines investigated for CO_2 capture, 2-amino-2-methyl-1-propanol (AMP) has gained significant attention because of its steric hindrance, high CO_2 loading capacity, and improved resistance to degradation (Gabrielsen et al., 2007; Osagie et al., 2018; Sartorl & Savage, 1983; Yoon & Hwang, 2021). Following CO_2 capture, hydrothermal catalytic hydrogenation enables conversion of the captured carbon species into formate under relatively mild operating conditions (Quintana-Gómez et al., 2024).

Despite the successful conversion of captured CO_2 to formate, the resulting hydrothermal reaction mixture contains multiple ionic species, including formate, bicarbonate, and protonated amine species (Park et al., 2020; Quintana-Gómez et al., 2024), posing significant separation challenges. Conventional separation approaches are often energy-intensive and operationally complex (Hoque et al., 2024; Zeidan & Marti, 2019). Therefore, ion-exchange resins offer a promising alternative because of their selectivity toward anionic species, operational simplicity, and regeneration potential.

This study evaluates the performance of commercially available anion-exchange resins for the selective separation and recovery of formate from hydrothermal CO_2–amine reaction mixtures.

Experimental

Hydrothermal reaction products were generated by chemisorption of CO_2 in 0.5 M aqueous AMP solution, followed by catalytic hydrogenation using gaseous H_2 in a 50 mL Parr reactor. Reactions were conducted at 70 °C and 75 bar H_2 pressure for 40 minutes using Pd/C catalyst.

Three commercial anion-exchange resins were investigated: Amberlite IRN-78 (OH), Amberlyst A-26 (OH), and Amberlite HPR900 (OH). Adsorption experiments were performed using diluted hydrothermal reaction mixtures containing formate and bicarbonate species. Resin dosages of 0.5 g and 1.0 g were evaluated under agitation conditions for 4 hours.

Regeneration experiments employed sodium hydroxide solutions or distilled water to recover adsorbed species. Formate and bicarbonate concentrations before and after adsorption were used to assess the separation efficiency.

Summary

All investigated resins demonstrated the ability to remove formate and bicarbonate from hydrothermal CO_2–amine reaction mixtures, with adsorption performance improving significantly at higher resin dosage. At a resin dosage of 1.0 g, all resins achieved more than 96% formate removal and over 90% bicarbonate removal, with Amberlite IRN-78 (OH) showing the best overall adsorption performance.

Regeneration using sodium hydroxide solutions enabled effective recovery of the adsorbed formate and bicarbonate species, achieving up to 66.50% formate recovery and 70.34% bicarbonate recovery with Amberlite IRN-78 (OH). In contrast, regeneration with water alone resulted in negligible recovery. In addition, total nitrogen analysis and ^{1}H NMR measurements confirmed that the amine structure after separation remained comparable to that of the original reaction mixture, indicating chemical stability during the process.

The results demonstrate that anion-exchange resins provide a promising approach for selective separation and recovery of formate from hydrothermal CO_2–amine systems and may contribute to the development of integrated carbon capture and utilization processes.

Acknowledgment

This research is being carried out within the framework of the PHyCO_2 project (PID2023-150529OB-I00), financed by the State Research Agency (AEI, 10.13039/501100011033), the European Union through ERDF Funds (*"Europe drives our growth"*), and the Ministry of Science, Innovation and Universities.

Godwin Aturagaba is financed under the call for UVa 2024 predoctoral contracts, co-financed by Banco Santander.

References

Gabrielsen, J., Svendsen, H. F., Michelsen, M. L., Stenby, E. H., & Kontogeorgis, G. M. (2007). Experimental validation of a rate-based model for CO2 capture using an AMP solution. *Chemical Engineering Science*, *62*(9), 2397–2413.

Hoque, M. A., Abad, K., Kharel, P., Omosebi, A., & Thompson, J. (2024). Downstream Separation of Formic Acid with Anion-Exchange Resin from Electrocatalytic Carbon Dioxide (CO2) Conversion: Adsorption, Kinetics, and Equilibrium Modeling. *Industrial and Engineering Chemistry Research*, *63*(6), 2779–2790.

Osagie, E., Biliyok, C., Di Lorenzo, G., Hanak, D. P., & Manovic, V. (2018). Techno-economic evaluation of the 2-amino-2-methyl-1-propanol (AMP) process for CO2 capture from natural gas combined cycle power plant. *International Journal of Greenhouse Gas Control*, *70*(January), 45–56.

Park, K., Gunasekar, G. H., Kim, S. H., Park, H., Kim, S., Park, K., Jung, K. D., & Yoon, S. (2020). CO2 hydrogenation to formic acid over heterogenized ruthenium catalysts using a fixed bed reactor with separation units. *Green Chemistry*, *22*(5), 1639–1649.

Quintana-Gómez, L., Dos Santos, L. C., Cossio-Cid, F., Ciordia-Asenjo, V., Almarza, M., Goikoechea, A., Ferrero, S., Álvarez, C. M., Segovia, J. J., Martín, Á., & Bermejo, M. D. (2024). Hydrothermal reduction of CO2 captured by aqueous amine solutions into formate: Comparison between in situ generated H2 and gaseous H2 as reductant and evaluation of amine stability. *Carbon Capture Science and Technology*, *13*(October).

Sartorl, G., & Savage, D. W. (1983). Sterically Hindered Amines for CO2 Removal from Gases. *Industrial and Engineering Chemistry Fundamentals*, *22*(2), 239–249.

Yoon, B., & Hwang, G. S. (2021). First-Principles Assessment of Anomalous Thermal Degradation of Aqueous 2-Amino-2-methyl-1-propanol for CO2Capture. *Energy and Fuels*, *35*(20), 16705–16712.

Zeidan, H., & Marti, M. E. (2019). Separation of Formic Acid from Aqueous Solutions onto Anion Exchange Resins: Equilibrium, Kinetic, and Thermodynamic Data. *Journal of Chemical and Engineering Data*, *64*(6), 2718–2727.

Three-Phase Drug Carriers for Periodontal Diseases Treatment

Maciej Grabowski

Wrocław University of science and Technology, Department of Micro, Nano and Bioprocess Engineering, Faculty of Chemistry,

email: maciej.grabowski@pwr.edu.pl

Introduction

Periodontal diseases, including gingivitis and periodontitis, are among the most prevalent oral infections worldwide. They are characterized by a slow, chronic progression that leads to the degradation of the tissues supporting the teeth. If left untreated, they result in progressive alveolar bone loss, gingival recession, tooth mobility, and ultimately tooth loss. The scale of this phenomenon is global. According to the *Global Burden of Disease* study, severe periodontitis is the eleventh most common disease worldwide. Between 1990 and 2010, its prevalence increased by more than 57% [1]. In 2021, over one billion people suffered from severe periodontitis. Current projections indicate that population aging will contribute to a further increase in disease prevalence. Preliminary forecasts for 2050 are also alarming, predicting a 44.32% increase in incidence, meaning that more than 1.5 billion individuals may be affected by this condition. Beyond tooth and alveolar bone loss, periodontal diseases are increasingly associated with systemic disorders, including vascular dysfunction and neurodegenerative diseases. Growing evidence suggests that chronic oral inflammation may contribute to the pathogenesis of Alzheimer's disease, indicating that periodontal disease may constitute a potential link between systemic inflammation and central nervous system pathology [1,2]. Although systemic antibiotic therapy effectively eliminates pathogens, it simultaneously disrupts the natural microbiota of the body and fails to ensure adequate drug concentrations directly at the site of infection. A potential solution to this problem is the development of local drug delivery systems. As illustrated in Figure 1, a potential local drug delivery system may be based on a three-phase drug carrier consisting of an antibiotic-loaded sorbent core (e.g., graphene oxide, insoluble starch, or montmorillonite), a hydrogel matrix, and an outer polymeric envelope. Such a structure could provide efficient drug loading and controlled local release at the target site.

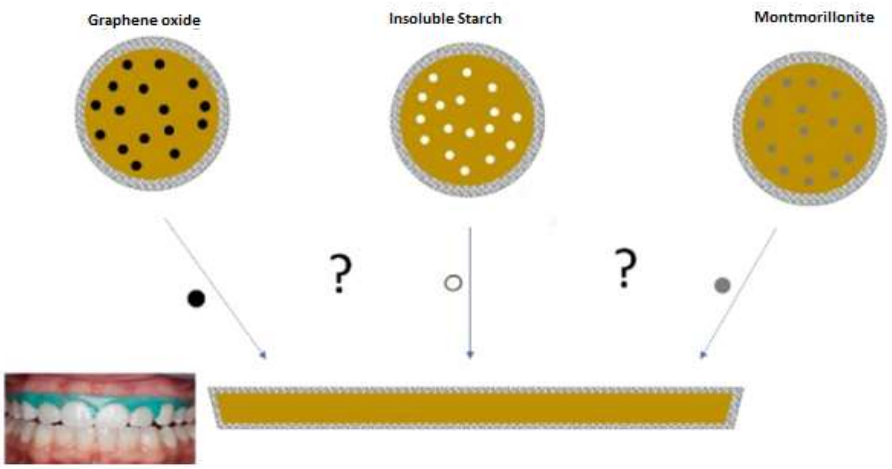

Fig. 1 Possible variants of 3-phase carriers [3]

Experimental

Metronidazole and clindamycin were chosen owing to their effectiveness against anaerobic pathogens associated with periodontal diseases. Sorption studies were conducted to identify the most promising sorbent for use as a drug reservoir within the proposed local delivery system. As the final formulation is designed as a multicomponent carrier, sorbents demonstrating inadequate affinity for metronidazole were excluded from further evaluation with clindamycin. Sorption equilibrium was established at 36.8°C, reflecting intraoral physiological conditions, over a range of initial antibiotic concentrations and sorbent types. The sorption results obtained for the investigated sorbents are presented in Figure 2.

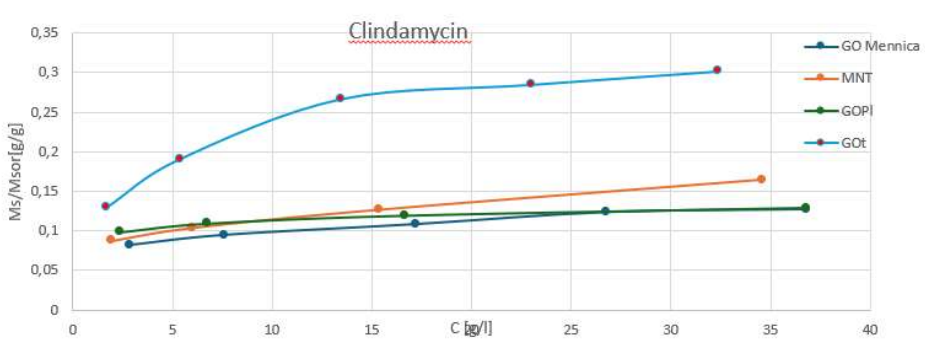

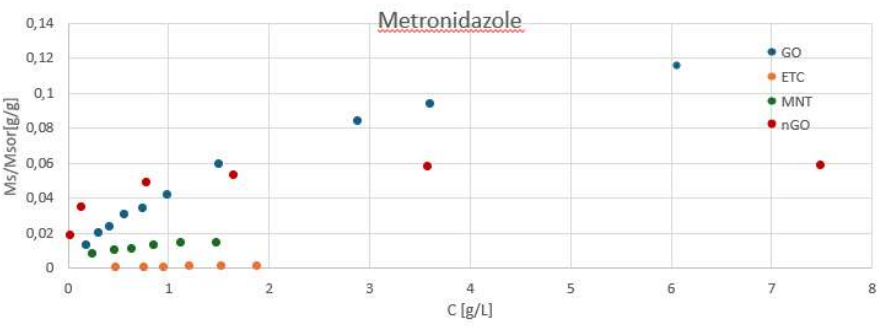

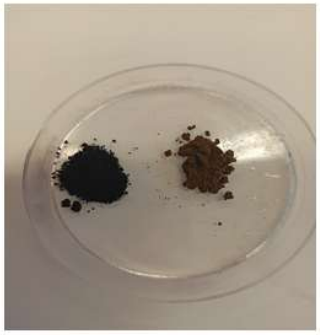

Fig. 2 Results of sorption studies for clindamycin and metronidazole

The occurrence of sorption was confirmed by Fourier-transform infrared spectroscopy (FTIR) analysis. Alginate was identified as a promising hydrogel component for the envisioned drug delivery platform. Metronidazole-loaded alginate microspheres were fabricated and evaluated in release studies, revealing near-complete drug release within 30 min (Figure 3). To improve release kinetics, analogous microspheres incorporating the selected sorbent were developed (Figure 4). The presence of the sorbent significantly prolonged metronidazole release (up to 6 times) (Figure 5); nevertheless, the release period remained too short to ensure therapeutic drug levels throughout the intended treatment duration.

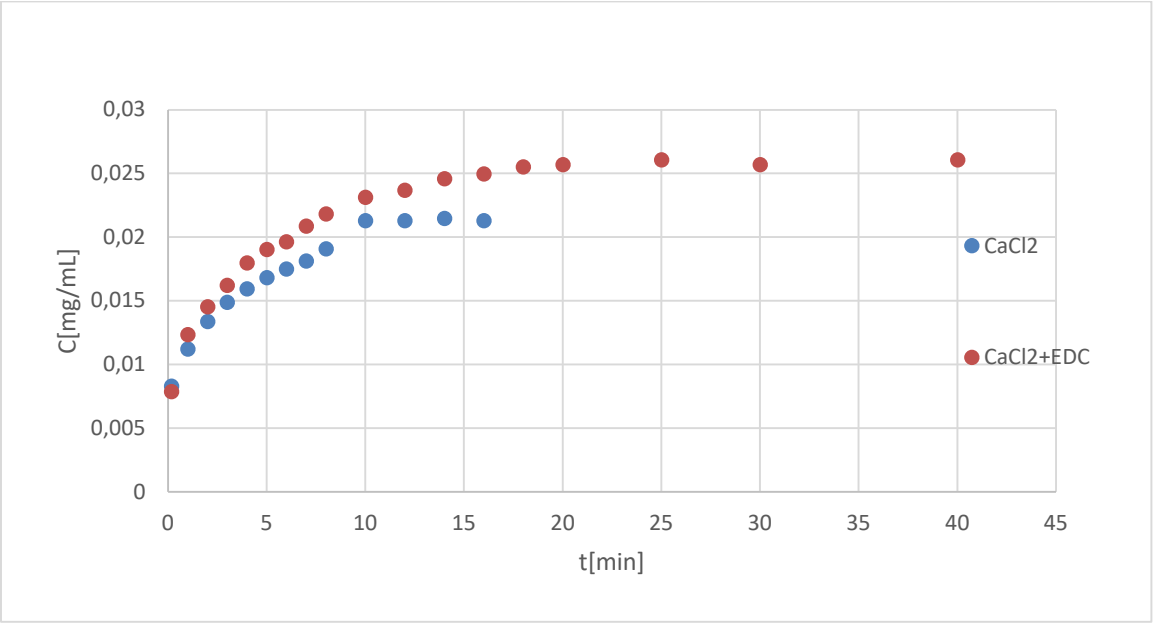

Fig 3. Metronidazole release profile from alginate spheres (chemical and physical crosslinking)

Fig. 4 Alginate microspheres, both with and without the sorbent

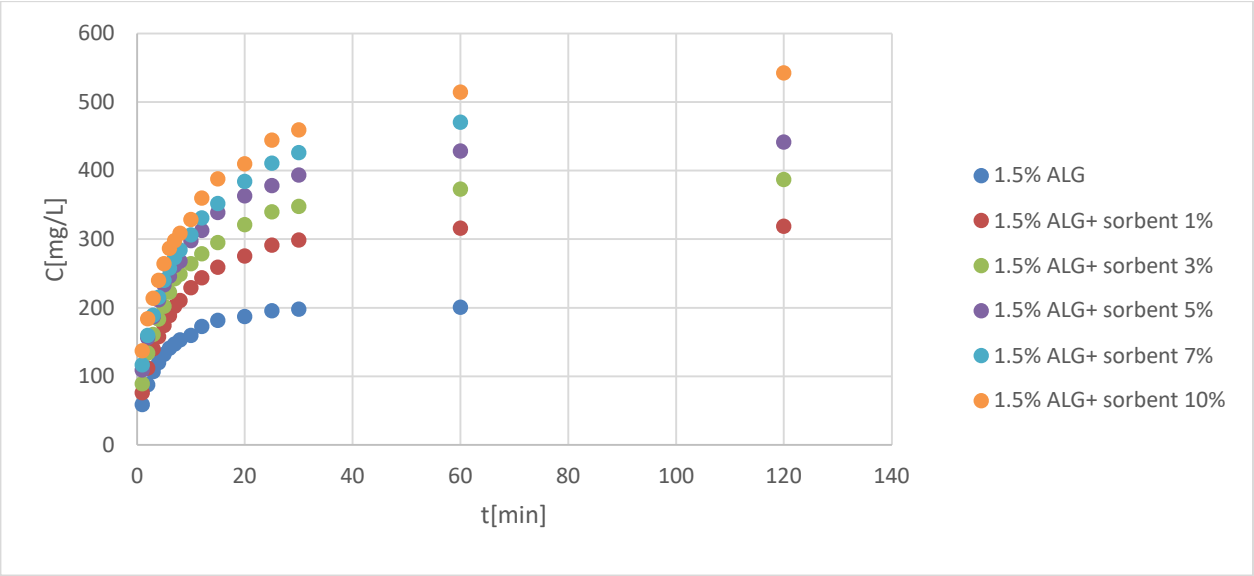

Fig. 5 Metronidazole release profile from carriers with and without sorbent

Due to the insufficient release duration achieved with the alginate-based systems, the introduction of additional diffusional barriers was considered necessary. To reduce the rapid mass transport characteristic to hydrogel matrices, the carriers were coated with a polymeric layer. Specifically, a dry polylactide coating was applied to surround the hydrogel core and limit drug diffusion. This modification resulted in an approximately 40-fold increase in the release time, demonstrating the crucial role of the polymeric envelope in achieving prolonged drug delivery. The coated carriers and coating procedure are presented in Figure 6.

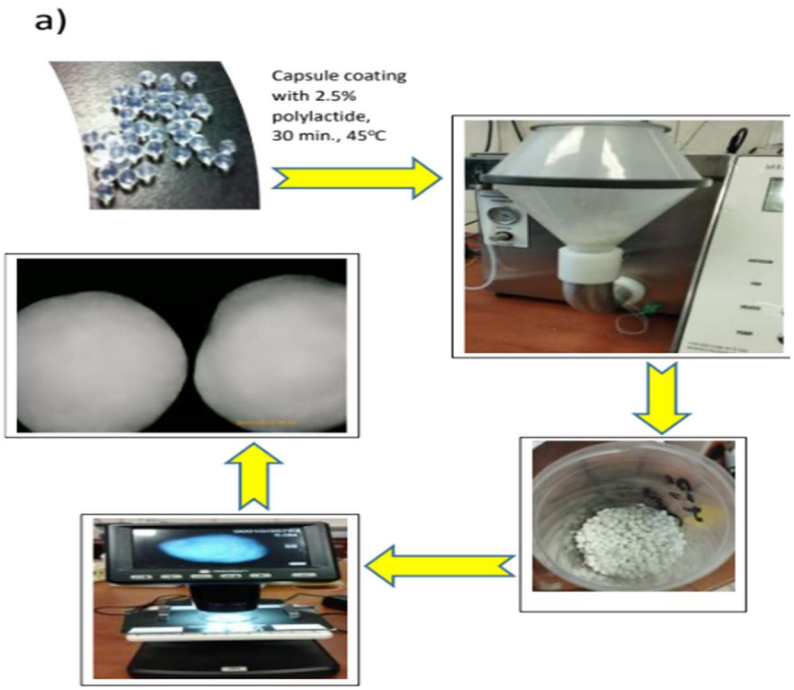

Fig. 6 The procedure for coating capsules with PLA [4]

Subsequently, a hydrogel bioprinter was employed to fabricate carriers with geometries more closely resembling the anatomical contours of gingival tissues. An approximate geometric model of the intended carrier is shown in Figure 7, while the printed constructs are presented in Figure 8. The maximum sorbent concentration was established at 5% (w/v), as higher loadings resulted in nozzle clogging and compromised printability. Drug release profiles obtained from the printed carriers differed only slightly from those observed for the spherical structures.

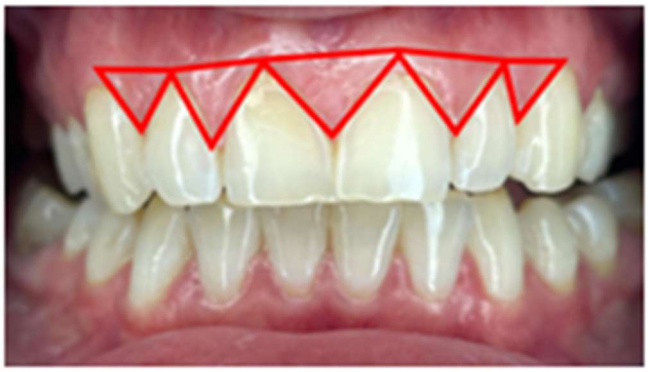

Fig. 7 An approximate geometric model

Fig 8. Printed structures with different sorbent content

Summary

The obtained results demonstrate the feasibility of a three-phase carrier concept for local periodontal therapy. The combination of a sorbent-based drug reservoir and a polymer-coated hydrogel matrix significantly prolonged antibiotic release compared with conventional alginate systems. Future work will focus on optimizing the carrier composition and geometry, as well as determining the minimum lethal concentration of the selected antibiotics against microorganisms responsible for periodontal diseases to establish therapeutically effective local dosing strategies.

References

[1] Hashim, N.T.; Babiker, R.; Padmanabhan, V.; Ahmed, A.T.; Chaitanya, N.C.S.K.; Mohammed, R.; Priya, S.P.; Ahmed, A.; El Bahra, S.; Islam, M.S.; et al. The Global Burden of Periodontal Disease: A Narrative Review on Unveiling Socioeconomic and Health Challenges. Int. J. Environ. Res. Public Health 2025, 22, 624. https://doi.org/10.3390/ijerph22040624

[2] Shawkatova, I.; Durmanova, V.; Javor, J. Alzheimer's Disease and Porphyromonas gingivalis: Exploring the Links. Life 2025, 15, 96. https://doi.org/10.3390/life15010096

[3]www.ncn.gov.pl/sites/default/files/listy-rankingowe/2022-09-15du59ho/streszczenia/571000-pl.pdf

[4] Trusek, A.; Grabowski, M.; Ajayi, O.; Kijak, E. Hyaluronic Acid–Alginate Homogeneous Structures with Polylactide Coating Applied in Controlled Antibiotic Release. Gels 2023, 9, 526. https:// doi.org/10.3390/gels9070526

Modeling Monomer Phase Partitioning During Emulsion Polymerization of Vinyl Acetate

Jonas Geider, Timo Melchin, Kristina Maria Zentel*

Ernst-Berl-Institute of Technical and Macromolecular Chemistry, Technical University of Darmstadt, 64287 Darmstadt/Germany, e-mail: *kristina.zentel@pre.tu-darmstadt.de

Introduction

Accurate modeling of phase partitioning is a considerable obstacle in emulsion polymerization modeling, often simplified to a description of monomer partitioning between the aqueous and particle phase.[1] The PC-SAFT equation of state (eos) enables the calculation of aqueous, gaseous, polymer particle and monomer droplet phase partitioning of water, vinyl acetate, polyvinyl acetate and nitrogen. A consideration of the gaseous phase can be advantageous in the description of monomers with a high vapor pressure and offers an extendibility to the ethylene-vinyl acetate copolymerization. Therefore, a PC-SAFT model for the polyvinyl alcohol stabilized emulsion polymerization of vinyl acetate has been parameterized and coupled with a kinetic model.[2]

Modeling

Figure 1 schematically shows the structure of the coupled kinetic and thermodynamic model, which utilizes the Cape Open Interface implemented in Predici® 11. As thermodynamic equilibrium is commonly assumed to be reached significantly faster than the polymerization itself occurs, the total mass of all substances is transferred from the kinetic model to the thermodynamic model after every time step. Subsequently, a flash calculation at reactor temperature and volume is conducted and the mass of all substances in each phase is transferred to the kinetic model. This is the starting composition for the next kinetic time step.

As shown in Figure 1, pure component parameters (e.g. ε, m and σ) and the binary interaction parameter k_{ij} are needed to calculate phase equilibria using the PC-SAFT eos. Depending on the amount of literature studies conducted regarding the involved substances, pure component parameter sets with different strengths and weaknesses as well as considering different conditions exist. Therefore, the model utilized in this work consists of the pure substance parameters found in the literature, which are best suited to

reproduce experimental pure substance data. All binary interaction parameters have been estimated based on thermodynamic data of the corresponding binary systems.

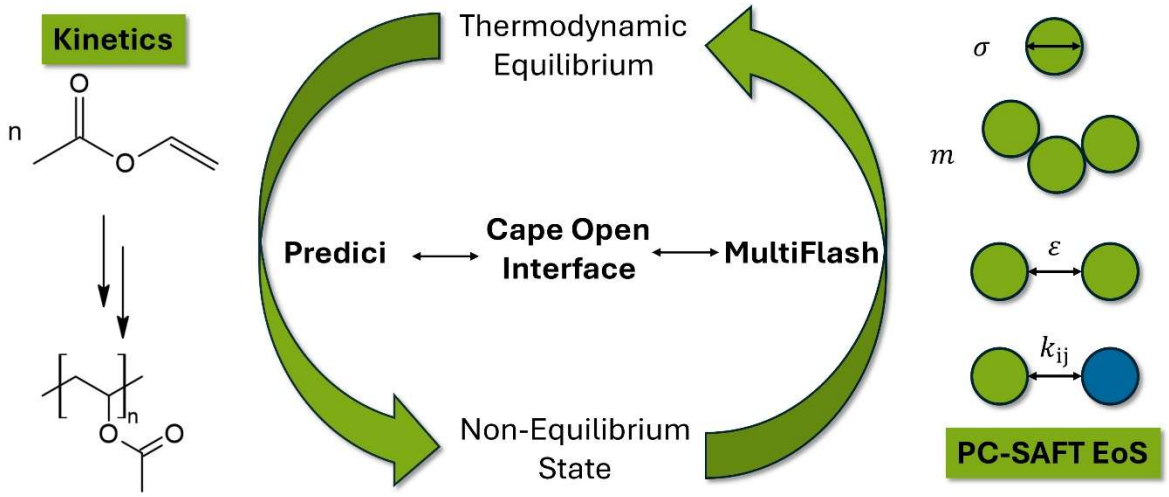

Fig. 1.: Visualization of the coupled kinetic and thermodynamic model for the emulsion polymerization of vinyl acetate: polymerization kinetics are modeled within Predici® 11 and the phase compositions are calculated within *Multiflash™* 7.0.

A deterministic model based on the kinetic scheme shown in Table 1 is applied to describe the polymerization reaction itself. The scheme can be divided into reactions in the aqueous and the particle phase as well as oligoradical particle entry and exit. Note that entry and exit are technically no reactions but are modeled as such based on the method developed by Asua[3] and utilized by Agirre et al.[4].

Regarding the aqueous phase, 2,2'-Azobis(2-methylpropionamidine)dihydrochloride (AIBA) decomposition, chain initiation, oligomer propagation and oligomer disproportionation are considered. The effect of solids content on termination rate in all phases is described using the version of the composite model presented by Johnston-Hall and Monteiro[5]. Even though other polymerization reactions (e.g. transfer reactions, macromer propagation) also occur, they are neglected based on the low polymer mass formed in the aqueous phase. Oligoradicals are assumed be able to enter a polymer particle at a chain length of 8. The Smith-Ewart equation is applied to describe the distribution of radicals across the particle phase according to the method developed by Hungenberg and Wulkow[6].

In addition to propagation and termination, transfer to monomer is considered in the particle phase. Note that transfer to monomer is described in two reaction steps due to the possibility of monomer radical exit. The particle diameter is described using a fit to the experimental data, leading to an accurate description of particle number, if the thermodynamic model calculates particle mass and composition in a sufficient manner. Particle nucleation and coagulation are therefore considered implicitly. A more detailed explanation of the model can be found in reference 2.

Tab. 1.: Reaction steps and phases (w: water, p: particle) of the kinetic model. i and j are the respective radical chain length and z the radical chain length at which particle entry can occur. I^*: initiator radical, $\mathrm{PVAc}_i^{*\mathrm{m}}$: radical of length i in phase m, $\mathrm{PVAc}_i^{\mathrm{m}}$: polymer chain of length i in phase m.

Reaction Step	Reactants	Products	
Aqueous Phase			
AIBA decomposition	$AIBA$	$2\,I^* + N_2$	
Chain Initiation	$I^* + VAc^{\mathrm{w}}$	$PVAc_1^{*\mathrm{w}}$	
Propagation	$PVAc_{i-1}^{*\mathrm{w}} + VAc^{\mathrm{w}}$	$PVAc_i^{*\mathrm{w}}$	$2 \leq i \leq z$
Disproportionation	$PVAc_i^{*\mathrm{w}} + PVAc_j^{*\mathrm{w}}$	$PVAc_i^{\mathrm{w}} + PVAc_j^{\mathrm{w}}$	$1 \leq i,j \leq z$
Phase Transitions			
Phase Transfer	$PVAc_1^{*\mathrm{p}}$	$PVAc_1^{*\mathrm{w}}$	
Phase Transfer	$PVAc_{\mathrm{z}}^{*\mathrm{w}}$	$PVAc_{\mathrm{z}}^{*\mathrm{p}}$	
Particle Phase			
Reinitiation	$PVAc_{\mathrm{z}}^{*\mathrm{p}} + VAc^{\mathrm{p}}$	$PVAc_{\mathrm{z}+1}^{*\mathrm{p}}$	
Propagation	$PVAc_i^{*\mathrm{p}} + VAc^{\mathrm{p}}$	$PVAc_{i+1}^{*\mathrm{p}}$	$i \geq 1$
Transfer to Monomer	$PVAc_i^{*\mathrm{p}} + VAc^{\mathrm{p}}$	$PVAc_i^{\mathrm{p}} + PVAc_1^{*\mathrm{p}}$	$i \geq 1$
Chain Initiation	$PVAc_1^{*\mathrm{p}} + VAc^{\mathrm{p}}$	$PVAc_2^{*\mathrm{p}}$	$i \geq 1$
Disproportionation	$PVAc_i^{*\mathrm{p}} + PVAc_j^{*\mathrm{p}}$	$PVAc_i^{\mathrm{p}} + PVAc_j^{\mathrm{p}}$	$i,j \geq 1$

Summary

Even though the PC-SAFT model can accurately reproduce the binary system data utilized to determine the binary interaction parameters, this does not necessarily translate to a good description of multi component systems. Therefore, the coupled model has been applied to semi-batch emulsion polymerization experiments with different starting pressures. The reactor pressure is easily accessible and an interesting parameter both from the perspective of reactor safety and additional model validation. During all experiments, a rise in pressure due to the dosing of vinyl acetate as well as aqueous AIBA and polyvinyl alcohol solutions and a decrease in pressure due to sampling can be observed. The model results show reasonable agreement to the experimental data.[2]

Seeded semi-batch emulsion polymerizations have been chosen to validate the kinetic model. The experimental and simulated solids content profiles are in good agreement with each other.[2] Additionally, the thermodynamic model can be utilized to predict the residual amount of monomer present in each phase, which enables a prediction of monomer content in consumer products. Results for the simulation of three experiments are shown in Figure 2. Note that the monomer feed rate of the experiment shown in Figure 2a is significantly higher than the monomer feed rate of the other experiments. According to the model prediction, no droplet phase is formed over the course of the experiments, regardless of monomer feed rate, as the residual monomer is sufficiently soluble in polyvinyl acetate and water. However, the total amount of vinyl acetate is significantly higher in the experiment shown in Figure 2a. After the vinyl acetate dosage is stopped, the mass of vinyl acetate in each phase decreases, due to the ongoing polymerization. As the vinyl acetate content further decreases, the ratio of monomer dissolved in the aqueous phase to monomer dissolved in the particle phase increases.

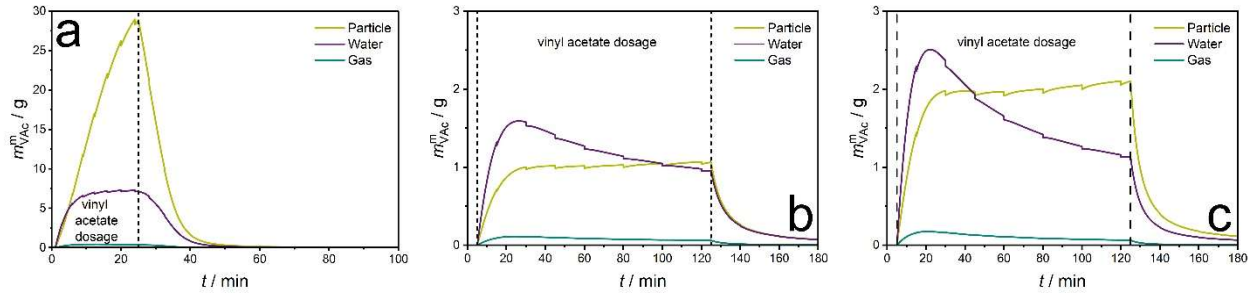

Fig. 2.: Predicted distribution of vinyl acetate across the present phases during three semi-batch polymerizations. The data of b and c has previously been published in the Supporting Information of reference 2.

Acknowledgment

The authors would like to acknowledge Dr. Michael Wulkow for the implementation of the Predici®-*MultiFlash™* interface and his constant, excellent support with respect to Predici®. The authors want to thank Lana Klindt and Matti Schierholz for their help in conducting polymerization experiments.

References

(1) Gugliotta, L. M.; Arzamendi, G.; Asua, J. M. Choice of monomer partition model in mathematical modeling of emulsion copolymerization systems. *J. Appl. Polym. Sci.* **1995**, *55*, 1017–1039.

(2) Geider, J.; Warnecke, F.; Viernickel, J.; Schilling, C.; Melchin, T.; Zentel, K. M. Modeling Emulsion Polymerization of Vinyl Acetate: Redox Initiation Kinetics and Rigorous Phase Equilibrium Calculations with the PC-SAFT Equation of State. *Ind. Eng. Chem. Res.* [Online early access].

(3) Asua, J. M. A New Model for Radical Desorption in Emulsion Polymerization. *Macromolecules* **2003**, *36*, 6245–6251.

(4) Agirre, A.; Weitzel, H.-P.; Hergeth, W.-D.; Asua, J. M. Process intensification of VAc–VeoVa10 latex production. *Chemical Engineering Journal* **2015**, *266*, 34–47.

(5) Johnston-Hall, G.; Monteiro, M. J. Bimolecular radical termination: New perspectives and insights. *J. Polym. Sci. A Polym. Chem.* **2008**, *46*, 3155–3173.

(6) Hungenberg, K.-D.; Wulkow, M. *Modeling and Simulation in Polymer Reaction Engineering: A Modular Approach*; John Wiley & Sons, 2018.

Molecular Modelling and Molecular Dynamic Studies of Water Vapour Adsorption on Silica Gel Surface Models with Varying Degrees of Condensation and Porosity of the Gel Matrix

Jörg Schäffer, Sabine Grüner

Fakultät für Bioingenieurwissenschaften, Hochschule Weihenstephan-Triesdorf,
joerg.schaeffer@hswt.de

Introduction

Silicic acid, in its various stages of condensation, degrees of polymerisation and states of dispersion, is a substance that occurs almost ubiquitously both in the living biosphere and in the rest of the Earth's non-living spheres. It is found in its natural form and also as a product of industrial manufacture. Its diverse and controllable properties make it a valuable raw material and refined product in numerous industrial sectors, in medicine, agriculture, the arts and for personal use. In addition to being used as a filler, construction material, binder, adsorbent, texturiser or carrier, the material is frequently employed as a desiccant due to its hygroscopic properties and exceptional water absorption capacity. Due to their numerous silanol groups, these highly hydrophilic materials, combined with high porosity, enable highly dispersed silica preparations to achieve specific surface areas of 500 m^2/g or more (sciencedirect, 2027). This study uses molecular dynamics simulations to investigate the relationships between water vapour adsorption and the degree of condensation of the gel matrix, its porosity, specific surface area and loading capacity, based on specifically modelled silica gel structures at the molecular level. The results are compared with experimental water vapour sorption isotherms obtained by the authors.

Experimental

Modelling and molecular dynamics

Modelling and molecular dynamics were carried out using standard methods (Frenkel D., 2002) with Windows 11-OS on an Intel®-Core™-Prozessor (i5-6600 CPU at 3.30GHz, 32 GB RAM)). VSORP-, AmorphusCell- (var. Legacy) and Forcite-Subroutines together with the Polymer-, Crystal-, and Surface-Builder of the Biovia/Materials Studio 2025 program-suite were employed. Unless otherwise stated, molecular dynamic calculations were carried out as indicated in tab. 1.

Tab. 1: Used settings for molecular modelling and molecular dynamics calculations

Variable	Value
Forcefield	COMPASS III
Assign forcefield types and charges	Automatically[1)]
Accuracy	0,0001 kcal/mol
Cut Off distance	15,5 Å
Time step	1 fs
Convergence tolerance	Fine[2)]
Temperature	298 K (25 °C)
pressure	1,000 bar

[1)] Depending on molecular context, [2)] Energy: < $1 \cdot 10^{-4}$ kcal/mol, Force: < $5 \cdot 10^{-3}$ kcal/mol/Å, stress: $5 \cdot 10^{-3}$ GPa, displacement: $5 \cdot 10^{-5}$ Å.

The modelling starts usually with tetragonal coordinated tetrasiloxo-components as monomers. The variation in porosity was achieved by adjusting the density during the automated polymer design process in the simulation cell. Different degrees of condensation were achieved by varying the number (one to three) of side-chain options on the monomer and by varying the branching frequency. The resulting free, monovalent silicon-bonded oxygen atoms in the obtained siloxane scaffolds were then converted into silanol groups by automated hydrogenation.

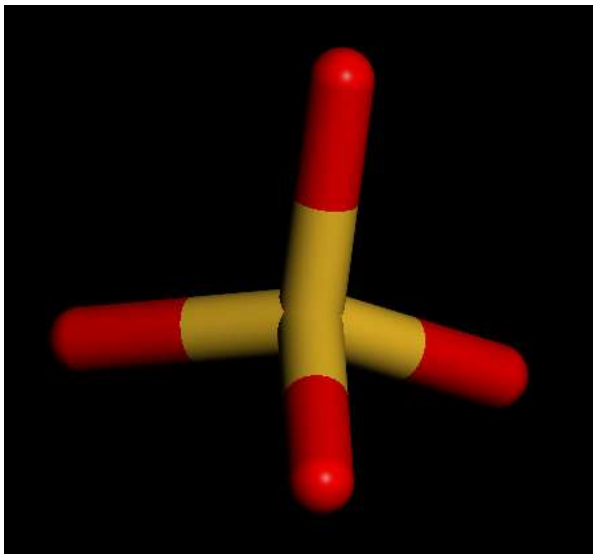

Fig 1: Tetrasiloxo-Monomer before hydrogenation used as building block for amorphous silica surfaces. Colour coding: yellow: silicon, red: oxygen

This is followed by a step-by-step structural optimisation with decreasing convergence tolerances. The extent to which subsequent additional molecular dynamic runs or molecular annealing leads to further geometric optimisation is still under investigation. Figure 1 shows two modelling results with different degrees of condensation but similar porosity.

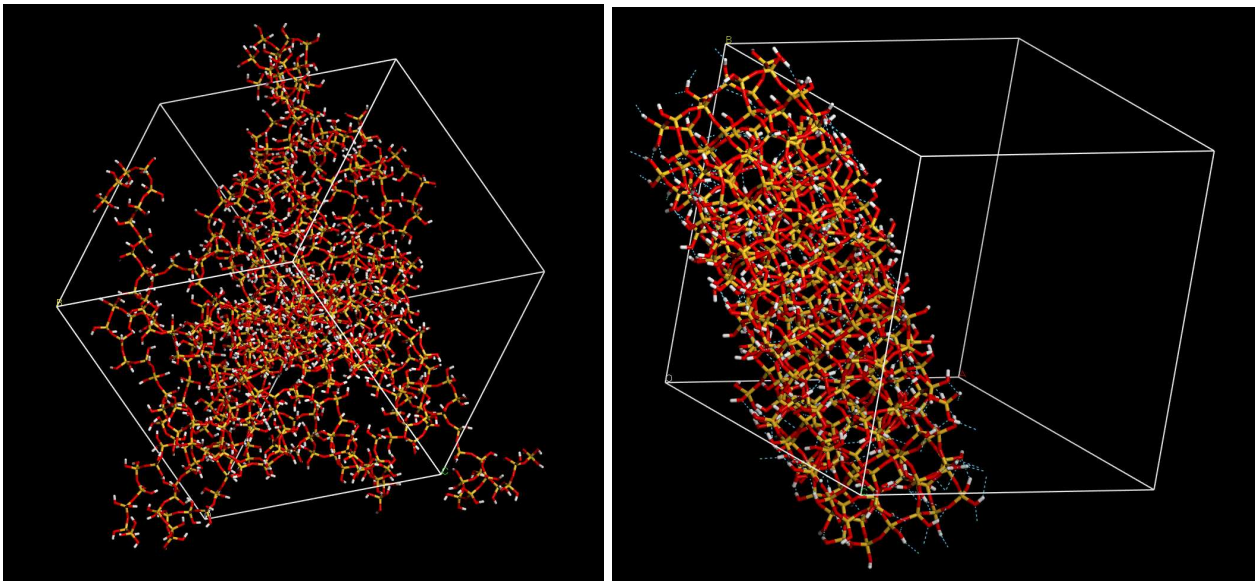

Fig 2: Two simulation cells with periodic boundary conditions of amorphous silicic acid with equal porosity (62%) but different degrees of condensation. Left: $Si_{500}O_{1510}H_{1020}$ (degree of condensation: 49 %) edge length of the simulation cell: 30,2 Å, Right: $Si_{320}O_{820}H_{360}$ (degree of condensation: 78 %), edge length of the simulation cell: 43 Å. Color coding as in Fig. 1, in addition white: hydrogen.

The water vapour adsorption isotherms in the modelled silica structures were simulated using the Metropolis method (Monte Carlo variant (Metropolis N., 1953)) at 298 K in twelve steps at vapour pressures ranging from 0.3166 kPa to 3.166 kPa (vapour pressure at saturation of water at 25 °C). The sampling period was 100 ps per step. Desorption isotherms exhibiting hysteresis, as observed in experiments, cannot be reproduced using molecular dynamics methods, since the underlying processes - such as capillary condensation - require significantly larger particle scales.

Analysis of the simulated adsorption isotherms based on the BET theory (see below) yields a specific surface area of 0.35 m²/g and 0.15 m²/g for the variants with 49% and 78% degree of condensation, respectively. The relative increase in mass ranges from 0.2% to 0.4% at 3.166 kPa water vapour pressure (100 % rH).

Water vapour sorption experiments

The experimental sorption isotherms were recorded gravimetrically using a VSorp (Proumid) sorption balance at 298 K (25 °C) without weight fluctuations and with a resolution of ± 20 µg. That reflects a precision of 10^{-6} or 0,0001 % when a mass of 20 g is applied. To determine the adsorption isotherms, the water vapor partial pressure was increased in 5% increments from 5% to 90% following an initial starting phase at 3% while maintaining a constant weighing frequency of 1,667 mHz (every 10 minutes). The incline was adjusted each time a plateau phase was reached, with a maximum increase of 0.0002 to 0.0005% per 60 minutes. The subsequent desorption isotherm was obtained by decreasing the water vapor partial pressure in 5% increments.

In addition to precipitated silica preparations, the materials examined included crystalline silicon dioxide surfaces (quartz sand) that had undergone varying degrees of weathering or corrosion. The results are particularly clear for the latter, as precipitated silica tends to swell due to its high water absorption capacity and requires long equilibration times.

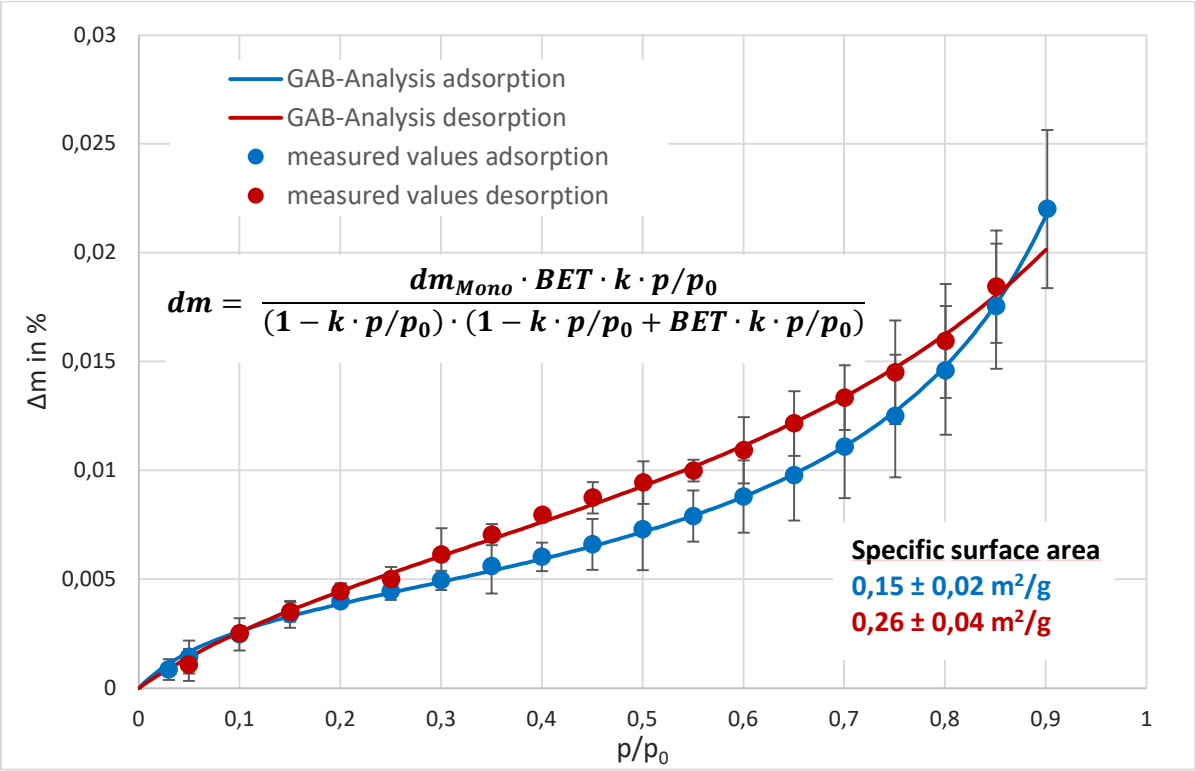

Fig. 3: Relative mass change of new sand in dependency of rel. humidity, done with VSorp sorption balance. Duplicate samples, duration: 2d, time step: 10‘, abs. mass of sample: ca. 25 g, temperature: const. at 25 °C. Solid lines: calculated isotherms in accordance with Guggenheim-Anderson-de Boer-theory. The specific surface area was obtained by fitting the experimental data to the GAB theory, assuming an effective cross-sectional area of 0.1 nm² for a water molecule.

The obtained isotherms can be well described by BET theory (Brunauer, 1938) for low water vapor partial pressures (5 % - 30 %). GAB theory (Arthur, 2018), which is an extension of BET theory, can describe the gravimetric results obtained across the entire range of water vapor partial pressures. From the mathematical modelling of the results based on both BET and GAB theory, the weight contribution of a single layer of the adsorbate (water) can be derived. Given the known density or known effective cross-sectional area of the adsorptive, this yields the specific surface area of the adsorbent.

Summary

The adsorptions isotherms of water on silicic acid surfaces can be simulated with molecular dynamic methods and can give an insight of the molecular structure of the surface. as well as the interactions between the adsorbate and the adsorbent. The adsorption isotherms obtained from the experimental data and the simulated dynamics, respectively, are similar and yield comparable specific surface areas, although the loading in the simulation reaches values approximately 10 times higher.

References

Arthur, E., Tuller, M., Moldrup, P., Greve, M. H., Knadel, M., & de Jonge, L. W. (2018). Applicability of the Guggenheim–Anderson–Boer water vapour sorption model for estimation of soil specific surface area. *European Journal of Soil Science*, *69*(2), 245-255. https://doi.org/10.1111/ejss.12524

Brunauer, S., P. H. Emmett, P. H., E. Teller, E.: *Adsorption of Gases on Multimolecular Layers.* In: *J.Am.Chem.Soc.* 60, Nr. 2, 1938, S. 309–319

Frenkel, D.; Smit, B. *Understanding Molecular Simulation: From Algorithms to Applications*, 2nd Edition, Academic Press: San Diego (2002).

Metropolis, N.; Rosenbluth, A. W.; Rosenbluth, M. N.; Teller, A. H.; Teller, E. *J. Chem. Phys.*, **21**, 1087 (1953).

https://www.sciencedirect.com/topics/chemical-engineering/silica, accessed on 27.5.2027

Liquid Hot Water Hydrolysis for the Extraction of β-Glucans from Industrial Residues

Jesan Joy

Hamburg University of Technology, Institute of Thermal Separation Processes
Eißendorfer Straße 38, D-21073 Hamburg
Email : jesan.joy@tuhh.de

Introduction

β-Glucans (BG) are non-starch polysaccharides composed of β-linked D-glucose units and are widely distributed in nature. They are predominantly found in cereals such as barley and oats, cereal-processing residues including brewer's spent grain and wheat bran, as well as in microbial sources such as yeast, fungi, bacteria, and certain algae. In cereal-derived biomass, β-glucans mainly occur as mixed-linkage polymers containing β-(1→3) and β-(1→4) glycosidic bonds. Their molecular architecture strongly influences their techno-functional behavior and biological effects, including cholesterol reduction, modulation of glycemic response, and prebiotic activity. Consequently, β-glucans are increasingly used as functional ingredients in food, nutraceutical, pharmaceutical, and feed applications.

The demand for β-glucans aligns with increasing interest in sustainable biomass utilization. Large volumes of cereal-processing residues generated by brewing and milling industries are rich in β-glucans but remain underutilized, often serving as low-value animal feed. Their conversion into high-value functional ingredients offers a promising route toward circular bioeconomy and resource-efficient biomass valorization.

Despite their abundance, the extraction of β-glucans from industrial residues remains technologically challenging. β-Glucans are embedded within complex lignocellulosic matrices and interact strongly with cellulose, hemicellulose, lignin, and proteins. Furthermore, β-glucans are sensitive to processing conditions, and uncontrolled depolymerization during extraction can significantly impair their functional properties. Conventional extraction methods, including hot water extraction, acid or alkaline treatment, and enzymatic hydrolysis, are predominantly operated in batch mode and are often associated with long processing times, high chemical consumption, extensive downstream neutralization, and significant batch-to-batch variability. Broad residence time distributions and limited control over reaction severity frequently lead to inconsistent molecular weight profiles and variable product quality.

Liquid hot water (LHW) hydrolysis has emerged as a promising alternative for biomass fractionation and polysaccharide extraction. In LHW processing, biomass is treated with pressurized water at temperatures above 100 °C, maintaining water in the liquid state. Under these conditions, the physicochemical properties of water are altered, including a reduced dielectric constant and an increased ionic product, which promote hydrolytic reactions without the addition of external acids or bases. LHW hydrolysis therefore represents a chemical-free and environmentally benign processing route.

For β-glucan extraction, controlled LHW treatment can enhance solubilization by partially depolymerizing high-molecular-weight polymers and disrupting interactions with other biomass components. However, reaction severity primarily governed by temperature and residence time has a decisive influence on extraction efficiency, molecular integrity, and the formation of degradation products. Excessive severity can result in extensive depolymerization and loss of functional properties, whereas insufficient severity may lead to poor extraction yields. Consequently, systematic investigation of LHW process parameters is essential to establish suitable operating windows for β-glucan extraction.

The objective of the present work is to evaluate the feasibility of β-glucan extraction from selected industrial biomass residues using batch liquid hot water hydrolysis. The study focuses on establishing reproducible experimental conditions, validating reactor operation, and generating a robust dataset that serves as the foundation for subsequent process optimization and future transition toward continuous LHW processing.

Experimental

A series of liquid hot water hydrolysis experiments were conducted to investigate β-glucan extraction from selected β-glucan-rich industrial residues. The raw materials were chosen based on their availability and relevance for sustainable biomass valorization. Prior to hydrothermal treatment, the biomass was mechanically processed to obtain a homogeneous particle size distribution, ensuring reproducible heat and mass transfer during batch processing.

All experiments were performed in high-pressure batch reactors under controlled operating conditions to ensure reproducibility and operational stability. The experimental setup consisted of a multi-reactor batch system with six individual reactors, each having a working volume of 30 mL. The reactors were sealed using high-temperature-resistant rubber O-rings designed to withstand elevated pressures and temperatures. Each reactor

was individually equipped with a heating jacket, allowing precise and independent temperature control across the reactor array.

Magnetic stirring was applied at a constant speed of 250 rpm in all experiments to ensure uniform heat distribution and effective contact between the solid biomass and the liquid phase. Biomass was processed as an aqueous suspension at a defined solids loading, and the reactors were pressurized to approximately 10 bar to maintain water in the liquid state during hydrothermal treatment.

Fig. 1 Experimental setup

The LHW hydrolysis experiments were conducted at temperatures ranging from 100 to 180 °C, with residence times between 2 and 20 minutes. These conditions were selected to represent mild to moderate hydrothermal severity, aiming to promote partial solubilization of β-glucans while minimizing excessive polymer degradation. To quantitatively compare the applied hydrothermal treatment conditions, reaction severity was evaluated using the severity factor (R_0), which integrates the combined effects of temperature and residence time into a single parameter. The logarithmic severity factor was calculated according to:

$$\log R_0 = \log\left(t \cdot \exp\left(\frac{T-100}{14.75}\right)\right)$$

where *T* is the reaction temperature (°C), *t* is the residence time (min), 100 °C is the reference temperature, and 14.75 is an empirical constant related to the apparent activation energy of hydrothermal reactions. The severity factor provides a standardized

framework for comparing different LHW operating conditions and identifying suitable operating windows that balance extraction efficiency and polymer preservation.

The reaction mixtures were subsequently subjected to centrifugation to separate the liquid extract from the solid residue. The liquid fractions, containing solubilized β-glucans and other water-soluble components, were collected and preserved for further analysis. The solid residues were retained for mass balance considerations and assessment of biomass fractionation.

At the current stage of the project, analytical evaluation of the liquid fractions is actively ongoing. β-Glucan concentrations are being determined using the Mixed-Linkage β-Glucan Assay Kit supplied by Megazyme. This enzymatic method enables selective and reliable quantification of mixed-linkage β-glucans present in biomass derived extracts. All analyses are performed in accordance with the manufacturer's protocol, and results are reported as grams of β-glucan per 100 grams to ensure consistency and comparability across different experimental conditions.

The completed experimental campaign enabled validation of the batch reactor setup, confirmation of safe and stable operation under pressurized conditions, and establishment of standardized sampling and handling procedures. The generated samples and analytical data form the basis for systematic evaluation of process performance.

Summary

This work demonstrates the technical feasibility of extracting β-glucans from industrial biomass residues using batch liquid hot water hydrolysis under controlled hydrothermal conditions. The conducted experiments confirmed stable and reproducible reactor operation and enabled systematic investigation of β-glucan solubilization at mild to moderate reaction severities. The batch reactor setup proved suitable for generating consistent β-glucan-rich hydrolysates and for establishing standardized operating and sampling procedures.

Preliminary results indicate that key process parameters particularly temperature and residence time strongly influence β-glucan extraction efficiency, molecular weight distribution, and overall product quality. These findings highlight the importance of precise control of hydrothermal conditions to balance improved extractability with preservation of functional β-glucan structure. The ongoing analytical evaluation will provide quantitative insight into the relationship between liquid hot water process parameters and β-glucan yield, forming the basis for systematic process optimization.

The current batch based investigation focuses on the reproducible production of β-glucan-rich hydrolysates and the identification of robust operating windows. These findings establish the foundation for future transition to continuous liquid hot water hydrolysis, enabling improved process control, reproducibility, and scalability.

Overall, this work addresses a key technological gap in β-glucan production by developing a severity-based framework for chemical-free extraction and providing a pathway toward industrial implementation and sustainable biomass valorization.

References

Auinger, A., Riede, L., Bothe, G., Busch, R., & Gruenwald, J. (2013). Yeast (1,3)-(1,6)-beta-glucan helps to maintain the body's defence against pathogens: a double-blind, randomized, placebo-controlled, multicentric study in healthy subjects. *European Journal of Nutrition*, *52*(8), 1913. https://doi.org/10.1007/s00394-013-0492-z

Benito-Román, Alonso, E., & Cocero, M. J. (2013). Pressurized hot water extraction of β-glucans from waxy barley. *The Journal of Supercritical Fluids*, *73*, 120–125. https://doi.org/10.1016/j.supflu.2012.09.014

Benito-Román, Ó., Alonso, E., Gairola, K., & Cocero, M. J. (2013). Fixed-bed extraction of β-glucan from cereals by means of pressurized hot water. *Journal of Supercritical Fluids*, *82*, 122–128. https://doi.org/10.1016/j.supflu.2013.07.003

Benito-Román, Ó., Martín-Cortés, A., Cocero, M. J., & Alonso, E. (2016). Dissolution of (1-3),(1-4)-β-Glucans in Pressurized Hot Water: Quantitative Assessment of the Degradation and the Effective Extraction. *International Journal of Carbohydrate Chemistry*, *2016*(1), 2189837. https://doi.org/10.1155/2016/2189837

Carvalheiro, F., Duarte, L. C., Gírio, F., & Moniz, P. (2016). Hydrothermal/Liquid Hot Water Pretreatment (Autohydrolysis): A Multipurpose Process for Biomass Upgrading. *Biomass Fractionation Technologies for a Lignocellulosic Feedstock Based Biorefinery*, *6*(2), 315–347. https://doi.org/10.1016/B978-0-12-802323-5.00014-1

Chioru, A., & Chirsanova, A. (2023). β-Glucans: Characterization, Extraction Methods, and Valorization. *Food and Nutrition Sciences*, *14*(10), 963–983. https://doi.org/10.4236/fns.2023.1410061

Doehlert, D. C., Simsek, S., & McMullen, M. S. (2012). Extraction of β-glucan from oats for soluble dietary fiber quality analysis. *Cereal Chemistry*, *89*(5), 230–236. https://doi.org/10.1094/CCHEM-08-11-0103

Du, B., Meenu, M., Liu, H., & Xu, B. (2019). A Concise Review on the Molecular Structure and Function Relationship of β-Glucan. *International Journal of Molecular Sciences*, *20*(16), 4032. https://doi.org/10.3390/ijms20164032

Gautério, G. V., Silvério, S. I. D. C., Egea, M. B., & Lemes, A. C. (2022). β-glucan from brewer's spent yeast as a techno-functional food ingredient. *Frontiers in Food Science and Technology*, *2*, 1074505. https://doi.org/10.3389/frfst.2022.1074505

Jantason, N., Suphantharika, M., Wipatanawin, A., Chansong, S., & Payongsri, P. (2024). Valorization of Spent Grains from Beer Production through β-Glucan Extraction. *Foods*, *13*(3), 440. https://doi.org/10.3390/foods13030440

Lante, A., Canazza, E., & Tessari, P. (2023). Beta-Glucans of Cereals: Functional and Technological Properties. *Nutrients*, *15*(9). https://doi.org/10.3390/nu15092124

Maheshwari, G., Sowrirajan, S., & Joseph, B. (2017). Extraction and Isolation of β-Glucan from Grain Sources—A Review. *Journal of Food Science*, *82*(7), 1535–1545. https://doi.org/10.1111/1750-3841.13765

Nirmala Prasadi, V. P., & Joye, I. J. (2020). Dietary fibre from whole grains and their benefits on metabolic health. *Nutrients*, *12*(10), 1–20. https://doi.org/10.3390/nu12103045

Özen, S., Ünlü, A., Özbek, H. N., & Göğüş, F. (2024). β-Glucan Extraction from Hull-Less Barley by a Novel Approach: Microwave-Assisted Pressurized CO2/H2O. *Food and Bioprocess Technology 2024 17:12*, *17*(12), 4781–4793. https://doi.org/10.1007/s11947-024-03420-1

Rogalinski, T., Liu, K., Albrecht, T., & Brunner, G. (2008). Hydrolysis kinetics of biopolymers in subcritical water. *The Journal of Supercritical Fluids*, *46*(3), 335–341. https://doi.org/10.1016/j.supflu.2007.09.037

Steiner, J., Kupetz, M., & Becker, T. (2023). Influence of Hydrothermal Treatment of Brewer's Spent Grain on the Concentration and Molecular Weight Distribution of 1,3-1,4-β-D-Glucan and Arabinoxylan. *Foods*, *12*(20). https://doi.org/10.3390/foods12203778

Zhu, F., Du, B., & Xu, B. (2016). A critical review on production and industrial applications of beta-glucans. *Food Hydrocolloids*, *52*(1), 275–288. https://doi.org/10.1016/j.foodhyd.2015.07.003

Carriers and Cocrystals for Carbamazepine Aqueous Solubility Enhancement

Seyedabbas Shahrtash

Faculty of Chemistry, Wrocław University of Science and Technology, Wrocław, Poland
seyedabbas.shahrtash@pwr.edu.pl

1. Introduction

Carbamazepine (CBZ) is a first-line antiepileptic and a classic Biopharmaceutics Classification System (BCS) Class II drug, with high permeability but low aqueous solubility. This often results in poor bioavailability and requires higher doses, which can cause adverse side effects [1]. Researchers have addressed CBZ's solubility limitations using solid-state modification techniques. Pharmaceutical cocrystallization is particularly effective, as combining the active pharmaceutical ingredient (API) with a conformer such as nicotinamide (NAM) improves physicochemical properties without changing pharmacological activity. The CBZ-NAM cocrystal system is notable for its robust hydrogen-bonded supramolecular synthons and improved stability and solubility compared to pure CBZ [2]. Drug solubility can be further improved by incorporating APIs into highly porous carrier systems, which increase the surface area exposed to gastrointestinal fluids. Starch aerogels with a highly porous internal structure are an ideal carrier for this purpose [3,4].

Traditional drying technology creates capillary forces that collapse hydrogels' pores, producing dense xerogels. Supercritical carbon dioxide ($scCO_2$) drying of alcogels, however, addresses this challenge by bypassing the vapor-liquid two phase region, allowing for the production of mesoporous aerogels [5].

This research examines the synthesis of CBZ-NAM cocrystals via different methods and the production of optimized corn starch aerogels as carriers via supercritical technology.

2. Experimental

2.1. Materials

Corn starch from Sigma Aldrich was used to prepare aerogels. CBZ (purity > 98%) and NAM (purity > 99.5%), both from Sigma Aldrich, were used to prepare cocrystals. Absolute ethanol (purity 99.9%, Sigma Aldrich) served as the water-switching solvent.

2.2. *Aerogel Preparation*

To prepare hydrogels, 10 g of corn starch was added to 100 mL of distilled water and stirred with a magnetic stirrer at room temperature to make a 10% (w/v) suspension. The beaker was placed in an oil bath heated to 160°C, which brought the mixture to 90°C, while stirring continued with an overhead stirrer. After gelatinization, the gels were poured into Petri dishes to a thickness of about 1 cm. One sample was kept at 3°C for 5 days to allow prolonged retrogradation, and the second sample was subjected to a step-wise solvent exchange immediately after cooling.

Supercritical drying was carried out using a Eurotechnica HPE-250 drying unit. This system has a 400 cm^3 stainless steel high-pressure vessel with an electric heating jacket. Drying was performed at 35°C and 20 MPa. The drying process comprised four cycles of scCO2 flow at 7 L_N/min, with 30 min of batch exposure between cycles and a one-hour batch exposure at the beginning and at the end of the process. The system was then slowly depressurized at 0.3 MPa/min.

2.3. Cocrystal formation

CBZ-NAM cocrystals were prepared using the cryomilling and solvent evaporation methods. Cryomilling was performed in a RETSCH CryoMill equipment. A 5 g mixture of CBZ-NAM at a 1:1 molar ratio was placed in a 50 mL grinding cell with five stainless steel balls, and three cryomilling cycles of 10 min each were conducted at a frequency of 30 s^{-1}.

For the solvent evaporation method, CBZ and NAM mixture, according to a 1:1 molar ratio, was transferred into a glass beaker. Ethanol was then added as the solvent. For the 0.01 mol scale, 60 mL of ethanol was added. The mixture was placed on a magnetic stirrer equipped with heating, and the temperature was set to 50 °C. Stirring was performed at approximately 400–500 rpm. A clear solution was generally obtained after approximately 30-40 min of hot-plate stirring. Then, the clear solution was removed and allowed to evaporate slowly at room temperature.

2.4. Characterization Techniques

The textural properties and internal morphology of the aerogels were characterized utilizing Brunauer–Emmett–Teller (BET) nitrogen adsorption and Scanning Electron

Microscopy (SEM). Additionally, Fourier Transform Infrared Spectroscopy (FTIR) and Differential Scanning Calorimetry (DSC) were employed to confirm cocrystal formation.

3. Results and Discussion

3.1. Morphological Analysis and Retrogradation Effect

The textural properties of both starch aerogels were evaluated. Both aerogels showed high specific surface area S_{BET}, in the range 200-215 m^2/g. The prolonged, 5-day retrogradation resulted in an overall higher adsorption capacity, a 13.2% increase in total pore volume, and an 8.3% increase in average pore diameter, confirmed by BET analysis. The Scanning electron microscopy (SEM) micrographs of cross sections of both starch aerogels are shown in Figure 1, revealing their highly porous structures.

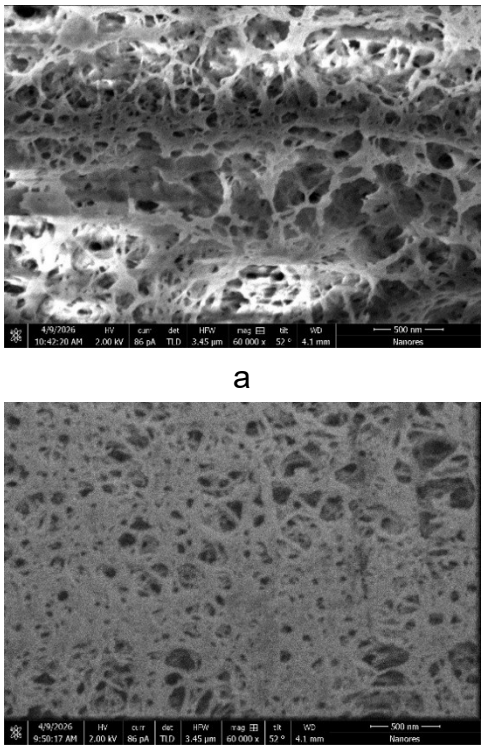

a

b

Fig. 1 SEM micrographs of the internal cross-sectional architecture of aerogels with minimal retrogradation (a) and prolonged, 5-day retrogradation (b). Scale bars represent 500 nm

3.1. Fourier Transform Infrared (FTIR) Spectroscopy

As shown in Figure 2, the FTIR spectrum of CBZ shows characteristic N-H stretching bands at 3463 cm^{-1} and 3152 cm^{-1}. A strong carbonyl band also appears at 1674 cm^{-1}. The FTIR spectrum of NAM shows two N-H stretching bands at 3356 and 3147 cm^{-1}. In the carbonyl region, a strong and sharp absorption is observed at 1674 cm^{-1}.

The FTIR spectrum of the both CBZ-NAM cocrystals show characteristic N-H peaks at 3444 cm^{-1}, 3387 cm^{-1} and 3208 cm^{-1}, which indicate shifts from the pure CBZ and NAM N-H stretching bands. Furthermore, the CBZ-NAM cocrystals show peaks around 1682 and 1655 cm^{-1}, indicating shifts in the carbonyl stretching bands of CBZ and NAM. These shifts in the N-H and C=O stretching bands confirm the new hydrogen bonds and CBZ-NAM complex formation [6].

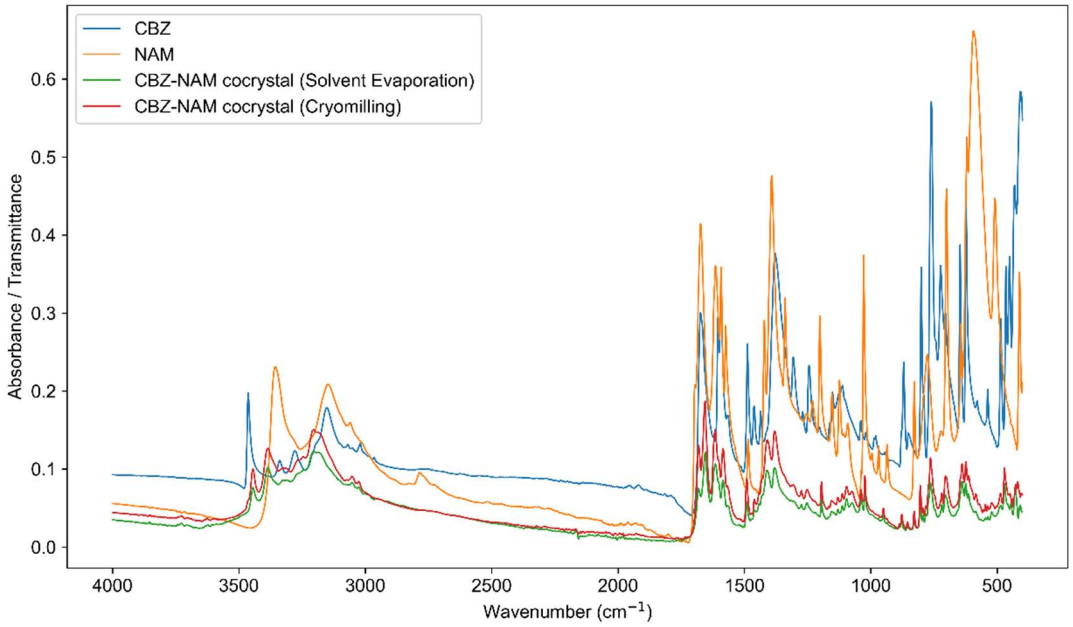

Fig. 2. FTIR spectra of CBZ, NAM, and CBZ-NAM cocrystals produced using cryomilling and solvent evaporation techniques

3.2. Differential Scanning Calorimetry (DSC)

Figure 3 shows Differential Scanning Calorimetry (DSC) thermograms of CBZ-NAM cocrystals obtained using the solvent evaporation method as well as pure CBZ and NAM. As shown, a single sharp melting endotherm near 160°C confirms the formation of a distinct crystalline phase, distinct from both CBZ and NAM.

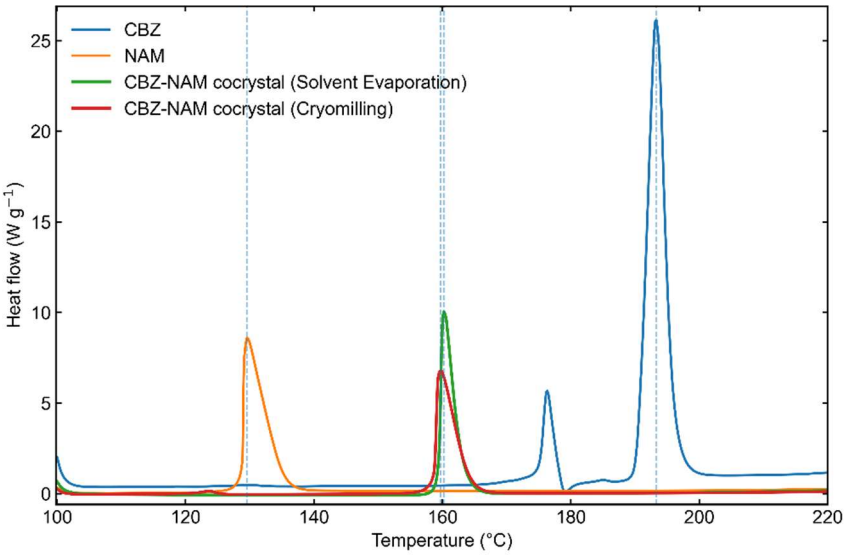

Fig. 3. DSC thermogram of CBZ, NAM and CBZ-NAM cocrystals obtained using cryomilling and solvent-evaporation methods

Summary and Outlook

This study presents the comparison of corn starch aerogels obtained with a short and a 5-day long retrogradation time. A 5-day retrogradation period led to a 13% increase in total pore volume and a larger mesopore diameter. The aerogel obtained with a prolonged retrogradation will be further used as a CBZ-NAM cocrystal carrier.

References

[1] M. A. García *et al.*, "Biowaiver Monograph for Immediate-Release Solid Oral Dosage Forms: Carbamazepine," *Journal of Pharmaceutical Sciences*, vol. 110, no. 5, pp. 1935–1947, May 2021, doi: 10.1016/j.xphs.2021.02.019.

[2] J. Ouyang *et al.*, "Cocrystals of carbamazepine: Structure, mechanical properties, fluorescence properties, solubility, and dissolution rate," *Particuology*, vol. 90, pp. 20–30, Jul. 2024, doi: 10.1016/j.partic.2023.11.016.

[3] S. Milovanovic, D. Markovic, I. Jankovic - Castvan, and I. Lukic, "Cornstarch aerogels with thymol, citronellol, carvacrol, and eugenol prepared by supercritical CO2-assisted techniques for potential biomedical applications," *Carbohydrate Polymers*, vol. 331, p. 121874, May 2024, doi: 10.1016/j.carbpol.2024.121874.

[4] C. A. García-González, M. Alnaief, and I. Smirnova, "Polysaccharide-based aerogels - Promising biodegradable carriers for drug delivery systems," *Carbohydrate Polymers*, vol. 86, no. 4, pp. 1425–1438, Oct. 2011, doi: 10.1016/j.carbpol.2011.06.066.

[5] E. B. Chemere, T. L. Mhlabeni, W. Mhike, M. L. Mavhungu, and M. B. Shongwe, "A comprehensive review of types, synthesis strategies, advanced designing and

applications of aerogels," *R. Soc. Open Sci.*, vol. 12, no. 5, p. 241975, May 2025, doi: 10.1098/rsos.241975.

[6] Z. Rahman, C. Agarabi, A. S. Zidan, S. R. Khan, and M. A. Khan, "Physico-mechanical and Stability Evaluation of Carbamazepine Cocrystal with Nicotinamide," *AAPS PharmSciTech*, vol. 12, no. 2, pp. 693–704, Jun. 2011, doi: 10.1208/s12249-011-9603-4.

Response Surface Optimization of Microwave-Assisted Extraction of Bioactive Compounds from Blueberry Leaves and Assessment of Their Functional Properties

Mihailo Mladenović, Milica Milutinović, Mirjana Rajilić-Stojanović

Faculty of Technology and Metallurgy, Department of Biochemical Engineering and Biotechnology, University of Belgrade, mladenovicm@tmf.bg.ac.rs

Introduction

Blueberry leaves (*Vaccinium myrtillus*), an underutilized by-product of berry production, have recently attracted attention as a rich source of polyphenolic compounds with significant biological potential [1-2]. These compounds are known for their strong antioxidant activity and their ability to modulate carbohydrate metabolism through the inhibition of key digestive enzymes such as α-amylase [3], thereby contributing to the control of postprandial hyperglycemia.

The efficiency of polyphenol recovery is highly dependent on the extraction technique and processing conditions. Microwave-assisted extraction (MAE) has emerged as a rapid and efficient method that enhances mass transfer and reduces extraction time and solvent consumption compared to conventional techniques [4-5]. However, the optimization of extraction parameters is crucial to maximize the yield and preserve the bioactivity of the obtained extracts.

Response surface methodology (RSM) is a powerful statistical tool that enables the evaluation of multiple variables and their interactions, allowing the identification of optimal extraction conditions [6]. Therefore, the aim of this study was to optimize MAE parameters for the recovery of polyphenol-rich extracts from blueberry leaves using RSM, and to evaluate their antioxidant, antimicrobial, prebiotic, and α-amylase inhibitory properties.

Experimental

Microwave-assisted extraction of blueberry leaves was optimized using response surface methodology (RSM). A central composite design (CCD) was applied to evaluate the effects of three independent variables: ethanol content in the solvent (%), extraction time (s), and liquid-to-solid ratio (mL/g). The coded and actual levels of the investigated factors are presented in Table 1.

Table 1. The coded and actual levels of the investigated factors.

Factor	-1 level	0 level	+1 level
Ethanol proportion (%)	20	50	80
Time (s)	60	120	180
Liquid to solid ratio (mL/g)	15	22,5	30

For each experimental run, 2 g of finely ground blueberry leaves were mixed with the appropriate ethanol–water solvent mixture in 300 mL Erlenmeyer flasks. The extractions were performed at a constant microwave power of 90 W, according to the experimental matrix generated by the CCD. After extraction, the samples were vacuum filtered, and the obtained supernatants were stored in the dark at 4 °C until further analysis.

The experimental design consisted of 17 runs, including three central points used to estimate experimental variability and model reproducibility. The investigated responses were total polyphenol content (TPC), antioxidant activity determined by DPPH and FRAP assays and reduction of α-amylase activity.

The obtained experimental data were fitted to a second-order polynomial model in order to describe the relationship between the extraction variables and the measured responses. The model included linear, quadratic, and interaction terms. The adequacy of the model was evaluated by analysis of variance (ANOVA), coefficient of determination (R^2), adjusted R^2, and the statistical significance of model terms. Three-dimensional response surface plots were generated to visualize the effects of two independent variables on each response while keeping the third variable constant.

Summary

The obtained results demonstrated that extraction conditions significantly influenced the total polyphenol content (TPC) of blueberry leaf extracts, with values ranging from 301.35 to 699.13 mg GAE/g d.m. (Table 1). The highest TPC value was obtained in experiment 16 (699.13 mg GAE/g d.m.), performed at 80% ethanol, 180 s extraction time, and a liquid-to-solid ratio of 15 mL/g. High TPC values were also observed in experiments 17, 15, and 12, indicating that longer extraction times and lower liquid-to-solid ratios generally favored polyphenol recovery. In contrast, lower TPC values were mainly associated with higher liquid-to-solid ratios and less favorable solvent compositions. The results further confirmed that microwave-assisted extraction parameters, particularly ethanol concentration and

liquid-to-solid ratio, strongly affected the extraction efficiency and recovery of bioactive compounds from blueberry leaves.

Table 1. Experimental design setup and obtained results.

Experiment	Ethanol proportion (%)	Time (s)	Liquid-to-solid ratio (mL/g)	TPC (mg GAE / g d.m.)	Reduction in α-amylase activity (IU / g d.m.)	DPPH (%)	FRAP (mmol $FeSO_4$/ g d.m.)
1	20	180	30	301.35	0.089	48.0	1.77
2	0	120	22.5	359.71	0.191	57.6	2.26
3	100	120	22.5	340.14	0.204	43.5	2.21
4	80	60	15	365.94	0.127	68.6	2.21
5	50	220.91	22.5	328.74	0.069	73.5	1.97
6	50	120	22.5	386.35	0.111	62.1	2.25
7	80	180	30	332.29	0.039	39.6	2.06
8	80	60	30	346.18	0.129	27.6	2.60
9	20	60	15	497.97	0.063	78.5	2.95
10	50	120	35.11	346.19	0.079	39.3	2.14
11	20	60	30	364.84	0.196	41.7	2.48
12	20	180	15	574.03	0.200	85.3	3.32
13	50	19.09	22.5	434.47	0.108	52.5	2.60
14	50	120	22.5	511.03	0.137	65.3	3.14
15	50	120	22.5	590.83	0.158	65.3	3.52
16	80	180	15	699.13	0.299	85.2	4.24
17	50	120	9.89	614.93	0.443	92.3	3.26

The antioxidant activity of blueberry leaf extracts, determined by DPPH and FRAP assays, varied considerably depending on the extraction conditions. DPPH radical scavenging activity ranged from 27.6% to 92.3%, while FRAP values varied between 1.77 and 4.24 mmol $FeSO_4$/g d.m., indicating substantial differences in antioxidant potential among the obtained extracts. The highest DPPH activity was observed in experiment 17

(92.3%), followed by experiments 12 and 16 (85.3% and 85.2%, respectively). Similarly, the highest FRAP value was recorded in experiment 16 (4.24 mmol $FeSO_4$/g d.m.), while experiments 15, 12, and 17 also exhibited high reducing capacity. These results suggest that longer extraction times and lower liquid-to-solid ratios positively influenced the recovery of antioxidant compounds. Correlation analysis revealed a strong and highly significant positive relationship between TPC and antioxidant activity determined by both DPPH and FRAP assays ($p < 0.001$). The correlation between TPC and FRAP was particularly high ($R^2 = 0.966$), indicating that phenolic compounds are the major contributors to the reducing antioxidant capacity of the extracts. A positive correlation was also observed between TPC and DPPH radical scavenging activity ($R^2 = 0.753$), although the relationship was somewhat weaker, suggesting that additional bioactive compounds may also contribute to radical scavenging activity.

The reduction in α-amylase activity varied substantially among the investigated extracts, range from 0.039 to 0.443 IU/g d.m., indicating a strong influence of extraction conditions on enzyme inhibitory potential. The highest inhibitory activity was observed in experiment 17 (0.443 IU/g d.m.), followed by experiment 16 (0.299 IU/g d.m.) and experiments 3, 11, and 12, which also showed elevated values. In contrast, the lowest activity was recorded in experiment 7 (0.039 IU/g d.m.), while experiments 5 and 9 also exhibited relatively weak inhibitory effects. The obtained results suggest that lower liquid-to-solid ratios and longer extraction times generally favoured the recovery of compounds responsible for α-amylase inhibition. Similar to antioxidant activity, the inhibitory effect showed a highly significant although moderate positive correlation with TPC ($R^2 = 0.634$, $p < 0.001$), indicating that α-amylase inhibition does depend on the quantity of phenolic compounds, but also on their qualitative composition and structural characteristics.

Mathematical models developed using RSM successfully described the influence of extraction parameters on all investigated responses. Quadratic models for TPC, DPPH, FRAP, and reduction in α-amylase activity showed good agreement with experimental data, with high coefficients of determination (R^2 values up to 0.976). Among the investigated factors, the liquid-to-solid ratio exhibited the strongest effect on most responses, while ethanol concentration and extraction time also significantly contributed to extraction efficiency and biological activity. Three-dimensional response surface plots revealed the existence of optimal extraction regions, particularly for reduction in α-amylase activity, at high ethanol concentrations and low liquid-to-solid ratios (Figure 1).

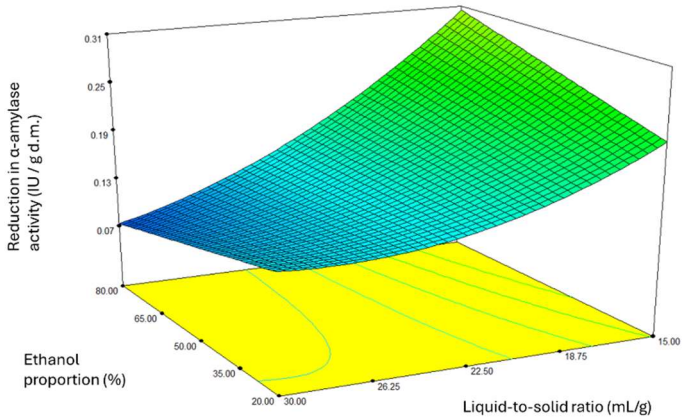

Figure 1. Response surface plot showing the effect of ethanol proportion and liquid-to-solid ratio on reduction in α-amylase activity of blueberry leaf extracts obtained by microwave-assisted extraction.

Numerical optimization ($Y = 0.150 + 0.005A + 0.0034B - 0.062C - 0.035AC - 0.063BC - 0.030B^2 + 0.031C^2$) predicted that the optimal extraction conditions for maximizing reduction in α-amylase activity were 84% ethanol, 193 s extraction time, and a liquid-to-solid ratio of 11.5 mL/g. Validation experiments performed under these conditions confirmed the adequacy and predictive ability of the developed model, as the experimentally obtained value (0.575 IU / g d.m.) was within the corresponding 95% prediction intervals. Importantly, this value was higher than the highest activity observed among the experimental runs (0.443 IU/g d.m.), highlighting the effectiveness of the RSM optimization approach in identifying improved extraction conditions.

The α-amylase inhibitory activities of the blueberry leaf extracts and the positive control (acarbose) were evaluated and compared based on their IC_{50} values. The extract obtained under the optimized MAE conditions exhibited a potent inhibitory effect with an IC_{50} value of 73.84 μg/mL. This represents a remarkable, approximately 10.4-fold increase in inhibitory activity compared to the conventional maceration extract of the same plant material (IC_{50} = 770 μg/mL). Such a drastic improvement strongly demonstrates the efficiency of the optimized MAE process in rupturing plant cell walls and selectively recovering highly active polyphenolic compounds without thermal degradation. Furthermore, while the commercial drug acarbose expectedly displayed the highest potency (IC_{50} = 2.76 μg/mL) due to its nature as a pure, isolated chemical compound, the optimized crude MAE extract remained highly competitive, being only 26.7 fold less potent than the pharmaceutical standard. These findings confirm the successful validation of the

optimization model and underline the potential of optimized blueberry leaf MAE extracts as powerful natural alternatives in managing postprandial hyperglycemia.

Taken together, these findings indicate that MAE combined with RSM represents an efficient approach for the recovery of biologically active compounds from blueberry leaves. Although MAE demonstrated high efficiency in the extraction of bioactive compounds from blueberry leaves, other non-conventional extraction techniques may further improve extraction yield and biological activity. Therefore, future studies should investigate and compare alternative green extraction technologies to identify the most effective approach for polyphenol recovery. The study demonstrated that blueberry leaf extracts possess significant antioxidant and enzyme inhibitory potential, supporting their possible application in functional foods, nutraceuticals, and formulations intended for modulation of carbohydrate metabolism and prevention of postprandial hyperglycemia. Future studies should focus on detailed characterization of individual phenolic compounds, evaluation of synergistic effects, and *in vivo* confirmation of the observed biological activities.

Acknowledgment

This work was supported by the Ministry of Science, Technological Development and Innovation of the Republic of Serbia (Contract No. 451-03-34/2026-03/ 200135 and 451-03-33/2026-03/ 200135)

References

[1] Wang, J., Tian, J., Li, D., Gao, N., Deng, J., Yang, X., He, Y., Li, B., & Wang, L. (2025). Blueberry leaves as a promising sustainable source of polyphenols: Chemical composition, functional activities and future application perspectives. *Food Research International*, 207, 116110.

[2] Piljac-Žegarac, J., Belščak, A., & Piljac, A. (2009). Antioxidant capacity and polyphenolic content of blueberry (*Vaccinium corymbosum* L.) leaf infusions. *Journal of medicinal food*, 12(3), 608-614.

[3] Nyambe-Silavwe, H., Villa-Rodriguez, J. A., Ifie, I., Holmes, M., Aydin, E., Jensen, J. M., & Williamson, G. (2015). Inhibition of human α-amylase by dietary polyphenols. *Journal of Functional Foods*, 19, 723-732.

[4] Kaufmann, B., & Christen, P. (2002). Recent extraction techniques for natural products: microwave-assisted extraction and pressurised solvent extraction. *Phytochemical*

Analysis: An International Journal of Plant Chemical and Biochemical Techniques, 13(2), 105-113.

[5] Routray, W., & Orsat, V. (2012). Microwave-assisted extraction of flavonoids: a review. *Food and Bioprocess Technology*, 5(2), 409-424.

[6] Bezerra, M. A., Santelli, R. E., Oliveira, E. P., Villar, L. S., & Escaleira, L. A. (2008). Response surface methodology (RSM) as a tool for optimization in analytical chemistry. *Talanta*, 76(5), 965-977.

Magnetic Bacterial Nanocellulose Sphere Nanocomposites as Functional Adsorbents for Wastewater Treatment

Kaja Gajšt[a], Katja Vasić[a,b], Mateja Primožič[a]

[a] Laboratory for Separation Processes and Product Design, Faculty of Chemistry and Chemical Engineering, University of Maribor, Slovenia; mateja.primozic@um.si

[b] Laboratory for Applied Electromagnetics, Faculty of Electrical Engineering and Computer Science, University of Maribor, Slovenia

Introduction

Bacterial nanocellulose (BNC) represents a pure, sustainable, and biocompatible alternative to traditional plant-derived cellulose (Barja, 2021). Due to its exceptional physicochemical properties, such as high crystallinity, excellent mechanical strength, remarkable water-holding capacity, and a well-defined three-dimensional porous structure, it serves as an excellent platform for the development of advanced materials and nanocomposites (Wasim et al., 2022). Despite these advantages, native BNC lacks certain key functional properties, among which magnetic responsiveness is particularly important. To overcome this limitation, the incorporation of magnetic nanoparticles (MNPs) has emerged as an effective strategy. This modification results in magnetic bacterial nanocellulose (MBNC), a nanocomposite that combines the structural and biophysical benefits of BNC with magnetic functionality, thus enabling external magnetic control and improving performance in applications such as targeted drug delivery and separation systems (Sriplai and Pinitsoontorn, 2021). An important factor in MBNC design is BNC morphology. While static cultivation produces BNC membranes, dynamic fermentation enables the formation of BNC beads with higher surface area, uniform porosity, and improved adsorption properties, making them more suitable for nanoparticle incorporation and targeted applications (Diaz-Ramirez et al., 2021; El-Gendi et al., 2022).

In this study, MBNC beads were synthesized using two different approaches. In the *in situ* method, BNC acts as a reaction matrix for nanoparticle formation within its porous structure. In the second approach, MNPs were added directly into the culture medium during BNC biosynthesis, enabling their entrapment within the developing fibrillar network. The influence of different synthesis parameters on MBNC properties was investigated to optimize nanocomposite production. The synthesized MBNC beads were characterized.

Furthermore, the applicability of the developed nanocomposites for the removal of Cr(VI) ions from aqueous solutions was assessed. Heavy metals are among the most common

pollutants present in industrial wastewater and represent a major environmental concern due to their persistence, toxicity, and adverse effects on aquatic ecosystems and human health. In particular, hexavalent chromium (Cr(VI)) is considered one of the most hazardous heavy metal contaminants because of its high solubility, mobility, and carcinogenicity (Sharma et al., 2022). Among various wastewater treatment technologies, adsorption is widely regarded as an effective and economical approach owing to its high efficiency, simple operation, and rapid kinetics (Satyam and Patra, 2024).

Experimental

BNC beads were produced using microorganism *Komagataeibacter xylinus* cultivated in Hestrin and Schramm (HS) medium (Hestrin and Schramm, 1954) under dynamic conditions. After cultivation, the obtained BNC beads were purified by alkaline treatment with NaOH and washed until a neutral pH was achieved.

Magnetic nanoparticles (MNPs, Fe_3O_4) were synthesized by a coprecipitation method using Fe^{2+} and Fe^{3+} salts in alkaline conditions (Šulek et al., 2010). The resulting nanoparticles were magnetically separated, washed, dried, and ground into powder.

MBNC beads were prepared using two different approaches (Fig.1). In the first approach, an *in situ* coprecipitation method was applied, where pre-formed BNC beads were impregnated with iron ion solution under nitrogen atmosphere, followed by ammonia-induced formation of Fe_3O_4 nanoparticles directly within the porous BNC structure. In the second approach, MBNC beads were synthesized during agitated fermentation by adding pre-synthesized MNPs directly into the HS culture medium prior to inoculation. Different nanoparticle concentrations and agitation speeds were evaluated to optimize bead formation and magnetic properties.

Before characterization, samples were freeze-dried. The morphology and elemental composition of the MBNC beads were analysed using scanning electron microscopy (SEM) and energy dispersive spectroscopy (EDS), while their magnetic properties were evaluated by VSM at 300 K.

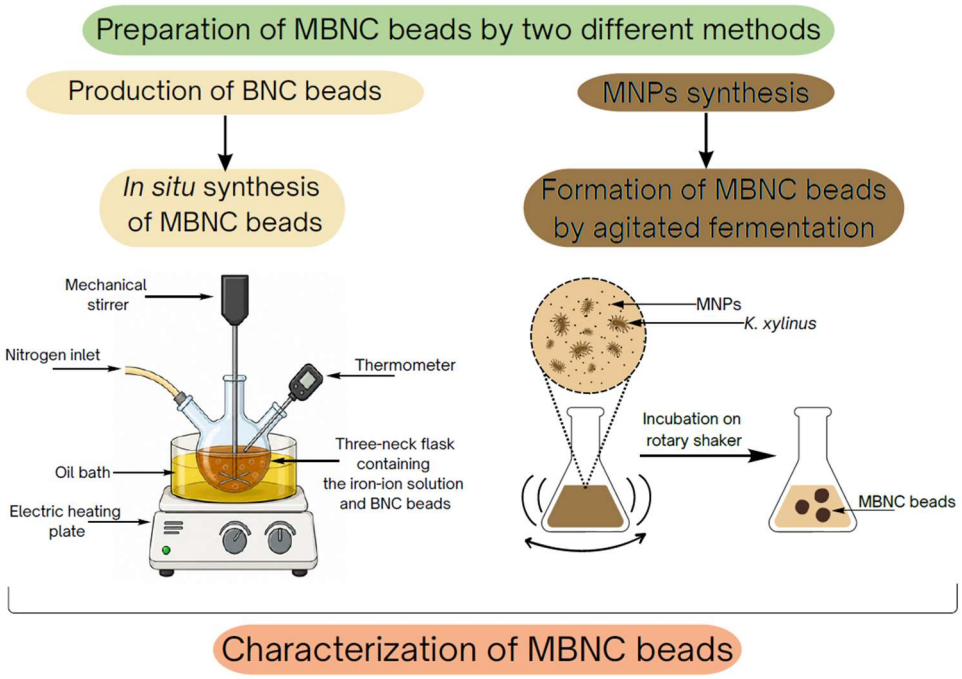

Fig. 1: Process scheme of MBNC beads preparation

The applicability of the prepared MBNC beads for wastewater treatment was further investigated through Cr(VI) adsorption experiments. Batch adsorption studies were performed using aqueous Cr(VI) solutions with different initial concentrations. The adsorption efficiency of MBNC beads was evaluated under shaking conditions at room temperature, while residual Cr(VI) concentrations were determined spectrophotometrically using the 1,5-diphenylcarbazide method (Lace et al., 2019; Vasic et al., 2023). In addition, the regeneration and reusability of the adsorbent were assessed over multiple adsorption–desorption cycles using HCl as the desorbing agent.

The SEM and EDS results presented in Fig. 2 and Fig. 3 confirmed the successful incorporation of MNPs into the nanocellulose network. The SEM micrographs clearly revealed the characteristic three-dimensional network structure of BNC, composed of long interconnected fibers forming a porous and entangled matrix. Numerous spherical and hemispherical structures, corresponding to MNPs aggregates, were observed both on the fibre surfaces and within the interfibrillar spaces. EDS analysis confirmed the presence of all three elements characteristic of MBNC composition (C, O, and Fe) in both samples, with the sample prepared via the *in situ* synthesis exhibiting a higher mass fraction of Fe. The magnetic properties evaluated by VSM showed saturation magnetization values of 61 emu/g for the *in situ* MBNC sample and 41 emu/g for the MBNC sample synthesized by agitated fermentation.

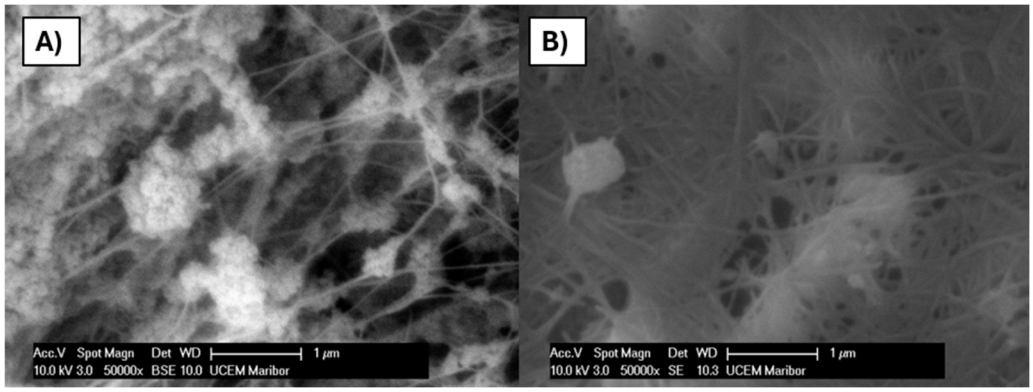

Fig. 2: SEM image of the MBNC sample synthesized by A) the *in situ* method and B) agitated fermentation.

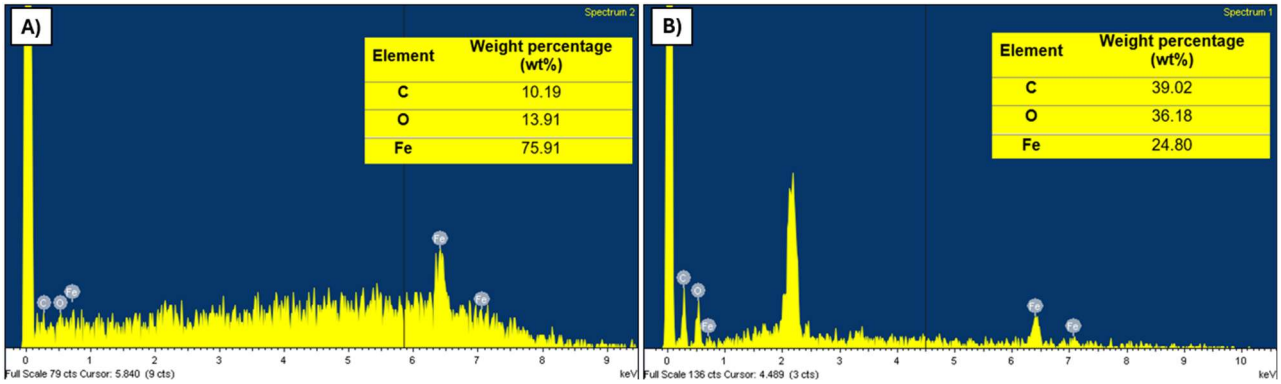

Fig. 3: EDS spectrum with mass fractions [%] of elements for MBNC sample synthesized by A) the *in situ* method and B) agitated fermentation.

The results of the adsorption studies demonstrate that MBNC beads exhibited the highest Cr(VI) removal efficiency at lower initial concentrations, achieving nearly complete removal at 1 mg/L, while adsorption efficiency decreased at higher concentrations due to saturation of active adsorption sites (Fig. 4a). Furthermore, the MBNC beads maintained stable removal performance over five reuse cycles (Fig. 4b), indicating good reusability and stability for potential wastewater treatment applications.

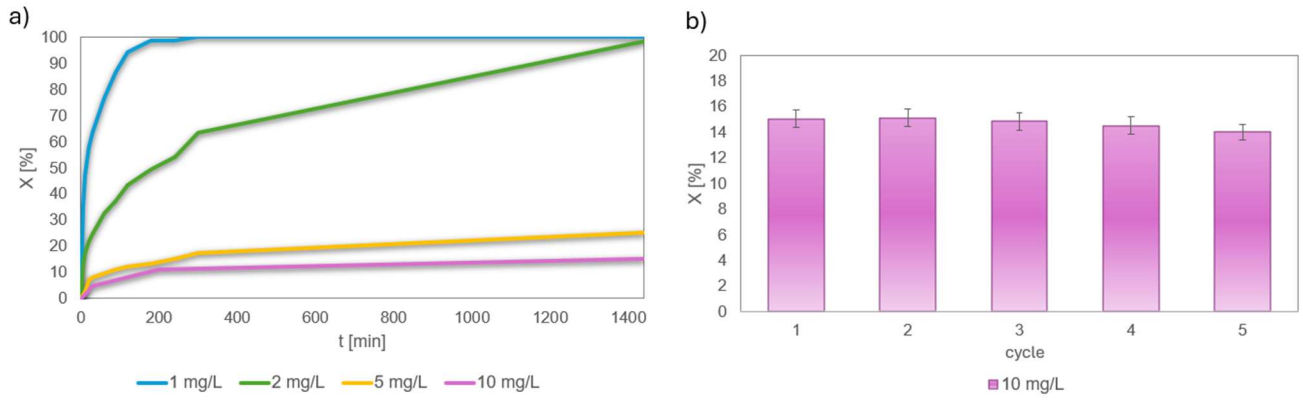

Fig. 4: a) The removal efficiency of Cr(VI) by MBNC beads and b) The removal efficiency of Cr(VI) by MBNC beads at initial Cr(VI) concentration of 10 mg/L during five reuse cycles.

Summary

Two different synthesis approaches were successfully employed for the preparation of spherical magnetic bacterial nanocellulose nanocomposites. Both approaches enabled the effective introduction of magnetic responsiveness into the BNC polymer matrix, thereby broadening the material's functional applicability. Comparative characterization demonstrated that the *in situ* synthesized MBNC exhibited slightly superior properties compared to those obtained by agitated fermentation. The prepared nanocomposites proved to be efficient adsorbents for the removal of Cr(VI) ions from aqueous media. Overall, this work highlights the importance of spherical BNC functionalized with Fe_3O_4 MNPs and underscores its considerable potential for environmental applications, particularly in the field of wastewater treatment.

Acknowledgment

This research was supported by the Slovenian Research and Innovation Agency (ARIS) within the framework of program P2-0046 (Separation Processes and Production Design), program P2-0114 (Applied Electromagnetics), and a young researcher ARIS fellowship contract, number 2894/FKKT-2025.

References

Barja, F., 2021. Bacterial nanocellulose production and biomedical applications. J Biomed Res 35, 310–317. https://doi.org/10.7555/JBR.35.20210036

Diaz-Ramirez, J., Urbina, L., Eceiza, A., Retegi, A., Gabilondo, N., 2021. Superabsorbent bacterial cellulose spheres biosynthesized from winery by-products as natural carriers for fertilizers. International Journal of Biological Macromolecules 191, 1212–1220. https://doi.org/10.1016/j.ijbiomac.2021.09.203

El-Gendi, H., Taha, T.H., Ray, J.B., Saleh, A.K., 2022. Recent advances in bacterial cellulose: a low-cost effective production media, optimization strategies and applications. Cellulose 29, 7495–7533. https://doi.org/10.1007/s10570-022-04697-1

Hestrin, S., Schramm, M., 1954. Synthesis of cellulose by Acetobacter xylinum. 2. Preparation of freeze-dried cells capable of polymerizing glucose to cellulose. Biochem J 58, 345–352. https://doi.org/10.1042/bj0580345

Lace, A., Ryan, D., Bowkett, M., Cleary, J., 2019. Chromium Monitoring in Water by Colorimetry Using Optimised 1,5-Diphenylcarbazide Method. International Journal of Environmental Research and Public Health 16. https://doi.org/10.3390/ijerph16101803

Satyam, S., Patra, S., 2024. Innovations and challenges in adsorption-based wastewater remediation: A comprehensive review. Heliyon 10, e29573. https://doi.org/10.1016/j.heliyon.2024.e29573

Sharma, P., Singh, S.P., Parakh, S.K., Tong, Y.W., 2022. Health hazards of hexavalent chromium (Cr (VI)) and its microbial reduction. Bioengineered 13, 4923–4938. https://doi.org/10.1080/21655979.2022.2037273

Sriplai, N., Pinitsoontorn, S., 2021. Bacterial cellulose-based magnetic nanocomposites: A review. Carbohydrate Polymers 254, 117228. https://doi.org/10.1016/j.carbpol.2020.117228

Šulek, F., Drofenik, M., Habulin, M., Knez, Ž., 2010. Surface functionalization of silica-coated magnetic nanoparticles for covalent attachment of cholesterol oxidase. Journal of Magnetism and Magnetic Materials 322, 179–185. https://doi.org/10.1016/j.jmmm.2009.07.075

Vasic, K., Primozic, M., Knez, Z., Leitgeb, M., 2023. Efficient Removal of Cr(VI) Ions from Aqueous Solutions Using Arabinogalactan Coated Magnetic Nanoparticles. Chemical Engineering Transactions 99, 205–210. https://doi.org/10.3303/CET2399035

Wasim, M., Mushtaq, M., Khan, S.U., Farooq, A., Naeem, M.A., Khan, M.R., Salam, A., Wei, Q., 2022. Development of bacterial cellulose nanocomposites: An overview of the synthesis of bacterial cellulose nanocomposites with metallic and metallic-oxide nanoparticles by different methods and techniques for biomedical applications. Journal of Industrial Textiles 51, 1886S-1915S. https://doi.org/10.1177/1528083720977201

Determination of Total Phenolic Content of Ultrasound Assisted Extracts of Tomato Residues

Marlene Metzler, Adrian Drescher, Marlene Kienberger

Graz University of Technology, Institute of Chemical Engineering and Environmental Technology, metzler@student.tugraz.at

Introduction

In the context of circular economy, the potential for extracting bioactive molecules from tomato plant residues generated in agricultural production is investigated. Tomato production leads to significantly more plant residues compared to other vegetables grown in greenhouses, accounting for 49 tonnes of plant residues per hectare of greenhouse annually. While those residues are often improperly disposed of, they bear the potential to be utilised as an inexpensive renewable feedstock for biorefinery approaches [1]. The goal of this work is to investigate an added value processing of tomato plant residues by isolating bioactive substances, particularly phenolic compounds. Phenolic compounds are a type of secondary metabolites and consist of an aromatic ring and one or more hydroxyl substituents [2, 3]. Due to the structural form of phenols or polyphenols, they act as antioxidants [4]. Bioactive molecules are increasingly in demand, because they can be used in various fields including modern pharmacology, agrochemicals, cosmetics, food industry, plant science and many more [5].

When choosing a solvent, the principles of Green Chemistry should be considered by favouring greener solvents that minimize environmental and health impacts while still ensuring efficient extraction performance [6]. Hexane for example has a wide range of industrial applications, including extracting oil from oilseeds and other food ingredients in the food industry. Estimates indicate that approximately two million tons of hexane are produced annually. Its toxicity is well known and associated with occupational health risks. Therefore, replacing hexane with greener solvents where possible is important to achieve a toxic-free environment, as required by the European Green Deal [7].

Experimental

4 g of dried tomato plant residues were used in the experiments, mixed with both pure solvents and solvent mixtures of varying polarity, all experiments were carried out in duplicate. All samples were pretreated using an ultrasound bath for 15 minutes with the purpose of improving mass transfer by breaking down the cell structures.

For the solid-liquid extraction, the solids were diluted with the solvent with a ratio of 1:10 g:ml (s:l). For the used Soxhlet extractor at least 200 ml of solvent were required to operate. Both extraction techniques were running for 24 hours at 50°C.

All extracts were then concentrated using a rotatory evaporator (Heidolph, coupled with a Lauda ECO RE 630 chiller) until all the liquid evaporated and only solid matter or a highly viscous oil remained, which were then diluted with a mixture of ethanol and naphthalene with 150 ppm naphthalene. Samples where a mixture of two solvents was used for extraction were first diluted with ethanol, then hexane.

To quantify the total phenolic content (TPC) of the extracted samples the Folin-Ciocalteu assay was tailored to tomato plant residue extracts. The absorbance was then measured three times per sample at 765 nm with the spectrophotometer "UV 1800 Shimadzu".

The spectrophotometry measurements were recorded as absorbance values. To be able to compare the results quantitatively, the results are expressed as mg of gallic acid equivalents (GAE) per kg of dried tomato plant residues (kg_{dw}^{-1}). The calibration curve in figure 1 was generated by measuring a series of gallic acid solutions with different concentrations.

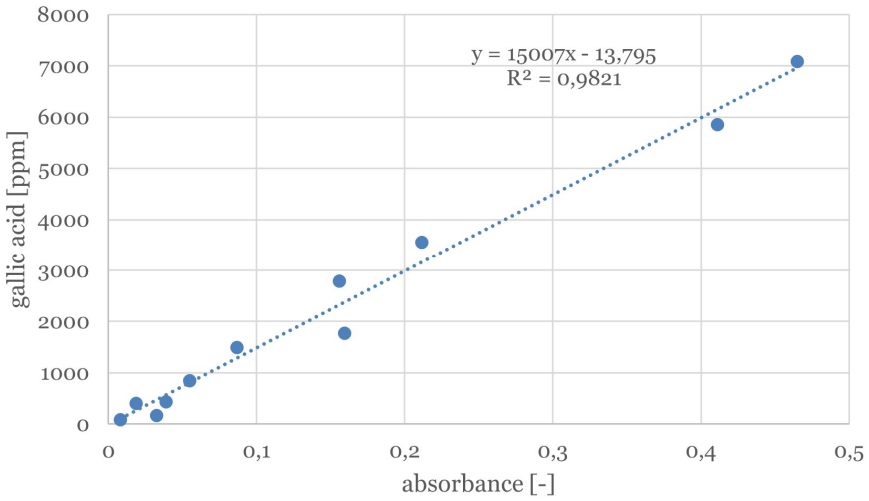

Fig. 1.: Standardised UV-VIS spectrophotometry results of different concentrations of gallic acid measured in absorption.

Equation 1 describes the conversion from the concentrations of GAE in the sample to mg GAE per kg dry weight.

$$\frac{mg\ GAE}{kg\ dry\ weight} = ppm\ GA\ * \frac{kg\ solvent}{kg\ dry\ weight} \quad (1)$$

Based on the calibration curve, the TPC of all extracted samples was quantified and compared for the different solvents and extraction techniques.

Figure 2 shows the TPC of the samples in mg of GAE per kg of dried tomato plants for the different solvents and mixtures of solvents of Soxhlet extraction and solid-liquid extraction, both preceded by ultrasonic pretreatment. As expected, the Soxhlet extractions yield higher TPC values than the corresponding solid-liquid extractions regardless of the solvent.

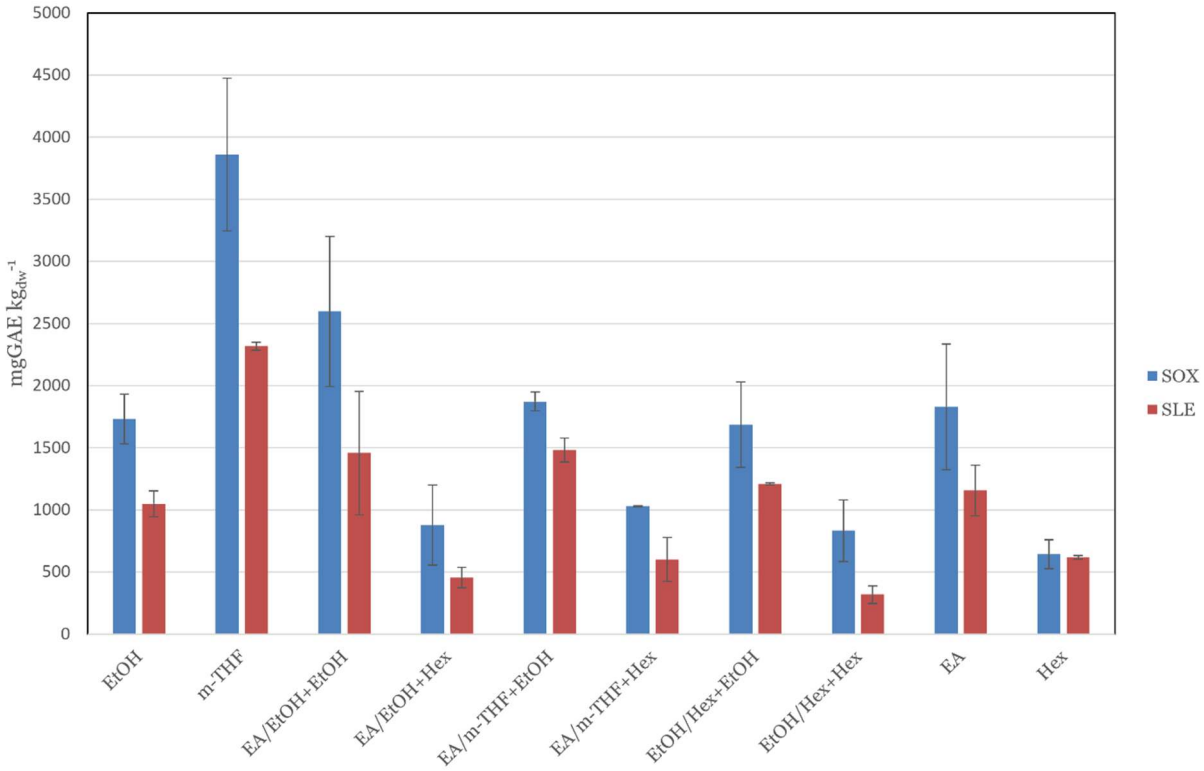

Fig. 2.: TPC in mg GAE kg_{dw}-1 for each solvent measured by spectrophotometry. Samples extracted with Soxhlet extraction (SOX) in blue, samples extracted with solid-liquid extraction (SLE) in red.

The Soxhlet extraction using m-THF shows the highest yield of phenols of all measured samples with 3860.655 ± 615.675 mg GAE kg_{dw}^{-1}. However, the variance between the two measured samples has to be considered. The corresponding solid-liquid extraction yields a significantly lower TPC, with 2316.713 ± 33.327 mg GAE kg_{dw}^{-1}.

The results of the conducted extractions using ethyl acetate is 10.27 % higher in solid-liquid extraction and 5.75 % higher in Soxhlet extraction compared to using ethanol. The

samples from the Soxhlet extraction using ethyl acetate show 1830.632 ± 506.495 mg GAE kg_{dw}^{-1}, the samples from solid-liquid extraction 1156.551 ± 203,893 mg GAE kg_{dw}^{-1}.

Samples where a mixture of two solvents was used for extraction were first diluted with ethanol, then hexane. Comparing the first dilution of the dried extracts that were extracted with mixtures of solvents, the amounts measured in the samples of solid-liquid extraction using ethyl acetate and ethanol (1457.851 ± 497.242 mg GAE kg_{dw}^{-1}) are very similar to those in the solid-liquid extraction using ethyl acetate and m-THF (1481.796 ± 95.427 mg GAE kg_{dw}^{-1}). The mixture of ethanol and hexane shows a lower TPC (1207.759 ± 9.008 mg GAE kg_{dw}^{-1}) in the solid-liquid extraction than the other two mixtures. The second highest TPC (2597.530 ± 603.301 mg GAE kg_{dw}^{-1}) of all samples was measured in the first dilution with ethanol of the Soxhlet extraction using a mixture of ethyl acetate and ethanol. In the first dilution of the sample extracted with a mixture of ethyl acetate and m-THF 1872.134 ± 77.061 mg GAE kg_{dw}^{-1} were measured while the mixture of ethanol and hexane show 1685.956 ± 343.853 mg GAE kg_{dw}^{-1}. All three samples using mixtures of solvents for extraction show that despite the used solvents, in the second dilution with hexane only about a third to half of the TPC compared to the first dilution with ethanol was found. This is consistent with the literature research that phenols dissolve better in polar than non-polar solvents due to their chemical structure.

The lowest values were observed in extractions using hexane, indicating the limited suitability of the nonpolar solvent for the extraction of phenols from the scrutinized solvents with 643.510 ± mg GAE kg_{dw}^{-1} in Soxhlet extraction and 617.223 ± 15.61 mg GAE kg_{dw}^{-1} in solid-liquid extraction.

Generally, the error indicators vary significantly (up to ± 615.675 mg GAE kg_{dw}^{-1}) across experiments, which must be considered when evaluating and comparing the results. The differences in the failure bars are inconsistent, and no pattern related to the polarity of the solvent or to the extraction technique can be observed. Contributing to these fluctuations is the inherently heterogeneous composition of the tomato plant residue feedstock, which is typical for agricultural side streams. Since only 4 g of dry biomass was used per extraction, even small differences in the proportion of stems, leaves, and other plant components can significantly influence the concentration of the extracted compounds and consequently lead to noticeable variations between samples.

Summary

This work investigates the extraction of phenolic compounds from tomato plant residues using ultrasound-assisted Soxhlet and solid-liquid extraction with solvents of different polarities. Tomato plant residues represent a promising renewable feedstock for future biorefinery applications. Focus was placed on the use of greener solvent alternatives and on the determination of the TPC by spectrophotometry using the Folin-Ciocalteu assay.

Among the investigated solvents, m-THF is the most effective solvent for obtaining a high TPC (Soxhlet extraction 3860.655 ± 615.675 mg GAE kg_{dw}^{-1}, solid-liquid extraction 2316.713 ± 33.327 mg GAE kg_{dw}^{-1}), whereas hexane (Soxhlet extraction 643.510 ± mg GAE kg_{dw}^{-1}, solid-liquid extraction 617.223 ± 15.613 mg GAE kg_{dw}^{-1}) proved to be the least effective. Generally, it is observed that phenols dissolve better in polar solvents. However, a combination of polar and non-polar solvents also shows efficacy in extracting phenols from plant materials. Among the extraction methods, soxhlet extraction consistently yields a higher TPC across almost all samples, compared to solid-liquid extraction.

References

[1] Fernández-Gómez, M. J., Díaz-Raviña, M., Romero, E., Nogales, R. 2013. Recycling of environmentally problematic plant wastes generated from greenhouse tomato crops through vermicomposting. *International Journal of Environmental Science and Technology*, 10, 697- 708.

[2] Kulbat, K., 2016. The role of phenolic compounds in plant resistance. *Biotechnology and Food Science*, 80(2), pp.97-108.

[3] Balasundram, N., Sundram, K. and Samman, S., 2006. Phenolic compounds in plants and agri-industrial by-products: Antioxidant activity, occurrence, and potential uses. *Food chemistry*, 99(1), pp.191-203.

[4] Lattanzio, V., 2013. Phenolic compounds: introduction 50. *Nat. Prod*, pp.1543-1580.

[5] Guaadaoui, A., Benaicha, S., Elmajdoub, N., Bellaoui, M. and Hamal, A., 2014. What is a bioactive compound? A combined definition for a preliminary consensus. *International Journal of Nutrition and Food Sciences*, 3(3), pp.174-179.

[6] Matlack, A., 2010. Introduction to green chemistry. CRC press.

[7] Cravotto, C., Fabiano-Tixier, A. S., Claux, O., Abert-Vian, M., Tabasso, S., Cravotto, G., Chemat, F., 2022. Towards substitution of hexane as extraction solvent of food products and ingredients with no regrets. *Foods*, 11(21), 3412.

Influence of Cs Promotion on Alkene Formation during CO_2 Hydrogenation over Iron-Based Catalysts

Jan Hendrik Westerbarkei, Kai Laichter, Thomas E. Müller

Carbon Sources and Conversion, Ruhr-Universität Bochum, Germany
jan.westerbarkei@ruhr-uni-bochum.de

Introduction

The chemical industry faces the challenge of reducing its dependence on fossil carbon resources while maintaining the supply of essential platform chemicals. Ethene is among the most important building blocks of the chemical industry and is currently produced predominantly by steam cracking of fossil feedstocks such as naphtha or ethane [1]. Although highly established, this process is energy-intensive and contributes substantially to global greenhouse gas emissions associated with light olefin production [2].

Catalytic hydrogenation of CO_2 using renewable hydrogen has emerged as a promising alternative route for the production of value-added chemicals and fuels [3,4]. In particular, the conversion of CO_2 to light olefins offers the possibility of combining carbon utilization with the production of key chemical intermediates. However, the selective formation of ethene remains challenging because CO_2 hydrogenation involves a complex network of parallel and consecutive reactions, including reverse water-gas shift (RWGS), hydrocarbon chain growth, olefin formation, and undesired methanation [3,5].

The reaction pathway considered in this work is based on the combination of RWGS and Fischer–Tropsch-type chemistry. In this concept, CO_2 is first converted into CO via RWGS (Eq. 1), followed by C–C bond formation and olefin synthesis through Fischer–Tropsch-like reaction pathways (Eq. 2) [5,6].

$$CO_2 + H_2 \rightleftharpoons CO + H_2O \qquad (1)$$

$$2\ CO + 4\ H_2 \rightleftharpoons C_2H_4 + 2\ H_2O \qquad (2)$$

Iron-based catalysts are particularly attractive for this approach because they combine RWGS activity with hydrocarbon synthesis capability while relying on abundant and inexpensive metals [5]. Numerous studies have shown that alkali promoters influence catalyst basicity, iron carbide formation, hydrogen coverage, CO_2 adsorption, and hydrocarbon selectivity during CO_2 hydrogenation over iron-based catalysts [7,8]. Nevertheless, the relationship between promoter identity and product distribution remains insufficiently understood.

Previous screening experiments performed with Fe-based catalyst systems promoted by different alkali metals revealed pronounced differences in catalytic performance and product selectivity [8–10]. Depending on the promoter, the product spectrum shifted between CO formation, methane production, and the formation of C_2–C_6 hydrocarbons. Among the investigated systems, Cs-promoted catalysts showed particularly promising olefin formation, highlighting the strong influence of alkali promotion on product selectivity. These observations highlight the importance of alkali promotion for controlling product selectivity during CO_2 hydrogenation and motivate a closer examination of promoter effects in iron-based catalyst systems.

Figure 1 summarizes the conceptual reaction pathway for CO_2 hydrogenation to olefins via RWGS and Fischer–Tropsch-like chain growth.

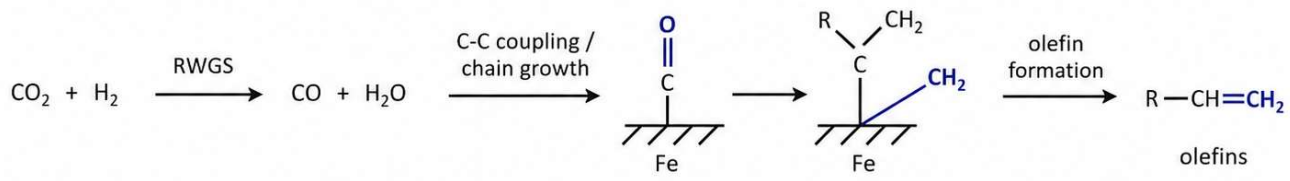

Figure 1: Conceptual reaction pathway for CO_2 hydrogenation to olefins via RWGS and Fischer-Tropsch-like chain growth.

Experimental

Alkali-promoted iron-based catalyst systems were prepared and evaluated for the hydrogenation of CO_2 to hydrocarbons. Preliminary screening experiments were conducted using Fe^0 powder combined with Al_2O_3-supported alkali promoters (Li_2O, Na_2O, K_2O, Rb_2O, and Cs_2O). Catalytic tests were performed in a fixed-bed reactor using $CO_2/H_2/N_2$ feed mixtures at elevated pressure. Product compositions were determined by on-line gas chromatography.

Prior to catalytic testing, the catalyst mixtures were activated in hydrogen at 400 °C for 12 h to generate catalytically relevant iron species. Based on the screening results, the Cs-promoted system was selected for more detailed investigation.

Catalyst characterization was performed using nitrogen physisorption (BET) for surface area determination, X-ray diffraction (XRD) for phase analysis, scanning electron microscopy coupled with energy-dispersive X-ray spectroscopy (SEM-EDX) for

morphological and elemental analysis, and inductively coupled plasma optical emission spectroscopy (ICP-OES) for quantitative elemental composition.

Catalytic performance was evaluated as a function of reaction temperature under fixed-bed reactor conditions. CO_2 conversion and product selectivities were determined from the chromatographic analysis of the reactor effluent.

Initial Experimental Results

As part of the preliminary investigations, alkali-promoted catalyst systems for CO_2 hydrogenation were synthesized, characterized and evaluated under fixed-bed reactor conditions. Among the investigated alkali promoters, Cs_2O supported on Al_2O_3 exhibited particularly promising olefin selectivity and was therefore selected for a more detailed analysis.

Figure 2 shows a representative SEM image of the $Cs_2O@Al_2O_3$ material. The catalyst exhibits pronounced surface deposits and a heterogeneous particle morphology, indicating successful promoter deposition on the support surface. Such structural features may influence reactant adsorption, local hydrogen availability and hydrocarbon formation pathways.

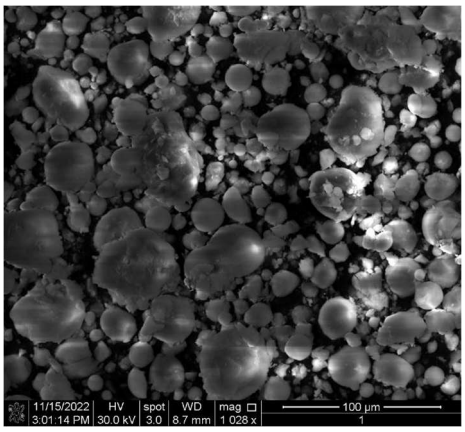

Figure 2: SEM image of $Cs_2O@Al_2O_3$

To investigate the catalytic performance, a catalyst mixture consisting of Fe^0 powder and $Cs_2O@Al_2O_3$ was tested in CO_2 hydrogenation experiments between 350 °C and 400 °C under elevated pressure. The product distributions, including the reference measurement at 350 °C after temperature cycling, are summarized in Figure 3.

The catalyst produced methane together with C_2–C_6 alkenes and alkanes, and the product distribution was strongly temperature dependent. Methane remained dominant and

increased from 5.60% at 350 °C to 33.90% at 400 °C (6.05-fold). In parallel, the summed C_2–C_6 alkene selectivity rose from 1.78% to 10.67% (6.01-fold), with ethene and propene increasing to 4.59% and 3.93%, respectively. At 400 °C, the total alkene fraction exceeded the summed C_2–C_6 alkanes (6.81%) by 56.7%, corresponding to an alkene/alkane ratio of 1.57.

Repeated operation at 350 °C revealed pronounced catalyst evolution. After exposure to 400 °C, the selectivity at 350 °C no longer returned to the initial state: methane increased from 5.60% to 19.48%, the summed C_2–C_6 alkene selectivity from 1.78% to 5.69% (3.20-fold), and the corresponding alkane selectivity from 0.77% to 4.42% (5.75-fold). Because the external reaction conditions were identical, these shifts point to structural or chemical modifications of the active catalyst phase during operation.

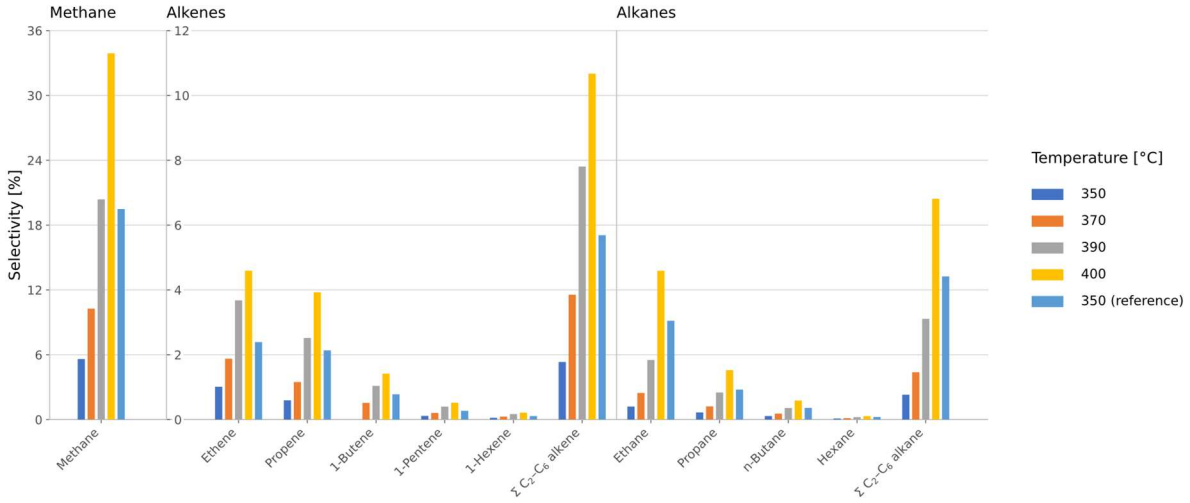

Figure 3: Catalytic performance of Fe + Cs_2O@Al_2O_3 in the hydrogenation of CO_2

Changes in catalyst activity and selectivity may arise from carbon deposition, particle growth, and phase transformations, as illustrated in Figure 4. The temperature-dependent product distributions and the altered 350 °C reference measurement therefore indicate catalyst evolution under reaction conditions. Figure 4 summarizes possible evolution pathways that may explain the observed selectivity shifts during temperature cycling.

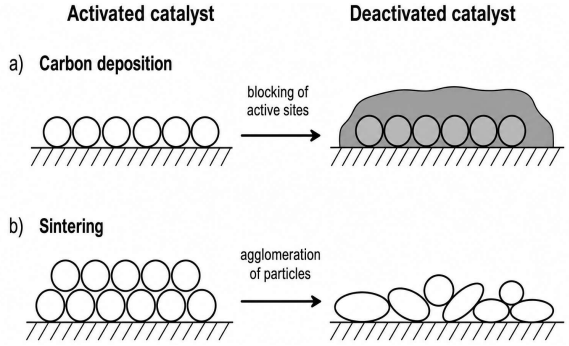

Figure 4: Proposed catalyst evolution pathways during long term CO_2 hydrogenation.

The results demonstrate that alkali promotion strongly influences hydrocarbon formation during CO_2 hydrogenation over iron-based catalysts. For the Cs-promoted system, Figure 3 shows C_2–C_6 alkene selectivities up to 10.67%, with alkene-to-alkane ratios between 1.57 and 2.64 during the initial temperature sweep. These findings underline the importance of promoter selection for controlling product distribution and highlight the potential of Cs-promoted iron catalysts for selective olefin synthesis from CO_2.

Conclusions and Outlook

This study investigated alkali-promoted iron-based catalyst systems for the hydrogenation of CO_2 to hydrocarbons with a focus on olefin formation. Screening experiments demonstrated that promoter identity strongly affects activity and product distribution, with Cs promotion giving the most pronounced formation of C_2–C_6 olefins among the investigated systems.

For Fe^0 + $Cs_2O@Al_2O_3$, fixed-bed reactor experiments revealed a strong temperature dependence. Increasing the temperature from 350 °C to 400 °C increased methane selectivity from 5.60% to 33.90% and the summed C_2–C_6 alkene selectivity from 1.78% to 10.67%. At 400 °C, alkenes were 56.7% more abundant than the corresponding C_2–C_6 alkanes, while ethene and propene reached 4.59% and 3.93%, respectively.

The altered product distribution after temperature cycling further indicates catalyst evolution under reaction conditions. Upon returning to 350 °C, C_2–C_6 alkene selectivity remained 3.20 times higher than in the initial 350 °C measurement, while the alkane fraction increased 5.75-fold. These changes are consistent with structural or chemical modifications of the catalyst and emphasize the need to relate promoter chemistry to active iron phases and catalyst stability.

The pronounced influence of Cs promotion on olefin formation motivates further investigations into the interaction between alkali promoters, iron carbide formation, hydrogen availability, and long-term stability. Such insight may support the development of more selective and stable catalyst systems for producing light olefins from CO_2 and renewable hydrogen.

Acknowledgement

The authors gratefully acknowledge the Chair of Carbon Sources and Conversion at Ruhr-Universität Bochum for supporting this work.

References

[1] W. Shin, B. Lin, H. Lai, G. A. Ibrahim, G. Zang, Decarbonization approaches for ethylene production: comparative techno-economic and life-cycle analysis, Green Chemistry 27 (2025) 3655-3675. DOI: 10.1039/D4GC04538F.

[2] O. Mynko et al., Reducing CO_2 emissions of existing ethylene plants: evaluation of different revamp strategies to reduce global CO_2 emission by 100 million tonnes, Journal of Cleaner Production 362 (2022) 132127. DOI: 10.1016/j.jclepro.2022.132127.

[3] M. Ronda-Lloret, G. Rothenberg, N. R. Shiju, A Critical Look at Direct Catalytic Hydrogenation of Carbon Dioxide to Olefins, ChemSusChem 12 (2019) 3896-3914. DOI: 10.1002/cssc.201900915.

[4] C. G. Okoye-Chine, C. O. L. Mbuya, N. C. Shiba, K. O. Otun, Effective catalysts for hydrogenation of CO_2 into lower olefins: A review, Carbon Capture Science & Technology (2024) 100251. DOI: 10.1016/j.ccst.2024.100251.

[5] J.-Y. Jia et al., Review of Iron-Based Catalysts for Carbon Dioxide Fischer-Tropsch Synthesis, Transactions of Tianjin University 30 (2024) 178-197. DOI: 10.1007/s12209-024-00392-3.

[6] C. G. Visconti et al., CO_2 hydrogenation to lower olefins on a high surface area K-promoted bulk Fe-catalyst, Applied Catalysis B: Environmental 200 (2017) 530-542. DOI: 10.1016/j.apcatb.2016.07.047.

[7] J. Wei, J. Sun, Z. Wen, C. Fang, Q. Ge, H. Xu, New insights into the effect of sodium on Fe_3O_4-based nanocatalysts for CO_2 hydrogenation to light olefins, Catalysis Science & Technology 6 (2016) 4786-4793. DOI: 10.1039/C6CY00160B.

[8] Q. Yang et al., Identifying Performance Descriptors in CO_2 Hydrogenation over Iron-Based Catalysts Promoted with Alkali Metals, Angewandte Chemie International Edition 61 (2022) e202116517. DOI: 10.1002/anie.202116517.

[9] T. Liese, I. Graef, F. Heck, V. Hagen, T. E. Müller, Produktion von Ethen aus Recycleströmen und erneuerbaren Kohlenstoffquellen als eine nachhaltige und ökonomische Route zu Grundbausteinen der chemischen Industrie; SynGas2Ethene, Technische Informationsbibliothek, 2025. DOI: 10.34657/27229.

[10] Laichter, K. Heterogen-katalytisches Verfahren zur Synthese von Ethen und weiteren kurzkettigen Alkenen ausgehend von CO_2 als Kohlenstoffquelle PhD Thesis, Ruhr-Universität Bochum, 2024. https://d-nb.info/1360819223.

Investigation of the Structure Dependence of the Melt Flow Index in the High-Pressure Polymerization of Ethylene

Xaver-Philipp Possehl, Markus Busch

Ernst-Berl-Institute of Technical and Macromolecular Chemistry, Technical University Darmstadt, markus.busch@pre.tudarmstadt.de

Introduction

Polyethylene (PE) applications range from packaging materials and films to pipe and cable insulation. Depending on the application, PE must be brought into the appropriate shape, which is also known as processing. For this purpose, the polymer obtained in the reactor is transferred to an extruder and granulated.[1] Afterwards, the pellets can then be processed using all known forming processes. The most widely used are injection molding, extrusion and blow molding. The forming processes take place under different conditions and are therefore also designed for different properties of the starting materials. For example, PE types with low viscosity are used in injection molding. An easy and quick-to-measure parameter, the melt flow index (MFI), was introduced to design the processing. This parameter indicates the amount of polymer, that can be pressed through a nozzle in a certain unit of time at a certain temperature using a specified weight.[2]

The goal of this work is the investigation of the influence of polymer properties and topology of different LDPE samples on the MFI based on a database created using samples produced in the high-pressure lab scale autoclave. This work uses a simulation-based approach to describe the topology of the investigated polymer samples.

Experimental

When determining the MFI, a distinction is made between the melt volume flow rate (MVR) and the melt mass flow rate (MFR). The results differ depending on the melt density of the polymer. Generally, the MFI indicates how much polymer flows through a standardized opening (nozzle) in a certain unit of time (10 min) under a certain pressure applied by a load. The MVR values were measured using a Göttfert MI-4 capillary rheometer (Göttfert *Werkstoff-Prüfmaschinen* GmbH). A schematic sketch of the setup of the measuring device is shown in Fig. *1*.

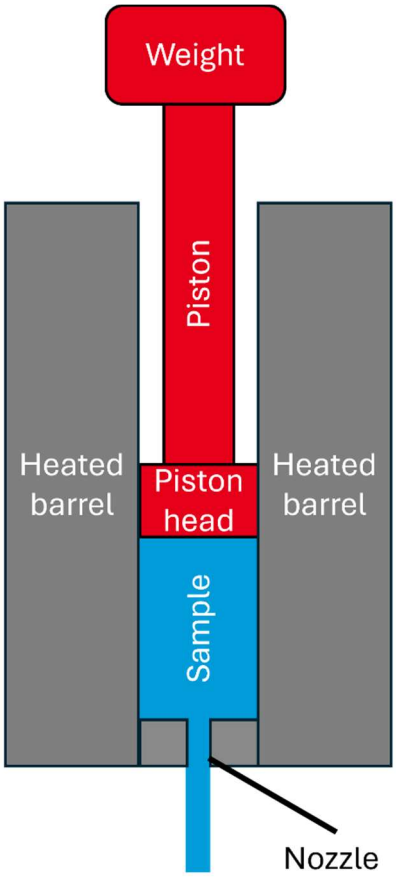

Fig. 1: Schematic illustration of a MVR measuring device.

For the measurement itself, the heat barrel is first heated to the desired temperature. Next, the MVR measuring device is filled with the polymer sample, the plunger is placed on top of the sample, and the measurement is started. The process begins with the melt-up time, during which the sample is melted. The actual measurement then begins. Here, a weight is used to press the sample through a nozzle. This measures how much polymer is forced through the nozzle within a specific time. After 40 measurement points, an average value is calculated, and the extrusion phase begins. Here, a heavier weight is used to force the remaining polymer out of the MVR measuring device. In this work, the measurements were carried out in accordance with the *ISO 1133* norm. According to the *ISO 1133* norm, the measurement begins at a starting point of 50 mm (fill level) and requires a piston travel of 30 mm (fill level).

This study investigated the dependence of the MVR, as measured using the above-described method, as a function of polymer structure and weight-average molecular weight (M_w). M_w was obtained from the molecular weight distribution (MWD), which was determined using size exclusion chromatography (SEC). The polymer structure was determined using a three-step modelling approach, which is schematically illustrated in Fig. 2.

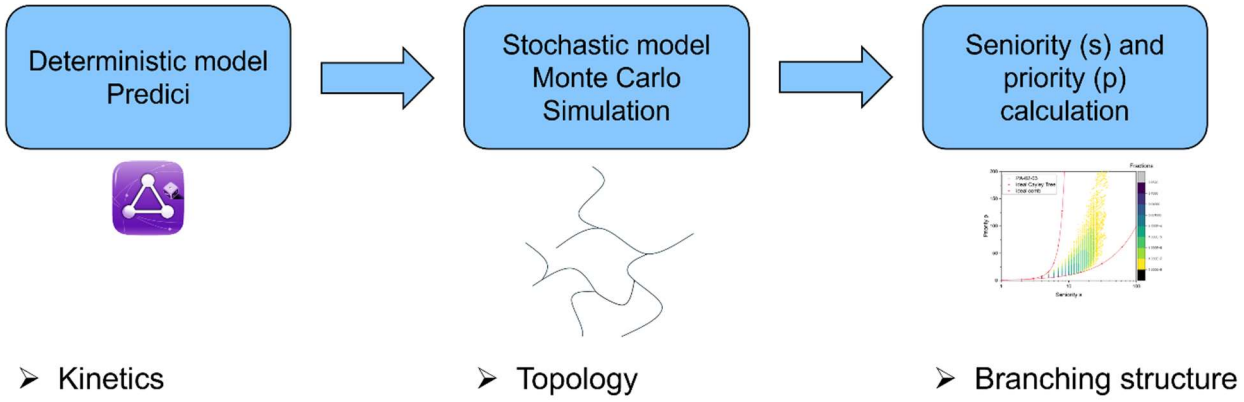

Fig. 2: Schematic overview of the three-step modelling approach: Step 1: Deterministic modelling using Predici®; Step 2: Stochastic modelling using a Monte Carlo simulation; Step 3: Determination of the polymer structure based on the seniority (s) and priority (p) concept.

In the context of deterministic modeling, the software *Predici*® (Polyreaction Distribution by countable System Integration) by CiT (Computing in Technology) was used to predict time-dependent temperature, pressure and concentration profiles. To do this, *Predici*® requires the corresponding kinetic information for each individual substance. The reaction kinetics of ethylene homopolymerization established by Busch [3] are used here. It should be noted that the individual reaction rate constants depend on temperature and pressure. The temperature and pressure dependence of the individual reaction steps is described using an Arrhenius equation (Equation 1). Here, k_0 is the pre-exponential factor, E_A is the activation energy, and $\Delta V^\ddagger$ is the activation volume.

$$k = k_0 \exp\left(\frac{-E_\mathrm{A} + \Delta V^\ddagger p}{RT}\right) \tag{1}$$

Based on these kinetics, the mass balance can be derived, considering the reactor geometry. The samples used here were prepared in a 100-ml lab-scale autoclave under isobaric and isothermal conditions. Therefore, these boundary conditions were used for modeling. Based on these kinetics and the reactor geometry, the mass balance can be derived. Which is then solved numerically based on the implicit linear Euler method.[4]

For stochastic modeling, only the reaction frequencies r were required as input from the results of deterministic modeling. Further information on temperature or pressure is not required for stochastic simulation, as these are already included in the reaction frequencies. The stochastic modeling of the polymer structure is carried out using a Monte Carlo (MC) simulation. Here a single-molecule approach is used, which means that molecules are built up one by one, step by step, within the Monte Carlo simulation. The

algorithm begins with a molecule initialization, in which the residence time of the molecule in the reactor is determined based on a random number. The simulation of the molecules through the reactor then begins. For this, two random numbers are always generated. The first random number describes the translation step, a time step taken within the simulation. If the molecule's residence time exceeds the residence time specified during molecule initialization, the last reaction is executed, and a new molecule is initialized. After this translation step, a reaction is carried out. To do this, the probability for a specific reaction is determined based on the reaction frequencies r, which are viewed as the frequency of occurrence of a particular reaction. It must also be noted that not all species can carry out all reactions. Based on this approach, a total of 10 million molecules are simulated to replicate a polymer sample. As a result, the molecular weight distribution (MWD) can then be calculated from discrete information for each individual molecule. Since it is known which reaction step was carried out and when, in addition to the MWD, the polymer topology for each individual molecule is also obtained, which is stored in a topology array. This describes the microstructure of polymer molecules.

The topology array is then used to calculate seniority (s) and priority (p) plots. For this process, the molecule is broken down into individual segments, which is done when the topology array is created. A segment runs either from one chain end to a branch point, from one branch point to another, or, in the case of a linear molecule, from one chain end to the other. The seniority s is the longest linear path from a segment to the end of the chain, including the segment itself. The shorter of the two possible paths is specified as the seniority. The priority p is the smallest number of chain ends on one side of the segment. The priority p is rheologically related to the non-linear flow properties of the polymer melt and describes the maximum elongation of a segment.[5] Fig. 3 provides a schematic representation of how a segment's seniority and priority are determined.

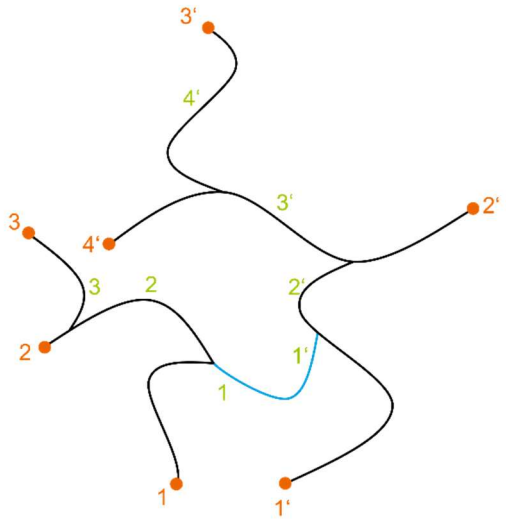

Fig. 3: Schematic representation of how to determine the seniority and priority of a segment. Seniority s and priority p are determined for the blue segment. To determine seniority s, the longest path to the end of the chain is first determined on both sides of the segment (green numbers); right side 4, left side 3 segments. The shorter of the two distances is taken, resulting in $s = 3$. To determine priority p, the number of chain ends on one side of the segment is determined (orange numbers); right side 4, left side 3 segments. The smaller number is used, resulting in $p = 3$; overall result: $s = 3$; $p = 3$.

Two ideal polymer structures can be derived based on this concept. One is the ideal Cayley tree, whose structure can be described by the formula $p = 2^{(s-1)}$, and the other is the ideal comb, which can be described by the formula $p = s$. These are always plotted alongside the polymer sample. The s and p plots resulting from this process were then visually compared, as shown in Fig. *4*. Samples with the same M_w but different MVRs were compared. From this, trends were identified regarding how the structure of the polymer sample affects the MVR.

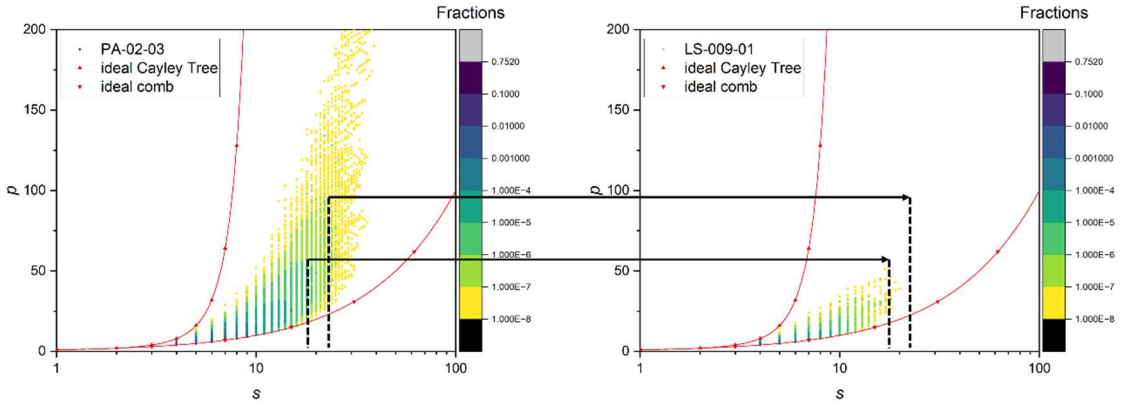

Fig. 4: Visual comparison of s and p plots; red curves: ideal comb and ideal tree; coloured points: calculated s and p values for all segments within the 10-million-molecule sample generated using Monte Carlo simulation. The color reflects the frequency with which a segment occurs with the shown s and p combination; sample PA-02-03 (left) is significantly more tree-like than sample LS-009-01 (right).

Summary

As part of this study, a database of samples with different MVR values was created. These were then simulated using a three-step modelling approach. A deterministic model was used to describe the kinetics, followed by a stochastic model to describe the topology of each individual polymer molecule within the generated polymer sample, and finally, the structure was described based on the seniority s and priority p concept. In parallel, M_{w} was determined using size-exclusion chromatography (SEC). Subsequently, insights into the structure dependence of the MVR were obtained based on the structure and M_{w}.

References

[1] *Extrusion: The definitive processing guide and handbook*, William Andrew Pub, Norwich, NY, **2005**.

[2] AtlasFibre, Ed., Understanding Melt Flow Index.

[3] M. Busch, *Macromolecular Theory and Simulations* **2001**, *10*, 408–429.

[4] Dr. Michael Wulkow, Dr. Regina Telgmann, Dr. Thomas Hockswender, Dr. Niklas Wulkow, Predici11 - A collection of documents, (Ed.: © 2023 Dr. M. Wulkow Computing in Technology GmbH, Rastede, Germany All rights reserved.), **2023**.

[5] D. J. Read, *Journal of Polymer Science Part B: Polymer Physics* **2015**, *53*, 123–141.

Durability of Thermoplastics Exposed to High-Pressure Hydrogen

Lorenzo Zamagni

Department of Civil, Chemical, Environmental and Materials engineering, University of Bologna, via Terracini 28, Bologna (Italy)
DPI, John F. Kennedylaan 2, 5612 AB Eindhoven, the Netherlands
Lorenzo.zamagni5@unibo.it

Introduction

The escalating concerns surrounding climate change have raised attention on the critical evaluation and implementation of comprehensive strategies for the decarbonization of the global economy. A diverse portfolio of low-carbon alternatives must be considered, spanning renewable electricity generation, energy storage technologies, and carbon-neutral fuels to serve sectors that are difficult to electrify directly, such as heavy industry, shipping, and aviation.

Among the most promising alternatives to fossil fuels is hydrogen, which stands out as an exceptionally attractive energy carrier. Its specific energy is the highest of any known fuel [1]. Despite its promise, the widespread deployment of hydrogen as an energy vector faces significant technical and infrastructural challenges. Among these, the efficient and safe transportation and storage of hydrogen at scale still remains challenging. Due to its exceptionally low molecular weight and density under ambient conditions, hydrogen must be compressed to high pressures or liquefied at cryogenic temperatures to achieve volumetric energy densities that are practical for storage and distribution. Pressures in the order of 350 to 700 bar are those encountered in hydrogen storage vessels while pipelines are usually operated between 70 and 100 bar. These harsh operating conditions introduce serious concerns regarding the long-term integrity and compatibility of the structural and barrier materials used throughout the hydrogen supply chain [2].

Metallic components are well known to be susceptible to hydrogen embrittlement, potentially leading to catastrophic failure [3]. Instead, the interactions and potential failure mechanisms between polymeric materials and hydrogen remain poorly understood, having received limited attention in the literature; further investigation is therefore needed, especially considering that such infrastructure is typically designed for service lifetimes spanning several years.

In light of these requirements, semicrystalline polymers have emerged as the most technically viable class of materials for use as liners in hydrogen pipelines and storage tanks [1]. Their suitability is the result of a favorable combination of properties that is

difficult to achieve with other material classes. The crystalline domains within these polymers act as physical barriers to gas diffusion, yielding relatively low hydrogen permeability compared to fully amorphous thermoplastics or elastomers [5]. At the same time, the amorphous regions confer flexibility and toughness, enabling the material to withstand the mechanical stresses associated with pressurization and depressurization cycles. Additionally, semicrystalline polymers are generally cost-effective to manufacture and process, an important consideration for the scale-up of the hydrogen infrastructure. Common representatives of this class, including polyethylene, polyamides, and fluorinated polymers, are already employed in various pipeline and pressure vessel applications. The interconnection between crystallinity, mechanical, and gas transport properties must be systematically characterized, and the long-term effects of sustained hydrogen exposure on performance require careful investigation. Such knowledge is indispensable for the rational design and qualification of polymer liners that can meet the demanding safety and durability standards imposed by hydrogen infrastructure applications.

Experimental

Polymers exposed to high-pressure gases can be subjected to two different ageing processes, chemical and physical. Chemical ageing involves modifications of the functional groups due to reactions or breakage of the polymeric chains. Conversely, physical ageing is related to structural and morphological changes in the amorphous and/or crystalline regions of the polymer [6].

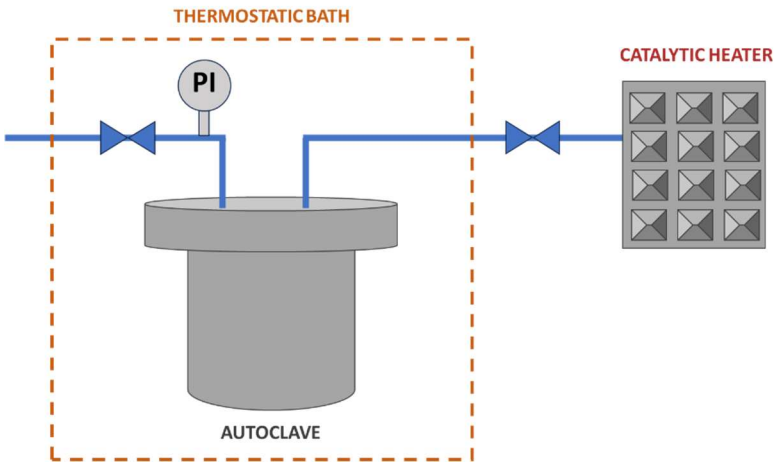

Fig. 1: Testing setup for exposure of polymers to high-pressure hydrogen

To tackle the issues related to the ageing and durability of polymers exposed to high-pressure hydrogen, an experimental setup has been developed. This setup includes an autoclave designed to withstand pressures of up to 100 bars of hydrogen, along with a catalytic heater to ensure the safe decompression of the gas as shown in Fig. 1 . The decompression rate is intentionally kept below 1 bar/min to prevent any damage to the polymer samples from Rapid Gas Decompression and to inspect long term degradation phenomena, only [7].

After the ageing process, a wide variety of testing methods are used to inspect possible differences between the pristine materials and the aged ones, the summary of the tests is presented in *Fig. 2*.

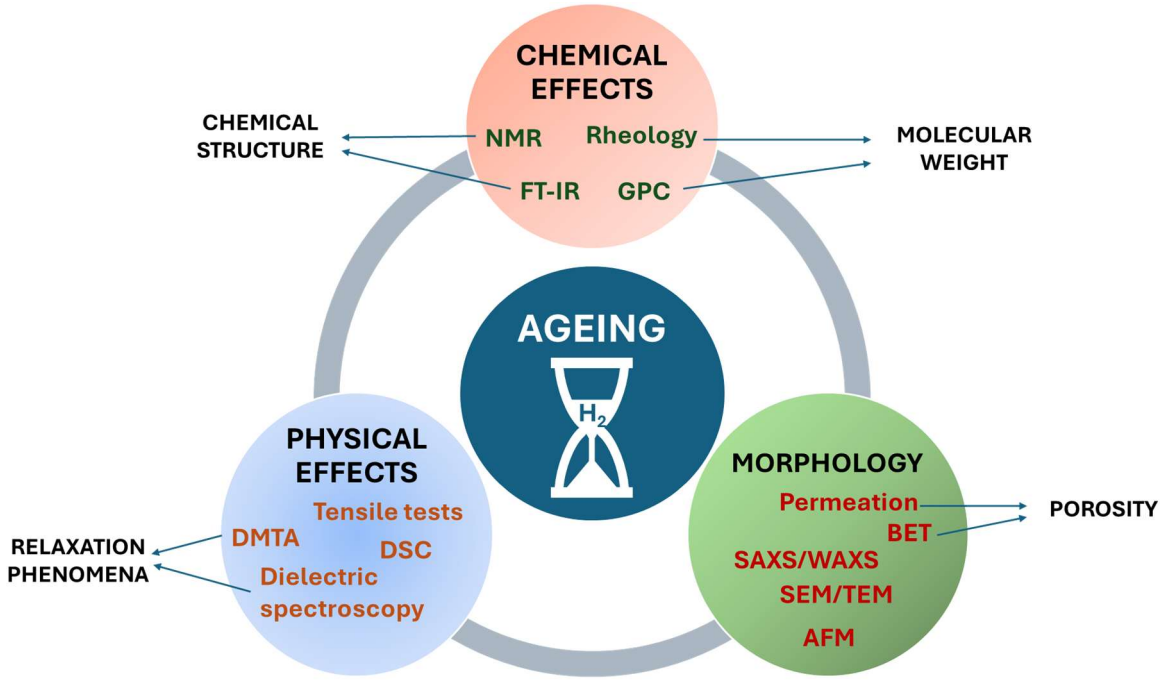

Fig. 2: Overview of the tests performed on pristine and aged samples

Chemical ageing

The evaluation of chemical ageing variations is conducted using four distinct analytical methods: solid-state Nuclear Magnetic Resonance (NMR), Fourier Transform Infrared Spectroscopy (FT-IR), Gel Permeation Chromatography (GPC), and zero shear rate viscosity measurements (rheology).

By monitoring changes in the intensity and position of characteristic absorption bands, FT-IR allows the identification of structural alterations such as new functional groups resulting from the interaction between hydrogen and the polymer matrix. Solid-state NMR provides complementary molecular-level information by probing the local chemical environment of specific nuclei, enabling the detection of subtle changes in chain mobility, and the

formation of new chemical bonds that may not be apparent through other techniques. GPC is a widely recognized and reliable technique that provides insight into the molecular weight distribution of polymeric chains. This method enables the acquisition of detailed information about the size and distribution of polymer molecules. The principal limitation of GPC is the requirement for a mobile phase that solubilizes the polymer, which is not always feasable. To overcome such limitation, rheological measurements can be used as the value of viscosity in the limit of zero shear rate is linked to the molecular weight of the polymer.

Physical ageing

The durability of thermoplastic materials is evaluated not only in terms of mechanical and thermal properties, but also in terms of long-term structural and morphological changes occurring at the molecular level. Among the most commonly employed characterization techniques, tensile testing allows the assessment of key mechanical parameters including Young's modulus, tensile strength, and elongation at break, all of which can change significantly upon ageing. Differential Scanning Calorimetry (DSC) allows the monitoring of thermodynamic transitions such as the glass transition, crystallization, and melting events, which can shift or broaden as a consequence of physical ageing. Dynamic Mechanical Analysis (DMA) provides information on the viscoelastic behaviour of the material, including storage modulus, loss modulus, the glass transition temperature (T_g), and secondary relaxations of the polymeric chains. Dielectric Relaxation Spectroscopy (DRS) probes molecular mobility and relaxation dynamics at the segmental level, offering insight into sub-T_g relaxation processes that are directly associated with physical ageing phenomena.

Morphological changes

Morphological changes in thermoplastic materials are investigated through a combination of complementary characterization techniques. Atomic Force Microscopy (AFM) and Electron Microscopy (SEM/TEM) provide direct visual information on surface and bulk microstructural evolution, enabling the observation of features such as crystalline domains, phase separation, and interfacial modifications at the nanoscale. Small and Wide Angle X-ray Scattering (SAXS/WAXS) offer quantitative insight into changes in crystallinity, lamellar periodicity, and long-range order within the polymer matrix. BET analysis allows the evaluation of surface area and porosity variations, which are

particularly relevant in the context of ageing-induced microstructural rearrangements. Finally, permeation measurements provide an indirect but sensitive probe of morphological changes, as the transport of small molecules through the polymer is strongly governed by free volume, chain packing, and the degree of crystallinity.

Summary

The safe and efficient storage and transportation of H_2 is definitely a significant challenge, which opens up new questions related to the long-term durability of the materials employed. With focus on semicrystalline polymers for liner applications in hydrogen pipelines, the impact of high-pressure hydrogen exposure to polymer properties are investigated. Assessing the long-term durability of polymer liners in hydrogen infrastructure requires a multi-scale characterization strategy that simultaneously accounts for chemical degradation, structural relaxation, and morphological evolution. The combination of complementary techniques operating at different length scales and sensitivity ranges enables a thorough understanding of the underlying degradation mechanisms, ultimately supporting the development of reliable lifetime prediction models for these critical components.

Acknowledgment

This research forms part of the research programme of DPI project #878 and of TKI Green Chemistry and Circularity

References

[1] W. Balasooriya, C. Clute, B. Schrittesser, e G. Pinter, «A Review on Applicability, Limitations, and Improvements of Polymeric Materials in High-Pressure Hydrogen Gas Atmospheres», *Polymer Reviews*, vol. 62, fasc. 1, pp. 175–209, gen. 2022, doi: 10.1080/15583724.2021.1897997.

[2] N. C. Menon, A. M. Kruizenga, K. J. Alvine, C. San Marchi, A. Nissen, e K. Brooks, «Behaviour of Polymers in High Pressure Environments as Applicable to the Hydrogen Infrastructure», in *PVP2016*, Volume 6B: Materials and Fabrication, lug. 2016. doi: 10.1115/PVP2016-63713.

[3] A. K. M. A. Habib, A. N. Sakib, Z. T. Mona, M. M. H. Bhuiyan, P. Kazempoor, e Z. Siddique, «Hydrogen-Assisted Aging Applied to Storage and Sealing Materials: A Comprehensive Review», *Materials*, vol. 16, fasc. 20, p. 6689, ott. 2023, doi: 10.3390/ma16206689.

[4] J. Zhao, G. Ding, P. Feng, e C. Wu, «High-pressure hydrogen effects on thermoplastics: A comprehensive review of permeation, decompression failure, and mechanical properties», *Advanced Industrial and Engineering Polymer Research*, vol. 8, fasc. 3, pp. 387–407, lug. 2025, doi: 10.1016/j.aiepr.2025.05.001.

[5] H. Fujiwara, H. Ono, K. Ohyama, M. Kasai, F. Kaneko, e S. Nishimura, «Hydrogen permeation under high pressure conditions and the destruction of exposed polyethylene-property of polymeric materials for high-pressure hydrogen devices (2)-», *International Journal of Hydrogen Energy*, vol. 46, fasc. 21, pp. 11832–11848, mar. 2021, doi: 10.1016/j.ijhydene.2020.12.223.

[6] J. Li, R. Lv, C. Gu, Y. Liu, J. Li, e X. Li, «An Ageing Test Standards Analysis on Thermoplastic Liners of Type IV Composite Hydrogen Storage Tanks», *Energies*, vol. 16, fasc. 6, p. 2818, mar. 2023, doi: 10.3390/en16062818.

[7] T. A. Yersak *et al.*, «Predictive model for depressurization-induced blistering of type IV tank liners for hydrogen storage», *International Journal of Hydrogen Energy*, vol. 42, fasc. 48, pp. 28910–28917, nov. 2017, doi: 10.1016/j.ijhydene.2017.10.024.

Development of Potent *SALVIA OFFICINALIS* Extracts for Targeted Correction of Vaginal Microbiota Composition

Nevena Đukić, Milica Milutinović, Mirjana Rajilić-Stojanović

Faculty of Technology of Metallurgy, University of Belgrade, Karnegijeva 4, Belgrade, Serbia; ndjukic@tmf.bg.ac.rs

Introduction

The vaginal microbiota plays an essential role in maintaining vaginal health and protecting against pathogenic microorganisms. In healthy women, the vaginal microbiome is typically dominated by *Lactobacillus* species, particularly *Lactobacillus crispatus*, *Lactobacillus gasseri*, *Lactobacillus iners*, and *Lactobacillus jensenii*, which contribute to the maintenance of a low vaginal pH and inhibition of pathogen bacteria colonization (Punzón-Jiménez & Labarta, 2021; Witkin & Linhares, 2017). Among these species, *L. crispatus* is considered particularly beneficial due to its production of D-lactic acid, which helps protect against upper genital tract infections and adverse pregnancy outcomes.

Disruption of the vaginal microbial balance may lead to the overgrowth of pathogens such as *Streptococcus agalactiae*, a clinically important bacteria associated with adverse pregnancy outcomes and neonatal infections, including pneumonia, meningitis, and sepsis (Han et al., 2021; Larsen & Sever, 2008). Although antibiotic treatment is routinely used following screening during late pregnancy, growing evidence indicates that antibiotic exposure may alter the maternal and infant microbiome and increase susceptibility to childhood infections (Miller et al., 2018). These concerns highlight the need for alternative strategies capable of selectively inhibiting pathogenic bacteria while preserving beneficial vaginal microbiota.

Plant-derived bioactive compounds have gained increasing attention due to their antimicrobial potential. Sage (*S. officinalis*) is recognized as a rich source of biologically active compounds that may contribute to pathogen inhibition (Al-Qaysi & Al-Tulaibavi, 2022). The prebiotic index, introduced by Palfman et al. (2003), represents a quantitative measure used to evaluate prebiotic effects on microbiome composition, where increases in beneficial bacteria are considered positive and pathogen growth negative. Higher prebiotic index values indicate a stronger prebiotic effect. In this study, a sage extract is evalueted as an prebiotic.

The recovery of bioactive compounds from plant materials strongly depends on the extraction technique and processing conditions. Microwave-assisted extraction (MAE) has emerged as an efficient method that uses electromagnetic radiation to generate heat

through ionic conduction and dipole rotation, promoting cell wall disruption and facilitating the release of secondary metabolites into the solvent (López-Salazar et al., 2023). Compared to conventional techniques, MAE offers shorter extraction time and improved extraction efficiency.

In addition, response surface methodology (RSM) is a valuable statistical approach for evaluating the effects and interactions of multiple extraction parameters and identifying optimal conditions. Therefore, the aim of this study was to model the prebiotic index and optimize MAE conditions for *S. officinalis* extracts using RSM in order to maximize the inhibition of *S. agalactiae* while preserving *L. crispatus* to the greatest extent possible.

Experimental

The extraction of bioactive compounds from sage was performed using microwave-assisted extraction with a statistically designed experiment in program Design Expert 10, according to the plan shown in Table 1.

Table 1. Experimental design and obtained results

Experiment	Time (s)	Ethanol proportion (%)	Liquid-to-solid ratio (mL/g)	Prebiotic index. (%)
1	30	70	21	12.17
2	45	55	15	51.12
3	60	70	21	-8.85
4	60	70	9	44.82
5	60	40	21	69.75
6	45	55	15	53.27
7	45	55	25	2.39
8	45	55	5	68.61
9	45	55	15	49.22
10	20	55	15	10.53
11	45	80	15	-6.39
12	45	55	15	25.71

13	30	40	9	**78.51**
14	45	55	15	55.15
15	60	40	9	69.18
16	45	30	15	40.14
17	45	55	15	56.01
18	30	70	9	44.47
19	70	55	15	-0.90
20	30	40	21	76.79

Microwave-assisted extraction was performed using 3 g of *S. officinalis* plant material. For each extract, the time of the extraction, volume and concentration of ethanol were adjusted according to Table 1. All extractions were carried out at a microwave power of 180 W.

After completed extraction, each extract was evaporated at 60 ºC for 1 h to remove ethanol and adjusted to a final concentration of 2.5 mg/mL. Microbial cultures of *S. agalactiae* and *L. crispatus* were prepared in appropriate liquid media (tryptone soy broth, TSB, for *S. agalactiae* and MRS broth for *L. crispatus*) and incubated overnight for 24 h at 37 ºC. The following day, cultures were suspended in sterile saline to obtain a final concentration of 5×10^7 CFU/mL.

To evaluate the effect of sage extracts on microbial growth, sterile tubes containing 2 mL of nutrient medium (TSB or MRS broth), 2 mL of extract (2.5 mg/mL), and 100 µL of bacterial suspension were prepared. Extract sterility control consisted of nutrient medium with extract only, while microbial growth control included nutrient medium and bacterial suspension without extract.

For each of the 20 extracts, all treatments and controls were tested in duplicate for both *L. crispatus* and *S. agalactiae*. Initial optical density was measured at 600 nm, after which samples were incubated for 24 h at 37 ºC. *L. crispatus* cultures were maintained under anaerobic conditions, whereas *S. agalactiae* cultures were incubated under aerobic conditions. After incubation, optical density was measured again at 600 nm and the obtained data were used to calculate the prebiotic index, adapted from Palframan et al. (2003):

$$\text{Prebiotic index} = \frac{PR24-PR0}{PRK24-PRK0} - \frac{PA24-PA0}{PAK24-PAK0} \times 100\%$$

PR24 – Optical density (OD) of probiotic bacteria with added extract after 24 hours of growth; PR0 – OD of probiotic bacteria with added extract at the initial time of growth; PRK24 – OD of probiotic bacteria without added extract (control) after 24 hours of growth; PRK0 – OD of probiotic bacteria without added extract (control) at the initial time of growth; PA24 – OD of pathogenic bacteria with added extract after 24 hours of growth; PA0 – OD of pathogenic bacteria with added extract at the initial time of growth; PAK24 – OD of pathogenic bacteria without added extract after 24 hours of growth; PAK0 – OD of pathogenic bacteria without added extract (control) at the initial time of growth.

The results obtained for the prebiotic index are shown in Table 1.

Further, a mathematical model was developed based on the data obtained in the experiment and this equation was used to optimize the process, using a statistically planned experiment in Design Expert 10, with the aim of obtaining an extract with the highest prebiotic index value. The statistically planned experiment, based on the previous results specified new experimental conditions shown in Table 2.

Table 2. Optimized extraction conditions for achieving maximum prebiotic index

time	ethanol	ratio l/s	Predicted prebiotic index
s	%	mL/g	%
30.345	40.188	9.081	78.730

An extract was obtained using extraction conditions predicted to maximize the recovery of compounds associated with the highest prebiotic index. Extraction conditions included time of extraction of 30.345s, ethanol concentration of 40.188% and liquid to solid ration of 9.081 mL/g. The prebiotic index was assessed and a value of 78.59% was obtained. For the optimization model to be considered valid, the prebiotic index of the optimized extract should have values between 77.24% and 80.22%, which the value of 78.59% meets. Using this extract, more than 99% of *S. agalactiae* was inhibited, and 80% od *L. crispatus* was preserved**.**

Summary

This study focused on the optimization of bioactive compound extraction from sage (*Salvia officinalis*) with the aim of obtaining extracts capable of modulating the vaginal microbiota. In healthy women, the vaginal microbiota is predominantly composed of beneficial *Lactobacillus* species, particularly *L. crispatus*, which plays an important role in maintaining microbial balance and protecting against pathogens. During pregnancy, colonization with *S. agalactiae* may increase the risk of severe neonatal infections, leading to routine screening and antibiotic treatment. However, antibiotic exposure may disrupt the maternal and infant microbiota and contribute to adverse outcomes, emphasizing the need for alternative approaches that selectively inhibit pathogens while preserving beneficial bacteria.

As an alternative aproach, microwave-assisted extraction (MAE) of sage was optimized to maximize the recovery of biologically active compounds with desirable antimicrobial and prebiotic properties. The prebiotic index was used as a quantitative measure to evaluate the ability of extracts as prebiotics to inhibit *S. agalactiae* while preserving *L. crispatus*. By applying response surface methodology (RSM) and statistically planned experiments, the optimal extraction conditions were identified. The most favorable extraction parameters included a microwave extraction time of 3.345 s, ethanol concentration of 40.188% and solvent-to-solid ratio of 9.081 mL/g, resulting in prebiotic index of 78.59%, *S. agalactiae* inhibition of >99% and preservation of *L. crispatus* growth of 80%.

These findings demonstrate that optimization of extraction parameters significantly influences the biological activity of sage extracts and highlights their potential application in formulations for vaginal microbiota correction, such as vaginalettes, as a supplement or alternative to antibiotics during pregnancy.

References

Punzón-Jiménez, P., & Labarta, E. (2021). The impact of the female genital tract microbiome in women health and reproduction: a review. Journal of assisted reproduction and genetics, 38(10), 2519-2541.

Witkin, S. S., & Linhares, I. M. (2017). Why do lactobacilli dominate the human vaginal microbiota?. BJOG: An International Journal of Obstetrics & Gynaecology, 124(4), 606-611.

Han, Y., Liu, Z., & Chen, T. (2021). Role of vaginal microbiota dysbiosis in gynecological diseases and the potential interventions. Frontiers in microbiology, 12, 643422

Larsen, J. W., & Sever, J. L. (2008). Group B Streptococcus and pregnancy: a review. American journal of obstetrics and gynecology, 198(4), 440-450

Miller, J. E., Wu, C., Pedersen, L. H., de Klerk, N., Olsen, J., & Burgner, D. P. (2018). Maternal antibiotic exposure during pregnancy and hospitalization with infection in offspring: a population-based cohort study. International journal of epidemiology, 47(2), 561-571

Al-Qaysi, D. B. A., & Al-Tulaibawi, N. A. J. (2022). Antibacterial efficacy of Salvia officinalis extract against Staphylococcus aureus and Escherichia coli. International Journal of Design & Nature and Ecodynamics, 17(5), 789–794

López-Salazar, H., Camacho-Díaz, B. H., Arenas Ocampo, M. L., & Jiménez-Aparicio, A. R. (2023). Microwave-assisted extraction of functional compounds from plants: A review. BioResources, 18(3), 6614–6638.

Palframan, R., G. R. Gibson, and R. A. Rastall. “Development of a quantitative tool for the comparison of the prebiotic effect of dietary oligosaccharides.” Letters in Applied Microbiology 37.4 (2003): 281-284

Climate-Informed Optimization of Solid Lignin-Based Products

Natalia Gala

Institute of Thermal Separation Processes, Hamburg University of Technology and United Nations University Hub on Engineering to Face Climate Change at the Hamburg University of Technology, United Nations University Institute for Water, Environment and Health (UNU INWEH), Hamburg, Germany, natalia.gala@tuhh.de

Introduction

Lignin, one of the most underutilized natural polymers, has noteworthy potential for functional and environmentally friendly material applications. This project focuses on investigating the influence of climate conditions on lignin properties and, consequently, on its advanced applications.

Lignin is an aromatic biopolymer and the second most abundant biopolymer on Earth. As a major component of wood, it acts as a natural glue that binds wood cells together, enhancing mechanical strength and rigidity while also contributing to barrier properties. Owing to its hydrophobic and chemically versatile structure, lignin is a promising material for applications such as the reduction of wettability in hydrophilic biopolymeric materials.

Although every year, 50–70 million tons of technical are produced as by-products of biomass fractionation, only a small fraction is currently used commercially. Technical lignin differs from native lignin not only in its botanical origin, but also as a result of extraction processes and possible chemical modifications [1].

Lignin gained the special interested as a biopolymer mainly because of its aromatic structure (Fig 1.), resembling high-performance petroleum-based syntactic polymers, commonly known as plastics. Lignin as a renewable polymer was identified as promising bio-based carbon source for polymer production. As it does not compete with food production and is widely available at low cost, it offers significant potential for the development of next-generation sustainable materials [2]. Nevertheless, lignin is still largely confined to use as a low-cost energy source in the forestry sector, representing a major bottleneck for its valorisation, due to its lack of traceability and molecular heterogeneity [3-4].

Technical lignins differ significantly from the *in planta* lignin in both structure and properties. During extraction chemical transformations, such as cleavage of ester and ether linkages, occur. As a result, lignin exhibits a wide variability in molecular weight distribution, functional group content, solubility, and thermal behaviour [5]. These variations can directly affect its performance in material applications.

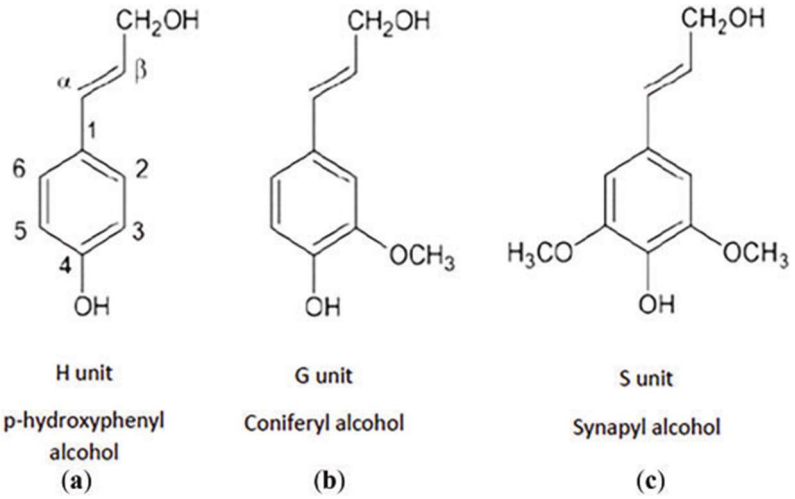

Fig. 1. Molecular structure of monolignols composing lignin [6].

In recent years, lignin has gained increasing attention as a building block for aerogels and porous materials, which require precise control over network formation and drying-induced structural stability [7]. Aerogels are promising materials due to their high porosity, low density and large surface area. Bio-based aerogels, especially alginate-based, show limited stability under moisture and mechanical load. Since native lignin acts as a natural barrier in plant cell walls, enhancing mechanical strength and contributing to water resistance, considerable research has focused on exploiting these properties in material science, particularly for coatings and hydrophobization applications [1],[8].

At the same time, climate change introduces an additional, largely unexplored layer of variability. Temperature, precipitation patterns, CO_2 concentration, light intensity, and environmental stress conditions influence lignin biosynthesis in plants. These factors affect not only lignin content but also monomer composition and bonding patterns within the plant cell wall. However, it remains largely unknown how these climate-driven variations translate into the properties of technical lignins after industrial extraction, and how they influence subsequent material processing such as gelation and aerogel formation [9-11].

Understanding this relationship is particularly important for sustainable material design, as it enables the transition from empirical processing strategies toward data-informed and climate-aware lignin valorisation pathways.

Experimental

The present work aims to establish correlations between biomass origin, climate conditions, extraction processes, and lignin performance in aerogel systems, with a specific focus on high-pressure drying routes.

1. Lignin sourcing and preparation

Lignin samples will be obtained from multiple biomass sources, primarily wheat straw and beech wood, representing herbaceous and hardwood feedstocks. To capture process-induced variability, several extraction methods are included: kraft pulping, organosolv extraction, Milled Wood Lignin (MWL) isolation, and Liquid Hot Water (LHW) treatment.
Among these, LHW is of particular interest, as it represents a hydrothermal, solvent-free fractionation method performed under elevated temperature and pressure. LHW lignin is expected to preserve more native-like structural features compared to harsh chemical pulping methods, while still exhibiting controlled depolymerization.

2. Lignin characterization

Comprehensive physicochemical characterization will be performed to assess structural variability:

- Molecular weight distribution
- Functional group analysis and structural linkages
- Solubility in polar and non-polar solvent systems
- Hydrodynamic radius
- Surface properties including polarity and wettability
- Optical properties including colour variation

Special attention is given to molecular weight, as this parameter can strongly influence lignin self-assembly, aggregation behaviour, and gelation potential [8]. Additionally, colour variation is considered as a fast and indirect indicator of structural differences between lignin batches.

3. Applications: Lignin & Nanoporous Materials

<u>Lignin Coatings on Porous Matrices</u>

Lignin particles from different origins will be investigated as coating materials for biopolymeric substrates, particularly alginate-based particles and aerogels. The self-assembly and behaviour of lignin during coating will be evaluated.

Coating performance will be analysed using wettability measurements, optical microscopy, SEM imaging, mechanical testing, and dynamic vapour sorption studies. The influence of lignin source, extraction method, and climatic origin on coating formation and stability will be systematically assessed.

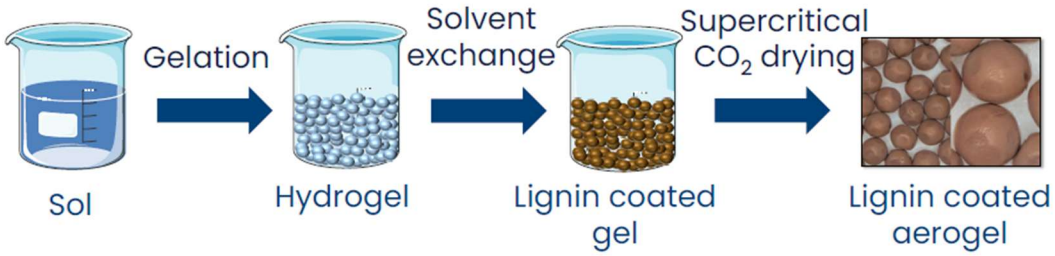

Fig. 2. Synthesis and coating of alginate aerogel beads.

'All-lignin' Gels & Aerogels

Lignin will be processed into hydrogel systems, which serve as precursors for aerogel formation. The behaviour of lignin molecules during gel formation will be studied with respect to: concentration effects, solvent environment, and molecular weight distribution. The resulting aerogels are evaluated in terms of: porosity and surface area (BET analysis) And microstructure (SEM and optical microscopy).

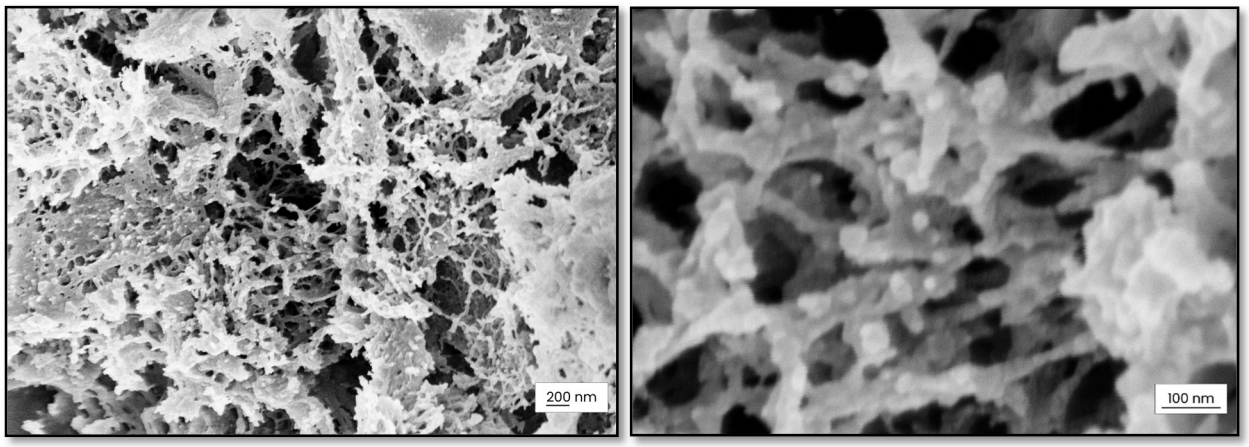

Fig. 3. SEM pictures of first syntesized '*all-lignin*' aerogels.

Summary

This work aims to establish a systematic understanding of how climate-driven biomass variability translates into functional differences in technical lignins and their performance in aerogel systems.

A central hypothesis is that lignin properties are not only defined by the extraction method, but also indirectly by climatic growth conditions of the biomass source. These differences

manifest in molecular weight distribution, structural condensation, and surface properties, which ultimately govern self-assembly and gelation behaviour.

By combining climate data, lignin chemistry, and high-pressure drying-based material processing, this study proposes a multiscale framework linking environmental conditions to advanced material performance.

The expected outcomes include:

- Identification of key parameters controlling lignin coating and gel formation
- Improved understanding of structure–property relationships in heterogeneous lignins
- Guidelines for selecting lignin feedstocks for targeted applications

Ultimately, this approach contributes to the development of sustainable, climate-informed biomaterial design strategies, enabling more predictable and efficient use of lignin in high-value coatings and porous materials.

Acknowledgment

This project is funded by the Deutsche Forschungsgemeinschaft (DFG, German Research Foundation) – GRK 3068: Climate-informed Engineering – 531249004.

References

[1] J. Ruwoldt, F. H. Blindheim, and G. Chinga-Carrasco, 'Functional surfaces, films, and coatings with lignin – a critical review', *RSC Adv.*, vol. 13, no. 18, pp. 12529–12553, 2023, doi: 10.1039/D2RA08179B.

[2] O. Y. Abdelaziz *et al.*, 'Recent strides toward transforming lignin into plastics and aqueous electrolytes for flow batteries', *iScience*, vol. 27, no. 4, p. 109418, Mar. 2024, doi: 10.1016/j.isci.2024.109418.

[3] A. Ayoub and L. A. Lucia, Eds, *Introduction to renewable biomaterials: first principles and concepts*. Hoboken, NJ: John Wiley & Sons, 2018.

[4] B. L. Tardy, E. Lizundia, C. Guizani, M. Hakkarainen, and M. H. Sipponen, 'Prospects for the integration of lignin materials into the circular economy', *Materials Today*, vol. 65, pp. 122–132, May 2023, doi: 10.1016/j.mattod.2023.04.001.

[5] S. Laurichesse and L. Avérous, 'Chemical modification of lignins: Towards biobased polymers', *Progress in Polymer Science*, vol. 39, no. 7, pp. 1266–1290, Jul. 2014, doi: 10.1016/j.progpolymsci.2013.11.004.

[6] R. Ribeiro *et al.*, 'High Lignin Content Polymer Filaments as Carbon Fibre Precursors', *JOURNAL OF RENEWABLE MATERIALS*, pp. 1–10, Jul. 2025, doi: 10.32604/jrm.2025.02025-0071.

[7] R. Altarabeen *et al.*, 'Lignin Polyurethane Aerogels: Influence of Solvent on Textural Properties', *Gels*, vol. 10, no. 12, p. 827, Dec. 2024, doi: 10.3390/gels10120827.

[8] R. Altarabeen, B. Schroeter, M. Finšgar, A. Smit, A. Sadeq, and I. Smirnova, 'Lignin coating of alginate aerogels', Feb. 20, 2026, *Social Science Research Network, Rochester, NY*: 6275422. doi: 10.2139/ssrn.6275422.

[9] X. Zhao *et al.*, 'High temperature increased lignin contents of poplar (Populus spp) stem via inducing the synthesis caffeate and coniferaldehyde', *Front. Genet.*, vol. 13, Sep. 2022, doi: 10.3389/fgene.2022.1007513.

[10] G. Resente and A. Crivellaro, 'Environmental Impacts on Plant Cell Wall Lignification', *Journal of Bioresources and Bioproducts*, vol. 10, no. 1, pp. 4–6, Feb. 2025, doi: 10.1016/j.jobab.2024.11.001.

[11] L. M. San-Emeterio, M. D. Hidalgo-Galvez, J. M. de la Rosa, I. Pérez-Ramos, and J. A. González-Pérez, 'Impact of future scenarios of climate change on lignin dynamics in soil: A case study in a Mediterranean savannah', *Science of The Total Environment*, vol. 946, p. 174317, Oct. 2024, doi: 10.1016/j.scitotenv.2024.174317.

Influence of Gasification Char on Biogas Production in Anaerobic Digestion Systems in a Continuously Operated Reactor

Ann Sophie Mossauer, Christian Margreiter, Angela Hofmann, Andreas Otto Wagner
Umwelt-, Verfahrens- und Energietechnik, Management Center Innsbruck
amossauer@student.tugraz.at

Introduction

With the increasing pollution of the aquatic environment, there is a growing need for new innovative methods of wastewater treatment. When these compound are found in the water systems they can have harmful effects on humans and animals .The use of activated char as an adsorbent is considered as a promising method of purification. [1-2] Yet not just clean water but also a growing demand of green energy is a challenge for the future. Anaerobic digestion (AD) is a bioenergy technology that produces methane from sludge. If the char however is added in the wastewater treatment plant, it will eventually end up in the biogas plant.

The goal of this thesis was to evaluate the effect of gasification char on the anaerobic processes in a biogas plant. To investigate this influence biogas production, performance parameters such as production quantity, quality of methane (CH_4) content and the pH-value and volatile fatty acids (VFA) are determined. For these an experimental setup with six continuously run anaerobic reactors were used. Instead of adding char directly to the reactor, the substrate was obtained from a bypass WWTP operated with char.

Experimental

The reactors were filled with 3,5 L of sewage sludge and operated for 104 days. This time span was divided into three phases. The adaptation phase (AP), the stabilization phase (SP), and the char phase (CP). During the AP and SP, samples were taken twice per week and in the CP samples were taken three times per week. The experiment was conducted under anaerobic conditions at 37 °C with continuous mixing. The biochar was provided by Innsbrucker Kommunalbetriebe AG (IKB). The char is a by-product of the gasification of forest residues in a fixed-bed fluidized-bed reactor developed by Syncraft. [3]. The characterization of the biochar is presented in the cited study [4] The Experimental setup is depicted in Figure 1.

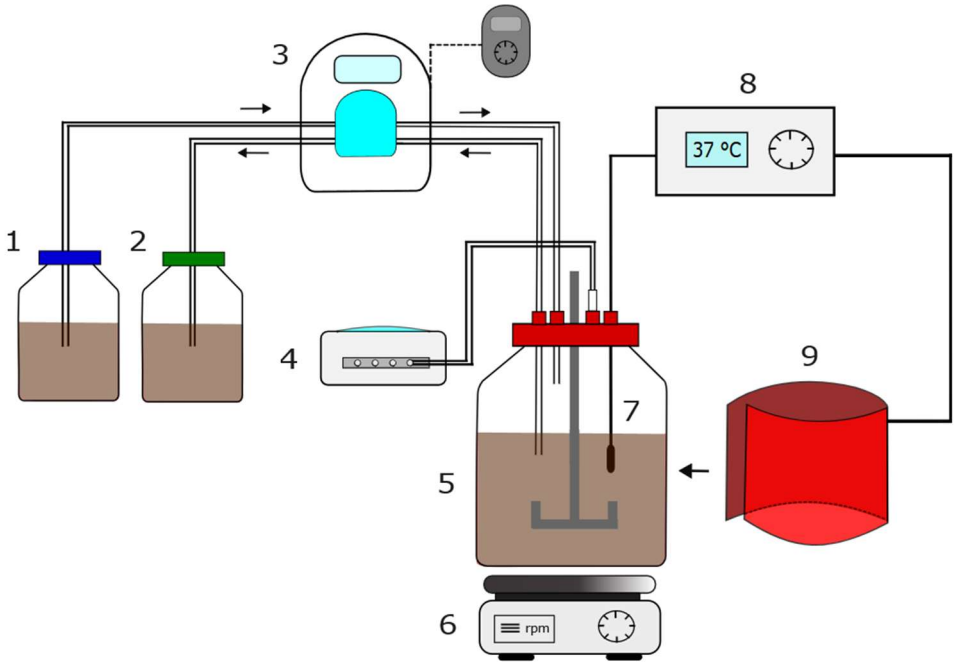

Figure 1. Schematic representation of the experimental setup. (1) Substrate bottle, (2) Waste bottle, (3) Peristaltic pump, (4) Gas meter, (5) Reactor, (6) Magnetic stirrer, (7) Temperature sensor, (8) Temperature controller, (9) Heating mat.

The organic loading rate (ORL) of 0.05 g VS L^{-1} d^{-1} with a total substrate dosage of 0.07 L $d^{-1}$of substrate. In the CP the reactors were separated in reactor with char (RC) and rectors without char (RNC). The homogeneity of variances is tested using Levene's test. An Anova analysis is subsequent performed with different combinations of reactors until a combination with a p-value of $p > 0.05$ is obtained. The substrate applied during the CP originated from a bypass plant.

Weekly samples of gas and sludge were taken. The gas samples were analysed using Gas chromatography GC (Shimadzu GmbH,Japan). Only the methane concentration was used for further analysis.[5] To monitor the performance and stability the production of the VFAs was analysed. These samples were analysed using HPLC (LC-20AD Liquid (Shimadzu GmbH, Deutschland). The volatile solids (VS) content was determined using a TGA analyser (STA449 F5 Jupiter Netzsch, Germany) to calculate the actual OLR of the substrate and to monitor nutrient removal in the reactor.

Results

Due to data protection and confidentiality requirements, some displayed numerical values and axis scales were adjusted or anonymized without affecting the scientific interpretation

of the result. Figure 2 shows the normalized methane production of RC and RNC. The CH_4 production was normalized to a basis OLR of 1 g VS L^{-1} d^{-1}. During the CP, a significant difference was observed between the normalized CH_4 production of the RC and the RNC ($p < 0.05$). The RC showed an approximately 30 % higher normalized CH_4 production compared to the RNC during the evaluated period. This is consistent with the results reported by Wang et al.[6] where an increase in CH_4 production of 22.4% to 40.3% was observed after the addition of biochar. In comparison, a batch experiment conducted by Wei et al.[7] reported an increase in CH_4 production ranging from 8.6% to 17.8%.

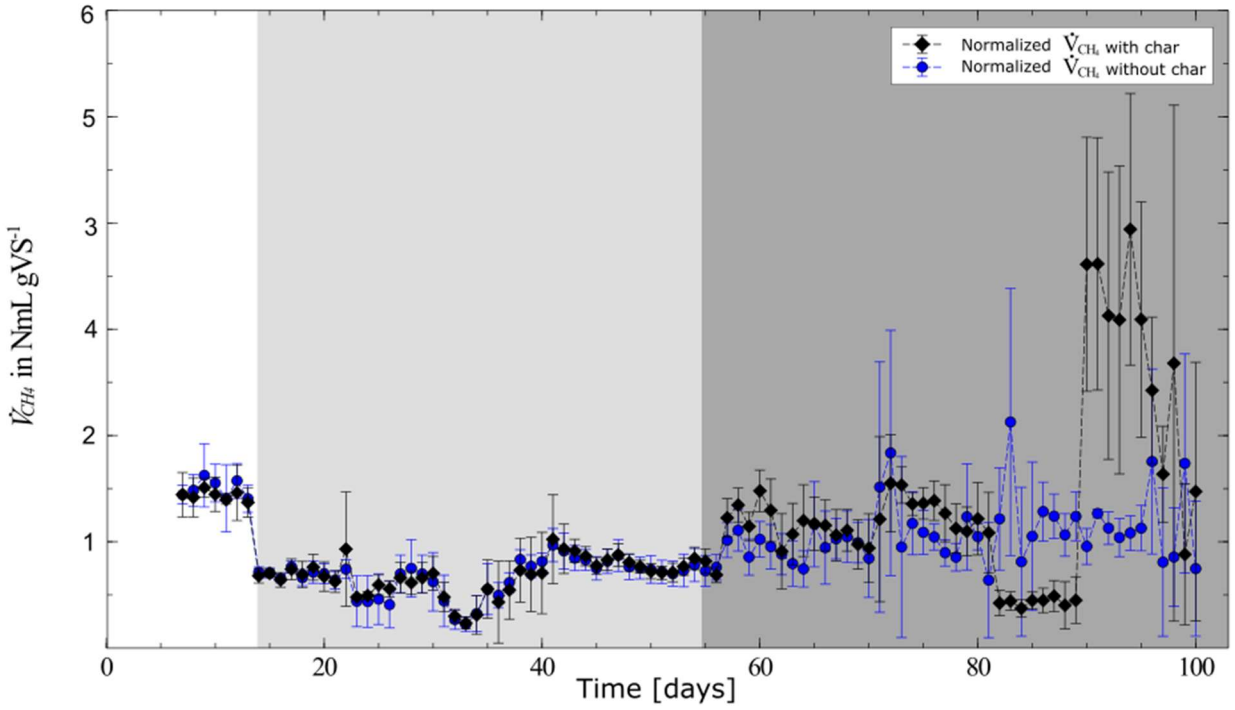

Figure 2: Normalized volumetric flow rate of the produced CH_4 per day for RC and RNC. The data points are connected by dashed lines for better visualization. The graph is divided into three phases: AP (white), SP (light grey), and CP (dark grey

In Figure 3 the average concentration of the VFAs. The VFA values are calculated as the sum of the VFAs (formate, acetate, propionate, isobutyrate, butyrate, isovalerate, and valerate). The t-test showed that the reactors RC and RNC did not differ significantly in their VFA concentrations ($p > 0.05$). This indicates that the process conditions remained stable throughout the entire experiment.

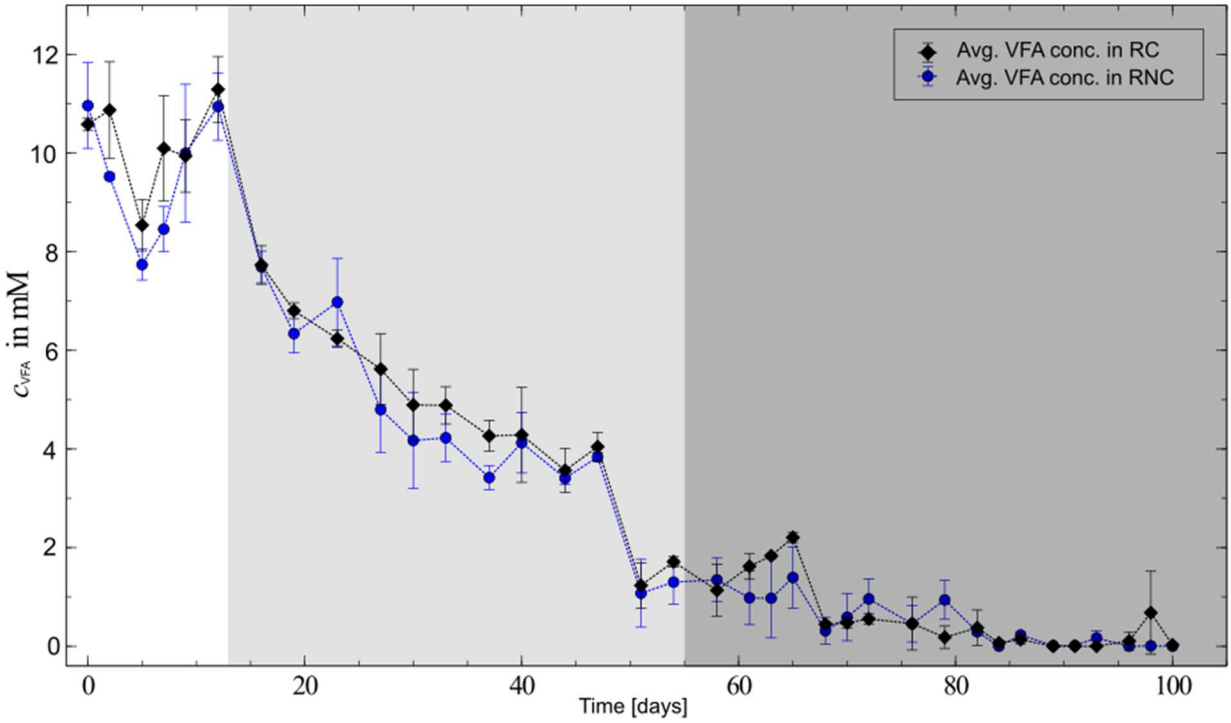

Figure 3: Average concentration of VFAs in mM per day for the reactors with char (black graph) and without char (blue graph). The data points are connected by dashed lines.

Summary

In Summary the use of char had a positive effect on the AD system. An average increase of approximately 30 % in CH_4 in the reactors with char compared to the reactors without char. These findings are consistent with previous studies. Although no statistically significant differences in VFA concentrations were observed, the decreasing trend may indicate stable process condition. Further investigations are required to gain a better understanding of the long-term effects of biochar. It would be interesting to investigate whether recycling the biochar in the WWTP could further reduce its effectiveness. Furthermore, the decrease in buffering capacity caused by using biochar in WWTPs should be examined in more detail.

Acknowledgment

I would like to sincerely thank the Josef Ressel Center for their support during this thesis. I would also like to thank my supervisor for their guidance and valuable assistance throughout this work .and everyone who contributed to the successful completion of this thesis.

References

[1] H. Schaar, J. Krampe, and N. Kreuzinger, ‘Einsatzbereiche und Grundlagen für die 4. Reinigungsstufe in Österreich’, Österr. Wasser- Abfallwirtsch., vol. 75, no. 9–10, pp. 549–557, Oct. 2023, doi: 10.1007/s00506-023-00984-8.

[2] ‘Schadstoffe’, Umweltbundesamt. Accessed: May 14, 2026. [Online]. Available: https://www.umweltbundesamt.de/themen/wasser/gewaesser/meere/nutzung-belastungen/schadstoffe

[3] M. Huber, M. Huemer, A. Hofmann, and S. Dumfort, ‘Floating-fixed-bed-gasification: From Vision to Reality’, Energy Procedia, vol. 93, pp. 120–124, Aug. 2016, doi: 10.1016/j.egypro.2016.07.159.

[4] C. Margreiter, M. Probst, E. M. Prem, A. Hofmann, and A. O. Wagner, ‘Gasification chars and activated carbon: Systematic physico-chemical characterization and effect on biogas production’, Heliyon, vol. 10, no. 10, p. e31264, May 2024, doi: 10.1016/j.heliyon.2024.e31264.

[5] A. O. Wagner, C. Malin, P. Lins, and P. Illmer, ‘Effects of various fatty acid amendments on a microbial digester community in batch culture’, Waste Manag., vol. 31, no. 3, pp. 431–437, Mar. 2011, doi: 10.1016/j.wasman.2010.10.020.

[6] Y. Wang, M. Huo, Q. Li, W. Fan, J. Yang, and X. Cui, ‘Comparison of clogging induced by organic and inorganic suspended particles in a porous medium: implications for choosing physical clogging indicators’, J. Soils Sediments, vol. 18, no. 9, pp. 2980–2994, Sep. 2018, doi: 10.1007/s11368-018-1967-6.

[7] W. Wei et al., ‘Enhanced high-quality biomethane production from anaerobic digestion of primary sludge by corn stover biochar’, Bioresour. Technol., vol. 306, p. 123159, Jun. 2020, doi: 10.1016/j.biortech.2020.123159.

Improvement of Sulfamethoxazole Physicochemical Properties by Spray Drying and Ionic Gelation

A. Sander, I. Blažević, A. Ančić, M. Gašpar, N. Ivančić Jokić, F. Medulin, M. Milčić, D. Paponja, I. Pinušić, A. Sander, P. Santro

Faculty of Chemical Engineering and Technology/Department of Mechanical and Thermal Process Engineering, University of Zagreb, iblazevic@fkit.unizg.hr

Introduction

Sulfamethoxazole is a sulfonamide antibacterial drug that remains widely used for treating urinary tract infections, respiratory infections and certain gastrointestinal infections. As a BCS Class IV compound, it is characterized by low solubility and low permeability, making it a suitable candidate for formulation optimization.[1,2,3]

Among available formulation technologies, spray drying is especially attractive because it is scalable, rapid, and capable of converting solutions or suspensions into dry powders with controlled particle size and morphology. Also, spray drying is widely used to create amorphous or partially amorphous dispersions to increase surface area and wettability, all of which can promote faster dissolution. Earlier studies found that solid dispersion combined with polymers increased solubility, particularly when carriers such as HPMC were used.[4]

At the same time, the search for improved bioavailability increasingly includes natural products such as essential oils and extracts or isolated bioactive compounds. Essential oils are composed of hydrophobic volatile organic compounds obtained from plant material with methods such as steam or water distillation. Extracts, on the one hand, are compounds pulled from plants or raw materials using solvents or other extraction methods. Isolated bioactive compounds, on the other hand, are purified compounds from natural sources that can affect living organisms or body functions.[5]

Recent studies show that some plant extracts can fight bacteria in different ways, such as damaging bacterial membranes, disrupting enzymes and metabolism, preventing biofilm formation, and affecting bacterial communication.

Because of that, essential oils and extracts have gained attention as bioactive compounds because synergistic combinations can improve antimicrobial efficacy against resistant microorganisms. Overall, this positions essential oils and extracts not only as formulation excipients, but also as compounds that improve antibiotic delivery systems.[6]

Within this group of natural compounds, piperine, caffeine and curcumin are particularly relevant. Piperine has been highlighted as a natural bioenhancer and as a potentially useful antibacterial and immunomodulatory compound. Curcumin is attractive because of its anti-inflammatory, antioxidant, and antimicrobial activities. Caffeine can stimulate gastric acid secretion and microcirculation, which may enhance absorption of pharmaceuticals into the bloodstream. However, piperine and curcumin have poor aqueous dispersibility and limited bioavailability, unlike caffeine, so their effective use usually requires an appropriate formulation strategy.[7,8,9]

Essential oils are volatile and sensitive to oxidation, while piperine and curcumin are hydrophobic and difficult to disperse equally in aqueous systems. Spray-drying encapsulation is therefore good option because it can transform unstable or poorly dispersible bioactive compounds into powders with improved characteristics. Recent studies highlight the importance of wall materials such as gum arabic and carefully chosen emulsification conditions, while newer case studies show that spray drying can improve the dispersion of essential oils in water.[6,7,8,9]

At the same time, alginate-based ionic gelation provides a low-temperature method for encapsulation. Sodium alginate cross-linked with calcium ions forms biocompatible systems suitable for encapsulating drugs, extracts, and essential oils under mild processing conditions. Therefore, alginate-$CaCl_2$ gelation is especially useful for formulations containing volatile oils or sensitive hydrophobic compounds that may not tolerate more aggressive processing conditions equally well. [9]

The present work investigates two formulation strategies for improving sulfamethoxazole properties. The first strategy uses spray drying for preparing powders from suspensions or hydroalcoholic feeds containing sulfamethoxazole and essential oils, extracts or isolated bioactive compound, while the second uses sodium alginate and calcium chloride to produce ionic gelled beads under milder conditions. The hypothesis is that polymeric carriers can improve the physicochemical properties of sulfamethoxazole, while the selected natural extracts, essential oils, and isolated bioactive compounds may provide additional functional effects. [4,10]

Experimental

As it is previously said, the experiment is based on two formulation strategies: spray drying and ionic gelation. In the spray-drying, sulfamethoxazole was combined with natural bioactive compounds, including essential oils, extracts, or isolated bioactive

compound, together with HPMC, gum Arabic, and Tween 80 as auxiliary formulation components, as shown in Figure 1.

First stage of research work is focused on black pepper and anise essential oil. Essential oils were prepared by hydrodistillation, while plant extracts were made using extraction followed by filtration and solvent removal. Essential oils and extracts were mixed into sulfamethoxazole feeds together with HPMC, gum arabic, and Tween 80, after which the formulations were processed by spray drying.

In the next stage of the work, the spray-drying method was upgraded by comparing suspension-based and solution-based feeds. Initial suspension feeds were prepared in water with HPMC, gum Arabic, and Tween 80, followed by the addition of sulfamethoxazole and the selected bioactive compounds. To solve the problem of suspension, MeOH/H_2O and EtOH/H_2O mixtures (40:60) were added to the hydroalcoholics systems to make more homogeneous feeds before spray drying.

The other experimental method was based on ionic gelation. In this approach, sodium alginate dispersions containing sulfamethoxazole and the oil phase, extracts, or isolated bioactive compounds were added as droplets into calcium chloride solution, forming calcium-alginate beads. The collected beads were filtered, washed, and further evaluated. This mild encapsulation method was introduced as an alternative to spray drying, particularly for systems containing essential oils or other sensitive components.

Fig. 1.

Summary

This work presents an attempt to improve the physicochemical properties of sulfamethoxazole by combining sulfamethoxazole with natural bioactive compounds. Sulfamethoxazole is a suitable candidate for solubility improvement, while spray drying and ionic gelation are effective methods for poorly water-soluble drugs and sensitive

bioactive compounds. Extracts, essential oils, piperine, caffeine and curcumin may also contribute to the additional antimicrobial and bioenhancing effects.

Acknowledgment

This research was conducted within the LiBiDES project, funded by the European Union through the NextGenerationEU fund from source 581 - the Recovery and Resilience Facility, within the framework of program funding for public higher education institutions and public scientific institutes in the Republic of Croatia.

References

1) Roy, P., Chakraborty, S., Pandey, N., Kumari, N., Chougule, S., Chatterjee, A., Chatterjee, K., Mandal, P., Gorain, B., Dhotre, A. V., Bansal, A. K., & Ghosh, A. (2023). *Study on Sulfamethoxazole-Piperazine Salt: A Mechanistic Insight into Simultaneous Improvement of Physicochemical Properties. Molecular pharmaceutics*, *20*(10), 5226–5239. doi.org/10.1021/acs.molpharmaceut.3c00646

2) Ahmadi F, McArthur E, Garcia-Bournissen F, Rieder MJ, Muanda FT. *Trimethoprim-Sulfamethoxazole and Acute Failure in Adolescents and Young Adults. JAMA Netw Open.* 2025;8(11):e2545251. doi:10.1001/jamanetworkopen.2025.45251

3) Greenwood, D. (2010). Sulfonamides. In R. G. Finch, D. Greenwood, S. R. Norrby, & R. J. Whitley (Eds.), Antibiotic and chemotherapy (9th ed., pp. 337–343). W.B. Saunders. doi.org/10.1016/B978-0-7020-4064-1.00029-4

4) Davis, M., & Walker, G. (2018). *Recent strategies in spray drying for the enhanced bioavailability of poorly water-soluble drugs*. *Journal of controlled release : official journal of the Controlled Release Society*, *269*, 110–127. doi.org/10.1016/j.jconrel.2017.11.005

5) Zouine, N., El Ghachtouli, N., El Abed, S., & Ibnsouda Koraichi, S. (2024). *A comprehensive review on medicinal plant extracts as antibacterial agents: Factors, mechanism insights and future prospects*. *Scientific African, 26*, e02395. doi.org/10.1016/j.sciaf.2024.e02395

6) Altay, Ö., Köprüalan, Ö., İlter, I., Koç, M., Ertekin, F. K., & Jafari, S. M. (2024). Spray drying encapsulation of essential oils; process efficiency, formulation strategies, and applications. *Critical reviews in food science and nutrition*, *64*(4), 1139–1157. doi.org/10.1080/10408398.2022.2113364

7) Murase, L. S., Perez de Souza, J. V., Meneguello, J. E., Palomo, C. T., Fernandes Herculano Ramos Milaré, Á. C., Negri, M., … Cardoso, R. F. (2023). *Antibacterial and immunological properties of piperine evidenced by preclinical studies: a systematic review. Future Microbiol*, *18*, 1279–1299. doi.org/10.2217/fmb-2023-0101

8) Evans, J., Richards, J. R., & Battisti, A. S. (2024). *Caffeine*. In *StatPearls*. StatPearls Publishing. NCBI Bookshelf

9) Hewlings, S. J., & Kalman, D. S. (2017). *Curcumin: A Review of Its Effects on Human Health. Foods (Basel, Switzerland)*, *6*(10),92. https://doi.org/10.3390/foods6100092

10) Kumari, A., Varunteja, B., Mohanty, S., Mishra, A., Gupta, N., Mukherjee, T., Sharma, B., & others. (2026). *Advancement in sodium alginate-based drug delivery systems: Applications and future prospects*. *AAPS PharmSciTech, 27*, 196. https://doi.org/10.1208/s12249-025-03284-4

Investigation of the Vapor-Liquid Phase Equilibrium of a Binary Mixture of Eucalyptol and Various Alcohols

Atád Vészi and László T. Mika

Department of Chemical and Environmental Process Engineering, Budapest University of Technology and Economics, veszi.atad@vbk.bme.hu

Introduction

The development and selection of alternative, sustainable solvents have become a key focus in recent development of novel chemical processes, driven by the needs to replace volatile, toxic, and fossil-based organic solvents.[1] In this context, naturally derived compounds such as eucalyptol have gained increasing attention due to their favourable environmental and safety profiles.[2] However, the practical application of such solvents requires a thorough understanding of their thermodynamic behaviour, particularly in mixtures with common polar solvents such as short-chain alcohols.

The aim of this work was to investigate the thermodynamic and separation behaviour of binary liquid mixtures, specifically those composed of eucalyptol (Fig. 1) and three alcohols: methanol, ethanol, and n-propanol. Various activity coefficient models (Wilson[3], UNIQUAC[4], NRTL[5], UNIFAC[6]) were applied to describe component interactions and to evaluate the applicability of each model to these systems.

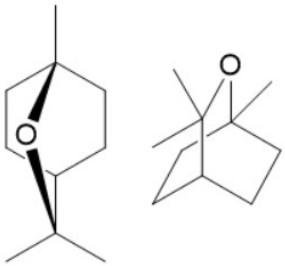

Fig. 1.: The chemical structure of the eucalyptol

Experimental

Experimental measurements were performed at atmospheric pressure, with a modified Gillespie-still[7] (Fig. 2.) covering a wide concentration range. The data, based on refractive index measurements, were processed using regression methods to fit the different thermodynamic models, and the binary interaction parameters (BIPs) required for vapor–liquid equilibrium calculations were determined.

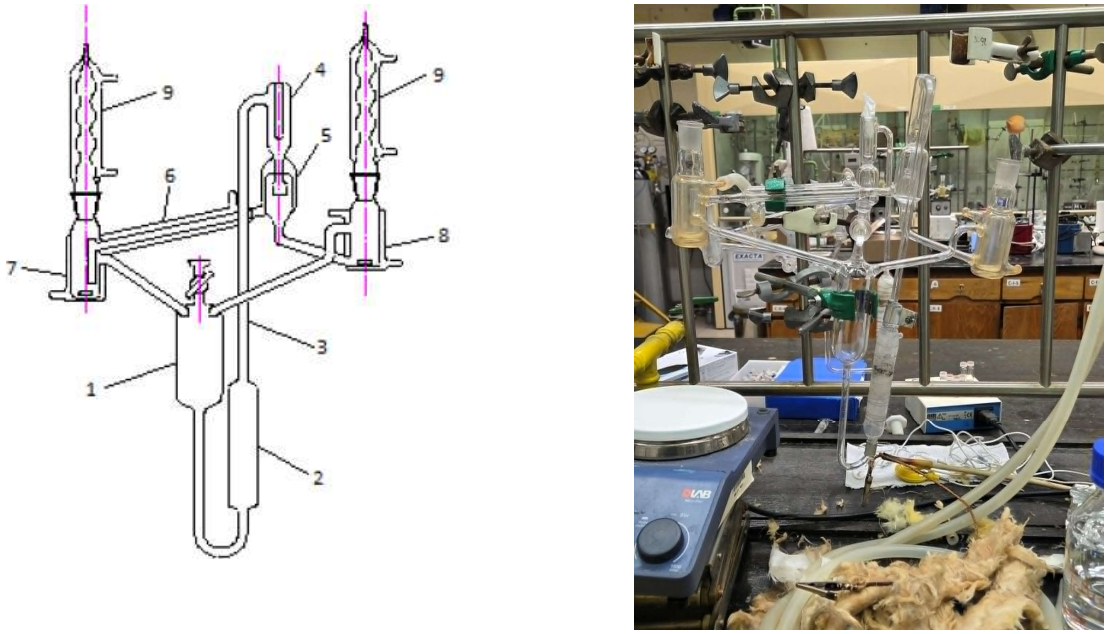

Fig. 2.: Modified Gillespie-still

Summary

In the case of the methanol–eucalyptol mixture, the UNIQUAC model showed the best fit for temperature data, while the Wilson model gave the most accurate results for the y_1 values. For the ethanol–eucalyptol system, the Wilson model matched the temperature trends more closely, whereas the NRTL model provided more accurate composition predictions. For the n-propanol mixture, the Wilson model again performed best in terms of temperature, while the UNIQUAC model gave better results for y_1. The results are presented in Tab. 1.:

	Wilson		**NRTL**		**UNIQUAC**	
	AADT	AADy1	AADT	AADy1	AADT	AADy1
Methanol - Eucalyptol	0.87	0.0272	0.79	0.0274	0.71	0.0275
Ethanol - Eucalyptol	0.38	0.0027	0.40	0.0025	0.43	0.0028
n-Propanol - Eucalyptol	0,.49	0.0059	0.51	0.0056	0.58	0.005

Tab. 1.: Average Absolute Deviations for T and y of different binary mixtures.

Notable differences were observed among the applied models. In the case of the methanol–eucalyptol system, azeotropic behaviour was indicated, which proved challenging for accurate representation by the models. In contrast, a better agreement between experimental and calculated data was achieved for the other mixtures. None of the systems could be described as ideal mixtures. Overall, the NRTL and UNIQUAC models provided the most reliable correlations.

Acknowledgment

The project, supported by the Doktoranduszi Kiválósági Ösztöndíj Program (DKÖP), was implemented based on a grant agreement concluded with the Minisztérium Nemzeti Kutatási Fejlesztési és Innovációs Alap, with the joint support of the Budapest University of Technology and Economics, and from the Nemzeti Kutatási, Fejlesztési és Innovációs Hivatal.

References

1.) Shuba, E. S.; Kifle, D.; *Renew. Sustain. Energy Rev.* **2018**, *81*, 743-755.

2.) Campos, J. F.; Berteina-Raboin, S.; *Catalysis Today*, **2020**, *358*, 138-142.

3.) G. M. Wilson, *J. Am. Chem. Soc.* **1964,** *86*, 127–130

4.) H. Renon and J. M. Prausnitz, *AIChE J.* **1968**, *14*, 135–144

5.) A. Fredenslund, R. L. Jones, J. Prausnitz, *AIChE J.* **1975**, *21*, 1086–1099

6.) A. Fredenslund, J. Gmehling, P. Rasmussen, *Elsevier Scientific Publ. Co.* **1977**

7.) Havasi, D.; Pátzay, G.; Kolarovszki, Z.; Mika, L. T., *J. Chem. Eng. Data.* **2016**, *61*, 3326–3333

Green Macroalgal Biorefinery of *Saccharina latissima* Using Pressurised Hot-Water Extraction

Mariem Hamed[1,2,3], Anandhu Padinjakkara[1], Carsten Zetzl[1], Andreas Liese[2,3], Irina Smirnova[1,3]

[1] Institute of Thermal Separation Processes, Hamburg University of Technology (TUHH), Hamburg

[2] Institute of Technical Biocatalysis, Hamburg University of Technology (TUHH), Hamburg

[3] United Nations University Hub on Engineering to Face Climate Change at the Hamburg University of Technology, United Nations University Institute for Water, Environment and Health (UNU-INWEH), Hamburg, Germany

Introduction

Brown macroalgae represent a promising third-generation biorefinery feedstock due to their fast growth rate, non-competition with arable land or freshwater resources, and rich content of high-value biopolymers [1,2]. Among cultivated European species, *Saccharina latissima* stands out for its high polysaccharide content, principally alginate (20-40 %DM), laminarin (10-35 %DM) and fucoidan (5-20 %DM) alongside moderate protein and minor lipid fractions, making it well-suited to aqueous cascade biorefinery approaches [3,4]. Conventional seaweed polysaccharides extraction relies on acidic or alkaline aqueous treatment at ambient pressure, requiring long extraction times and often producing chemically degraded products. Pressurised hot-water extraction (PHWE) offers a green alternative by operating above 100°C under pressure sufficient to maintain water in the liquid phase, exploiting the temperature-driven reduction in water dielectric constant to selectively solubilise target polysaccharides without using organic solvents [5,6]. However, systematic studies applying multi-variable statistical optimisation to simultaneously recover and characterise multiple polysaccharide fractions, namely alginate and laminarin, from *S. latissima* by PHWE remain scarce in the literature. Response surface methodology (RSM) using a Box-Behnken Design (BBD) provides a statistical framework for mapping the process design space and identifying interaction effects with fewer experimental runs [7]. In this work, a four-factor BBD was applied to *S. latissima* PHWE to optimise the simultaneous recovery of an ethanol-precipitated alginate fraction (ALG), a high-molecular-weight ultrafiltration retentate (RET, ≥10 kDa) and a low-molecular-weight filtrate (FIL, <10 kDa). The statistically selected optimum operating point was biochemically characterised using colorimetric and enzymatic assays, supplemented by FTIR-ATR spectroscopy for polysaccharide structural confirmation.

Experimental

All experiments used dried, milled *S. latissima* biomass (particle size ≤200 µm) harvested in April 2025. Prior to PHWE experiments, the raw biomass was subjected to biochemical characterisation including moisture, ash, total lipids, carbohydrates and organic acid [8], total protein [9], total sugars [10] and β-glucan contents [11]. PHWE experiments were performed in stainless-steel batch extraction vessels pressurised with nitrogen gas. A four-factor Box-Behnken Design was applied to *S. latissima* PHWE, varying temperature (25-120°C), pressure (10-40 bar), solid-to-liquid ratio (10-25 mL/g) and extraction time (10-60 min) using Minitab 22. The three response variables were the mass yields of ALG, RET and FIL, all expressed as percentage of dry biomass. Following each run, hydrolysates were centrifuged to separate the solid residue. The solid residue was subjected to alginate extraction using citric acid, sodium carbonate and ethanol precipitation, yielding ALG. The liquid hydrolysate supernatant (SUP) was concentrated by ultrafiltration through a 10 kDa MWCO Regenerated Cellulose discs to produce RET and FIL. The ALG, FIL and RET fractions were freeze-dried. Five confirmation experiments were conducted at model-predicted candidate conditions to validate predictive accuracy and the experimentally optimal operating point was identified using Minitab 22. The Run M2 fractions and the raw biomass were characterised by several assays: phenol-sulphuric acid (PSA) total sugar assay, Folin-Ciocalteu (FC) total phenolics assay, carbazole-sulphuric acid (CSA) total uronic acid assay, Pierce BCA™ protein assay and Megazyme K-YBGL β-glucan assay [10,11,12,13,14]. All assays were conducted in a 96-well microplate format on a Tecan Infinite 200 Pro reader. FTIR-ATR spectroscopy was also performed on these fractions with sodium alginate and cereal β-glucan standards as structural references.

Summary

The biochemical composition of the *S. latissima* feedstock confirmed a polysaccharide-dominated profile consistent with published data for cultivated European kelp (Table 1). Total sugars (67.47 %DM) and β-glucan (14.26 %DM) together established the substantial laminarin pool entering the PHWE experiments, while the high ash content (29.92%DM) confirmed the need for citric acid pre-treatment prior to alginate recovery. Across the 25 Box-Behnken runs, yield ranged from 58.1-80.4% for ALG, 5.2-43.7% for FIL and 0.4-23.5% for RET, demonstrating that no single factor simultaneously optimises all three responses.

Table 1: Biochemical composition of raw *S. latissima* feedstock

Chemical Composition	Value
Moisture, (% w/w)	12.82 ± 0.25
Ash, (% DM)	29.92 ± 1.77
Protein, (% DM)	15.00 ± 1,26
Total sugars, (% DM)	67.47 ± 1.53
β-Glucan, (% DM)	14.26 ± 2.19
Lipids, (% DM)	0.55 ± 0.05

Response surface model statistics are presented in Table 2. The RET model was the only response to achieve overall significance ($p = 0.042$, $R^2 = 80.9\%$). Although the ALG and FIL models did not reach $\alpha = 0.05$ threshold as a whole, the lack-of-fit test was non-significant for all three responses, confirming that the quadratic model form was adequate across the design space.

Table 2: RSM model fit statistics for the three PHWE response variables

Response variable	R^2	R^2adj	p-value
Alginate yield	74.4%	38.6%	0.124 (ns)
Filtrate yield	60.5%	5.3%	0.453 (ns)
Retentate yield	80.9%	54.2%	0.042*

ns = not significant ($p > 0.05$); * significant at $\alpha = 0.05$

Two process effects were identified from the response surface analysis. First, a statistically significant negative Pressure × Time interaction effect on ALG yield was identified ($p=0.022$), consistent with thermomechanical depolymerisation of β-D-mannuronic and α-L-guluronic acid glycosidic linkages under sustained high-pressure conditions, reducing the alginate polymer molecular weight below the threshold for effective ethanol precipitation. Second, solid-to-liquid ratio exerted the dominant and overriding influence on RET yield, operating through a dilution-volume mechanism whereby a larger hydrolysate feed volume produces a proportionally greater retained mass after ultrafiltration, independent of extraction temperature. Multi-response desirability optimisation in Minitab 22 identified Run M2 (112.3°C, 10 bar, 15.5 mL/g, 50.9 min; composite desirability $D = 0.573$) as the operating condition achieving the best three-way yield balance. Experimental confirmation of five candidate conditions validated the response surface models, with Run M2 yielding the smallest prediction errors of all tested

conditions with confirmed yields of ALG 79.8% (predicted 75.4%), FIL 19.3% (predicted 20.7%) and RET 18.7% (predicted 14.0 %), confirming three distinct fractions with different composition from a single hydrolysis run. Biochemical characterisation of Run M2 revealed a polysaccharide profile (Table 3). The total sugar assay showed that ALG yielded 35.98 %DM normalised to dry algal mass, while RET (25.25 %DM) and FIL (21.31 %DM) together accounted for 46.56 %DM of the total sugar pool, reflecting effective solubilisation of laminarin into the aqueous phase during PHWE. The total sugar recovery across all three fractions (82.54 %DM) slightly exceeds the raw biomass value (67.47 %DM), attributable to the known overestimation of the phenol-sulphuric acid assay in uronate-rich matrices when D-glucose is used as the calibration standard [10]. The uronic acid assay confirmed the selectivity of the alginate extraction sequence, with ALG accounting for 66.98 %DM of total uronate, compared with 16.71 %DM in RET and 5.43 %DM in FIL, demonstrating that the large majority of alginate-derived uronate was recovered in ALG. Total phenolic content was uniformly negligible across all three fractions (≤0.00042 %DM), consistent with the characteristically sparse phlorotannin pool of *S. latissima* and confirming the absence of phenolic interference in all parallel colorimetric assays. PHWE under Run M2 conditions effectively transferred laminarin from the *S. latissima* biomass into the aqueous phase, with SUP retaining 12.51 % DM β-glucan, representing 87.7% of the raw biomass β-glucan content (14.26 % DM). This confirms that the mild hydrothermal conditions preserved laminarin chain integrity rather than hydrolysing it to free glucose, yielding structurally laminarin-enriched fractions with potential for functional and bioactive applications.

Table 3: Biochemical composition of Run M2 fractions, % DM

Assay	Alginate	Filtrate	Retentate
Total sugars, % DM	35.98	21.31	25.25
Proteins, % DM	13.80	9.82	12.06
Uronic acids, % DM	66.98	5.43	16.71
Phenolic, % DM	0.00024	0.00042	0.00037
β-Glucan, % DM	-	12.51*	

* Measured on combined hydrolysate supernatant (RET + FIL fractions).

The FTIR-ATR spectroscopy provided independent structural confirmation of all quantitative assay findings. The ALG spectrum (Figure 1) closely matched the sodium alginate reference standard across the full fingerprint region, with the characteristic asymmetric (1611 cm^{-1}) and symmetric (1428 cm^{-1}) COO^- stretching bands and the mannuronate-rich anomeric fingerprint at 888 and 815 cm^{-1} confirming successful recovery of sodium alginate [15].

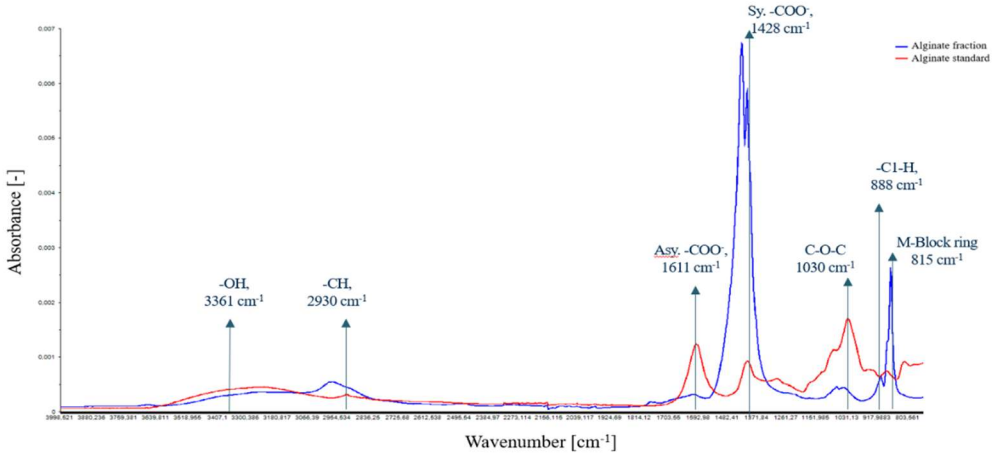

Figure 1: FTIR spectra of the extracted alginate fraction and commercial alginate

In the spectra of RET and FIL (Figure 2), the anomeric C-H deformation band appeared at 885-886 cm^{-1} with a downshift of approximately 44 cm^{-1} relative to the cereal β-glucan reference standards (928-930 cm^{-1}) providing spectroscopic evidence for the β-1,3-glycosidic linkage geometry of laminarin-type glucan. The barley standard additionally showed a β-1,4 C-O-C component at ~1149 cm^{-1} that was absent from both liquid fractions, further corroborating the exclusively β-1,3 linked nature of the extracted glucan. Fucoidan-diagnostic absorptions, specifically S=O stretching (1220-1260 cm^{-1}) and C-O-S stretching (836-840 cm^{-1}) were absent from all three fraction spectra, confirming that fucoidan did not co-partition at Run M2 conditions and that all three fractions are fucoidan-free [16].

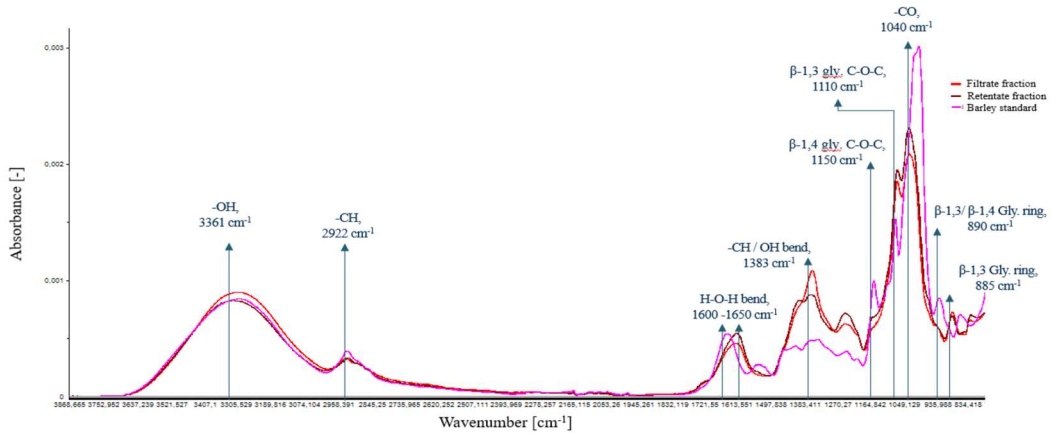

Figure 2: FTIR spectra of filtrate and retentate fractions and commercial barley β-glucan

These results demonstrate a statistically optimised green biorefinery concept for *S. latissima*, delivering three different fractions from a single hydrolysis run: an alginate-rich precipitate suitable for hydrocolloid and biomaterial applications, a laminarin-enriched retentate with immunomodulatory potential, and a low-molecular-weight filtrate containing laminarin oligomers. The identified mechanistic framework governing each fraction yield provides a quantitative basis for process scale-up, while the assays and FTIR-confirmed compositional dataset for downstream functional evaluation, life-cycle and techno-economic assessment of *S. latissima* biorefinery.

Acknowledgment

We are grateful to the Alexander Von Humboldt Foundation for financial support (1242674-HFST-P).

References

[1] Li, Y., Zheng, Y., Zhang, Y., Yang, Y., Wang, P., Imre, B., Wong, A.C.Y., Hsieh, Y.S.Y., Wang, D. (2021). Brown algae carbohydrates: Structures, pharmaceutical properties, and research challenges. Marine Drugs, 19(11), 620. doi.org/10.3390/md19110620

[2] Dobrinčić, A., Balbino, S., Zorić, Z., Pedisić, S., Bursać Kovačević, D., Elez Garofulić, I., & Dragović-Uzelac, V. (2020). Advanced technologies for the extraction of marine brown algal polysaccharides. Marine drugs, 18(3), 168. doi.org/10.3390/md18030168

[3] Holdt, S.L., Kraan, S. (2011). Bioactive compounds in seaweed: functional food applications and legislation. Journal of Applied Phycology, 23(3), 543–597. doi.org/10.1007/s10811-010-9632-5

[4] Lähteenmäki-Uutela, A., Rahikainen, M., Camarena-Gómez, M. T., Piiparinen, J., Spilling, K., & Yang, B. (2021). European Union legislation on macroalgae products. Aquaculture International, 29(2), 487-509. doi.org/10.1007/s10499-020-00633-x

[5] Plaza, M., & Turner, C. (2015). Pressurized hot water extraction of bioactives. TrAC Trends in Analytical Chemistry, 71, 39-54. doi.org/10.1016/j.trac.2015.02.022

[6] Bianchi, A., R. Rivera-Tovar, P., Sanz, V., Ferreira-Anta, T., Torres, M. D., Pérez-Correa, J. R., & Domínguez, H. (2021). Pressurized hot water extraction and bio-hydrogels formulation with Aristotelia chilensis [Mol.] Stuntz leaves. Molecules, 26(21), 6402. doi.org/10.3390/molecules26216402

[7] Della Posta, S., Gallo, V., Dugo, L., De Gara, L., & Fanali, C. (2022). Development and Box–Behnken design optimization of a green extraction method natural deep eutectic solvent-based for phenolic compounds from barley malt rootlets. Electrophoresis, 43(18-19), 1832-1840. doi.org/10.1002/elps.202200059

[8] Vagt, R., & Frerichs, H. (2021). Kohlenhydraten und organischen Säuren mittels Ionenausschlusschromatographie (Method No. M03.008, Version 03). Technische Universität Hamburg, Zentrallabor Chemische Analytik. https://www.tuhh.de/zentrallabor/methoden/oc-methoden/m03008

[9] Scholz, M., & Stahl, A. (2021). Bestimmung des Kjeldahl-Stickstoff (Method No. M02.011, Version 02). Technische Universität Hamburg, Zentrallabor Chemische Analytik. https://www.tuhh.de/zentrallabor/methoden/ac-methoden/m02011

[10] Masuko, T., Minami, A., Iwasaki, N., Majima, T., Nishimura, S. I., & Lee, Y. C. (2005). Carbohydrate analysis by a phenol–sulfuric acid method in microplate format. Analytical biochemistry, 339(1), 69-72. doi.org/10.1016/j.ab.2004.12.001

[11] Neogen Corporation. (2025). β-Glucan (Yeast and Mushroom): Product Instructions (K-YBGL, SKU: 700004358, September 2025 edition). Neogen Corporation, Lansing, MI, USA.

[12] Zhang, Q., Zhang, J., Shen, J., Silva, A., Dennis, D. A., & Barrow, C. J. (2006). A simple 96-well microplate method for estimation of total polyphenol content in seaweeds. Journal of applied phycology, 18(3), 445-450. doi.org/10.1007/s10811-006-9048-4

[13] Cesaretti, M., Luppi, E., Maccari, F., & Volpi, N. (2003). A 96-well assay for uronic acid carbazole reaction. Carbohydrate polymers, 54(1), 59-61. doi.org/10.1016/S0144-8617(03)00144-9

[14] Thermo Fisher Scientific. (2020). Pierce BCA protein assay kit: User guide (Pub. No. MAN0011430). Thermo Fisher Scientific.

[15] Leal, D., Matsuhiro, B., Rossi, M., & Caruso, F. (2008). FT-IR spectra of alginic acid block fractions in three species of brown seaweeds. Carbohydrate research, 343(2), 308-316. doi.org/10.1016/j.carres.2007.10.016

[16] Rajauria, G., Ravindran, R., Garcia-Vaquero, M., Rai, D. K., Sweeney, T., & O'Doherty, J. (2023). Purification and molecular characterization of fucoidan isolated from Ascophyllum nodosum brown seaweed grown in Ireland. Marine drugs, 21(5), 315. doi.org/10.3390/md21050315

Oxidative Ammonolysis of Technical Lignins as a Potential Route to Nitrogen-Enriched Humic-Like Soil Additives

Tanmay Tiwari, Giampiero P. Sorrentino, Thomas E. Müller

Carbon Sources and Conversion, Ruhr-Universität Bochum, Germany
tanmay.tiwari@ruhr-uni-bochum.de

Introduction

The phase-out of coal-based technologies in Germany creates a need for sustainable alternatives to coal-derived substances used in soil amendments for agriculture. Lignite-based products are valued for properties including cation-binding capacity, water retention, and biostimulant effects [1]. However, replacing fossil-derived carbon with renewable or industrial-residue streams would improve the sustainability of this application [2]. Technical lignins, generated in large quantities as by-products of industrial pulping processes (e.g., kraft, alkaline, and sulphite processes), are abundant aromatic by-products with partial structural similarity to humic substances [3]. Their direct use in agriculture is limited by low solubility, heterogeneous composition, and limited biological accessibility [4]. Targeted oxidative functionalization and nitrogen enrichment may therefore provide a route to lignin-derived humic-like materials while valorizing industrial residues [5]. This contribution investigates oxidative ammonolysis as a mild process for converting three industrially relevant technical lignin types into nitrogen-enriched, humic-like materials [6,7]. The experiments reported here were performed at 75°C and atmospheric pressure in aqueous ammonia using air as oxidant. The results provide a basis for later assessment of pressurized operation, gas-liquid oxygen transfer and reactor scale-up.

The working hypothesis is that lignin structure controls nitrogen incorporation and, consequently, the potential agronomic response of the treated materials.

Experimental

Three technical lignin feedstocks were investigated: kraft lignin (KL), alkaline lignin (AL), and lignosulfonates (LS). Prior to oxidative ammonolysis, the samples were dried at 60 °C and milled when necessary.

Oxidative ammonolysis was carried out in 15 wt.% aqueous ammonia (NH_4OH) at 75°C over 4 h under atmospheric pressure, using air as the oxidant and following the general approach described by Fischer et al. [8]. Fig. 1 illustrates the experimental workflow,

including feedstock drying, reaction in an aqueous ammonia/air system, and recovery of the nitrogen-enriched solid product. The experimental setup utilized for the oxidative ammonolysis consisted of a glass vessel reactor attached to a cooling system via a reflux condenser. For each run, technical lignin was introduced into a 15 wt.% NH_4OH solution at a liquid-to-solid (L/S) ratio of 30, with compressed air continuously introduced into the mixture at 75°C for 4 h. Elemental analysis (CHNS) was used to quantify nitrogen incorporation, while FTIR and ^1H NMR were used to assess qualitative changes in functional groups and aromatic structure.

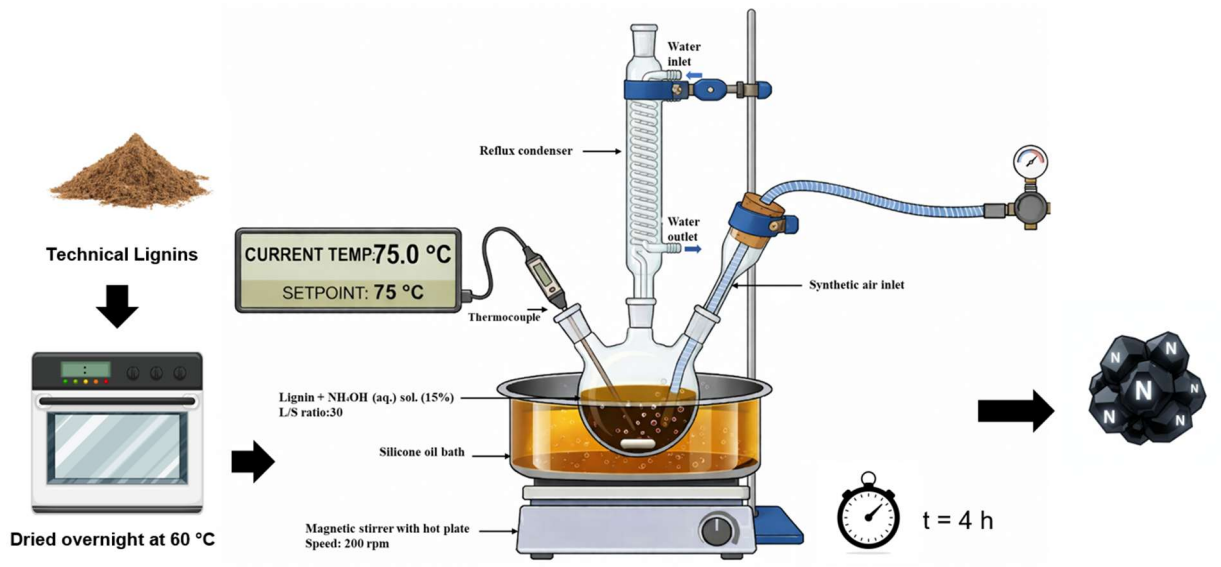

Figure 1. Process flow diagram of the experimental set-up

Summary

Pre-drying lignin at 60°C overnight eliminates moisture variations to ensure a consistent, comparable reaction stoichiometry and effective liquid-to-solid ratio. Without this step, extra water from wet feedstock causes excessive dissolution of lignin fragments into the aqueous phase, leading to substantial mass loss. Removing this moisture variability justifies using a dry-mass basis to accurately compare solid recoveries and elemental compositions across different lignin types (Table 1).

Table 1. Weight reduction in lignin after pre-drying overnight at 60 °C

Sample name	Initial weight (g)	Final weight (g)	Loss (wt. %)
Kraft Lignin B05.23	20.01	12.59	37.08
Kraft Lignin B14.23	20.02	10.46	47.75
Alkaline Lignin	20.01	12.16	39.22
Lignosulfonate SL-1	20.01	19.39	3.10

Elemental analysis indicated increased nitrogen content for all treated lignin samples, with KL showing the highest value among the tested feedstocks (2.20 wt.% N; Table 2).

Table 2. CHNS content of different lignin feedstock

		Kraft Lignin B05.23	Kraft Lignin B14.23	Alkaline	Lignosulfonate LS-251
C [wt.%]	**PRE**	66.92	62.48	47.82	44.08
	POST	60.14	63.02	46.77	41.68
	Difference	-6.78	0.54	-1.05	-2.40
H [wt.%]	**PRE**	6.54	6.12	6.12	5.60
	POST	6.13	6.13	4.88	4.82
	Difference	-0.41	0.01	-1.24	-0.78
N [wt.%]	**PRE**	0.12	0.10	0.08	0.11
	POST	2.20	1.77	0.62	0.42
	Difference	2.08	1.67	0.54	0.31
S [wt.%]	**PRE**	2.69	3.09	3.25	6.40
	POST	2.13	2.40	2.52	6.26
	Difference	-0.56	-0.69	-0.73	-0.14
C/H ratio	**PRE**	10.23	10.21	7.81	7.87
	POST	9.82	10.27	9.58	8.65
	Difference	-0.41	0.06	1.77	0.78
C/N ratio	**PRE**	557.67	624.80	597.75	400.73
	POST	27.41	35.82	75.68	99.41
	Difference	-530.26	-588.98	-522.07	-301.31

The higher nitrogen uptake observed for kraft lignin may be related to differences in molecular accessibility and reactive oxygenated sites compared with lignosulfonate. This enhanced reactivity is proposed to stem from the relatively open, free-phenolic structure of kraft lignin, which may offer greater accessibility for nucleophilic amination at carbonyl and quinone sites. The sulfonate groups in lignosulfonates are hypothesized to sterically and electronically hinder these nitrogen-incorporating reactions and the lower nitrogen uptake suggests that pre-existing polar substituents compete with or block these reactive sites, the exact chemical mechanisms remain unverified and require further analytics to be certain [10-11]. The observed changes are consistent with oxidative modification of lignin under ammonolysis conditions [5,9].

FTIR spectra show a consumption of C–O linkages (1215 cm^{-1} and 1030 cm^{-1}) paired with a growth of C=O bands (1710 cm^{-1}), pointing toward the oxidative cleavage of β-O-4

bonds into lower molecular weight fragments [12]. Concurrently, persistent broad aromatic signals (1600 cm^{-1} and 1510 cm^{-1} in FTIR; 6–8 ppm in ^{1}H NMR) indicate that the core aromatic scaffold is at least partially retained or re-assembled rather than completely degraded (Fig. 2).

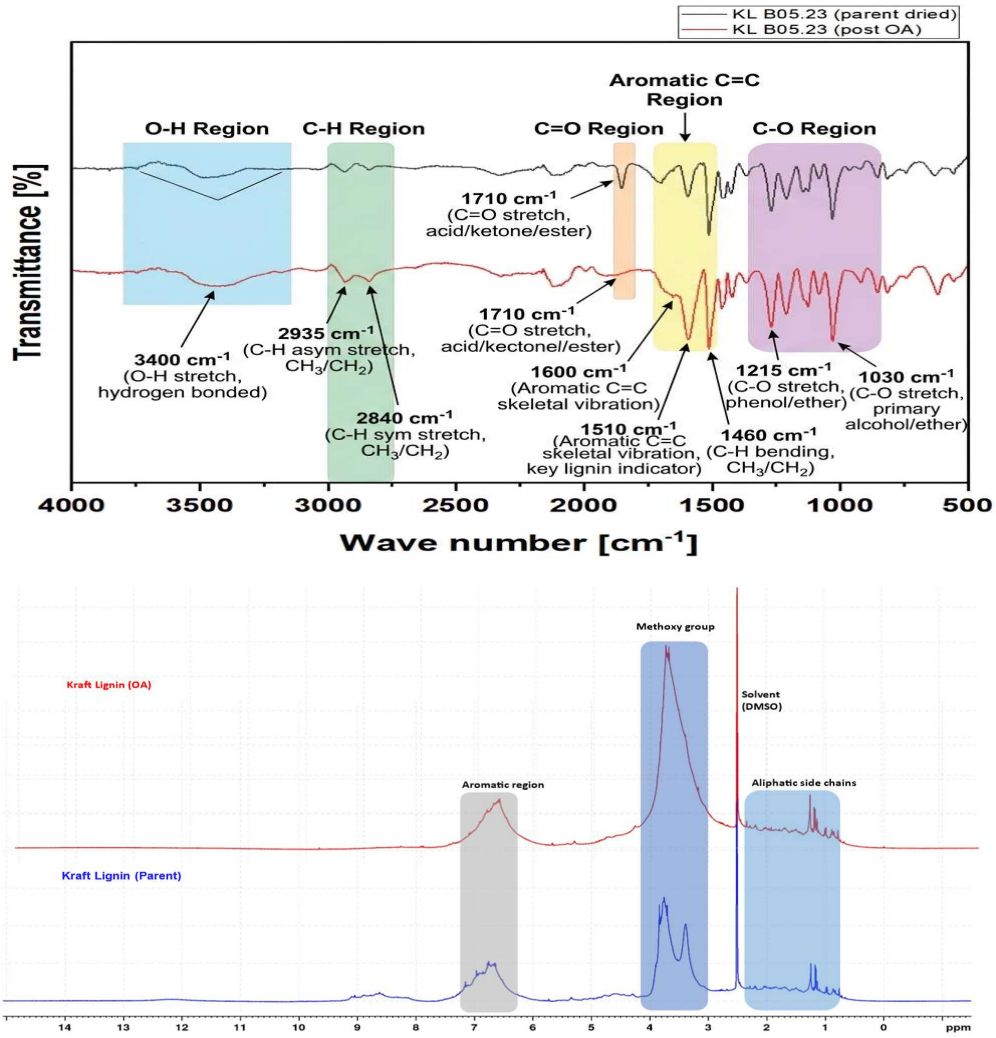

Figure 2. FTIR and ^{1}H NMR spectra used to assess structural changes in kraft lignin (KL)

Preliminary plant growth assays with Garden cress suggest a dose-dependent response of ammoxidized kraft lignin. Notably, while parent Kraft lignin feedstocks exhibited erratic or delayed growth-stimulating thresholds at higher concentrations (3–5 wt.%), the modified variants achieved peak biological efficacy strictly at lower thresholds (1 wt.%), beyond which phytotoxic suppression occurred. This behavior may be compatible with a hormesis-like response, where low levels of structurally complex, nitrogen-bearing aromatic compounds stimulate root and shoot development, while higher concentrations might suppress growth through phytotoxic effects [13]. This suggests improves water retention and cation exchange capacity at the soil-root interface, which untreated lignins,

lacking these functional groups, cannot replicate. Within the preliminary assay conditions, untreated lignins and blank references did not show an equivalent growth-stimulating response, suggesting that chemical modification may be important for the observed effect (Fig. 3).

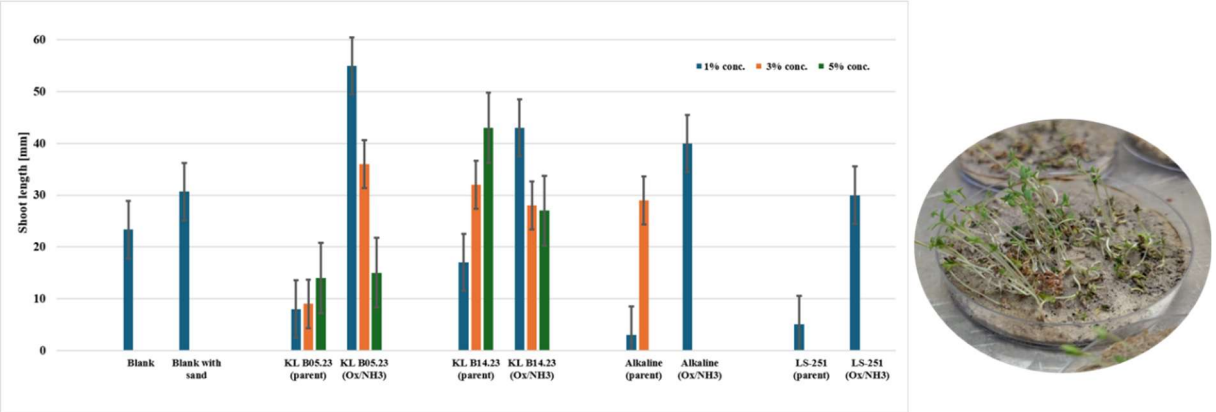

Figure 3. Lepidium sativum growth assay after 10 days lignin-based additive concentration at 1, 3 and 5 wt.%.

Conclusion

Overall, mild oxidative ammonolysis increased the nitrogen content of the tested technical lignins and produced preliminary evidence of biological activity in a Lepidium sativum assay, particularly for kraft lignin. This low-severity process route successfully valorises various industrial lignin streams into high-value, agronomically effective soil additives. Moving forward, future research will focus on the parametric optimisation of reaction conditions and a comprehensive scale-up assessment to pressurized conditions in batch reactors for higher nitrogen loading in lignin and its effects on plant growth.

Acknowledgement

The authors gratefully acknowledge the Chair of Carbon Sources and Conversion at Ruhr-Universität Bochum for supporting this work.

References

[1] Henderson, H. (2019). *2019 Green Transition Scoreboard Report*. Ethical Markets.

[2] Sutradhar, S., & Fatehi, P. (2023). Latest development in the fabrication and use of lignin-derived humic acid. *Biotechnology for Biofuels and Bioproducts*, *16*, 1–21. https://doi.org/10.1186/s13068-023-02278-3

[3] Wurzer, G. K., Bacher, M., Musl, O., Kohlhuber, N., Sulaeva, I., Kelz, T., Fackler, K., Bischof, R. H., Hettegger, H., Potthast, A., & Rosenau, T. (2023). From liquid to solid-state, solvent-free oxidative ammonolysis of lignins – an easy, alternative approach to generate "N-lignins". *RSC Advances*, *13*(14), 9479–9490. https://doi.org/10.1039/d3ra00691c

[4] Coniglio, R., Schütt, F., & Appelt, J. (2024). Challenges for the utilization of ammoxidized lignins and wood fibres as a peat substitute in horticultural substrates. *Journal of Cleaner Production*, *475*, 143737. https://doi.org/10.1016/j.jclepro.2024.143737

[5] Li, Y., Li, J., Ren, B., & Cheng, H. (2024). Conversion of Lignin to Nitrogenous Chemicals and Functional Materials. *Materials*, *17*(20), 5110. https://doi.org/10.3390/ma17205110

[6] Ghorbani, M., Konnerth, J., Budjav, E., Silva, A., Zinovyev, G., Van Herwijnen, H., Edler, M., Griesser, T., & Liebner, F. (2017). Ammoxidized Fenton-Activated Pine Kraft Lignin Accelerates Synthesis and Curing of Resole Resins. *Polymers*, *9*(2), 43. https://doi.org/10.3390/polym9020043

[7] Klinger, K. M., Liebner, F., Hosoya, T., Potthast, A., & Rosenau, T. (2013). Ammoxidation of Lignocellulosic Materials: Formation of Nonheterocyclic Nitrogenous Compounds from Monosaccharides. *Journal of Agricultural and Food Chemistry*, *61*(38), 9015–9026. https://doi.org/10.1021/jf401960m

[8] Fischer, K.; Schiene, R.; Katzur, J. (2004). Organic fertilizer having humic properties and its use. Patent application.

[9] Abdelaziz, O. Y., Clemmensen, I., Meier, S., Costa, A. E., Rodrigues, A. E., Hulteberg, C. P., & Riisager, A. (2022). On the oxidative valorization of lignin to high-value chemicals: A critical review of opportunities and challenges. *ChemSusChem*, *15*(23), e202201232. https://doi.org/10.1002/cssc.202201232

[10] Tkachenko, O., Grygorieva, O., Balahura, V., & Bandosz, T. J. (2023). Kraft lignin-derived microporous nitrogen-doped carbon adsorbent for air and water purification. *ACS Applied Materials & Interfaces*, *15*(50), 58448–58461. https://doi.org/10.1021/acsami.3c15659

[11] Areskogh, D., Li, J., Gellerstedt, G., & Henriksson, G. (2010). Investigation of the Molecular Weight Increase of Commercial Lignosulfonates by Laccase Catalysis. Biomacromolecules, 11(4), 904–910. https://doi.org/10.1021/bm901258v

[12] Serrano, L., Cecilia, J. A., García-Sancho, C., & García, A. (2019). Lignin depolymerization to BTXs. Lignin Chemistry, 169-196.

[13] Ngiba, Q.; Görgens, J. F.; Tyhoda, L. (2022). Lignin ammoxidation: synthesis of nitrogen releasing soil conditioning products from waste pulp liquor and their pot trial evaluation. Waste and Biomass Valorization, 13(12), 4785–4796.

Calorimetric Investigation of Peroxide Cocktail Decomposition as an Approach to Targeted Cocktail Design

Michelle Becker, Markus Busch

Ernst-Berl-Institute of Technical and Macromolecular Chemistry, Technical University Darmstadt, markus.busch@pre.tu-darmstadt.de

Introduction

Polyethylene is one of the most produced polymers worldwide with applications ranging from food packaging to construction industry. Industrially, low-density polyethylene (LDPE) is manufactured via high-pressure free-radical polymerization of ethylene at pressures up to 3000 bar and temperatures up to 300 °C.[1] The polymerization is initiated by introducing organic peroxides into the reactor, where homolytic cleavage of the peroxy bond generates the radicals required for polymerization initiation.

The decomposition behavior hereby has an impact on both the achievable conversions and the temperature profile inside the reactor and consequently on process control.[2] The initiation therefore offers potential for process optimization. By use of initiator cocktails, consisting of multiple peroxides with different decomposition ranges, radicals are provided over a wider temperature range and a smooth reactor start-up is enabled. For safe and stable reactor performance, especially a broad and uniform radical generation profile with as little fluctuations as possible is advantageous.[2]

This study therefore aims to reduce fluctuations in the decomposition profile of a given cocktail by specifically adjusting its composition. In this way, a first step towards targeted cocktail design is taken. To investigate the thermal decomposition behavior under process-near conditions, transitiometry, a special calorimetric method, is applied, taking advantage of the exothermic nature of the decomposition reaction.

Experimental

The investigations are carried out using a Standard Unit transitiometer from BGR TECH, whose setup is shown schematically in Figure 1.

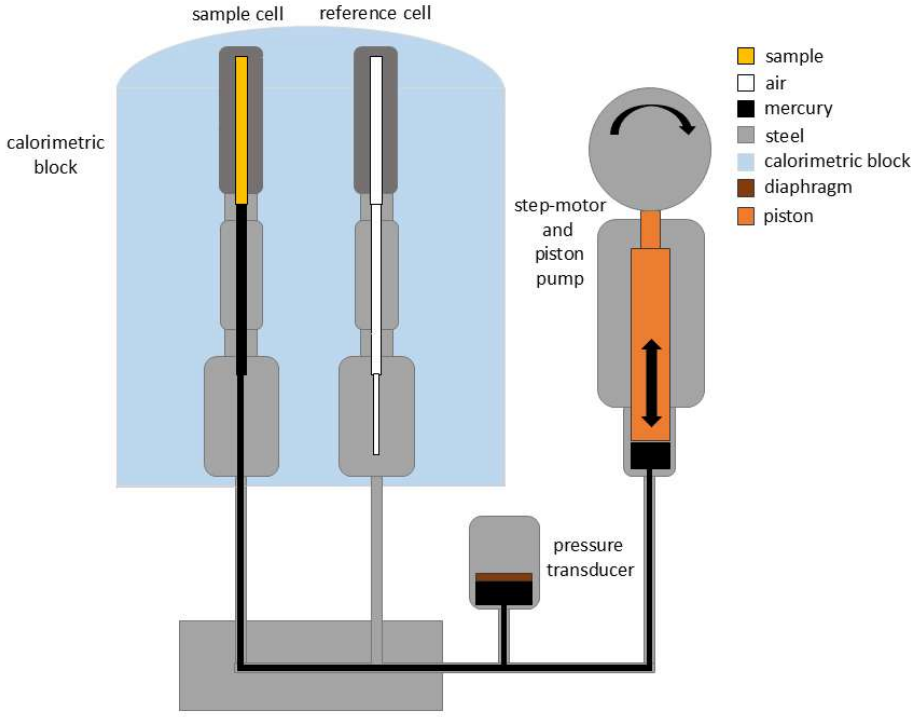

Fig. 1: Schematic setup of a Standard Unit transitiometer from BGR TECH. Modified from [3].

The transitiometer is configured as twin calorimeter, where heat flows from the sample cell are detected relative to an air-filled reference cell. Based on the TIAN-CALVET design, 672 thermocouples are arranged cylindrically around the cells to minimize heat losses and thus achieve high thermal resolution.

Mercury as almost incompressible medium is employed to generate pressure. The sample to be investigated, in this study a mixture of different peroxides diluted with an appropriate solvent, is positioned directly on the mercury column inside the sample cell. When the cell is sealed, a step-motor-driven piston pump is used to adjust the mercury level, resulting in changes in sample volume and pressure. This setup not only enables initial pressurization before the measurement, but also allows pressure, volume and temperature to be controlled at every time during the measurement.

In a typical experiment, one variable is fixed, one is systematically varied and the change in the third parameter is observed, in addition to the calorimetric signal. In this way, on the one hand, different thermophysical parameters are accessible.

In the context of peroxide cocktail decomposition, on the other hand, transitiometry offers the possibility for precise calorimetric measurements with accurate control of the experimental parameters. The realization of pressures up to 3000 bar and of temperatures

up to 673 K hereby allows measurements to be performed under industrially relevant process-near conditions. To investigate peroxide decomposition, isobaric temperature scans at 2000 bar are performed with a heating rate of 2 mK s^{-1}. Additionally, an isothermal plateau at the starting temperature is hold for 2000 s prior to each measurement to equilibrate the system.

In order to develop an approach to a more targeted design of peroxide cocktails, a cocktail composed of TBPND, TBPEH and TBPA in squalane is examined. The detected calorimetric signals are baseline-corrected and normalized to the mass of the lowest-decomposing peroxide TBPND, shown exemplarily for a cocktail with 15 mol% TBPND, 20 mol% TBPEH and 15 mol% TBPA in black in Figure 2. For kinetic evaluation, the contributions from the decomposition of the individual peroxides are separated by deconvolution, resulting in the coloured peaks in Figure 2. To derive kinetic parameters for the decomposition of the three peroxides, the BORCHARDT-DANIELS method is applied.[4]

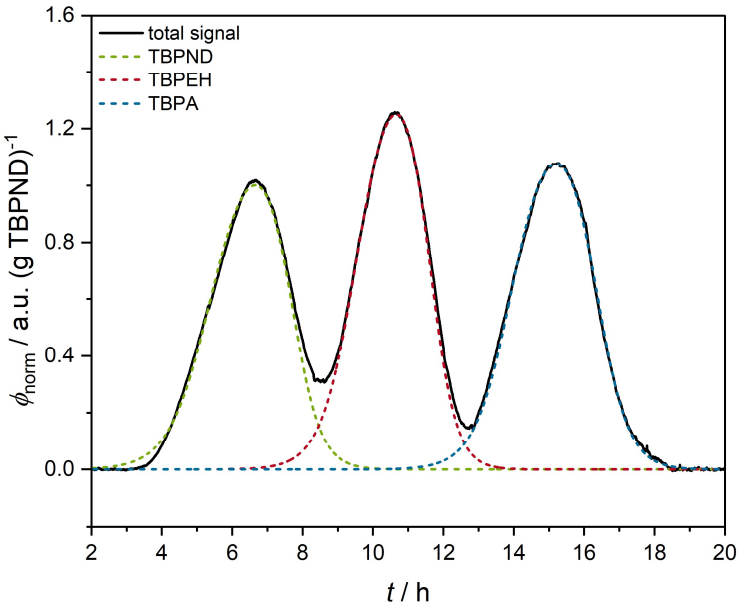

Fig. 2.: Calorimetric signal (black) of a cocktail of 15 mol% TBPND, 20 mol% TBPEH and 15 mol% TBPA in squalane, measured at 2000 bar in a temperature range from 300 K to 450 K with a heating rate of 2 mK s^{-1} and normalized to the mass of TBPND. In colour, the deconvoluted peaks of decomposition of the individual peroxides are shown.

The procedure for targeted cocktail design is shown schematically in Figure 3.

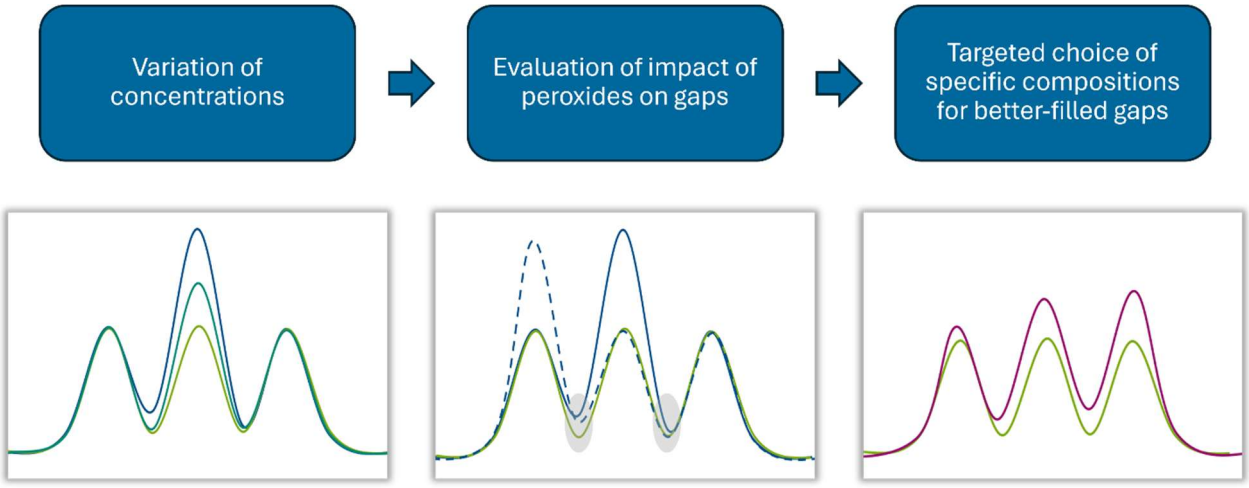

Fig. 3.: Schematic illustration of the developed approach to more targeted peroxide cocktail design. Through systematic variation of the concentrations (left), a basic understanding of the initiator system is gained. By comparison of the different variations (middle), the influence of the different peroxides on the inter-peak gaps is evaluated and compositions with reduced gaps are selected (right).

The targeted modulation of decomposition profiles requires a good understanding of the individual contributions of the peroxides to the overall calorimetric signal as well as their possible interactions. For this reason, in the first step, the concentrations of all peroxides are systematically varied one at a time, while the concentrations of the other peroxides are kept constant at 15 mol%. With the overall aim of reducing the fluctuations in the decomposition profile, the focus is hereby particularly placed on the gaps between the decomposition peaks. In the next step, therefore, the impact of the peroxides on the minima is examined in more detail by specifically comparing the trends observed in the inter-peak gaps as well as the degree to which these changes occur for the different variations.

Based on these investigations, peroxide cocktails with tailored compositions are subsequently designed. The concentrations are selected in a way that both gaps between the peaks are reduced to a similar extent, resulting in a somehow smoother overall decomposition profile.

Summary

This study aims to take an initial step towards more targeted peroxide cocktail design with the long-term objective of optimizing polymerization processes, for example with respect to stability and process control. For this purpose, a cocktail of TBPND, TBPEH and TBPA in squalane is investigated by transitiometry. By successive variation of the concentrations of the individual peroxides, their impacts on the total calorimetric signal and especially on the minima between the decomposition peaks are studied and compared. The improved understanding of the initiator system enables the targeted selection of specific compositions in order to smooth the decomposition profile by reducing the gaps between the peaks.

Acknowledgment

The authors thank United Initiators for providing the peroxides used in this study.

References

[1] S. Hinrichs, PhD thesis, Georg-August-University Göttingen, **2006**.

[2] H. Seidl, G. Luft, *Journal of Macromolecular Science: Part A - Chemistry* **1981**, 15, 1–33.

[3] S. Albus, J. Nowottny, J. Sartorius, M. Busch, *Journal of Solution Chemistry* **2024**, 53, 43–59.

[4] H. J. Borchardt, F. Daniels, *Journal of the American Chemical Society* **1957**, 79, 41–46.

Evaluation of Gas Diffusion Electrode Composition for Gas-Phase Electroreduction of CO_2 to Formate

Barbara Ruiz Bolado

Department of Chemical Engineering, University of Valladolid,
barbara.ruiz25@estudiantes.uva.es

Introduction

The accumulation of carbon dioxide (CO_2) in the atmosphere represents one of the main environmental challenges of our time and the primary driver of climate change. According to the most recent data from NOAA, in May 2025 the Mauna Loa Observatory recorded a new monthly maximum of 430.5 ppm, a value more than 50 % higher than pre-industrial levels [1]. This upward trend highlights the urgent need to implement effective CO_2 mitigation and valorisation strategies.

Within Carbon Capture, Utilisation and Storage (CCUS) technologies, the electrochemical conversion of CO_2 into value-added products emerges as a particularly promising alternative. This strategy enables emissions to be transformed into useful compounds such as formate ($HCOO^-$) or formic acid (HCOOH), which are used as hydrogen carriers, pH regulators in the textile and tanning industries, preservatives in animal feed, and reagents in fine chemical synthesis [2, 3]. The global formic acid market was valued at around USD 2.32 billion in 2024, with a projected compound annual growth rate of 4.75 % up to 2035 [4].

The complete CCUS chain integrates stages in which high pressure is essential: CO_2 captured from industrial sources is typically compressed to 70–150 bar for transport in dense or supercritical phase, reducing its specific volume and making long-distance pipeline transport economically viable [5]. Once at the point of use, this CO_2 could directly feed pressurised electroreduction reactors. Operating these systems at elevated pressure would increase the concentration of the reactant at the active electrode interface according to Henry's law, potentially improving the Faradaic Efficiency (FE) and suppressing the competing hydrogen evolution reaction (HER) [6].

The present work evaluates three Gas Diffusion Electrode (GDE) formulations at atmospheric pressure, based on $(BiO)_2CO_3$ as the catalyst and varying the ionomer: Nafion, Sustainion, and Sustainion with the hydrophobic additive PTFE. GDEs are key components of the electroreduction reactor: they facilitate simultaneous contact between the gaseous reactant, the liquid electrolyte and the solid catalyst at the so-called active

three-phase interface [7]. Their composition and surface properties determine CO_2 accessibility to the catalyst, flooding control and operational stability. The results obtained establish the experimental baseline required for the design of high-pressure systems.

Experimental

Catalyst synthesis

The $(BiO)_2CO_3$ catalyst was synthesised by controlled precipitation: 234 mg of Bi_2O_3 (99.9%, Merck) were dissolved in 3 mL of concentrated HNO_3 (65 %, VWR) in 10 mL of deionised water. A Na_2CO_3 solution (2.5 g in 10 mL) was slowly added until pH 7 was reached, inducing the precipitation of basic bismuth carbonate. The suspension was maintained at 85 °C for 3 hours to promote crystallisation. The resulting white solid was vacuum-filtered, washed five times with deionised water and dried at 70 °C for 12 hours [8].

GDE fabrication

Three catalyst ink formulations were prepared with different catalyst ratios: (i) Nafion D-521 at a 70:30 ratio, (ii) Sustainion XC-2 at a 90:10 ratio, and (iii) Sustainion XC-2 with PTFE as a hydrophobic additive at a 90:(7.5:2.5) ratio. The target catalyst loading was 0.75 $mg \cdot cm^{-2}$. The inks were prepared by dispersing the catalyst in isopropanol (IPA) with the corresponding ionomer, followed by ultrasonic agitation for 30 minutes. Deposition was carried out by manual airbrushing onto Sigracet 39 BB carbon paper at 70 °C and an air pressure of 0.5 - 1 bar [8].

Experimental system

The tests were performed in a filter-press electrochemical cell with an active area of 10 cm^2, operated in continuous mode at atmospheric pressure and room temperature. The cathode was the fabricated GDE, while the anode was a titanium DSA electrode. The ion-exchange membrane was Nafion 117 conditioned in 1 M KOH. The cathodic feed consisted of humidified CO_2 (0.2 $L \cdot min^{-1}$, water flow rate of 0.2 $g \cdot h^{-1}$), generated using a Controlled Evaporation Mixer (Bronkhorst®). The anolyte was 1 M KOH recirculated using a peristaltic pump. The current density was kept constant at 200 $mA \cdot cm^{-2}$ in all experiments. Tests of 1 hour and 3 hours were carried out to evaluate both initial performance and operational stability.

Analytical techniques

The concentration of $HCOO^-$ in the liquid product was quantified by ion chromatography (Dionex ICS 1100, AS9-HC column). The figures of merit evaluated were: (i) Faradaic Efficiency, FE (%) = $z \cdot F \cdot M/(j \cdot A) \cdot 100$, with z = 2 electrons per mole of $HCOO^-$; (ii) production rate ($mmol \cdot m^{-2} \cdot s^{-1}$) = $M/(A \cdot t)$; and (iii) specific energy consumption, EC ($kWh \cdot kmol^{-1}$) = $j \cdot A \cdot V/M$. The surface morphology of the GDEs was characterised by scanning electron microscopy (SEM, Zeiss EVO MA15), and hydrophobicity was assessed by contact angle measurement (DSA25, Krüss, Germany) [8].

Summary

Electrochemical performance

After the first hour of operation, the GDE formulated with Nafion 70:30 showed the best performance: a FE of 40.87 %, an $HCOO^-$ concentration of 343.09 $g \cdot L^{-1}$, a production rate of 4.24 $mmol \cdot m^{-2} \cdot s^{-1}$ and the lowest energy consumption (902.83 $kWh \cdot kmol^{-1}$). The Sustainion and Sustainion-PTFE formulations showed more modest values (FE ~19-22 %, $[HCOO^-]$ ~157-182 $g \cdot L^{-1}$), but with a different stability profile. Table 1 summarises the main results. However, after three hours of continuous operation, Nafion showed the sharpest decrease in FE (~48%, from 40.87 % to 21.29 %), whereas Sustainion and Sustainion-PTFE maintained a notably more stable product concentration, with decreases of 0.4 % and 5.7 %, respectively.

Tab. 1.: Main results of the three GDE formulations evaluated (j = 200 $mA \cdot cm^{-2}$).

GDE formulation	FE 1 h (%)	$[HCOO^-]$ 1 h (g/L)	FE 3 h (%)	$[HCOO^-]$ 3 h (g/L)	EC (kWh/kmol)
Nafion 70:30	40.87	343.09	21.29	209.21	954
Sustainion 90:10	18.67	156.75	12.07	156.10	1,533
Sustainion-PTFE 90:(7.5:2.5)	21.74	182.48	11.35	171.97	1,546

Morphological characterisation and hydrophobicity

SEM images reveal clear differences between the formulations. The GDE with Nafion shows a compact surface crossed by a network of finely distributed microcracks which, according to Kong et al. (2022) [9], act as auxiliary channels for liquid product removal through a perspiration mechanism, favouring electrode stability and explaining its superior

initial performance. The GDE with Sustainion shows a more uniform and ordered surface, favourable for CO_2 transport towards the active zone. The Sustainion-PTFE formulation presents a rougher and more porous structure, with a more homogeneous catalyst distribution [8].

Contact angle measurements confirm that Nafion is the most hydrophobic formulation (151°), followed by Sustainion-PTFE (141°) and pure Sustainion (131°). In GDE configurations operating in the gas phase, higher hydrophobicity minimises electrolyte accumulation inside the pores and reduces carbonate salt precipitation, which is the main deactivation mechanism observed: as salts deposit within the catalytic layer, they block the porous structure, require higher overpotentials to maintain the current density, and make controlled operation beyond three hours unfeasible under the studied conditions. However, excessive hydrophobicity may limit ionic conduction, so the Sustainion-PTFE formulation represents the best compromise between flooding resistance and conductivity [10].

Perspectives for high-pressure operation

The results obtained at atmospheric pressure provide critical information for the design of systems integrated into CCUS chains, where CO_2 reaches the reactor already compressed. Operating at elevated CO_2 pressures (10 - 80 bar) would increase the concentration of the reactant at the active interface according to Henry's law, with the potential to increase FE and suppress HER. However, the higher hydrostatic pressure may intensify flooding if the electrode hydrophobicity is not sufficient. The results of the present work indicate that the Sustainion-PTFE formulation, with flooding resistance already demonstrated at atmospheric pressure and a contact angle of 141°, would be the most promising candidate for operation under pressurised conditions. The balanced design between hydrophobicity, morphology and ionic conduction of the GDE, characterised in this study, is therefore a fundamental prerequisite for scaling towards high-pressure CO_2 systems.

Acknowledgment

The author thanks the DePRO research group at the University of Cantabria, especially the supervisors Guillermo Díaz Sainz and José Antonio Abarca González, for their guidance and support throughout the development of the Bachelor's Thesis on which this contribution is based. The author also thanks the Electrocatalysis group at the University

of Bern (Prof. Peter Broekmann) for the scientific collaboration that inspired part of the experimental design.

References

[1] Lan, X., Tans, P. and K.W. (2025). Thoning: Trends in globally-averaged CO_2 determined from NOAA Global Monitoring Laboratory measurements. https://doi.org/10.15138/9N0H-ZH07

[2] Fernández-Caso, K., Díaz-Sainz, G., Alvarez-Guerra, M., & Irabien, A. (2023). Electroreduction of CO2: Advances in the Continuous Production of Formic Acid and Formate. *ACS Energy Letters, 8*(4), 1992-2024. https://doi.org/10.1021/acsenergylett.3c00489

[3] Ewis, D., Arsalan, M., Khaled, M., Pant, D., Ba-Abbad, M. M., Amhamed, A., & El-Naas, M. H. (2023). Electrochemical reduction of CO2 into formate/formic acid: A review of cell design and operation. *Separation And Purification Technology, 316*, 123811. https://doi.org/10.1016/j.seppur.2023.123811

[4] Vantage Market Research. (2024, 2 septiembre). Formic Acid Market: Solutions, Growth & Trends. *Analysis Report,* 2025–2035. https://www.vantagemarketresearch.com/industry-report/formic-acid-market-2610

[5] Rubin, E. S., Davison, J. E., & Herzog, H. J. (2015). The cost of CO2 capture and storage. International *Journal of Greenhouse Gas Control, 40*, 378-400. https://doi.org/10.1016/j.ijggc.2015.05.018

[6] Rabiee, H., Ge, L., Zhang, X., Hu, S., Li, M., & Yuan, Z. (2021). Gas diffusion electrodes (GDEs) for electrochemical reduction of carbon dioxide, carbon monoxide, and dinitrogen to value added products: a review. *Energy & Environmental Science, 14*(4), 1959-2008. https://doi.org/10.1039/d0ee03756g

[7] Hernandez-Aldave, S., & Andreoli, E. (2020). Fundamentals of Gas Diffusion Electrodes and Electrolysers for Carbon Dioxide Utilisation: Challenges and Opportunities. *Catalysts, 10*(6), 713. https://doi.org/10.3390/catal10060713

[8] Abarca, J. A., Díaz-Sainz, G., Merino-Garcia, I., Irabien, A., & Albo, J. (2023). Photoelectrochemical CO_2 electrolyzers: From photoelectrode fabrication to reactor configuration. *Journal Of Energy Chemistry, 85*, 455-480. https://doi.org/10.1016/j.jechem.2023.06.032

[9] Kong, Y., Liu, M., Hu, H., Hou, Y., Vesztergom, S., De Jesus Gálvez-Vázquez, M., Montiel, I. Z., Kolivoška, V., & Broekmann, P. (2022). Cracks as Efficient Tools to Mitigate Flooding in Gas Diffusion Electrodes Used for the Electrochemical Reduction of Carbon Dioxide. *Small Methods, 6*(9). https://doi.org/10.1002/smtd.202200369

[10] Abarca, J. A., Warmuth, L., Rieder, A., Dutta, A., Vesztergom, S., Broekmann, P., Irabien, A., & Díaz-Sainz, G. (2025). GDE Stability in CO_2 Electroreduction to Formate: The Role of Ionomer Type and Loading. *ACS Catalysis, 15*(11), 8753-8767. https://doi.org/10.1021/acscatal.5c02052

Investigation of Gas Sorption and Transport Properties in Polymers for Hydrogen Transport Infrastructure

Gaia Lazzari

Department of Civil, Chemical, Environmental, and Materials Engineering
Alma Mater Studiorum – University of Bologna, gaia.lazzari6@unibo.it

Introduction

In the context of decarbonisation, hydrogen (H_2) is attracting growing interest as an energy carrier capable of reducing the dependence on fossil fuels and supporting the transition towards carbon neutrality [1]. Achieving these goals requires the deployment of a reliable hydrogen transport infrastructure, in which the selection of suitable materials plays a central role [2]. Polymers, in particular, are widely employed as seals, gaskets, and liners, and they must guarantee containment and mechanical integrity over long service lifetimes. To date, however, their interactions with hydrogen are still poorly characterised: although polymers are often considered chemically inert towards hydrogen, physical mechanisms such as gas permeation, sorption-induced swelling, and plasticization can compromise their functional performance and lead to premature component failure [2], [3]. These effects become particularly critical considering that the hydrogen infrastructure is expected to operate across a wide range of pressures, from a few bars in distribution networks up to 700 bar in storage, and temperature spanning from cryogenic conditions to elevated values in compressors, thus imposing severe demands on the polymeric materials employed [4]. Hydrogen can also be transported in the form of ammonia (NH_3) or blended with methane (CH_4) in existing natural gas networks, thus the behaviour of polymers in contact with these gases must be investigated as well, introducing additional compatibility considerations for materials originally designed for other service environments [1].

The challenge arises from the variety of gases involved: H_2, NH_3 and CH_4 differ significantly in molecular size, condensability, and affinity towards polymeric matrices, and capturing such diverse interactions within a single consistent description is far from trivial. A thorough characterisation of the relevant phenomena requires a detailed analysis of gas sorption and transport in polymers, with particular attention to their response under extreme operating conditions. Although this topic is of clear technological relevance, experimental data and modelling studies on these systems are still limited [5]. To this purpose, the present work adopts a thermodynamic modelling framework with the aim of providing a predictive tool to support the design and selection of components for

hydrogen-related applications. Several polymers belonging to the elastomeric and thermoplastic families are considered, such as HNBR, EPDM and FKM among elastomers, and PE, PTFE and PA among thermoplastics [2].

Modelling

The modelling approach describes solubility data through the Lattice Fluid (LF) Equation of State (EoS) for rubbery polymers, treated as equilibrium systems, and through its Non-Equilibrium extension (NELF) for glassy polymers, which are inherently out of equilibrium [6], [7]. Both approaches are based on the equality of chemical potentials between the gas and the polymer phase:

$$\mu_i^G(T,p) = \mu_i^S\left(T,p,\rho_{pol},\omega_i\right) \qquad \text{Equation 1}$$

For a system at equilibrium, the polymer density is computed as:

$$\rho_{pol} = \rho_{pol}^{EQ}(T,p,\omega) \qquad \text{Equation 2}$$

In glassy systems, Eq. 2 no longer holds, and a swelling coefficient k_{sw}, accounting for the dilation of the polymeric matrix induced by the penetrant, is introduced:

$$\rho_{pol} = \frac{\rho_{pol}^0}{(1+k_{sw}\cdot p)} \qquad \text{Equation 3}$$

Once the pure component parameters are identified, this framework allows the prediction of gas solubility under conditions that are difficult to access experimentally, such as high pressures or low temperatures relevant for the application. The model also predicts the system swelling, which allows the estimation of the fractional free volume (FFV), a key parameter related to the interstitial space between polymer chains that can be used to interpret gas transport properties [8]. FFV is computed through Eq.4:

$$FFV_{mix} = \frac{{}^1/_{\rho_{mix}} - {}^1/_{\rho_{mix}^*}}{{}^1/_{\rho_{mix}}} \qquad \text{Equation 4}$$

where ρ_{mix} is the density of the polymer-gas mixture at the temperature and pressure of interest obtained from SL or NELF, and ρ_{mix}^* is the close-packed density of the mixture, computed using mixing rules applied to the pure-component characteristic densities.

An example of how FFV varies with the sorbed gas is reported in Fig. 1, where two distinct trends emerge depending on the nature of the penetrant. For condensable gases such as methane and ammonia, gas-induced swelling prevails over mechanical compression, and FFV increases with pressure. The opposite is observed for hydrogen, whose limited

condensability results in negligible swelling, so that compression dominates and FFV decreases with pressure.

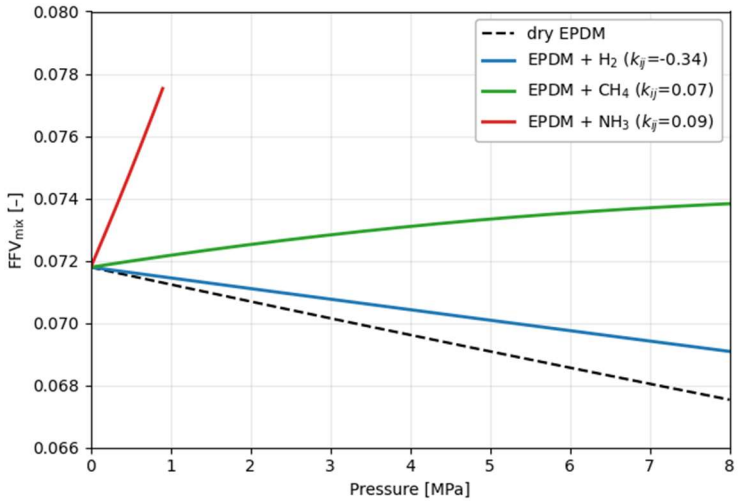

Figure 1. FFV_{mix} estimation for H_2, NH_3 and CH_4 inside EPDM at 298 K.

The solubility information obtained from the EoS is then combined with a description of gas mobility in the polymer to predict gas permeability through the Standard Transport Model (STM) [9], expressed as:

$$P_i = \frac{1}{(p_i^{up} - p_i^{down})} \int_{p_i^{down}}^{p_i^{up}} L\, S_i\, z_i\, dp_i \qquad \text{Equation 5}$$

In its classical formulation, L is the mobility coefficient of the gas in the polymer and is typically obtained through empirical correlations. In the present work, building on the free-volume theory by Vrentas and Duda [10], L is computed within the framework of the Lattice Free-Volume Theory [11], in which the mobility coefficient is directly linked to the free volume of the polymer-penetrant system:

$$L = \varphi \cdot exp\left(-\gamma \cdot \frac{\frac{\omega_1}{\rho_1^*} + \xi \frac{\omega_2}{\rho_2^*}}{1/\rho_{mix} - 1/\rho_{mix}^*}\right) \qquad \text{Equation 6}$$

The main parameters used for the modelling of PE with H_2, CH_4 and NH_3 are reported in Table 1.

Table 1. Modelling parameters used for the systems considered.

	ρ_1^* [g/cm^3]	ρ_2^* [g/cm^3]	φ [cm^2/s]	γ [-]
PE-H_2	0.078	0.90	3.8e-6	1.1
PE-CH_4	0.500		9.1e-1	2.5
PE-NH_3	0.803		2.0e-3	2.2

An example of the resulting permeability predictions is shown in Fig. 2, where the three gases display distinct trends. Hydrogen permeability slightly decreases with pressure, due to the reduction in mobility associated with the decrease of FFV. Methane shows a slight increase with pressure, reflecting the dominant role of swelling. Ammonia exhibits a non-monotonic behaviour, which the model is able to capture together with the phase change from gas to liquid.

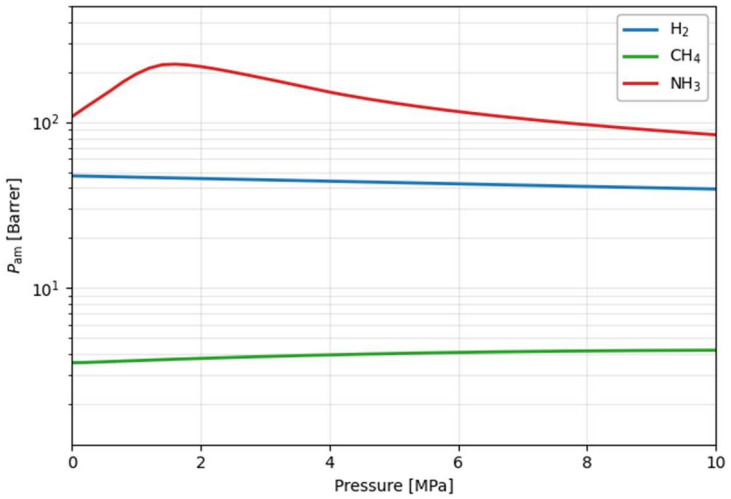

Figure 2. Permeability predictions for H_2, NH_3 and CH_4 in PE at 298 K.

Since an alternative mean of hydrogen transport is blended with methane, the analysis is also extended to gas mixtures, for which experimental sorption and permeability data are particularly scarce in the literature. The description of multicomponent systems is especially relevant, since the presence of a second penetrant can significantly affect both the solubility and the diffusivity of each species, leading to deviations from the behaviour observed in single-gas experiments. Nevertheless, single-gas sorption data remain essential as a starting point, as they provide the binary interaction parameters between each gas and the polymer matrix that are then used to predict the mixture behaviour [12].

Future developments will extend the same approach to a wider set of gas mixtures of relevance for the hydrogen value chain.

Summary

This work focuses on the thermodynamic predictions of sorption and transport properties of different gases in polymers commonly employed in the hydrogen transport infrastructure. To this end, the Lattice Fluid Equation of State and its non-equilibrium extension are combined with the Standard Transport Model and the Lattice Free-Volume Theory to describe both sorption and transport phenomena within a consistent framework. Particular attention must be given to high-pressure conditions and gas mixtures, which currently represent a significant gap in the literature. Designed to be coupled with experimental analysis, once validated the framework can be used to extrapolate the behaviour of these systems beyond the conditions accessible in the laboratory. A further strength of the proposed approach lies in its generality: although applied here to polymers and gases of interest for hydrogen transport, it can in principle be extended to any gas-polymer system, making it a versatile tool for the screening of materials in a broader range of applications.

Acknowledgment

The author acknowledges Ben Alcock and Vilde Elin Andreassen from SINTEF Industry for their precious help and guidance. This research is part of the Pol(Hy)mer project led by SINTEF, financially supported by The Research Council of Norway under grant 352862.

References

[1] H. Ameli, G. Strbac, D. Pudjianto, and M. T. Ameli, ‘A Review of the Role of Hydrogen in the Heat Decarbonization of Future Energy Systems: Insights and Perspectives’, *Energies*, vol. 17, no. 7, p. 1688, Apr. 2024, doi: 10.3390/en17071688.

[2] M. M. H. Bhuiyan, N. Subedi, and Z. Siddique, ‘Material compatibility in hydrogen infrastructure: Challenges, advances, and future prospects’, *Int. J. Hydrog. Energy*, vol. 190, p. 152138, Nov. 2025, doi: 10.1016/j.ijhydene.2025.152138.

[3] S. S. Kulkarni *et al.*, ‘Damage evolution in polymer due to exposure to high-pressure hydrogen gas’, *Int. J. Hydrog. Energy*, vol. 46, no. 36, pp. 19001–19022, May 2021, doi: 10.1016/j.ijhydene.2021.03.035.

[4] J. Klier *et al.*, ‘A new cryogenic high-pressure H2 test area: First results’, in *Proceedings of the 12th IIR International Conference: Dresden, Germany*, Sep. 2012.

[5] E. Sgambitterra and L. Pagnotta, ‘Permeability: The Driving Force That Influences the Mechanical Behavior of Polymers Used for Hydrogen Storage and Delivery’, *Energies*, vol. 17, no. 9, p. 2216, May 2024, doi: 10.3390/en17092216.

[6] I. C. Sanchez and R. H. Lacombe, ‘Statistical Thermodynamics of Polymer Solutions’, *Macromolecules*, vol. 11, no. 6, pp. 1145–1156, Nov. 1978, doi: 10.1021/ma60066a017.

[7] F. Doghieri and G. C. Sarti, ‘Nonequilibrium Lattice Fluids: A Predictive Model for the Solubility in Glassy Polymers’, *Macromolecules*, vol. 29, no. 24, pp. 7885–7896, Jan. 1996, doi: 10.1021/ma951366c.

[8] N. R. Horn, ‘A critical review of free volume and occupied volume calculation methods’, *J. Membr. Sci.*, vol. 518, pp. 289–294, Nov. 2016, doi: 10.1016/j.memsci.2016.07.014.

[9] M. Minelli and G. C. Sarti, ‘Permeability and diffusivity of CO2 in glassy polymers with and without plasticization’, *J. Membr. Sci.*, vol. 435, pp. 176–185, May 2013, doi: 10.1016/j.memsci.2013.02.013.

[10] J. S. Vrentas and J. L. Duda, ‘Molecular diffusion in polymer solutions’, *AIChE J.*, vol. 25, no. 1, pp. 1–24, Jan. 1979, doi: 10.1002/aic.690250102.

[11] L. I. Costa and G. Storti, ‘Self-diffusion of small molecules into rubbery polymers: A lattice free-volume theory’, *J. Polym. Sci. Part B Polym. Phys.*, vol. 48, no. 5, pp. 529–540, Mar. 2010, doi: 10.1002/polb.21918.

[12] E. Toni, M. Minelli, and G. C. Sarti, ‘A predictive model for the permeability of gas mixtures in glassy polymers’, *Fluid Phase Equilibria*, vol. 455, pp. 54–62, Jan. 2018, doi: 10.1016/j.fluid.2017.09.025.

Antimicrobial Potential of Natural Compounds and Their Derivatives

Gašper Vrečer [a], Matja Zalar [a], Urban Bren [a,b,c]

[a] University of Maribor, Faculty of Chemistry and Chemical Engineering, Laboratory of Physical Chemistry and Chemical Thermodynamics, Smetanova 17, SI-2000 Maribor, Slovenia

[b] Faculty of Mathematics, Natural Sciences and Information Technologies, University of Primorska, Glagoljaška 8, SI-6000 Koper,

[c] Slovenia Institute of Environmental Protection and Sensors, Beloruska 7, SI-2000 Maribor, Slovenia

gasper.vrecer@um.si

Introduction

I am Gašper Vrečer, a researcher working in the field of microbiology, physical chemistry and biochemistry, with a research focus on the antimicrobial activity of natural compounds and their chemically modified derivatives. My research is centered on understanding how bioactive molecules, particularly those derived from natural sources, inhibit bacterial growth and how their structural modification, influences their biological performance.

Pathogenic bacteria can cause disease in humans, animals, or plants. Their pathogenicity depends on multiple factors, including the ability to adhere to and colonize host tissues, toxin production, and evasion of the host immune system. Common pathogenic genera include *Escherichia*, *Staphylococcus*, *Streptococcus*, *Salmonella*, and *Pseudomonas*, which are responsible for a wide range of infections, from mild localized conditions to severe systemic diseases and even death. A key feature of many pathogenic bacteria is their ability to produce toxins. Exotoxins are secreted proteins that can damage host cells or disrupt physiological processes, while endotoxins, such as lipopolysaccharide (LPS) found in Gram-negative bacteria, can trigger strong inflammatory responses and lead to conditions such as septic shock [1]. Biofilms are structured communities of bacteria embedded in a self-produced extracellular matrix that adheres to surfaces providing protection against environmental stress, antibiotics, and host immune defenses [2]. Understanding the biology and behavior of pathogenic bacteria is essential for developing effective therapeutic strategies. With the increasing threat of antimicrobial resistance, research is increasingly focused on alternative approaches, including natural antimicrobial compounds and novel materials with antibacterial properties.

Bacterial resistance refers to the ability of bacteria to survive and proliferate in the presence of antibiotics or other antimicrobial agents that would normally inhibit or kill them. It represents one of the most serious challenges in modern medicine, as it reduces the effectiveness of standard medications and complicates infection control. Bacteria employ several mechanisms to resist the effects of antimicrobial agents such as enzymatic degradation or inactivation of antibiotics for example β-lactamases, modification of the antibiotic target site, decreased membrane permeability, limiting the entry of antimicrobial

agents into the cell and efflux pumps transporting antibiotics out of the bacterial cell. Horizontal gene transfer plays a crucial role in the spread of resistance. This enables rapid dissemination of resistance traits within and between bacterial populations. Understanding of these mechanisms is essential for the development of new antimicrobial strategies, including novel drugs, enzyme inhibitors, and alternative approaches such as natural antimicrobial compounds and functional antibacterial materials [3, 4].

Plants contain a wide range of bioactive substances, such as essential oils, tannins, flavonoids, and alkaloids, which exhibit antimicrobial properties and can help inhibit the growth of pathogenic microorganisms. This approach has become relevant following the ban on the use of antibiotics for non-therapeutic purposes in livestock production in Europe (70% of global antibiotic consumption), as there is a growing need for effective and safe alternatives to prevent disease and promote animal growth [9].

In modern biochemical and microbiological research, a combination of advanced analytical and separation techniques is essential for the isolation, purification, and characterization of biologically active compounds and their interactions with biomolecules. Among these, high-performance liquid chromatography (HPLC), and circular dichroism (CD) spectroscopy represent methods that enable detailed investigation of natural compounds and proteins at the molecular level [5, 6].

Experimental

A significant part of my work involves evaluating antibacterial activity of compounds including lignin, ellagitannins derived from chestnut wood such as vescalagin and castalagin, and tannins from pomegranate such as punicalagin. They are able to interact and bind to proteins, as this mechanism can disrupt microbial cell function by inactivating enzymes, destabilizing cell membranes, or interfering with nutrient uptake. Tannins, in particular, are well known for their strong protein-binding capacity forming hydrogen bonds, which contribute to their antimicrobial effects. Antibacterial activity is evaluated using well-established microbiological methods.

One of the primary techniques I employ is the agar diffusion assay, which provides an initial qualitative assessment of antimicrobial efficacy. In this method, bacterial cultures such as *Escherichia coli* are inoculated onto solid agar media, followed by the application of test compounds. The formation of inhibition zones indicates the ability of a compound to suppress bacterial growth. This approach is particularly useful for rapid screening and comparative analysis of different substances or formulations [7].

For a more precise and quantitative evaluation, I use the broth microdilution method to determine the minimum inhibitory concentration (MIC). MIC is defined as the lowest concentration of a compound that inhibits bacterial growth after incubation. In my work, this is carried out in Mueller-Hinton broth using serial dilutions of the tested compound. Bacterial suspensions standardized to 0.5 McFarland are introduced into each well, and growth is monitored after incubation at 37 °C, typically by measuring optical density at 600 nm. This method allows for accurate comparison of antimicrobial potency and is widely regarded as standard in antimicrobial testing of patients to provide them with right antibiotic and its concentration [7-9].

In addition to MIC, I also test the minimum bactericidal concentration (MBC), which provides further insight into the nature of antimicrobial activity. While MIC reflects growth inhibition, MBC represents the lowest concentration of an antimicrobial agent that results in bacterial death which is proven by the absence of colony formation after culturing and incubation. To determine MBC, samples from wells showing no visible growth in the MIC assay are plated onto agar media and incubated under the same conditions. The absence of colony-forming units (CFU) indicates bactericidal activity [7-9].

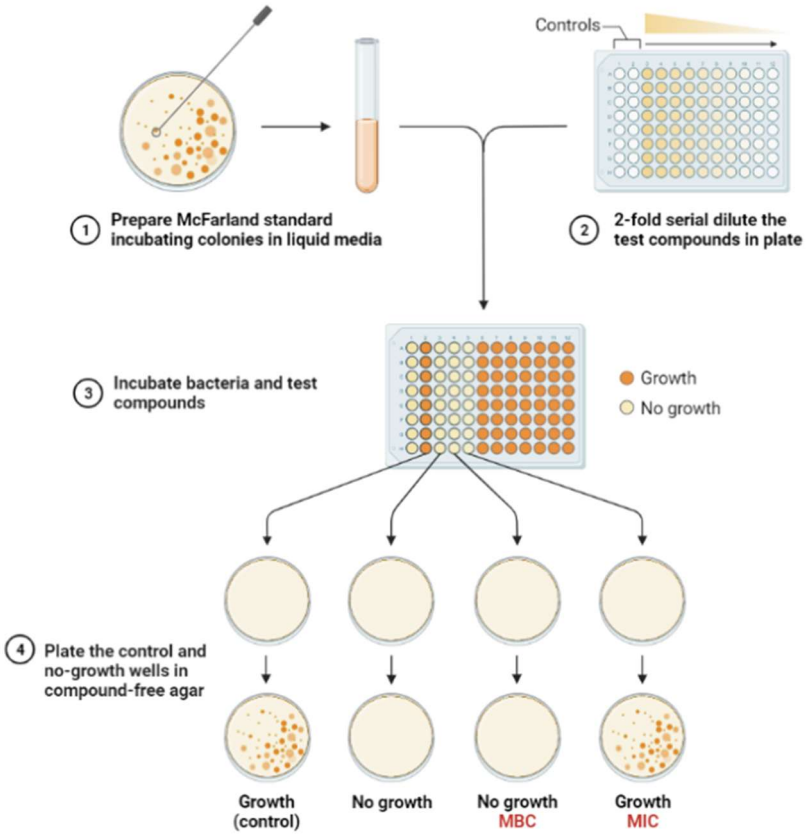

Fig. 1.: Method for determination of MIC in MBC
(https://www.biorender.com/template/mic-and-mbc-test)

My research extends to advanced materials such as polymers incorporating antimicrobial agents. I investigate the antibacterial activity of such materials using surface-contact assays, where bacterial suspensions are exposed to polymer surfaces over defined time intervals. After incubation, bacteria are recovered, plated, and quantified to determine viability. This approach enables the evaluation of time dependent antibacterial effects and provides information about the performance of antimicrobial materials in realistic conditions. This is presented in our article Paljevac, M., et al., in *Bio-based polyHIPEs from eugenol-derived methacrylates: morphology and antibacterial activity*, demonstrating that eugenol-based polymeric structures exhibit notable antibacterial properties, further supporting the potential of plant-derived compounds as alternatives to conventional antibiotics. [7, 10].

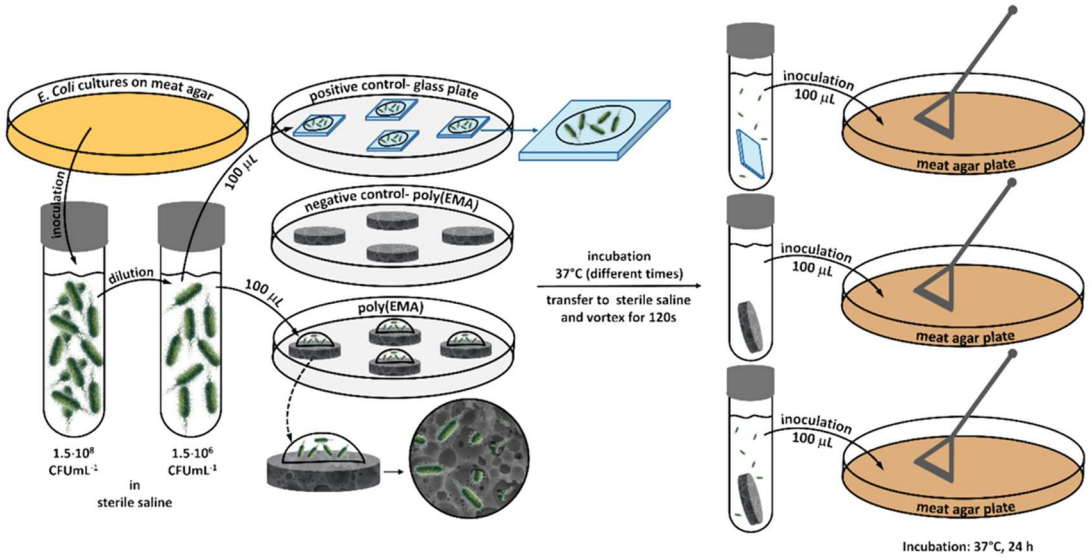

Fig. 2.: Method for determining the antimicrobial effect using a solid porous material contact assay [7]

To investigate the structural properties of purified proteins and their interactions with isolated natural compounds, circular dichroism (CD) spectroscopy is commonly employed. CD spectroscopy is a sensitive optical technique that measures the differential absorption of left and right circularly polarized light by chiral molecules, such as proteins. In the far-UV region (typically 190–280 nm), CD spectra provide information about the secondary structure content of proteins, including α-helices, β-sheets, and random coils. When a ligand, such as a natural bioactive compound, binds to a protein, it can induce conformational changes that affect the protein's secondary structure [11]. These changes are reflected as alterations in the CD spectrum, such as shifts in peak intensity or wavelength. By comparing spectra before and after ligand binding, researchers can gain valuable insights into protein folding, stability, and structural dynamics [6, 12].

Summary

Overall, my research integrates microbiology, biochemistry, and physical chemistry to contribute to the development of innovative antimicrobial strategies. Such an interdisciplinary approach is particularly relevant in the study of natural antimicrobial compounds, where both the chemical properties of the compounds and their biological effects on target microorganisms and their proteins must be understood. Our research ultimately contributes to the development of innovative solutions in medicine, biotechnology, and related fields.

References

1. He, H., et al., *Involvement of phosphatidylinositol-phospholipase C in immune response to Salmonella lipopolysaccharide in chicken macrophage cells (HD11).* Int Immunopharmacol, 2006. **6**(12): p. 1780–7.

2. Zhong, S., J. Yang, and H. Huang, *The role of single and mixed biofilms in Clostridioides difficile infection and strategies for prevention and inhibition.* Crit Rev Microbiol, 2024. **50**(3): p. 285–299.

3. Adedeji-Olulana, A.F., et al., *Two codependent routes lead to high-level MRSA.* Science, 2024. **386**(6721): p. 573–580.

4. Pang, Z., et al., *Antibiotic resistance in Pseudomonas aeruginosa: mechanisms and alternative therapeutic strategies.* Biotechnol Adv, 2019. **37**(1): p. 177–192.

5. Carvalho, C.T., et al., *Recovery of beta-galactosidase produced by Kluyveromyces lactis by ion-exchange chromatography: Influence of pH and ionic strength parameters.* An Acad Bras Cienc, 2022. **94**(1): p. e20200752.

6. Oyama, T., S. Suzuki, and K.-i. Akao, *Circular dichroism spectroscopy in protein engineering and pharmaceutical development: Applications in structural characterization and quality assessment.* Protein Expression and Purification, 2026. **237**: p. 106826.

7. Paljevac, M., et al., *Bio-based polyHIPEs from eugenol-derived methacrylates: morphology and antibacterial activity.* Reactive and Functional Polymers, 2026. **223**.

8. Ishak, A., et al., *Bactericidal versus bacteriostatic antibacterials: clinical significance, differences and synergistic potential in clinical practice.* J Antimicrob Chemother, 2025. **80**(1): p. 1–17.

9. Stumpf, S., et al., *The Influence of Chestnut Extract and Its Components on Antibacterial Activity against Staphylococcus aureus.* Plants (Basel), 2023. **12**(10).

10. Schneider, G., et al., *The use of antimicrobial-impregnated fabrics in health services: an integrative review.* Rev Lat Am Enfermagem, 2021. **29**: p. e3416.

11. Kuril, A.K., A. Vashi, and P.K. Subbappa, *A comprehensive guide for secondary structure and tertiary structure determination in peptides and proteins by circular dichroism spectrometer.* J Pept Sci, 2025. **31**(1): p. e3648.

12. Kelly, S.M. and N.C. Price, *The use of circular dichroism in the investigation of protein structure and function.* Curr Protein Pept Sci, 2000. **1**(4): p. 349–84.

Direct Conversion of Orange Peel and Sugar Beet Pulp into Nanoporous Aerogels by Disc Milling

Michel Groth

Institute of Thermal Separation Processes, Hamburg University of Technology and United Nations University Hub on Engineering to Face Climate Change at the Hamburg University of Technology, United Nations University Institute for Water, Environment and Health (UNU-12 INWEH), michel.groth@tuhh.de

Introduction

Orange peels (OP) and sugar beet pulp (SBP) are abundant agricultural residue generated in great amount while processing two of the worlds most produced crops, oranges (70Mt/a) and sugar beets (280 Mt/a). Despite their lager availability, they are predominantly used for low value applications such as animal feed. (1–5).

Both biomasses are rich in pectin and contain comparatively low amounts of lignin, making them attractive feedstocks for functional bio-based materials (1, 3, 6–12).

Aerogels are highly porous materials with low densities, large specific surface areas, and possibly attractive thermal insulation properties. They are typically produced by forming a wet gel network followed by solvent exchange and supercritical drying (SCD), which preserves the nanoscale pore structure by avoiding capillary collapse. (13, 14). In recent years, bio-based aerogels derived from renewable and waste biomass gained increasing interest (15, 16).

In this work, orange peels and sugar beet pulp were directly converted into biopolymer aerogels through disc-milling, Ca^{2+}-mediated gelation, and supercritical drying. While the OP route builds upon previous work (17), the production of highly mesoporous aerogels from sugar beet pulp is demonstrated for the first time.

Experimental

Production of OP- and SBP-derived aerogels followed the procedure proposed by Groth *et al.* (17). OP was washed extensively to remove water-soluble extractives, while SBP was washed only for dust removal. Deacetylation of SBP was performed by submerging SBP in water and adjusting the pH to approximately 1 using HCl. After two weeks, the biomass was drained and rinsed until neutral. Both OP and SBP were blended with water to obtain a 3 wt% dry mass suspension, which is subjected to milling in a disc

mill (GRANOMAT 177 JP150, Fuchs Maschinen AG, Granges-Paccot, Swiss) at 2200 rpm for 6 h in closed-circuit operation with a milling gap of -90 µm. After milling, pectin demethylation was performed by alkaline treatment (pH 10 for OP, pH 12 for SBP, 1 h room temperature). Monoliths were produced by filling suspension in sample tubes and covered with 10 wt% (OP) or 5 wt% (SBP) $CaCl_2$ solution and left for gelation overnight. Particles were produced by extruding suspension into a stirred gelation bath of the respective $CaCl_2$-solutions and left for full gelation overnight. After gelation, samples were washed, solvent-exchanged to ethanol (>98 wt%), and supercritically dried using CO_2. SCD was performed in a 4 L batch autoclave at 60 °C and 120 bar for 120 min, depressurization was 4 bar min^{-1} for particles and 2 bar min^{-1} for monoliths.

The resulting aerogels were characterized regarding density, porosity, specific surface area, pore size distribution and thermal conductivity.

Results

Both biomasses contain significant amounts of pectin, which is a polysaccharide build-up of galacturonic acid. The carboxyl-group of the galacturonic acid can be esterified with either methyl- or acetyl-groups. (18, 19) When pectin is gelled with multivalent ions like Ca^{2+} these esters reduce the number of negatively charged groups therefore reducing the gel strength or hindering the gelation at all (19, 20). OP pectin is only methyl-esterified therefore only a demethylation step after milling is performed to gain enhanced properties. It was observed that the SBP suspensions are not forming a stable gel after a demethylation step alone. Therefore an additional deacetylation step based on Pippen *et al.* was introduced prior to the milling process (21).

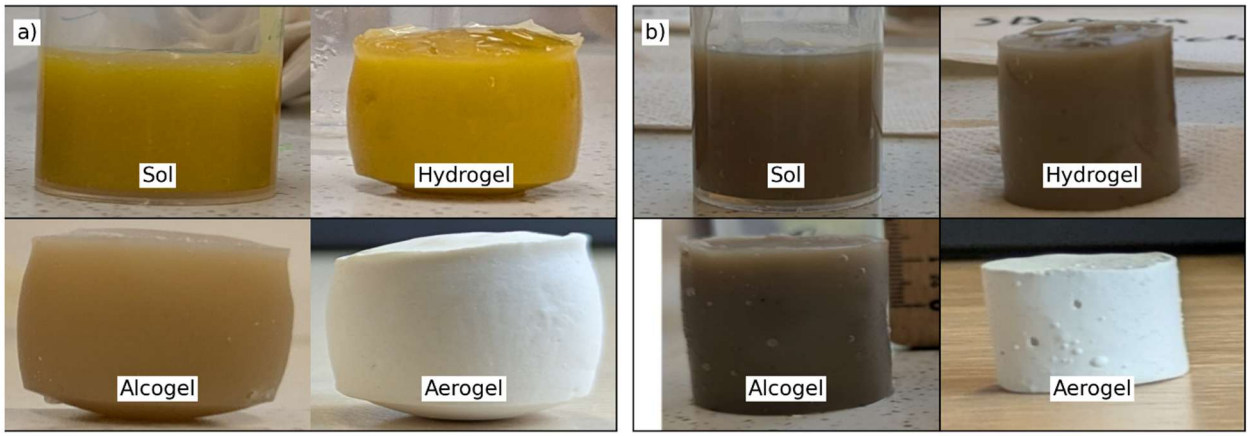

Figure 1 Change in colour of gels while processing a) orange peel b) sugar beet pulp.

Both gels undergo colour changes in the process (Figure 1) starting with an orange or brownish hydrogel for OP and SBP respectively. After solvent exchange the bright orange decreased to a faded orange for OP while SBP did not change colour in a significant way. The stronger discoloration observed for OP suggests a higher content of ethanol-soluble extractives, such as flavonoids. After SCD, both aerogels exhibit a white opaque appearance. This shows that the ethanol and the supercritical CO_2 effectively remove all native pigments. Significant volumetric reduction occurred during processing, resulting in a shrinkage of 41 vol% and 65 vol% for OP and SBP respectively. These values are in the typical range reported for biopolymer aerogels (15, 22). The amount of shrinkage has direct influence on the envelope density of the aerogels, resulting in 0.051 g cm^{-3} and 0.106 g cm^{-3} for OP and SBP respectively, showing that a higher shrinkage results in a higher density. Porosity follows this trend with 97% and 95% for OP and SBP respectively. Both suspensions were of the same solid concentration, therefore the higher density and shrinkage of SBP aerogels is a first indicator of worse gelling and network building of the SBP pectin-CNF matrix.

Further insight into network formation was obtained from nitrogen physisorption measurements. Isotherms of both aerogels exhibit type IV behaviour, with a hysteresis loop indicating mesoporous structure. The surface area of the OP aerogels is 509 $m^2 g^{-1}$ and of the SBP aerogel 291 $m^2 g^{-1}$, indicating more efficient network formation in the citrus-pectin-based aerogels. Pore size distributions (Figure 2) of OP and SBP show that both exhibit pores in the mesopore range, with OP exhibiting substantially larger mesopore volumes. The mesopore volume of OP is almost 2.5 times greater than that of SBP (2.49 $cm^3 g^{-1}$ vs. 1.04 $cm^3 g^{-1}$). Interestingly both mean mesopore diameters are in the same range with 18 nm (OP) and 20 nm (SBP).

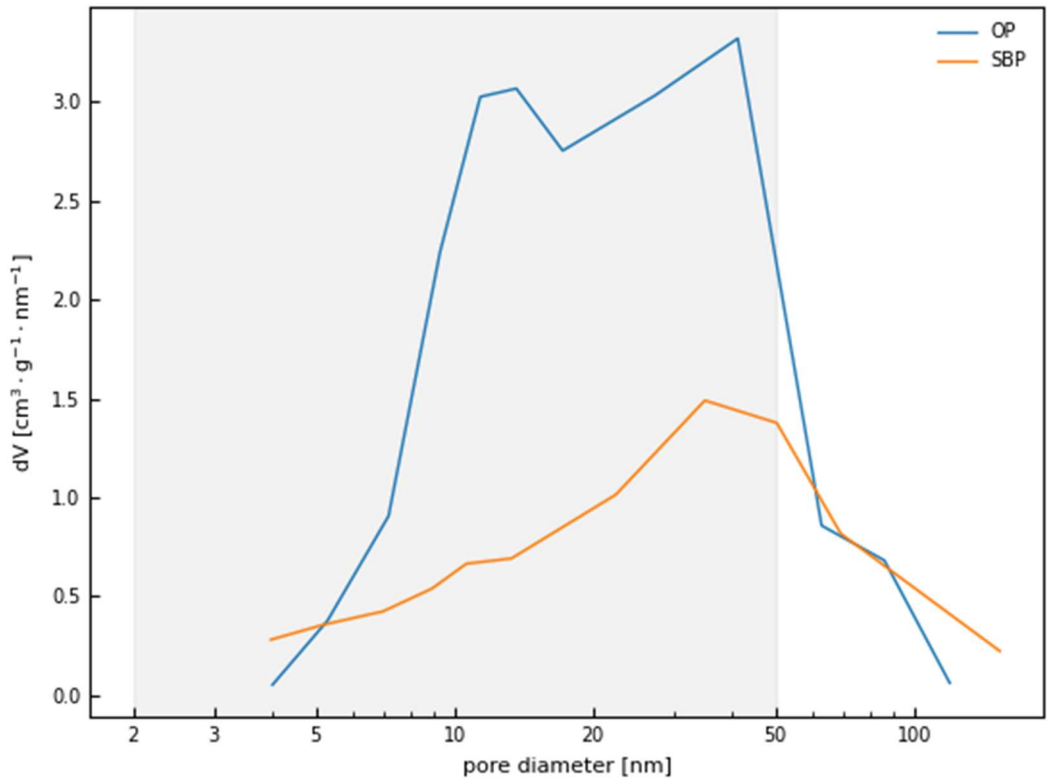

Figure 2 Pore size distribution of orange peel and sugar beet pulp derived aerogels. Highlighted in grey is the mesopore region.

Thermal conductivity of OP and SBP was 29 mW $(mK)^{-1}$ and 31 mW $(mK)^{-1}$ respectively. The slightly lower thermal conductivity of OP is consistent with its finer and more developed mesoporous structure, highlighting its potential for thermal insulation applications.

Summary

In this work the production of aerogels from orange peel and sugar beet pulp is shown, the latter for the first time. Despite identical solids content and processing conditions, OP aerogels consistently exhibited lower shrinkage, lower density, higher surface area, and larger mesopore volumes than SBP aerogels. This indicates superior network formation of citrus pectin during Ca^{2+}-mediated gelation. The results demonstrate that both agricultural residues can be directly converted into highly mesoporous aerogels, although citrus pectin appears to form more efficient pore networks than sugar beet pectin under otherwise identical processing conditions.

Acknowledgment

The German Federal Ministry for Economic Affairs and Energy has funded this work as part of the project “AEROLIGNOCEL” with funding code 03EN4104A.

References

1. Possari LT, Ávila PF, Brienzo M, Otoni CG, Budtova T, Bettini SH. Upcycling orange waste biomass into bio-aerogels; 2025. (vol 2).

2. Ma E, Cervera Q, Mejía Sánchez GM. Integrated utilization of orange peel. Bioresour Technol 1993; 44(1):61–3.

3. Rivas B, Torrado A, Torre P, Converti A, Domínguez JM. Submerged citric acid fermentation on orange peel autohydrolysate. J Agric Food Chem 2008; 56(7):2380–7.

4. Wirtschaftliche Vereinigung Zucker e.V.; Verein der Zuckerindustrie e.V. Jahresbericht der Zuckerwirtschaft 2022 2023. Berlin; 2023 [cited 2025 Aug 18].

5. FAO. Agricultural production statistics 2010-2023. Rom: FAO; 2024. FAOSTAT Analytical Briefs 96. Available from: URL: https://openknowledge.fao.org/items/ab36b259-d641-4ded-8832-32f579685be7.

6. Pascoli DU, Dichiara A, Roumeli E, Gustafson R, Bura R. Lignocellulosic nanomaterials production from wheat straw via peracetic acid pretreatment and their application in plastic composites. Carbohydr Polym 2022; 295.

7. Liang X, Wei S, Xu Y, Yin L, Wang R, Li P et al. Construction and Characterization of Fitting Equations for a New Wheat Straw Pulping Method. Polymers (Basel) 2023; 15(24).

8. Michel F, Thibault J-F, Barry J-L, Baynast R de. Preparation and characterisation of dietary fibre from sugar beet pulp. J Sci Food Agric 1988; 42(1):77–85.

9. Marzo-Gago C, Díaz AB, Blandino A. Sugar Beet Pulp as Raw Material for the Production of Bioplastics. Fermentation 2023; 9(7):655.

10. Santos LB, Silva RD, Alonso JD, Brienzo M, Silva NC, Perotto G et al. Bioplastics from orange processing byproducts by an ecoefficient hydrothermal approach. Food Packaging and Shelf Life 2023; 38:101114.

11. Gibowsky L, Berardinis L de, Plazzotta S, Manke E, Jung I, Méndez DA et al. Conversion of natural tissues and food waste into aerogels and their application in oleogelation. Green Chem. 2025; 27(17):4713–31.

12. Li C, McClements DJ, Dai T, Jiang D, Deng L, Liu C et al. Improving food sustainability by converting orange peel waste products into hydrogels using stirred media milling. Journal of Food Engineering 2024; 366:111813.

13. KISTLER SS. Coherent Expanded Aerogels and Jellies. Nature 1931; 127(3211):741.

14. Zhao S, Malfait WJ, Guerrero-Alburquerque N, Koebel MM, Nyström G. Biopolymer Aerogels and Foams: Chemistry, Properties, and Applications. Angew Chem Int Ed Engl 2018; 57(26):7580–608.

15. Budtova T. Cellulose II aerogels: a review. Cellulose 2019; 26(1):81–121.
16. France KJ de, Hoare T, Cranston ED. Review of Hydrogels and Aerogels Containing Nanocellulose. Chem. Mater. 2017; 29(11):4609–31.

17. Groth M, Heidorn F, Bueno A, Gibowsky L, Mutamba U, Schulze A-L et al. Integrated Disc-Milling and Sol–Gel Structuring of Waste Biomass into Cellulose–Pectin Biohybrid Aerogels [submitted]. Green Chem. 2026.

18. Barrera-Chamorro L, Fernandez-Prior Á, Rivero-Pino F, La Montserrat-de Paz S. A comprehensive review on the functionality and biological relevance of pectin and the use in the food industry. Carbohydr Polym 2025; 348(Pt A):122794.

19. Ropartz D, Ralet M-C. Pectin Structure. In: Kontogiorgos V, editor. Pectin: Technological and Physiological Properties. Cham: Springer International Publishing; 2020. p. 17–36.

20. Williams MAK. Pectin Gelation and Its Assembly into Functional Materials. In: Kontogiorgos V, editor. Pectin: Technological and Physiological Properties. Cham: Springer International Publishing; 2020. p. 125–48.

21. Pippen EL, McCready RM, Owens HS. Gelation properties of Partially Acetylated Pectins. Journal of American Chemicals Society 1950; 72(2):813–6.

22. Griffin JS, Nelson RT, Gurikov P, Smirnova I, Steiner SA. Gel-Phase Processing and Solvent Exchange. In: Aegerter MA, Leventis N, Koebel M, Steiner III SA, editors. Springer Handbook of Aerogels. Cham: Springer International Publishing; 2023. p. 71–92 (Springer Handbooks).

Fabrication and Physicochemical Evaluation of Biopolymer-Based Active Packaging Materials Containing Components of Plant Origin

Hira Anwar, Anna Witek-Krowiak

Department of Engineering and Technology of Chemical Processes, Faculty of Chemistry, Wroclaw University of Science and Technology, Gdanska 7/9, 50-344 Wroclaw, Poland.

hira.anwar@pwr.edu.pl

Abstract

Biopolymer-based active packaging materials are being developed as sustainable alternatives to conventional plastic packaging, whose environmental persistence and passive protective role remain limited. Biodegradable active packaging films containing plant-derived components are considered for food applications in the present study. As a preliminary film-forming system alginate-based films containing fruit extract of *Berberis vulgaris* obtained through solvent-based extraction using 50% ethanol were incorporated into biopolymeric matrix. The obtained films were crosslinked using 0.2 M calcium chloride solution. The influence of polymer concentration and crosslinking time was considered through initial visual and handling observations. It was observed that films prepared at a lower alginate concentration were very thin and fragile, whereas those prepared at a higher alginate concentration exhibited better film-forming ability. Further optimization and characterization are planned to evaluate mechanical properties, release and swelling behavior, color assay, and FTIR-based interaction of the developed films. This study is expected to contribute to the rational design of biodegradable active packaging materials with improved potential for food preservation and sustainable storage systems.

Introduction

Food packaging is required to protect food products against physical damage, oxygen exposure, microbial contamination, moisture transfer, and quality loss during storage and distribution. Conventional petroleum-based plastics are still widely used because good flexibility, barrier performance and mechanical strength can be achieved at low cost. However, these materials are generally non-biodegradable and may persist in the environment for a long time after disposal, and most conventional plastic packaging mainly acts as passive barriers and does not provide active protection against oxidation or microbial spoilage. Therefore, sustainable active packaging materials with both

biodegradability and active functionality are increasingly being investigated (A. A. Shah et al., 2008; Siracusa et al., 2008).

Biopolymer-based films and coatings have been proposed as promising materials for food packaging applications. Polysaccharides, proteins, and their derivatives can be processed into continuous films, and their properties can be modified using plasticizers, crosslinking, and active compounds. However, the direct application of many natural polymer films is still limited by high water sensitivity, weak barrier performance and insufficient mechanical strength. Therefore, the performance of such materials must be improved through a carefully designed formulation (Cazón et al., 2017; Garavand et al., 2017). Active packaging is distinguished from passive packaging by the incorporation of functional compounds into the packaging system. These compounds may be released gradually or interact with the surrounding environment to reduce oxidation, inhibit microbial growth, or slow quality deterioration. Plant-derived components including phenolics, flavonoids, alkaloids, anthocyanins, and other phytochemicals, have gained particular interest because of their antioxidant and antimicrobial properties, and have been widely incorporated into biopolymeric matrices (Wu et al., 2023; Yildirim et al., 2018). The general workflow for the development and evaluation of biodegradable active packaging films containing plant-derived components is shown in Fig.1.

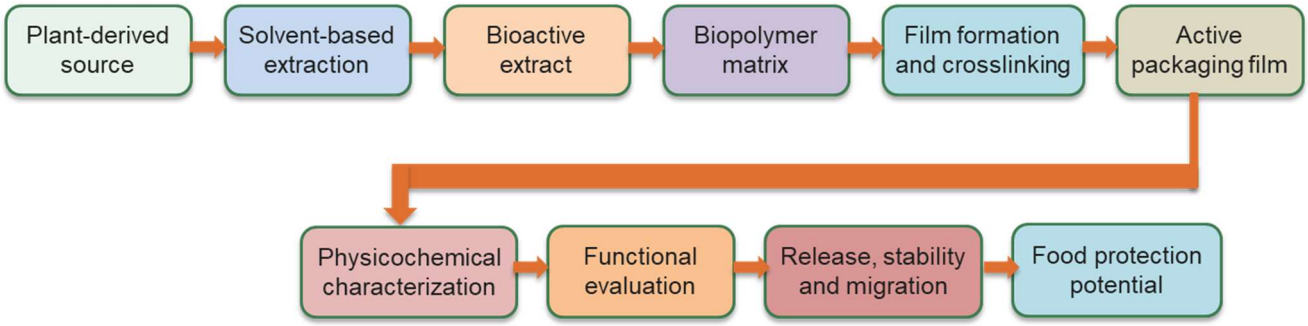

Fig. 1.: Conceptual workflow for the development and evaluation of biodegradable active packaging films containing plant-derived components.

Among potential plant sources, *B. vulgaris* is considered attractive because its fruits and other plant parts contain several bioactive compounds, including berberine, palmatine, phenolic acids and flavonoids-related constituents. These compounds have been associated with antioxidant, antimicrobial and health-promoting activities, making them suitable for food-related applications (Ali Redha et al., 2021). Several studies have shown that berberis species and their major bioactive constituents can be effectively used

in active edible and biodegradable films for food applications. Shah et al. developed sodium caseinate-based edible films infused with *B. pseudumbellata* fruit extract and reported improved optical, antimicrobial, and antioxidant performance, as well as potential application for refrigerated meat preservation (H. Shah et al., 2023). Ahmed et al. prepared collagen-carboxymethyl cellulose films enriched with *B. lyceum* root extract and evaluated their antioxidant activity, food-simulant release behavior, UV-Vis barrier properties and biodegradability (Ahmed et al., 2022). Similarly, Öztürk et al. incorporated berberine into chitosan films and showed that interaction between berberine and the polymer matrix could improve mechanical, antimicrobial and antioxidant properties, confirming the relevance of berberis-related compounds for active food packaging (Öztürk et al., 2025). These studies indicate that berberis extracts and compounds can act as promising natural additives for active film formation; however, their use in alginate-based matrices still requires further investigation.

Therefore, in the current study, alginate was selected as a biopolymeric matrix for preparing active films containing *B. vulgaris* fruit extract, a potential material for food preservation applications. Emphasis is placed on understanding how extract incorporation, polymer concentration and crosslinking conditions influence the formation and stability of the resulting films. This approach enables optimization of the basic formulation parameters before detailed evaluation of mechanical, optical, structural, functional, swelling and release-related applications of the developed active packaging films.

Experimental

The experimental workflow was designed to link the solvent-based extraction of plant-derived bioactive components to the preparation of biodegradable active packaging films. At this stage, early-stage fruit extract was obtained using an ethanol:water (50:50) extraction system and was considered a source of phenolic compounds. The obtained extract was characterized in terms of total phenolic content (TPC) using the Folin-Ciocalteu reagent and antioxidant activity was assessed by the DPPH radical scavenging assay. The extract was then incorporated into sodium alginate to form an initial polysaccharide film-forming matrix, while glycerol was used as a plasticizing component. Alginate-based films were prepared at different polymer concentrations and crosslinked with calcium chloride to improve the integrity of the films.

Tab. 1.: Preliminary and planned research framework for plant-extract containing biopolymer films

Stage	Material/process considered	Purpose	observation
Plant source and extraction	*B. vulgaris* fruit extract obtained using 50% ethanol-water system	To obtain plant-derived bioactive components	TPC and DPPH content were determined
Biopolymer matrix	Sodium alginate	To prepare biodegradable active films	Initial alginate-based films were performed
Film formulation	Alginate solutions (2% & 4%) polymer concentration, extract, and plasticizer	To assess film-forming ability and handling stability	Polymer concentration was identified as a key parameter for film formation.
Crosslinking	0.2 M calcium chloride solution	Crosslinked for 10 and 20 sec to improve alginate network integrity	Crosslinking duration requires further optimization
Planned characterization	Mechanical testing, color assay, swelling/release behavior, and FTIR analysis	To evaluate film performance and polymer-extract interactions	Planned as part of further research

Preliminary research was focused on the effect of alginate concentration, crosslinking time of the film formation, handling stability and visual appearance. It was observed that the films prepared with lower alginate concentrations were very thin and fragile, whereas those prepared with higher alginate concentrations exhibited better film-forming ability and handling stability. These observations indicate that polymer concentration and crosslinking duration should be further optimized before detailed material characterization.

Further characterization is planned to focus on the mechanical, optical, swelling, release, and functional properties of the developed films. Mechanical strength is planned to be evaluated using tensile testing, while FTIR analysis is considered to investigate possible interactions between the plant extract and the alginate matrix. Color assay, swelling and release behavior are also induced to assess the suitability of the films for active food packaging applications.

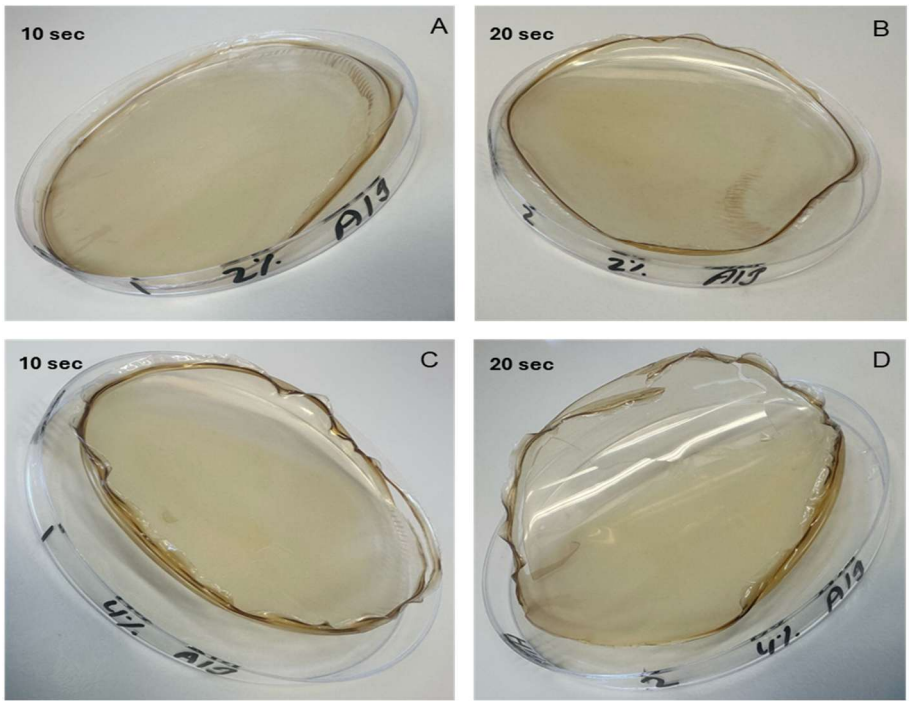

Fig. 2.: Alginate-based films containing *B. vulgaris* fruit extract: (A,B) 2% alginate crosslinked for 10 s and 20 s; (C,D) 4% alginate crosslinked under the same conditions.

Summary

The present work highlights the potential of plant-derived bioactive compounds as functional additives for biodegradable active packaging materials. The preliminary developments of alginate-based films provide an initial basis for understanding the role of polymer composition and crosslinking with calcium chloride in the film formation. The proposed research is expected to support the design of active packaging systems in which biodegradability, material stability and active food protection are considered together. The development of such materials may contribute to sustainable food preservation strategies by reducing the dependence on conventional plastic packaging and by offering additional protection against quality deterioration during storage.

Acknowledgment

The author grateful for The European Summer School in High Pressure Technology ERASMUS+ BIP ESS-HPT 2026.

References

Ahmed, M., Verma, A. K., & Patel, R. (2022). Physiochemical, antioxidant, and food simulant release properties of collagen-carboxymethyl cellulose films enriched with Berberis lyceum root extract for biodegradable active food packaging. *Journal of Food Processing and Preservation*, *46*(4). https://doi.org/10.1111/jfpp.16485

Ali Redha, A., Siddiqui, S. A., & Ibrahim, S. A. (2021). Advanced extraction techniques for Berberis species phytochemicals: A review. In *International Journal of Food Science and Technology* (Vol. 56, Number 11, pp. 5485–5496). John Wiley and Sons Inc. https://doi.org/10.1111/ijfs.15315

Cazón, P., Velazquez, G., Ramírez, J. A., & Vázquez, M. (2017). Polysaccharide-based films and coatings for food packaging: A review. *Food Hydrocolloids*, *68*, 136–148. https://doi.org/10.1016/j.foodhyd.2016.09.009

Garavand, F., Rouhi, M., Razavi, S. H., Cacciotti, I., & Mohammadi, R. (2017). Improving the integrity of natural biopolymer films used in food packaging by crosslinking approach: A review. In *International Journal of Biological Macromolecules* (Vol. 104, pp. 687–707). Elsevier B.V. https://doi.org/10.1016/j.ijbiomac.2017.06.093

Öztürk, S., Kalaycıoğlu, Z., Torlak, E., Akın-Evingür, G., & Erim, F. B. (2025). Chitosan films incorporated with berberine: enhanced mechanical, antioxidant, and antimicrobial properties as potential food packaging material. *Journal of Food Measurement and Characterization*, *19*(1), 264–275. https://doi.org/10.1007/s11694-024-02967-z

Shah, A. A., Hasan, F., Hameed, A., & Ahmed, S. (2008). Biological degradation of plastics: A comprehensive review. In *Biotechnology Advances* (Vol. 26, Number 3, pp. 246–265). https://doi.org/10.1016/j.biotechadv.2007.12.005

Shah, H., Ahmed, S., Urooj, F., Zaheer, S., & Safdar, N. F. (2023). Development, characterization and investigation of antimicrobial and antioxidant potential of sodium caseinate-based edible films infused with Berberis pseudumbellata fruit extract, and effects of the films on the quality of raw ground beef during refrigeration. *Meat Technology*, *64*(1), 1–12. https://doi.org/10.18485/meattech.2023.64.1.1

Siracusa, V., Rocculi, P., Romani, S., & Rosa, M. D. (2008). Biodegradable polymers for food packaging: a review. In *Trends in Food Science and Technology* (Vol. 19, Number 12, pp. 634–643). https://doi.org/10.1016/j.tifs.2008.07.003

Wu, Y., Yu, X., Ding, W., Remón, J., Xin, M., Sun, T., Wang, T. T. Y., Yu, L. (Lucy), & Wang, J. (2023). Fabrication, performance, and potential environmental impacts of polysaccharide-based food packaging materials incorporated with phytochemicals: A review. In *International Journal of Biological Macromolecules* (Vol. 249). Elsevier B.V. https://doi.org/10.1016/j.ijbiomac.2023.125922

Yildirim, S., Röcker, B., Pettersen, M. K., Nilsen-Nygaard, J., Ayhan, Z., Rutkaite, R., Radusin, T., Suminska, P., Marcos, B., & Coma, V. (2018). Active Packaging Applications for Food. In *Comprehensive Reviews in Food Science and Food Safety* (Vol. 17, Number 1, pp. 165–199). Blackwell Publishing Inc. https://doi.org/10.1111/1541-4337.12322

DLS-Based Estimation of Pullulan Chain Length to Hydrodynamic Radius as Basis for Evaluating Alginate Extraction Methods

Anna Lena Schuhmacher, Prof. Dr.-Ing. Sabine Grüner

Bioingeneurswissenschaften, HSWT, Anna.Schuhmacher@hswt.de

To evaluate the quality of polysaccharide extraction methods, a simple and reliable approach for estimating chain length is required. In this study, the hydrodynamic radius (R_h) of particles, measured by dynamic light scattering (DLS) at a backscattering angle of θ = 175°, is correlated with pullulan standards in alkaline buffers in varying concentrations. These results are used to estimate alginate chain lengths obtained from different extraction techniques and are compared with gel permeation chromatography coupled with evaporative light scattering detection (GPC-ELSD). The presentation will highlight selected experimental findings, discuss the transferability of pullulan-based correlations to alginate systems, and identify key influencing factors, particularly substrate agglomeration.

Introduction

Product quality is of particular importance when comparing different extraction methods. A key parameter for assessing the quality of the polysaccharide alginate extracted from algae is the chain length. This parameter correlates with particle size and hence with the hydrodynamic radius (R_h) which can be determined using dynamic light scattering (DLS). [1], [2] The aim of this work is to improve the reproducibility of the relationship between defined pullulan standard chain lengths and their corresponding hydrodynamic radii. Experiments are conducted under conditions compatible with size exclusion chromatography coupled with evaporative light scattering detection (SEC-ELSD), ensuring comparability between both analytical approaches.

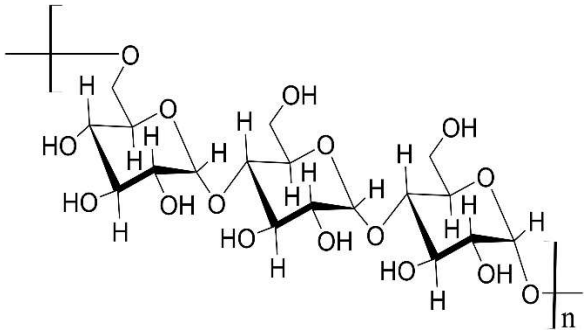

Fig. 1.: Structure of pullulan with maltotriose as repeating units. [3]

Dynamic light scattering (DLS) determines the size of particles or macromolecules in solution based on their Brownian motion and their ability to scatter light Time-dependent fluctuations in the intensity of scattered laser light are analyzed to obtain the intensity autocorrelation function. From this, the translational diffusion coefficient is derived, which can be converted into the hydrodynamic radius (R_h) using the Stokes–Einstein equation. Because DLS is highly sensitive to aggregation phenomena, concentration effects, and deviations from spherical particle geometry, careful sample preparation and cautious data interpretation are essential, particularly when investigating complex polymer systems.[4], [5]

Experimental

All liquids were filtered through 0,2 µm membranes, and vessels were kept covered with lids to minimize dust contamination. A 10 mM ammonium acetate buffer, adjusted to pH 8.0, was selected as the matrix to assure comparability with SEC-ELSD measurements. Pullulan standard (see Fig. 1, Tab. 1) was dissolved in water for 24 h to ensure complete solubilization. Sample concentrations of 0.207, 0.104, 0.052, 0.026, and 0,013 mg/mL were prepared by geometric dilution. Technical duplicates of samples and controls were each measured in triplicate using a ZetaSizer Ultra (Blue Label) at 25 °C, with an equilibration time of 30 s and a backscattering angle of θ = 174.7°.

Tab. 1.: CoA Pullulan Standard PolyCAL ® PUL-118K, Malvern Panlaytcal

	Weight-average moleculat weight M_w	**Number-average molecular weight M_n**	**Polydispersity Index $\frac{Mw}{Mn}$**	**mg/vial**
Mean	118,456	112,684	1,051	4,14
Standard Deviation	1,004	1,182		0,01
% RSD	0,85	1,05		0,29

Data were processed using ZS Xplorer 4.2.0 software. Data quality was critically evaluated by examining key parameters, including relaxation time, translational diffusion

coefficient, polydispersity index (PI), and z-average diameter. Selectable results will be presented and discussed in comparison with values reported in the literature [6], [7], [8].

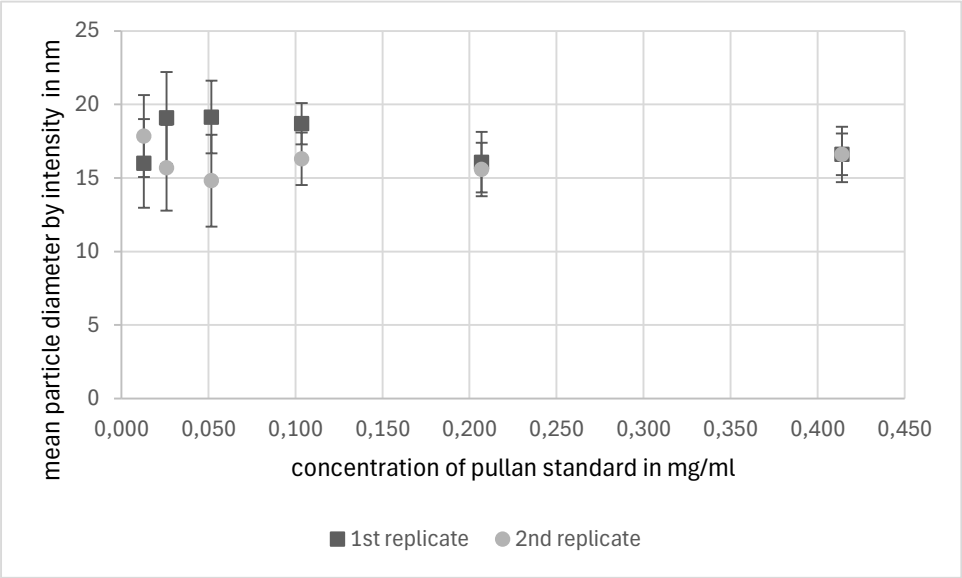

Fig. 2.: Particle size of pullulan standard 118K by DLS mean diameter of triplicates in nm. Error bars represent standard deviation.

The particle size of pullulan standard in different concentrations is shown in Fig. 2. as a representative result. Higher dilution levels exhibit greater variability in the measured values.

Summary

This study investigates the potential of dynamic light scattering (DLS) as a simple method for estimating polysaccharide chain length as a quality parameter in alginate extraction processes. The hydrodynamic radius of pullulan standards was measured at varying concentrations in an alkaline ammonium acetate buffer compatible with SEC-ELSD. The objective was to improve measurement reproducibility and to establish a correlation between pullulan chain length and hydrodynamic radius (R_h) Particular attention was given to polymer agglomeration and sedimentation, as both significantly influence DLS measurements and limit transferability to alginate systems. Selected results will be used to identify the conditions under which pullulan standards are most suitable as model compounds for estimating alginate chain lengths and for comparison with SEC-ELSD data.

Acknowledgment

The author would like to thank the research group Sustainable Bioengineering at HSWT for providing laboratory facilities and technical support. This work was partially funded by FH-Kooperativ Bundesministerium für Forschung, Technologie und Raumfahrt under the project INZELLA 13FH533KB2. The author also greatfully acknowledges the valuable feedback of Prof. Dr. Sabine Grüner and Dr. Jörg Schäffer. Special thanks are extended to Benjamin Weizenegger for his assistance with buffer preparation.

References

[1] A. M. F. Lima, V. Soldi, and R. Borsali, 'Dynamic light scattering and viscosimetry of aqueous solutions of pectin, sodium alginate and their mixtures: effects of added salt, concentration, counterions, temperature and chelating agent', *J. Braz. Chem. Soc.*, vol. 20, pp. 1705–1714, 2009, doi: https://doi.org/10.1590/S0103-50532009000900020.

[2] M. M. Nafureanu, L. Ghimici, M. Constantin, D. M. Suflet, E. A. Lopez-Maldonado, and C.-E. Brunchi, 'Insight of the viscometric behavior of pullulan and curdlan derivative solutions: Effect of the nature and salt concentration', *React. Funct. Polym.*, vol. 194, p. 105801, 2024, doi: https://doi.org/10.1016/j.reactfunctpolym.2023.105801.

[3] R. S. Singh, N. Kaur, D. Singh, B. K. Bajaj, and J. F. Kennedy, 'Downstream processing and structural confirmation of pullulan - A comprehensive review', *Int. J. Biol. Macromol.*, vol. 208, pp. 553–564, 2022, doi: https://doi.org/10.1016/j.ijbiomac.2022.03.163.

[4] J. Rodriguez-Loya, M. Lerma, and J. L. Gardea-Torresdey, 'Dynamic Light Scattering and Its Application to Control Nanoparticle Aggregation in Colloidal Systems: A Review', *Micromachines*, vol. 15, no. 1, p. 24, Dec. 2023, doi: 10.3390/mi15010024.

[5] F. Babick, 'Dynamic light scattering (DLS)', in *Characterization of Nanoparticles*, Elsevier, 2020, pp. 137–172. doi: 10.1016/B978-0-12-814182-3.00010-9.

[6] A. S. Gubarev, O. V. Okatova, A. A. Lezov, A. I. Kipper, M. E. Mikhailova, and G. M. Pavlov, 'Hydrodynamic Study of Linear Pullulan Standards in DMF Solutions and Metrology Aspects of Transport Methods', Dec. 09, 2024, *Chemistry and Materials Science*. doi: 10.20944/preprints202412.0668.v1.

[7] G. M. Pavlov, E. V. Korneeva, and N. P. Yevlampieva, 'Hydrodynamic characteristics and equilibrium rigidity of pullulan molecules', *Int. J. Biol. Macromol.*, vol. 16, no. 6, pp. 318–323, Dec. 1994, doi: 10.1016/0141-8130(94)90063-9.

[8] M. Grube, G. Cinar, U. S. Schubert, and I. Nischang, 'Incentives of Using the Hydrodynamic Invariant and Sedimentation Parameter for the Study of Naturally- and Synthetically-Based Macromolecules in Solution', *Polymers*, vol. 12, no. 2, p. 277, Jan. 2020, doi: 10.3390/polym12020277.

Modeling of *n*-Butyl Acrylate Solution Polymerization Using Deterministic and Stochastic Methods

Inka Helmer, Kristina Maria Zentel

Ernst-Berl-Institute of Technical and Macromolecular Chemistry,
Technical University of Darmstadt, kristina.zentel@pre.tu-darmstadt.de

Introduction

Acrylates are widely used as monomers in polymer production, with acrylate-based polymers being used predominantly in adhesive applications. In particular, *n*-butyl acrylate (nBA) is utilized for a variety of products, including pressure-sensitive adhesives as well as surface coatings for the paper industry. [1,2] Moreover, nBA can serve as a comonomer for tuning the glass transition temperature of polymers. [3] These applications underscore the industrial relevance of nBA and highlight the need for a detailed understanding of its polymerization behavior, as well as the correlation between process parameters and product properties. In this context, modeling represents a powerful tool for process optimization and scale-up.

The solution polymerization of nBA is governed by a complex kinetic network. Besides the fundamental steps of free-radical polymerization, the system includes chain-length dependent termination, backbiting, and β-scission, which increase its complexity and make it a challenging system to model. Modeling of nBA solution polymerization has been investigated in numerous publications employing a variety of modeling techniques. [4–6]

Among these, deterministic and stochastic methods are commonly used, each offering distinct advantages and complementary perspectives on the modeled system. Given their respective, unique characteristics, the application of both modeling techniques is advantageous for a comprehensive description of a reaction system. For this reason, deterministic and stochastic modeling of nBA solution polymerization was carried out and their results compared with the aim of achieving consistent outcomes.

Complementary Modeling

Deterministic and stochastic methods are both commonly used tools in the field of polymerization modeling. Deterministic approaches rely on the solution of differential equations, enabling short computation times and providing access to average polymer qualities as well as full molecular weight distributions. In contrast, stochastic methods,

such as Monte Carlo algorithms, follow a single-molecule approach in which each polymer chain is simulated individually. This allows for the extraction of detailed topological information. However, stochastic modeling is more computationally challenging in comparison to deterministic approaches and thus requires longer simulation times.

In this work, a model comparison is presented for nBA solution polymerization, as reported in greater detail in an earlier publication[7], using both deterministic and stochastic models. Deterministic simulations were performed using the software Predici, while the stochastic model was provided by DRACHE and implemented in the software mcPolymer.[8] Both models were constructed based on the kinetic scheme shown in Figure 1, with most reaction steps and kinetic parameters implemented the same. Initial comparisons of simulation results showed discrepancies in the molecular weight distributions (MWDs), particularly at high temperatures between 110 and 130 °C.

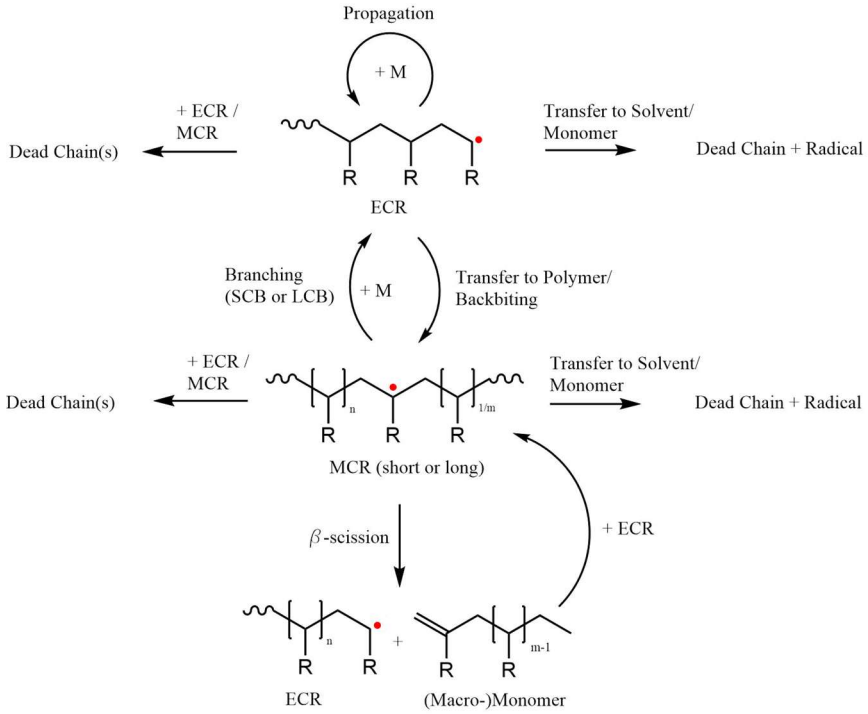

Fig. 1: Kinetic network of nBA solution polymerization. The figure has been taken from reference 7. Available under a CC BY 4.0 license. © 2026 Marco Drache, Inka Helmer, Sebastian Klepatz and Kristina Maria Zentel. Macromolecular Reaction Engineering published by Wiley-VCH GmbH. [7]

Further analysis of the reaction network revealed that the β-scission step was the source of these differences. In this reaction, scission occurs at the position of the radical functionality in a mid-chain radical, leading to the creation of chain fragments. In stochastic simulations, the exact position of the radical functionality is tracked, and scission is therefore represented accurately. In deterministic models, however, the radical position is

not known, and consequently, scission occurs with equal probability at any point within the chain. As a result, the fragment size distribution is not accurately reflected. For this reason, a different implementation of the β-scission step in the deterministic model is necessary, enabling the incorporation of chain topology and radical position effects on fragmentation.

The consideration of structural effects during β-scission can be achieved through so-called bathtub functions.[9] As shown in Figure 2, bathtub functions describe the probability with which fragments of certain sizes are formed, depending on the number of long-chain branches (LCBs), *N*, present in the polymer chain. Two distinct functions are differentiated, based on whether the polymer structure is more closely represented by a star-like or comb-like topology. As depicted in Figure 2, fragment sizes *x*, relative to the original chain's size, are formed with different probabilities. The formation of very small and very large fragments is favored, since the scission at small side chains occurs with high probability. In contrast, there are few possibilities for scission to result in two equally sized fragments, and consequently, the probability of forming fragments with medium size is low.

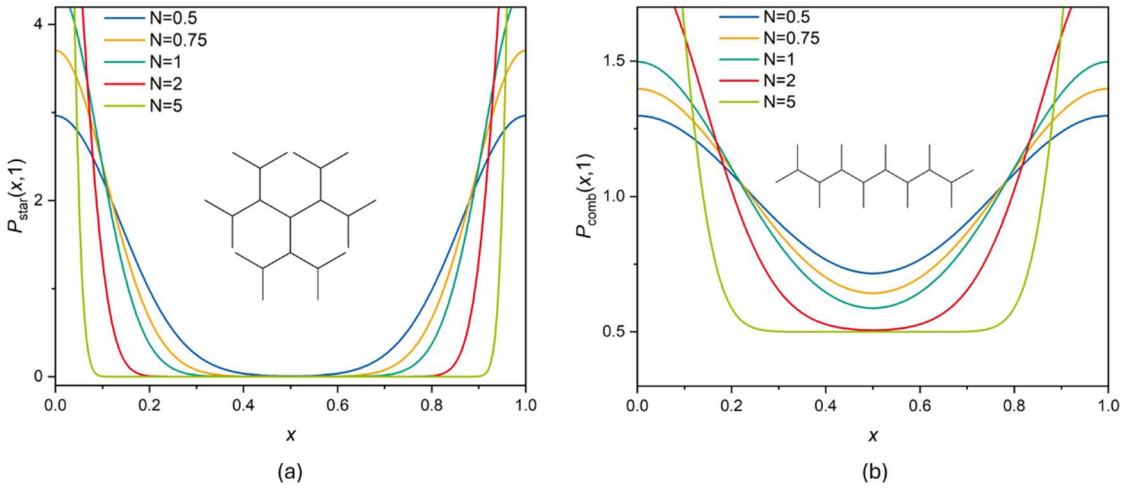

Fig. 2: Plotted bathtub functions for star-like (a) and comb-like (b) topology. The figure has been taken from reference 7. Available under a CC BY 4.0 license. © 2026 Marco Drache, Inka Helmer, Sebastian Klepatz and Kristina Maria Zentel. Macromolecular Reaction Engineering published by Wiley-VCH GmbH. [7]

By implementing bathtub functions into the deterministic model, the arbitrary scission and formation of all fragment sizes with equal probability is prevented. As a result, overall molecular weight increases, leading to a shift of the MWD toward higher molar masses. Comparison with the stochastic model shows that the incorporation of bathtub functions leads to consistent results between both models across the investigated temperature

range from 60 to 130 °C. Therefore, both the deterministic and the stochastic model now provide a comparable description of the nBA solution polymerization system.

Summary

In this work, the main focus lay on the complementary modeling of nBA solution polymerization, using deterministic and stochastic modeling approaches. A model comparison was carried out, aiming to demonstrate that the polymerization system at hand can be consistently described with both modeling techniques. Initial discrepancies between the simulated MWDs could be attributed to the β-scission step and its implementation. In order to account for the lack of exact structural information available in the deterministic model, bathtub functions were implemented. As a result, topology-based effects on the scission process could be taken into consideration in deterministic simulations, and the comparison between both models showed consistent results. Thus, nBA solution polymerization can be simulated through both models, from which a wide range of information can be obtained.

Overall, the results obtained in this work provide valuable insight into the solution polymerization of nBA and its description using different modeling techniques, thereby contributing to future modeling efforts.

Acknowledgment

The authors would like to thank Marco Drache for his contribution to this work and Michael Wulkow, CIT, for his support regarding Predici.

References

(1) Constantino, D. S.; Faria, R. P.; Ribeiro, A. M.; Rodrigues, A. E. Butyl acrylate production: A review on process intensification strategies. *Chemical Engineering and Processing - Process Intensification* **2019**, *142*, 107563. DOI: 10.1016/j.cep.2019.107563.

(2) Zhang, L.; Cao, Y.; Wang, S.; Czech, Z.; Shao, L.; Bai, Y. Synthesis of poly (n-butyl acrylates) by a novel microemulsion polymerization for PSAs applications. *International Journal of Adhesion and Adhesives* **2013**, *47*, 69–72. DOI: 10.1016/j.ijadhadh.2013.09.038.

(3) Former, C.; Castro, J.; Fellows, C. M.; Tanner, R. I.; Gilbert, R. G. Effect of branching and molecular weight on the viscoelastic properties of poly(butyl acrylate). *J. Polym. Sci. A Polym. Chem.* **2002**, *40* (20), 3335–3349. DOI: 10.1002/pola.10424.

(4) Mätzig, J.; Drache, M.; Drache, G.; Beuermann, S. Kinetic Monte Carlo Simulations as a Tool for Unraveling the Impact of Solvent and Temperature on Polymer Topology for Self-Initiated Butyl Acrylate Radical Polymerizations at High Temperatures. *Macro Theory & Simulations* **2023**, *32* (4). DOI: 10.1002/mats.202300007.

(5) Grotian Genannt Klages, H.; Ermis, N.; Luinstra, G. A.; Zentel, K. M. Coupling Kinetic Modelling with SAOS and LAOS Rheology of Poly(n-butyl acrylate). *Macromolecular rapid communications* **2022**, *43* (12), e2100620. DOI: 10.1002/marc.202100620. Published Online: Dec. 23, 2021.

(6) Lugo, F. A.; Trossaert, L.; Marien, Y. W.; Sabbe, M. K.; Edeleva, M.; D'hooge, D. R.; van Steenberge, P. H. M. Pulsed laser polymerization to retrieve kinetic parameters for a propagated mid-chain radical in poly(n -butyl acrylate) synthesis: a combined DFT and kinetic Monte Carlo study. *Polym. Chem.* **2025**, *16* (31), 3496–3510. DOI: 10.1039/D5PY00343A.

(7) Drache, M.; Helmer, I.; Klepatz, S.; Zentel, K. M. Modeling n-Butyl Acrylate Polymerization using Complementary Modeling Techniques. *Macro Reaction Engineering* **2026.** DOI: 10.1002/mren.70018.

(8) Drache, M.; Drache, G.; Sievers, P.; Klepatz, S. *mcPolymer - research software for kinetic Monte Carlo simulation of polymerization processes*; Zenodo, 2025. https://doi.org/10.5281/zenodo.16631171.

(9) Busch, M. Detaillierte Modellierung von Polymerisationsreaktionen und molekularen strukturellen Polymereigenschaften:Radikalische Hochdruck-Fluid-Phasen-Copolymerisationen als Beispielsysteme. Habilitation, University of Göttingen, 2003.

CFD Analysis of Flow Behavior and Pressure Distribution in Industrial Fluid Handling Components

[1,2] Jose Ruiz, [2] Daniel Chuquin-Vasco

[1] Department of Chemical and Environmental Process Engineering, Budapest University of Technology and Economics (BME), Hungary
[2] Grupo de Investigación Seguridad, Ambiente e Ingeniería (GISAI), Escuela Superior Politécnica de Chimborazo (ESPOCH), Ecuador
Corresponding author: jruizganchozo@edu.bme.hu

Introduction

Fluid flow analysis is essential in chemical and process engineering, particularly in the design and operation of piping systems, hydraulic equipment, and pressure-driven processes. Components such as Venturi tubes, valves, and pipe elbows generate localized pressure losses, turbulence effects, and flow recirculation phenomena that directly affect hydraulic performance and operational efficiency [1].

Experimental evaluation of these hydrodynamic phenomena often requires specialized laboratory equipment and controlled operating conditions, limiting the detailed visualization of internal flow behaviour in academic environments. In this context, Computational Fluid Dynamics (CFD) has become an important engineering tool for predicting pressure distribution, velocity fields, turbulence development, and localized energy losses in industrial flow systems [1].

This work applies CFD simulations to investigate flow behaviour and pressure distribution in a Venturi tube, a gate valve, and a 90° elbow under laminar and turbulent flow regimes. The numerical models were developed based on literature studies reported by Perumal and Ganesan [2], Esteves and Cristianini [3], and Tang et al. [4]. In addition to its educational application, the study focuses on hydraulic behaviour and pressure-loss mechanisms commonly encountered in industrial piping systems and process engineering operations.

Modeling Methodology

CFD simulations were performed in ANSYS® Fluent to analyse flow behaviour and localized pressure losses in a Venturi tube, a gate valve, and a 90° elbow. The geometries were developed in ANSYS® DesignModeler using dimensions and operating conditions obtained from literature studies and industrial specifications.

For the numerical discretization, different mesh strategies were applied according to each geometry. A structured hexahedral mesh with 191,964 elements was used for the Venturi

tube, while refined tetrahedral meshes were generated for the 90° elbow (222,055 elements) and the gate valve (108,095–109,577 elements depending on the valve opening). Fig. 1 presents the computational meshes used in the simulations.

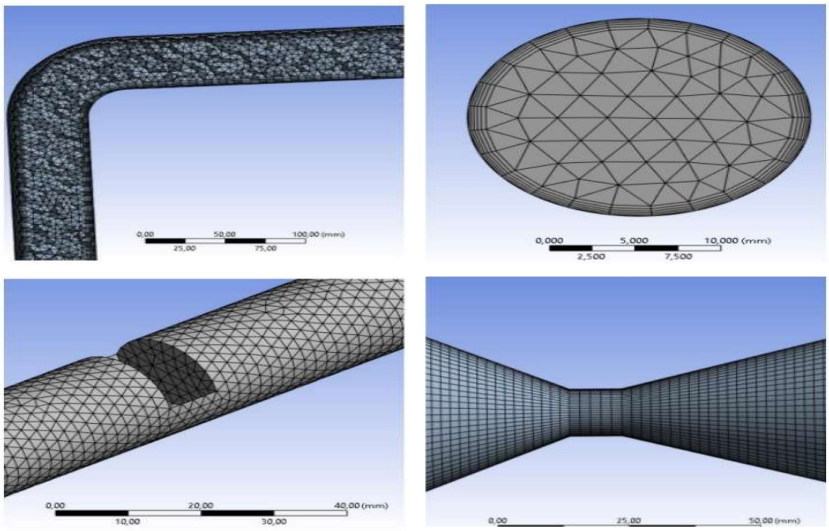

Figure 1: View of the computational meshes of the analyzed geometries.

Steady-state simulations were carried out under laminar and turbulent flow conditions to evaluate pressure distribution, velocity profiles, and recirculation zones. The numerical results were validated by comparing the calculated minor loss coefficients (k-values) with literature data reported for each hydraulic component [2–4].

Results and discussion

The CFD simulations successfully reproduced the hydrodynamic behaviour and pressure-loss trends reported in the literature, showing deviations below 15% for the calculated minor loss coefficients (k-values). The numerical results allowed the visualization of velocity fields, pressure contours, and recirculation regions under different flow regimes.

For the 90° elbow, significant pressure gradients were observed due to the change in flow direction. Higher pressure regions developed along the outer wall of the elbow, while lower pressure zones appeared near the inner radius. Velocity contours also revealed stagnation regions under laminar flow conditions, as shown in Fig. 2.

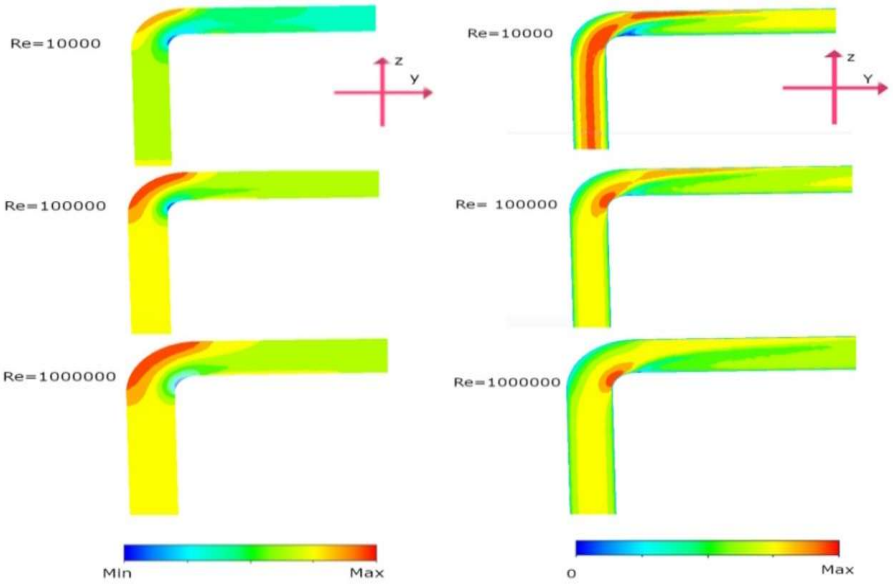

Figure 2: Pressure contour (left) and velocity contour (right) for the 90° elbow in different Reynolds numbers.

In the gate valve simulations, the reduction of the opening ratio increased flow acceleration and generated recirculation zones downstream of the restriction. These effects became more pronounced at higher Reynolds numbers, producing larger pressure losses and localized turbulence regions. The streamline behavior for both valve openings is presented in Fig. 3.

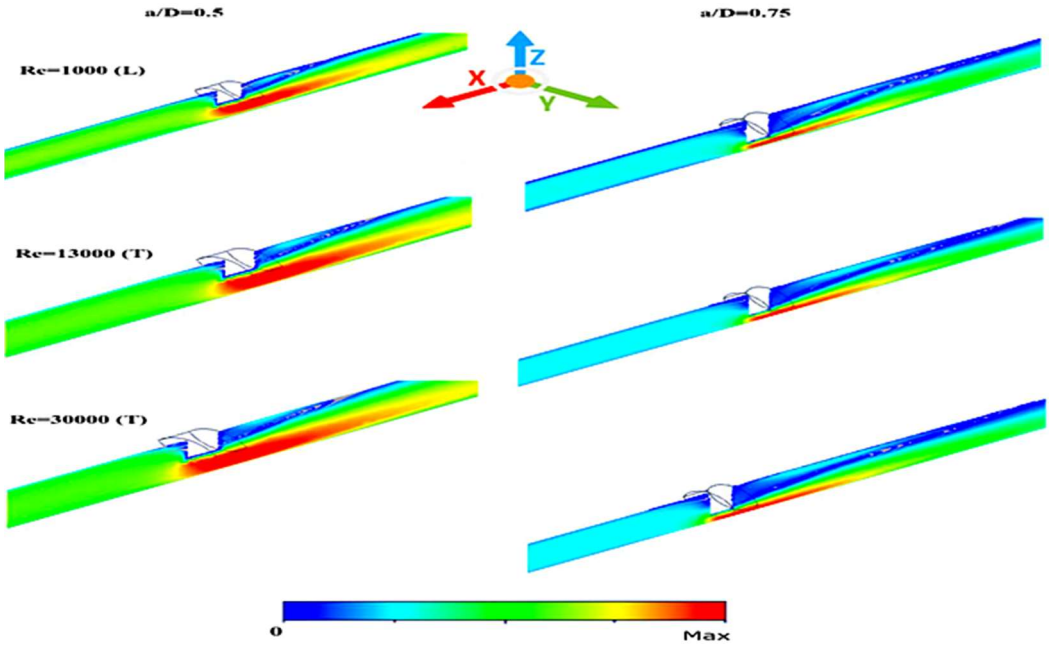

Figure 3: Streamlines for the gate valve at a/D=0.5(left) and a/D=0.75 (right), in laminar (L) and turbulent (T) regimes.

The Venturi tube simulations showed a significant pressure decrease at the throat section caused by flow acceleration, followed by partial pressure recovery in the diffuser region. The obtained pressure contours were consistent with the Venturi flow behavior described by Tang et al. [4], as illustrated in Fig. 4.

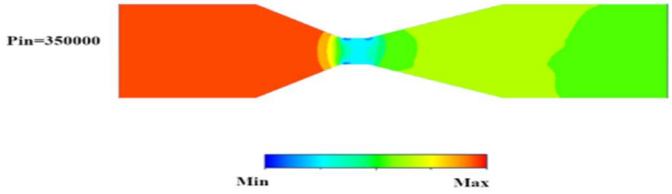

Figure 4: Pressure contour for the Venturi tube.

Summary

The present study demonstrated the applicability of CFD simulations for analysing hydraulic behaviour and localized pressure losses in common industrial flow components. The numerical models developed for the 90° elbow, gate valve, and Venturi tube successfully reproduced pressure distribution, flow acceleration, and recirculation effects under different flow regimes, showing good agreement with literature data.

The obtained results highlight the usefulness of CFD as both an engineering and educational tool for the visualization and interpretation of fluid dynamics phenomena. Furthermore, this work contributes to the integration of numerical simulation methodologies into undergraduate Chemical Engineering education through the development of a CFD-based learning guide using ANSYS® Fluent.

References

[1] Versteeg, H.K., Malalasekera, W., *An Introduction to Computational Fluid Dynamics: The Finite Volume Method*, 2nd ed., Pearson Education, 2007.

[2] Perumal, K., Ganesan, N., “CFD analysis of flow characteristics and pressure loss in pipe elbows under different Reynolds numbers,” *International Journal of Engineering Research*, 2016.

[3] Esteves, M., Cristianini, M., “Numerical analysis of flow behaviour in partially opened gate valves using CFD techniques,” *Journal of Applied Fluid Mechanics*, 2012.

[4] Tang, X. et al., “Numerical investigation of pressure distribution and flow behaviour in Venturi tubes,” *Flow Measurement and Instrumentation*, 2019.

Design of a Plant for the Production of 8000 t/year of Hydrogen by Methanol Steam Reforming

Salvia Frómesta Cuenca

Department of Chemical Engineering, University of Valladolid,
salvia.fromesta@estudiantes.uva.es

Introduction

Global energy demand has tripled over the last five decades, with fossil fuels still accounting for over 80% of total consumption. In 2023, greenhouse gas (GHG) emissions from the energy sector exceeded 40 $GtCO_2eq$ for the first time, intensifying the need for a rapid transition towards cleaner energy systems. In this context, green hydrogen has emerged as a key energy vector for the decarbonisation of hard-to-abate sectors such as heavy transport, steelmaking and the chemical industry.

However, the direct use of hydrogen is limited by significant logistical challenges: its low volumetric energy density requires either cryogenic liquefaction (at -253 °C) or high-pressure compression for storage and transport, and the existing pipeline infrastructure (currently ~5,000 km globally) falls far short of the ~45,000 km estimated to be needed by 2035. Liquid energy carriers offer an attractive alternative for the large-scale transport of renewable energy.

Methanol (CH_3OH) stands out among these carriers due to its compatibility with existing infrastructure, its ease of storage and transport at ambient conditions (20 °C, 1 atm), and the maturity of its synthesis and reforming technologies. Methanol steam reforming (MSR) allows hydrogen to be recovered at moderate temperatures (230–300 °C), generating low CO concentrations, which makes it particularly well-suited for integration with PEM fuel cells. Furthermore, the CO_2 released during reforming can be captured and recycled to produce new methanol, closing the carbon cycle.

This work presents the techno-economic design of a plant producing 8,000 t/year of hydrogen via MSR, with CO_2 capture using monoethanolamine (MEA) absorption. High-pressure technology plays a central role in the process: a three-stage compressor raises the reformed gas stream to 21.1 bar before feeding a Pressure Swing Adsorption (PSA) unit that delivers 99.99 %mol pure hydrogen.

Process Description and High-Pressure Operations

The plant operates 8,000 hours per year and is located at the Port of Hamburg, Germany — a strategic hub for hydrogen import and distribution, aligned with Germany's National Hydrogen Import Strategy. The process is divided into two main zones: reaction and separation/purification.

Reaction zone. A methanol stream (5,868 kg/h, 35 °C, 1.5 bar) is mixed with water in a molar ratio of 1.3 (H_2O/CH_3OH) and preheated to 250 °C before entering the fixed-bed plug-flow reactor (100-R-101). This multitubular reactor contains 2,020 tubes (12 m length, 2 cm diameter) packed with 3,200 kg of commercial $Cu/ZnO/Al_2O_3$ catalyst (BASF K3-110). The reactor operates at 250 °C and approximately 2.4 bar, conditions selected through sensitivity analysis performed in Aspen Plus V14 using the Langmuir–Hinshelwood kinetic model of Peppley et al. (1999). The three main reactions considered are methanol steam reforming (MSR), methanol decomposition (MD), and water-gas shift (WGS):

$$CH_3OH + H_2O \rightleftharpoons CO_2 + 3H_2 \quad \Delta H_{298}K = +49.47 \text{ kJ/mol (MSR)}$$

$$CH_3OH \rightleftharpoons CO + 2H_2 \quad \Delta H_{298}K = +90.60 \text{ kJ/mol (MD)}$$

$$CO + H_2O \rightleftharpoons CO_2 + H_2 \quad \Delta H_{298}K = -41.17 \text{ kJ/mol (WGS)}$$

Under the selected conditions, methanol conversion reaches 98.35% with H_2 selectivity of 74.9% and CO selectivity of only 0.58%, meeting the stringent purity requirements of downstream fuel cell applications. The reactor outlet (250 °C) is cooled through a train of heat exchangers and an air cooler to 30 °C before entering the first absorption column.

CO_2 capture (MEA absorption). The cooled syngas (72.65% H_2, 24.01% CO_2, 0.31% CO, 2.97% H_2O, 0.06% methanol, by mol) feeds the base of a 29-stage CO_2 absorber (100-T-102) operating at 30 °C and 1.5 bar. An aqueous MEA solution (37% w/w, 164,500 kg/h) selectively absorbs the CO_2 with a capture efficiency above 90%. The CO_2-rich amine is regenerated in a 29-stage desorber (100-T-103), producing a CO_2 stream of 95.03 %mol purity at 2 bar and 45 °C, ready for liquefaction or recompression.

High-pressure compression and PSA — central to this course. The hydrogen-rich gas leaving the absorber (92.6% H_2, 1,955 kg/h, 1.5 bar) is compressed in a three-stage centrifugal compressor (100-C-101 A/B/C) with an individual compression ratio of 2.6 per stage, raising pressure from 1.5 bar to 21.1 bar. Inter-stage coolers (100-E-108 and 100-E-109) reduce the temperature back to 35 °C between stages, and knock-out drums (100-

D-106 and 100-D-107) remove condensed liquid before each stage. This multi-stage compression strategy minimises compression work while protecting equipment integrity.

The compressed stream (1,263 kg/h, 99.01 %mol H_2, 21.1 bar) feeds the Pressure Swing Adsorption unit (100-PSA-101), where adsorption and desorption cycles at high pressure selectively remove residual CO_2, CO, water and methanol impurities, yielding 1,000 kg/h of product hydrogen at 99.99 %mol purity and 20.8 bar — fully compliant with ISO 14687:2019 specifications for fuel cell applications.

Tab. 1.: Key design and operating parameters of the hydrogen production plant.

Parameter	Value	Unit
Reactor temperature	250	°C
Reactor pressure	2.4	bar
Water/methanol molar ratio	1.3	mol/mol
Catalyst mass ($Cu/ZnO/Al_2O_3$)	3,200	kg
Methanol conversion	98.35	%
H_2 selectivity	74.9	%
Compressor outlet pressure (PSA feed)	21.1	bar
H_2 product purity (PSA outlet)	99.99	%mol

Sensitivity analysis. **Temperature:** methanol conversion increases progressively up to 250 °C, after which no significant improvement is observed, while CO selectivity increases continuously. **Pressure:** higher pressure markedly reduces methanol conversion; 2.4 bar was selected as the optimal trade-off minimising operating costs while maintaining acceptable CO selectivity. **Catalyst mass:** 3,200 kg ensures conversion above 98% without unnecessary over-sizing. **Water/methanol ratio:** 1.3 mol/mol maximises conversion and strongly suppresses CO formation, improving the downstream purification performance.

Summary

A techno-economic design study of an 8,000 t/year hydrogen production plant via methanol steam reforming has been presented. The process integrates a fixed-bed catalytic reactor, a MEA-based CO_2 capture unit, and — critically for high-pressure technology — a three-stage compressor train and a PSA unit operating at up to 21.1 bar to deliver 99.99 %mol pure hydrogen compliant with ISO 14687:2019. The main results are summarised in Table 2.

Tab. 2.: Summary of key performance and economic indicators.

Indicator	Value
Annual H_2 production	8,000 t/year
Annual methanol consumption	46,948 t/year
CO_2 captured	64,400 t/year
Energy intensity	8.79 MJ/kg H_2
GHG emissions	0.54 kgCO_2eq/kg H_2
Total investment (CAPEX)	€31.5 million
Annual operating costs (OPEX)	~€92 million/year
Break-even H_2 price (NPV = 0)	€12/kg (IRR = 2%)

The economic analysis shows that project viability strongly depends on the hydrogen selling price and the cost of green methanol (which accounts for over 35% of OPEX). At a price of €12/kg H_2, the project reaches break-even (NPV = 0, IRR = 2%). Sensitivity analysis indicates that revenues are the primary driver of profitability, followed by OPEX, while the impact of CAPEX is comparatively minor. European funding instruments (H2Global, IPCEI, Klimaschutzverträge) and the expected reduction in green methanol costs as renewable energy scales up could significantly improve future project economics.

From an environmental perspective, the plant achieves an energy intensity of 8.79 MJ/kg H_2 and specific emissions of 0.54 kgCO_2eq/kg H_2, reflecting the current reliance on natural gas for thermal energy supply. Future integration of renewable heat sources or electrification of heating demand would further reduce the carbon footprint of the process.

Acknowledgment

The author wishes to thank Dr. Luis Vaquerizo Martín (Department of Chemical Engineering and Environmental Technology, University of Valladolid) for his supervision and guidance throughout the development of this Final Degree Project.

References

[1] Peppley, B.A., Amphlett, J.C., Kearns, L.M., Mann, R.F. (1999). Methanol-steam reforming on Cu/ZnO/Al_2O_3 catalysts. Part 1: The reaction network. Applied Catalysis A: General, 179(1–2), 21–29.

[2] International Energy Agency (2024). Global Hydrogen Review 2024. IEA, Paris.

[3] Ong, C.W., Lin, J.X., Tsai, M.L., Thoe, K.S., Chen, C.L. (2024). Techno-economic and carbon emission analyses of a methanol-based international renewable energy supply chain. International Journal of Hydrogen Energy, 49, 1572–1585.

[4] ISO 14687:2019. Hydrogen fuel quality — Product specification. International Organization for Standardization.

[5] Lin, J.X., Wang, W.J., Yu, B.Y., Ong, C.W., Chen, C.L. (2024). Intensification of the CO_2-capturing methanol steam reforming process. Separation and Purification Technology, 347, 127612.

[6] Energy Institute (2024). Statistical Review of World Energy 2024. Energy Institute, London.

Preparation of Biocompatible PCL/PLA Scaffolds Reinforced with Chitosan Aerogels

Marko Pavlović, Milica Pantić, Zoran Novak

Faculty of Chemistry and Chemical Engineering, University of Maribor, Slovenia, zoran.novak@um.si

Introduction

The term tissue engineering was established in 1987; nonetheless, there are accounts of humans using skin grafts in 3000 BCE India. This shows that contemporary aspirations to repair injuries or replace the function of a failing organ with artificial tissues are far from new [1]. Most of the cells in the human body (excluding blood cells) are anchored inside a matrix called the extracellular matrix (ECM). Among its many functions, the ECM primarily provides structural and cell-adhesion support, secondly supplies bioactive cues, and finally degrades in response to cell growth and tissue development. Native ECM is the most suitable option, yet it is extremely rare and complex; therefore the contemporary concept of scaffolding in tissue engineering is to mimic its function [2].

The scaffold must be made from a non-toxic and biocompatible material suitable for cell proliferation and propagation. Various biopolymers, including polysaccharides such as chitosan, alginate, chitin, gellan gum and their derivatives, have been used clinically for tissue engineering [3]. Chitosan is a commercially available material derived from the natural polymer chitin, and possesses stability, suitable chemical properties, and biocompatibility [4].

In the past couple of decades, bio-based aerogels have been widely researched for biomedical applications due to their unique and tunable properties [5]. These advanced nanostructured materials, which have high mesoporosity and low density, and are obtained through supercritical CO_2 drying, are appropriate candidates for tissue engineering [6]. Nonetheless, designing pores in scaffolds remains the most significant challenge, as their influence on crucial parameters is evident. At the molecular level, adequate free volume enables biomaterial swelling and mechanical behaviour, while the presence of micro- and macropores provides cell binding sites and allows cellular infiltration, respectively [7]. Supercritical foams provide the precise open-cell macroporous architecture that aerogels lack. As with aerogels, using supercritical CO_2 as the foaming agent provides a non-toxic scaffold compared to other foaming agents [8].

Polycaprolactone (PCL) has attracted considerable interest in biomedical applications because of its biocompatibility and slow degradation profile. However, its inherent hydrophobicity, can be reduced by incorporating naturally derived materials, such as aerogels [9]. PCL has a low glass transition and melting temperature, of -50 °C and 60 °C, respectively [10]. It has high flexibility and a relatively low compressive modulus of 18.7 MPa. It is regarded as a soft and hard tissue compatible biodegradable material with long degradability (24 months). Studies have shown that blending PCL with poly (lactic acid) (PLA) improves its compressive strength tenfold. PLA is brittle, rigid and has high tensile strength; it is one of the most popular biodegradable polymers. Its high strength and rapid biodegradability make it an ideal candidate for melt blending with PCL [10-13].

The aim of this study was to prepare biodegradable PCL/PLA scaffolds for cell seeding, designed to support cell attachment and growth. Pre-synthesized chitosan aerogels were incorporated into PCL/PLA melt blends. Supercritical CO_2 foaming was used to create interconnected open-cell scaffolds containing chitosan aerogels. The combination of aerogels with foamed biodegradable polymer blends was expected to enhance both scaffold porosity and mechanical performance. The textural properties, morphology, and surface characteristics of the resulting scaffolds were evaluated using N_2 adsorption-desorption analysis and SEM.

Experimental

Chitosan aerogels were prepared via a physical sol-gel process induced by alkaline neutralisation, using a modified version of a previously reported method [14]. A homogeneous 2 wt.% chitosan solution was prepared by dissolving 3 g of chitosan powder in 150 mL of 0.1 M acetic acid under continuous stirring overnight at room temperature. The viscous chitosan solution was poured into a Petri dish to obtain hydrogels of uniform thickness. Gelation was induced by pouring a 3 M ethanolic NaOH solution over the chitosan sol. The system was then sealed and left overnight at room temperature to complete gel formation and ageing. Obtained alcogels were subsequently subjected to solvent exchange with fresh ethanol daily for four days to remove residual NaOH before drying. The alcogels were cut into rectangular shapes and dried using supercritical CO_2 under conditions of 40±1 °C and 120±10 bar at 200-300L/h of CO_2 flow (determined at 0.984 bar and 23°C) constantly for 6 hours. The obtained chitosan aerogels, initially in monolithic form, were subsequently powdered into particles to enable their incorporation into the polymer foams, as shown in Fig. 1.

The preparation of three different materials followed pure PCL foam, PCL/PLA foam, and PCL/PLA scaffolds containing 20 wt% powdered chitosan aerogel particles (PCL/PLA scaffold_20%A) were successfully obtained. PCL/PLA blends were prepared by melt blending. The weight ratio of PCL to PLA was 4:1. Blending was carried out by manually melt mixing the polymers in a stainless steel vessel. The PCL and PLA pellets were heated above their melting temperatures, and mixed until a homogeneous melt was obtained. The mixture was then shaped into a spherical shape and placed into a metal cylinder, which served as a mould. The mould was inserted into a high-pressure autoclave, heated to 70 °C, and pressurised with CO_2 to 200 bar. The polymer blend was left to saturate in CO_2 for 3 hours, after which the autoclave was depressurised by fully opening the valve and dropping the pressure within 5 seconds.

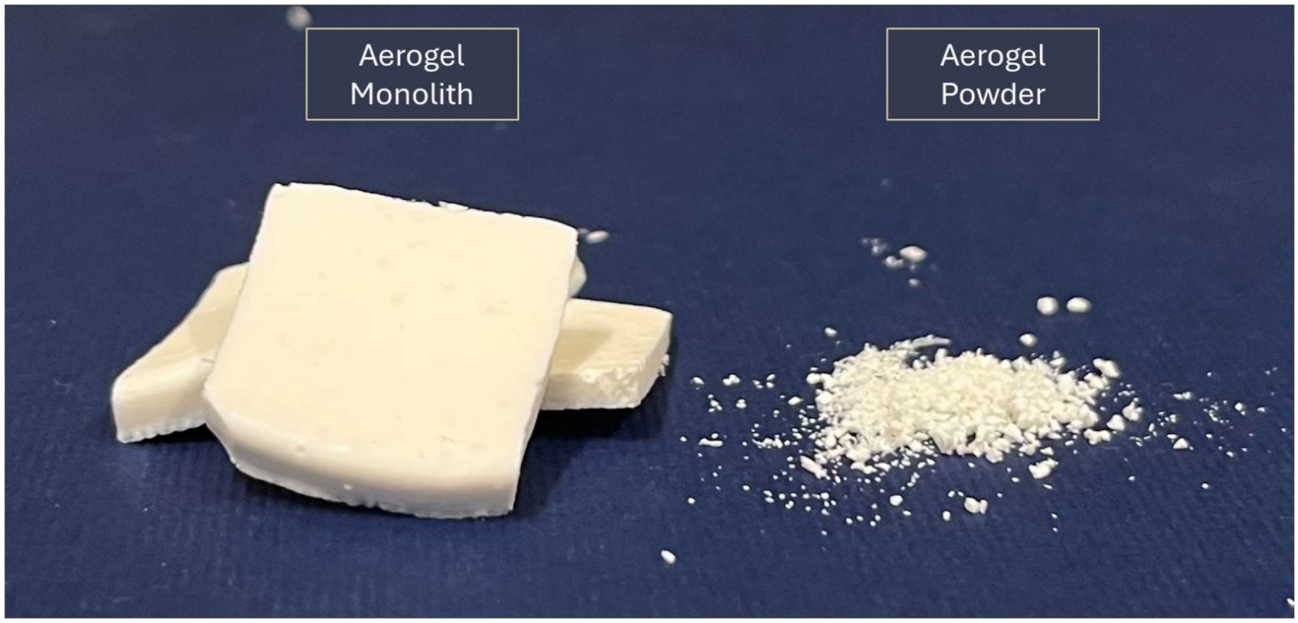

Figure 1: Chitosan aerogels: monolith (left), powdered aerogel particles (right).

The prepared scaffolds were characterized by N_2 adsorption desorption analysis on the ASAP 2020MP instrument (micromeritics, Norcross, GA, USA). Before the analysis, the samples were degassed under vacuum at 50 °C for 1000 min until a stable pressure was achieved. The specific surface area was calculated using the Brunauer-Emmett-Teller (BET) model. The structural properties were investigated by a two-beam microscope, SEM/Ga-FIB FEI Helios NanoLab TM 600i (FEI, Thermo Fisher Scientific). The preparation of the samples encompassed fractionation and splatter-coating with gold particles.

Results

Polymer foams and scaffolds were successfully prepared, with the successful incorporation of the chitosan aerogel particles. Representative images of the resulting materials are shown in Figure 2. It can be seen that the PCL foam is denser in the bottom but more porous in the top. This can be attributed to the foaming temperature exceeding the melting point of PCL. Namely, during depressurisation and the time taken for cylinder to cool below the melting point of PCL, the bottom part of the foam collapsed on itself. The PCL/PLA foam made from a blend of PCL and PLA, is homogeneously foamed, and has taken the shape of the mould. Lastly, PCL/PLA scaffold contains chitosan aerogel particles both inside and outside. The irregular shape can be attributed to the foam not adhering to the mould walls, which allowed it to expand beyond the mould boundaries.

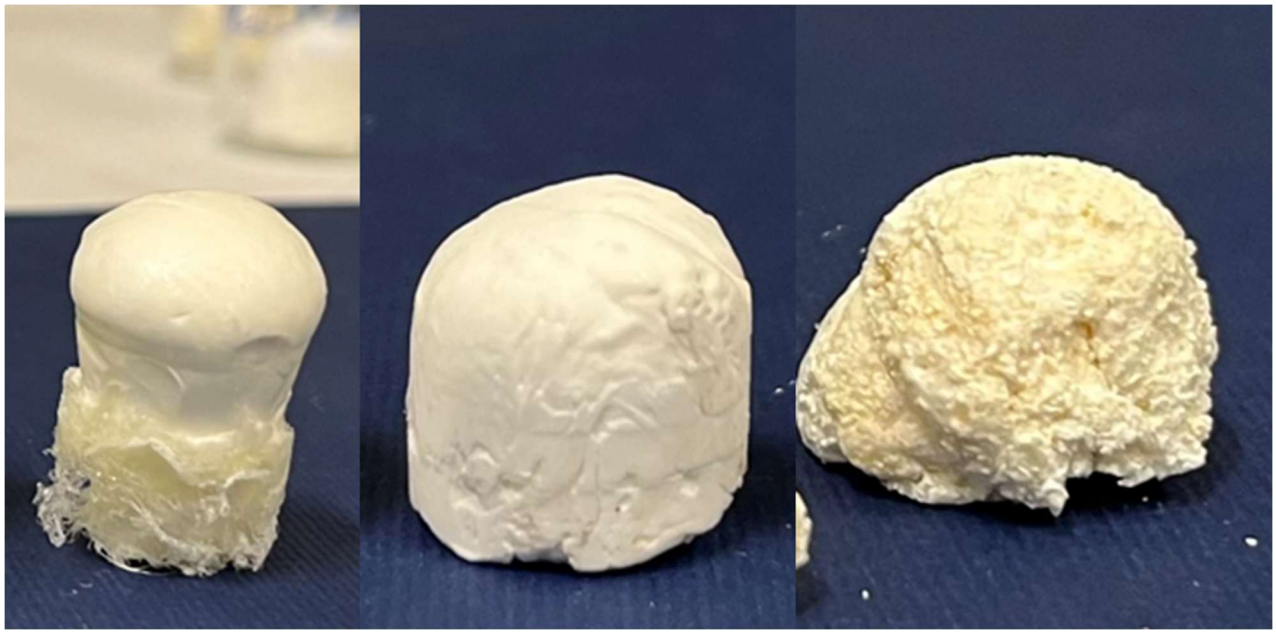

Figure 2: From left: PCL foam, PCL/PLA foam, PCL/PLA scaffold_20%A

Measured specific surface areas of the scaffolds using N_2 adsorption-desorption analysis are shown in

Table 1.

Table 1: Specific surface areas of prepared foams and scaffolds

Sample	S_{BET}, m^2/g
PCL foam	0.45±0.07
PCL/PLA foam	1.38±0.18
PCL/PLA scaffold _20%A	13.00±0.36
aerogel monolith	371±6
aerogel powder	352±5

First, the PCL and PCL/PLA foams showed very low specific surface areas. This phenomenon can be ascribed to their mostly macroporous structure, which is not effectively detected by N_2 physisorption analysis. In contrast, the PCL/PLA foam containing chitosan aerogel particles exhibited a specific surface area of 13 m^2/g. The addition of chitosan aerogels led to enrichment of the overall mesoporous structure of the final scaffold. This was expected since chitosan aerogels are well-known for their mesoporous structures [14]. The chitosan aerogels themselves possess surface areas of 352 and 371 m^2/g in particle and monolith form, respectively. The specific surface area of the chitosan aerogels was not significantly altered by their conversion from monolithic form to particles. This indicates that prepared aerogels possess a strong, well-developed, and mechanically stable porous network that is not easily disrupted. Figure 3 shows adsorption-desorption type IV isotherms for the scaffold and blend foam containing aerogel particles and aerogels in particle and monolith form. The type and shape of the adsorption isotherms indicate a predominantly mesoporous structure in the chitosan aerogels and a partially mesoporous structure in the PCL/PLA foam containing chitosan aerogel particles. The significantly higher adsorption capacities observed for the aerogels (both monolith and particle forms) compared to the PCL/PLA scaffold suggest a lower contribution from mesopores in the scaffold. This finding was expected, considering that the aerogel content in the composite foams was 20 wt%, resulting in a lower overall fraction of mesoporous part.

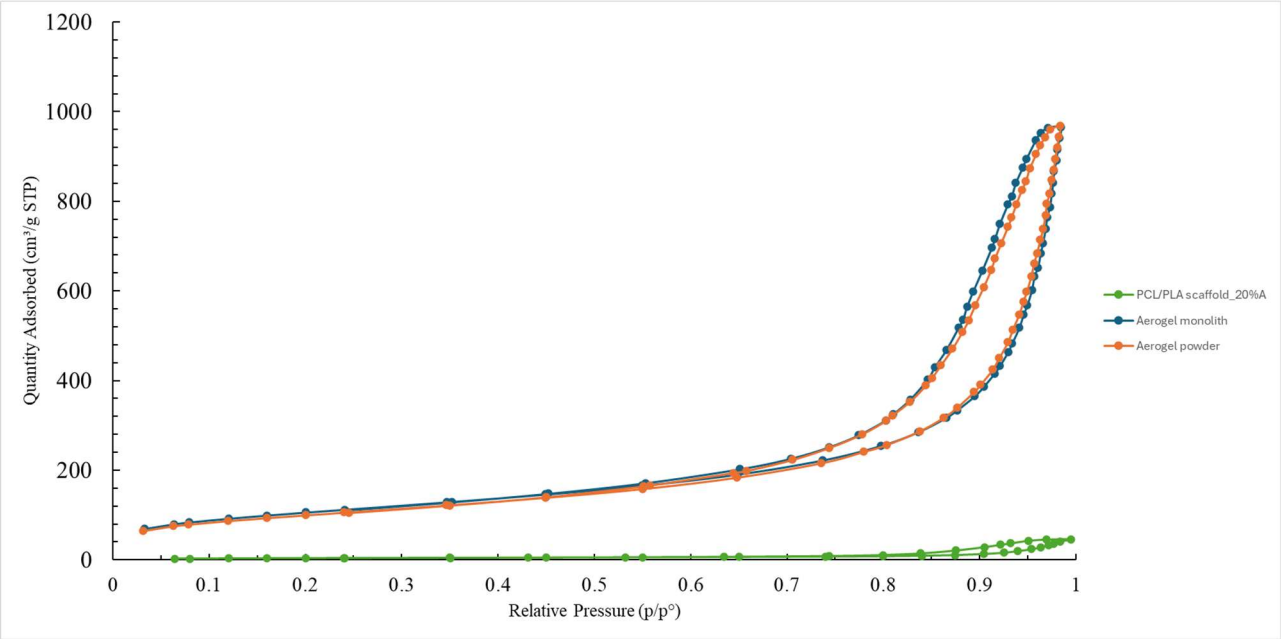

Figure 3: Adsorption isotherms for the PCL/PLA scaffold and chitosan aerogels in monolith and powder form

The morphology of the prepared foams and scaffolds was evaluated using SEM micrographs, as shown in Figure 4. The PCL foams (top images) exhibited a porous, interconnected structure with relatively smooth pore walls formed during the supercritical foaming process. The PCL/PLA foams (middle images) also showed a porous morphology; however, the structure appeared more irregular and compact compared to the pure PCL foams.

In contrast, PCL/PLA scaffolds containing chitosan aerogel particles (bottom images) displayed a rougher and more heterogeneous morphology. The incorporated aerogel particles were visible within the scaffold structure and introduced finer porous features alongside the larger macropores formed during foaming. The presence of these smaller pores is consistent with the mesoporous nature of the chitosan aerogels and correlates with the results obtained by N_2 adsorption-desorption analysis observed for the scaffolds.

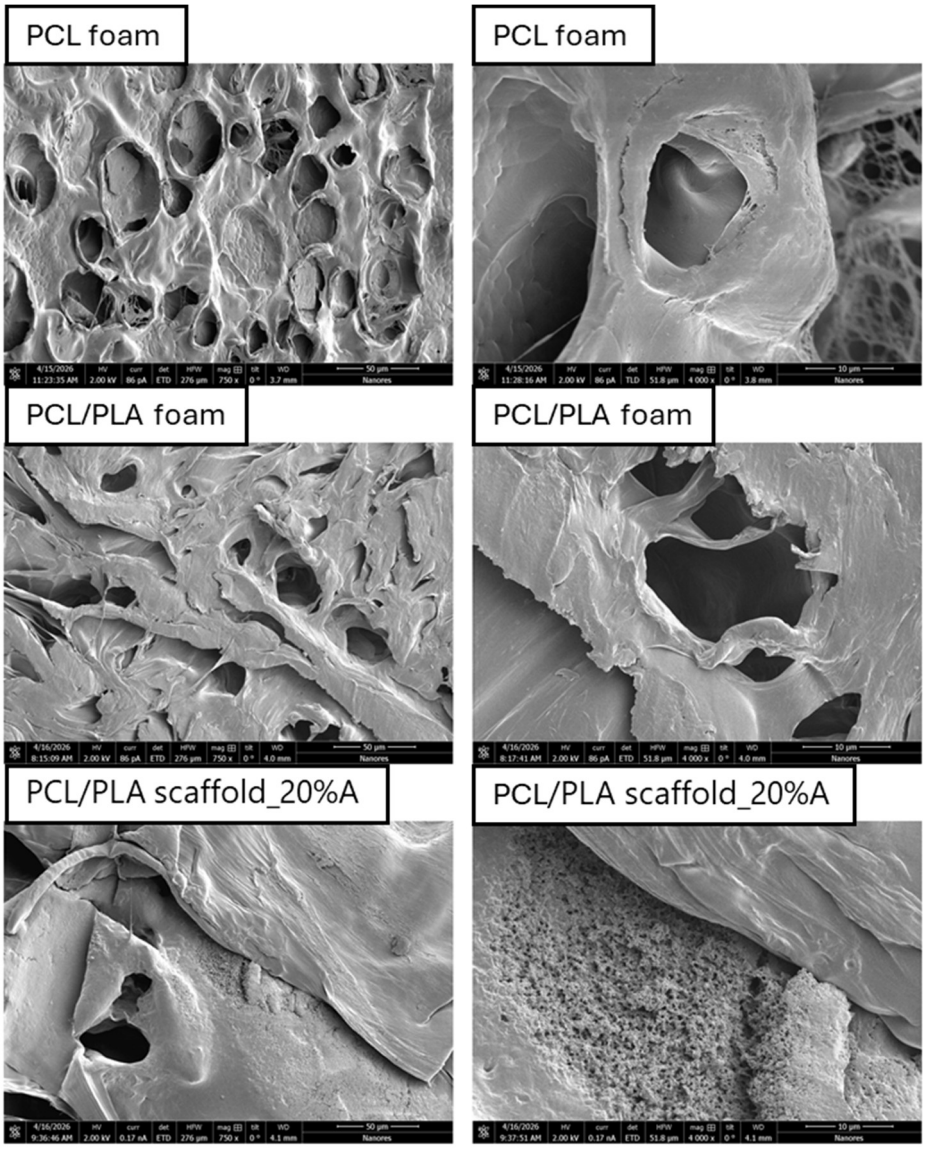

Figure 4: SEM micrographs of PCL foam, PCL/PLA foam, and PCL/PLA scaffold_20%A.

Summary

Biodegradable PCL/PLA scaffolds containing chitosan aerogel particles were successfully prepared using supercritical CO_2 foaming. Incorporating mesoporous aerogels into macroporous polymer foams led to scaffolds with increased specific surface area and adsorption capacities and more complex pore morphology. N_2 adsorption-desorption analysis showed a measurable surface area of 13 m^2/g for the aerogel-containing scaffold, while SEM analysis confirmed the formation of interconnected porous structures. The combination of PCL, PLA, and chitosan aerogels shows great potential for preparing porous biomaterials suitable for tissue engineering applications.

References

[1] F. Berthiaume, T. J. Maguire, in M. L. Yarmush, »Tissue Engineering and Regenerative Medicine: History, Progress, and Challenges«, *Annu. Rev. Chem. Biomol. Eng.*, let. 2, št. 1, str. 403–430, jul. 2011, doi: 10.1146/annurev-chembioeng-061010-114257.

[2] B. P. Chan in K. W. Leong, »Scaffolding in tissue engineering: general approaches and tissue-specific considerations«, *Eur Spine J*, let. 17, št. S4, str. 467–479, dec. 2008, doi: 10.1007/s00586-008-0745-3.

[3] J. F. Mano *idr.*, »Natural origin biodegradable systems in tissue engineering and regenerative medicine: present status and some moving trends«, *J. R. Soc. Interface.*, let. 4, št. 17, str. 999–1030, dec. 2007, doi: 10.1098/rsif.2007.0220.

[4] M. R. Ayers in A. J. Hunt, »Synthesis and properties of chitosan–silica hybrid aerogels«, *Journal of Non-Crystalline Solids*, let. 285, št. 1–3, str. 123–127, jun. 2001, doi: 10.1016/S0022-3093(01)00442-2.

[5] M. V. Reyes-Peces *idr.*, »Chitosan-GPTMS-Silica Hybrid Mesoporous Aerogels for Bone Tissue Engineering«, *Polymers*, let. 12, št. 11, str. 2723, nov. 2020, doi: 10.3390/polym12112723.

[6] A. Iglesias-Mejuto in C. A. García-González, »3D-Printed, Dual Crosslinked and Sterile Aerogel Scaffolds for Bone Tissue Engineering«, *Polymers*, let. 14, št. 6, str. 1211, mar. 2022, doi: 10.3390/polym14061211.

[7] G. D. Mahumane, P. Kumar, L. C. Du Toit, Y. E. Choonara, in V. Pillay, »3D scaffolds for brain tissue regeneration: architectural challenges«, *Biomater. Sci.*, let. 6, št. 11, str. 2812–2837, 2018, doi: 10.1039/C8BM00422F.

[8] S. Sun *idr.*, »Preparation of highly interconnected porous poly(ε-caprolactone)/poly(lactic acid) scaffolds via supercritical foaming«, *Polymers for Advanced Technologies*, let. 29, št. 12, str. 3065–3074, 2018, doi: 10.1002/pat.4427.

[9] I. Manavitehrani, A. Fathi, H. Badr, S. Daly, A. Negahi Shirazi, in F. Dehghani, »Biomedical Applications of Biodegradable Polyesters«, *Polymers (Basel)*, let. 8, št. 1, str. 20, jan. 2016, doi: 10.3390/polym8010020.

[10] F. Rezgui, M. Swistek, J. M. Hiver, C. G'Sell, in T. Sadoun, »Deformation and damage upon stretching of degradable polymers (PLA and PCL)«, *Polymer*, let. 46, št. 18, str. 7370–7385, avg. 2005, doi: 10.1016/j.polymer.2005.03.116.

[11] S. Wachirahuttapong, C. Thongpin, in N. Sombatsompop, »Effect of PCL and Compatibility Contents on the Morphology, Crystallization and Mechanical Properties of PLA/PCL Blends«, *Energy Procedia*, let. 89, str. 198–206, jun. 2016, doi: 10.1016/j.egypro.2016.05.026.

[12] A. Ostafinska, I. Fortelny, M. Nevoralova, J. Hodan, J. Kredatusova, in M. Slouf, »Synergistic effects in mechanical properties of PLA/PCL blends with optimized composition, processing, and morphology«, *RSC Adv.*, let. 5, št. 120, str. 98971–98982, 2015, doi: 10.1039/C5RA21178F.

[13] T. Patrício, M. Domingos, A. Gloria, U. D'Amora, J. F. Coelho, in P. J. Bártolo, »Fabrication and characterisation of PCL and PCL/PLA scaffolds for tissue engineering«, *Rapid Prototyping Journal*, let. 20, št. 2, str. 145–156, mar. 2014, doi: 10.1108/RPJ-04-2012-0037.

[14] M. Pantić *idr.*, »Evaluation of ethanol-induced chitosan aerogels with human osteoblast cells«, *International Journal of Biological Macromolecules*, let. 253, str. 126694, dec. 2023, doi: 10.1016/j.ijbiomac.2023.126694.

Pilot-Scale Biorefinery Processing of Wheat Straw for the Recovery of a Lignin-Rich Fraction

Ushe Mutamba

Institute of Thermal Separation Processes, Hamburg University of Technology
ushe.mutamba@tuhh.de

Introduction

Lignocellulosic biorefining relies heavily on efficient, low-emission fractionation technologies to separate biomass into cellulose, hemicellulose, and lignin matrices [1]. Among these, the aromatic framework of lignin represents a highly valuable precursor for advanced bio-based applications, including technical resins, functional coatings, and carbon-based materials. However, isolating high-purity lignin requires overcoming the highly recalcitrant, cross-linked lignocellulosic matrix in which it is naturally embedded.

To address this challenge, high-pressure hydrothermal pretreatment, specifically subcritical liquid hot water (LHW) processing offers a highly attractive, chemical-free pathway. By utilizing water at elevated temperatures (180–220 °C) under a controlled overpressure of approximately 50 bar to maintain the liquid phase, the autoionization of water is drastically altered. The resulting increase in the ionic product (K_w), together with acetic acid released from hemicellulose, promotes acid-catalysed hydrolysis thereby solubilizing the hemicellulose fraction without requiring supplementary chemical agents.

Despite these advantages, the industrial viability of high-pressure hydrothermal processing is constrained by the substantial energy demands required to heat, pressurize, and maintain the reaction medium at target conditions [2]. Excessive water consumption can furthermore dilute downstream product streams and increase capital equipment footprint. Consequently, precise thermodynamic and kinetic optimization is required to maximize lignin recovery while minimizing thermal and mechanical energy expenditure [3]. This work investigates the dynamics of high-pressure hydrothermal pretreatment using a 50 L pilot plant (Figure 1), assessing its efficiency within an integrated biorefinery pathway.

Figure 1: Pretreatment pilot plant for hydrothermal pretreatment

Experimental

The high-pressure hydrothermal pretreatment stage is conducted utilizing a dedicated pilot-scale plant engineered for subcritical fluid operations. In this process, the reaction medium is pressurized to approximately 50 bar to suppress flashing and ensure a stable liquid phase at operating temperatures between 180 °C and 220 °C for a specific residence time.

Prior to high-pressure charging, the wheat straw feedstock is washed to remove surface inorganic particulate matter and mineral residues. The biomass is subsequently packed into a specialized cartridge and sealed within a 50 L heavy-wall autoclave. Upon sealing, the system is pressurized, and subcritical water at approximately 200 °C is injected into the reactor. Under these high-pressure hydrothermal conditions, the hemicellulose fraction undergoes partial depolymerization and dissolves into the liquid phase along with minor water-soluble lignin fractions. The resulting liquid stream comprises hemicellulose-derived oligosaccharides, while the remaining solid matrix becomes highly enriched in accessible cellulose and lignin. The comprehensive integrated process configuration is detailed in Figure 2.

The hydrothermally altered solid residue features an expanded pore structure, significantly reducing mass-transfer limitations for subsequent enzymatic hydrolysis. This pretreated solid is transferred to a 200 L continuously stirred tank reactor (CSTR) for enzymatic saccharification via cellulase complexes under controlled thermal and pH bounds. Cellulase action converts the cellulose fraction into monomeric glucose. The slurry is then

mechanically dewatered utilizing an industrial decanter centrifuge, partitioning the glucose-rich liquor from the solid, highly concentrated lignin-rich residue.

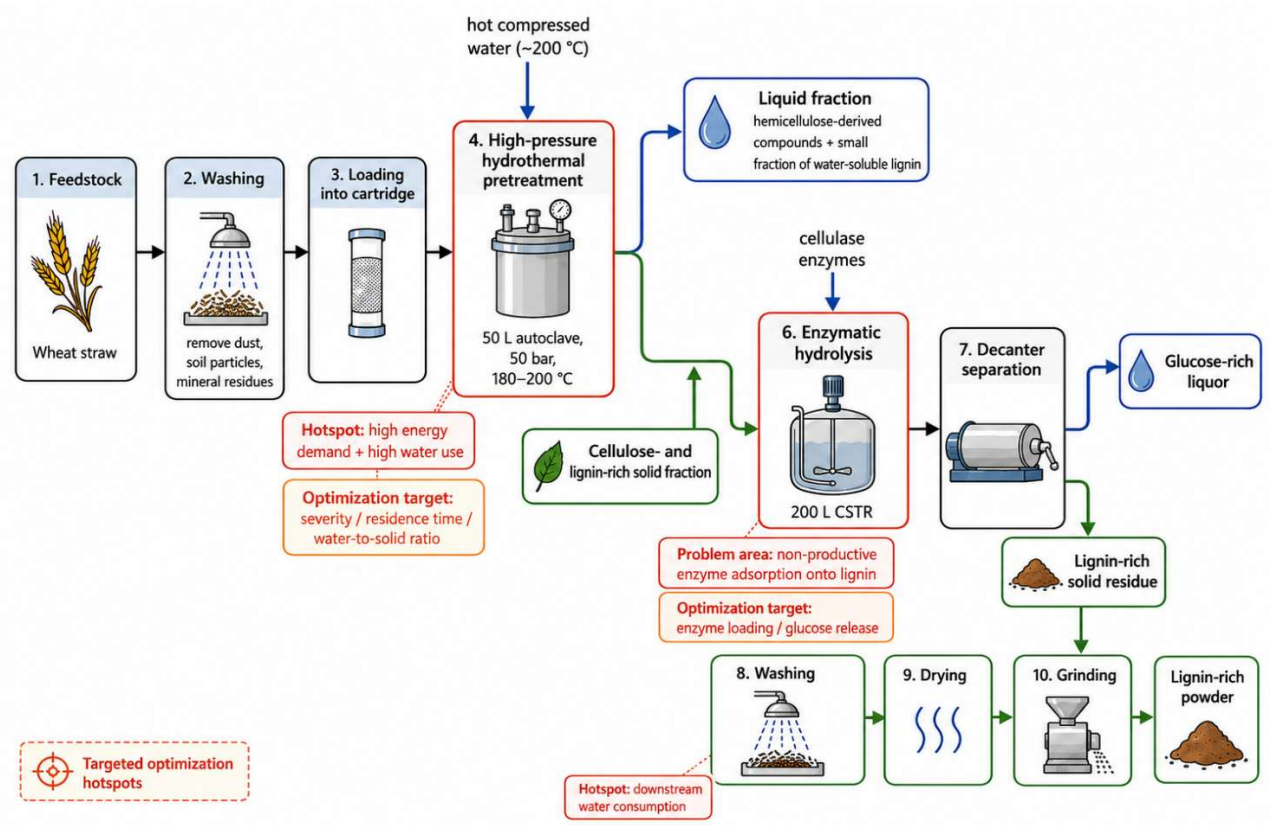

Figure 2: Experimental process route for lignin-rich fraction recovery from wheat straw, including high-pressure hydrothermal pretreatment, enzymatic hydrolysis, product separation, downstream lignin processing, and targeted optimisation hotspots.

To systematically evaluate the coupled impact of temperature and residence time during the high-pressure stage, the hydrothermal processing intensity is quantified using the semi-empirical severity factor (*Ro*):

$$R_0 = \log\left[t \cdot e^{\left(\frac{T-100}{14.75}\right)}\right]$$

where t represents the isothermal reaction time in minutes and T represents the processing temperature in °C.

The severity factor is utilized to establish the optimal processing window where hemicellulose solubilization and structural matrix opening are maximized, while minimizing the secondary degradation of carbohydrates into inhibitory compounds (e.g., furfural and HMF). Furthermore, the experimental design investigates how varying the high-pressure severity factor influences non-productive enzyme adsorption onto the remaining lignin surface, which can severely limit downstream hydrolysis kinetics and overall process throughput.

Summary

This work investigates an integrated high-pressure hydrothermal biorefinery route for producing a lignin-rich fraction from wheat straw. Sequential liquid hot water pretreatment and enzymatic hydrolysis are used to separate the biomass into hemicellulose-derived liquid products, glucose-rich liquor, and a lignin-rich solid residue. The process is evaluated by varying pretreatment severity and hydrolysis conditions to improve fractionation efficiency, minimise sugar degradation, and support lignin recovery. The main engineering challenges are the high thermal energy demand required to maintain pressurised water at reaction temperature and the water consumption associated with pretreatment and downstream washing. In addition, non-productive enzyme adsorption onto lignin is considered as a limitation during enzymatic hydrolysis. The generated pilot-scale process data provide a basis for identifying energy and water hotspots and supporting future scale-up of high-pressure lignocellulosic biorefineries.

Acknowledgement

The author gratefully acknowledges the United Nations University Hub on Engineering to Face Climate Change for supporting this research.

References

1. Saha, B. C.; Iten, L. B.; Cotta, M. A.; Wu, Y. V. Dilute acid pretreatment, enzymatic saccharification and fermentation of wheat straw to ethanol. Process Biochemistry, 2005, 40, 3693–3700.

2. Jimenez-Gutierrez, J. M.; Verlinden, R. A. J.; van der Meer, P. C.; van der Wielen, L. A. M.; Straathof, A. J. J. Liquid hot water pretreatment of lignocellulosic biomass at lab and pilot scale. Processes, 2021, 9, 1518.

3. Conrad, M.-J., 2023. Design of a continuous autohydrolysis pretreatment process of annual lignocellulose for industrial application. https://doi.org/10.15480/882.5105

Polycaprolactone Thermal History Effects on Foaming in Supercritical Carbon Dioxide

Zofia Wolny, Bartłomiej Kryszak, Konrad Szustakiewicz, Irena Žižović

Faculty of Chemistry, Wrocław University of Science and Technology,
zofia.wolny@pwr.edu.pl

Introduction

Supercritical carbon dioxide ($scCO_2$) foaming is a promising technique for producing advanced porous polymeric materials, with applications in fields such as tissue engineering [1] and active packaging [2]. In this technique, particular foam morphologies are typically achieved by varying processing parameters, but comparatively little work has been carried out on material properties and how they influence foaming. This is especially the case for semicrystalline polymers, which offer functional advantages but display more complex behaviour in $scCO_2$ than their amorphous counterparts [3]. Articles which consider crystallinity are sparse and often focus on the formation of microcellular structures [4] rather than the larger morphologies desirable for tissue engineering applications, where pore diameters of up to 400μm are optimal [5].

Polycaprolactone (PCL) is a biocompatible semicrystalline polymer which has been used for the fabrication of bone tissue scaffolds via numerous methods, including freeze-drying [6] and electrospinning [7]. Whereas these methods utilise organic solvents to dissolve the polymer before processing, the comparatively eco-friendly $scCO_2$ foaming technique does not require any organic solvent [8]. Instead, $scCO_2$ diffuses into the amorphous sections of the polymer and acts as a plasticiser; as a result, polymer crystals may still be present within the matrix if operating conditions are maintained below melting point of the polymer. This complicated relationship between processing conditions and crystal morphology poses an issue in designing consistent semicrystalline polymer foams, as crystals can affect scCO2 foaming in three major ways:

1) $ScCO_2$ sorption into the polymer matrix. Crystals act as physical barriers to CO_2 diffusion, slowing the rate of swelling.
2) Nucleation of pores. Pores may tend to nucleate preferentially at interfaces between the denser crystalline and less dense amorphous phases.

3) Growth of pores. Depending on the size and distribution of crystals within the plasticised, melt-like amorphous phase, the viscosity of the overall material may be different during pore growth.

It is hypothesized that by controlling crystallinity, the rate of sorption as well as pore nucleation and growth can be controlled, thereby providing another dimension for the optimisation of foam morphology.

This study explores the effects of thermal history on foaming of semicrystalline PCL in different $scCO_2$ conditions. PCL was submitted to 5 methods of thermal treatment to achieve various levels of crystallinity (45-60%). These samples were then foamed using 6 different $scCO_2$ foaming conditions and the effects on the resultant foams were studied.

This work suggests that thermal pretreatment of semicrystalline polymers is an important consideration when selecting conditions for foaming.

Experimental

PCL Preparation

PCL was prepared using 5 methods to obtain samples of varying crystallinity:

- As-received pellets from manufacturer
- Extruded onto air fan rack, followed by room temperature storage (ageing)
- Extruded onto air fan rack
- Extruded into water bath
- Extruded into liquid nitrogen bath

Extrusion was carried out in a co-rotating twin screw extruder at 100 RPM with temperature set at 100ºC across all zones. The extruded polymer was cooled immediately after exiting the die using the methods above, before being pelletised and stored in a freezer at -4ºC (except for the aged sample, which remained at room temperature). Crystallinity was confirmed via DSC.

PCL Foaming

Pressures of 14, 17, and 20 MPa and temperatures of 35, 40ºC were used for a total of 6 foaming conditions; soaking time (24 hour) and decompression rate (0.5 MPa/min) were consistent across all samples. 0.8g of polymer pellets were measured into custom-made Teflon moulds and placed into the pressure vessel. CO_2 was introduced and brought up

to the desired conditions, where it was maintained for 24 hours before depressurisation at 0.5 MPa/min.

Characterisation

These foams were studied under SEM to assess pore sizes and morphological features. Structural characterisation in the form of FTIR and XRD, as well as thermal DSC analysis was carried out.

Selected Results

It was found that even small differences in crystallinity resulted in variations in pore morphology and porosity. The extent of this variation was dependent on the conditions used; samples foamed at 40ºC presented an obvious increase in swelling with decreased crystallinity, whereas this trend was not evident at 35ºC. Trends of decreased pore size and more spherical pore shape with increased cooling rate were also more evident in samples foamed at 40ºC.

Pore surface morphology was also affected by crystallinity, suggesting varied melt strength during pore growth because of crystalline fraction in the melt-like plasticised state.

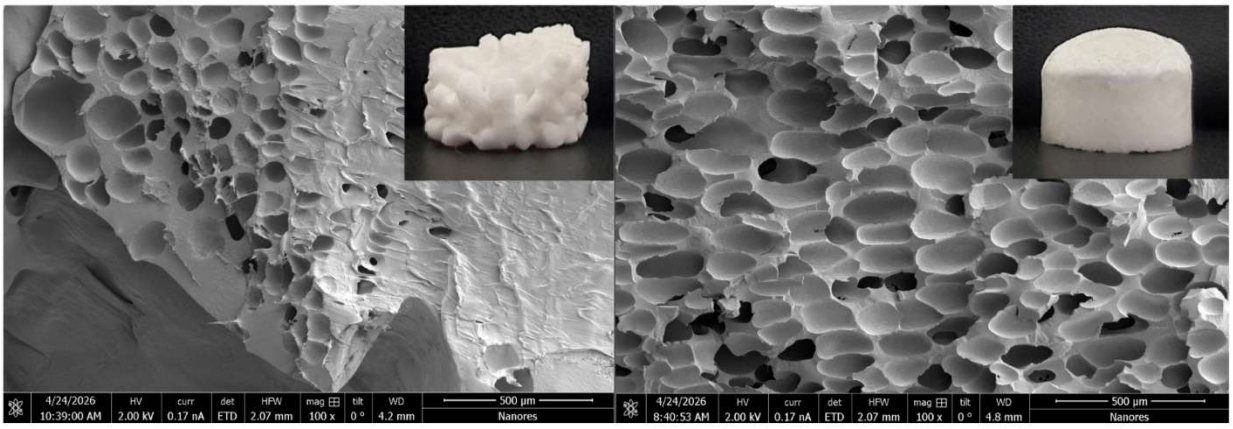

Fig. 1.: SEM and photograph of air-extruded foams (14 MPa, 35ºC). The left image shows aged air-extruded polymer foam, whereas the right shows the foam of air-extruded polymer that was stored at -4ºC.

Despite PCL's melting temperature of around 60ºC, it was found that room temperature storage had a significant effect on foams. Evidently diffusion still occurred in these conditions, leading to more developed crystalline domains which prevented foaming. This was particularly evident in the air-extruded samples foamed at 14 MPa, 35ºC, shown in figure 1, where the pellets in the aged sample are still visible in the resultant foam. SEM images also showed the lack of porosity in the aged sample when compared with freezer-

stored air-extruded samples. From this it is apparent that maintaining low crystallinity by the correct storage will greatly improve the foamability of polycaprolactone.

Summary

This work confirmed the need to standardise thermal treatment of semicrystalline PCL before foaming in $scCO_2$ conditions. Many studies on supercritical foaming of PCL neglect the effects of crystallinity in preparation of the polymer for foaming, leading to non-standardised optimised conditions for foaming. Results showed that maintaining low crystallinity by appropriate storage of the polymer greatly improved the uniformity of the porous structure. Increased cooling rate also resulted in improved swelling and porosity, particularly for samples at 40ºC. This study has highlighted the crystallinity-dependent behaviour of PCL during foaming, and the need to control thermal treatment.

Acknowledgment

This work is funded thanks to the OPUS 27 NCN grant nr 2024/53/B/ST8/00982 for “Re-co-crystallisation using supercritical carbon dioxide: a novel, ecological process for producing submicron cocrystals”.

References

[1] L. J. White, V. Hutter, H. Tai, S. M. Howdle i K. M. Shakesheff, „The effect of processing variables on morphological and mechanical properties of supercritical CO2 foamed scaffolds for tissue engineering,” *Acta Biomaterialia,* January 2012.

[2] S. Fabo, M. P. Arrieta, J. Romero, A. Aguero, A. Torres, S. Martinez, E. Rayon and M. J. Galotto, “Biodegradable nanocomposite poly(lactic acid) foams containing carvacrol-based cocrystal prepared by supercritical CO2 processing for controlled release in active food packaging,” *International Journal of Biological Macromolecules,* January 2024.

[3] S. Doroudiani, C. B. Park i M. T. Kortschot, „Effect of the crystallinity and morphology on the microcellular foam structure of semicrystalline polymers,” *Polymer Engineering & Science,* pp. 2645-2662, November 1996.

[4] Q. Yang , G. Zhang, Z. Ma, J. Li i X. Fan, „Effects of processing parameters and thermal history on microcellular foaming behaviors of PEEK using supercritical CO2,” *Journal of Applied Polymer Science,* July 2015.

[5] F. Mukasheva, L. Adilova, A. Dyussenbinov, B. Yernaimanova, M. Abilev i D. Akilbekova, „Optimizing scaffold pore size for tissue engineering: insights across various tissue types,” *Front. Bioeng. Biotechnol.,* November 2024.

[6] I. Gercek, R. S. Tigli i M. Gumusderelioglu, „A novel scaffold based on formation and agglomeration of PCL microbeads by freeze-drying," *J Biomed Mater Res A,* pp. 1012-22, September 2008.

[7] T. Xu, J. M. Miszuk, Y. Zhao, H. Sun i H. Fong, „Electrospun Polycaprolactone 3D Nanofibrous Scaffold with Interconnected and Hierarchically Structured Pores for Bone Tissue Engineering," *Advanced Healthcare Materials,* pp. 2238-2246, 2015.

[8] O. R. Davies, A. L. Lewis, M. J. Whitaker, H. Tai, K. M. Shakesheff i S. M. Howdle, „Applications of supercritical CO2 in the fabrication of polymer systems for drug delivery and tissue engineering," *Advanced Drug Delivery Reviews,* pp. 373-387, February 2008.

Synthetic Methane Production Plan by CO_2 Hydrogenation

Irene Ingelmo Flores

University of Valladolid
irene.ingelmo25@estudiantes.uva.es

Introduction

The global integration of renewable energy sources, such as wind and solar, has grown significantly, presenting a critical challenge due to their inherent intermittency. This variability often leads to a mismatch between electricity generation and demand, creating an urgent need for efficient energy storage solutions. One of the most promising strategies to address this issue is the Power-to-Gas (PtG) technology, and more specifically, the Power-to-Methane (PtM) process. This approach utilizes excess electricity generated from renewable sources to produce green hydrogen through water electrolysis. Subsequently, this hydrogen is combined with carbon dioxide captured from industrial emissions to synthesize methane.

The synthetic natural gas produced offers several distinct advantages. Primarily, it acts as a high-capacity energy carrier that can be stored over long periods, thereby balancing the electrical grid. Furthermore, synthetic methane is highly versatile, capable of generating heat and electricity, and can be seamlessly injected into the existing natural gas infrastructure for transport and distribution without requiring new infrastructural investments. This process also aligns perfectly with the principles of the circular economy; instead of being released into the atmosphere and contributing to global warming, industrial CO2 emissions are captured and repurposed as a valuable feedstock. Therefore, the PtM process stands out as a viable pathway to achieve carbon neutrality, reduce greenhouse gas emissions, and enhance climate resilience. The present work outlines the design, technical specifications, and economic feasibility of a large-scale synthetic methane production plant located in Spain, chosen for its high availability of solar resources.

Experimental

The proposed facility is designed to operate continuously for 52 weeks a year, leveraging solar energy to produce 0.77 kg/s of synthetic methane, which corresponds to an annual output of approximately 24,282 tons. The overall operation comprises several

interconnected stages: energy generation, water treatment and electrolysis, gas purification, CO_2 capture, and methanation.

First, electricity is sourced from a dedicated solar park. To avoid competing with human consumption and agricultural needs, the water used for the process is sourced from industrial wastewater that has been highly purified using technologies such as reverse osmosis. The conversion of electrical energy into chemical energy occurs in the electrolysis stage. For this project, Proton Exchange Membrane (PEM) technology was selected over Alkaline (ALK) or Solid Oxide (SO) alternatives. PEM electrolyzers are highly suitable for absorbing the intermittent energy loads typical of solar parks and offer superior hydrogen production rates due to the use of precious metal catalysts. The PEM electrolyzer operates at 80 ºC and 101 kPa, consuming 175,000 kJ per kg of hydrogen to produce a stream of 0.0124 kg H_2/s. As depicted in Figure 1., both the hydrogen and the oxygen byproducts emerge saturated with water vapor and must be cooled to 25 ºC to condense and recirculate the water back to the electrolyzer.

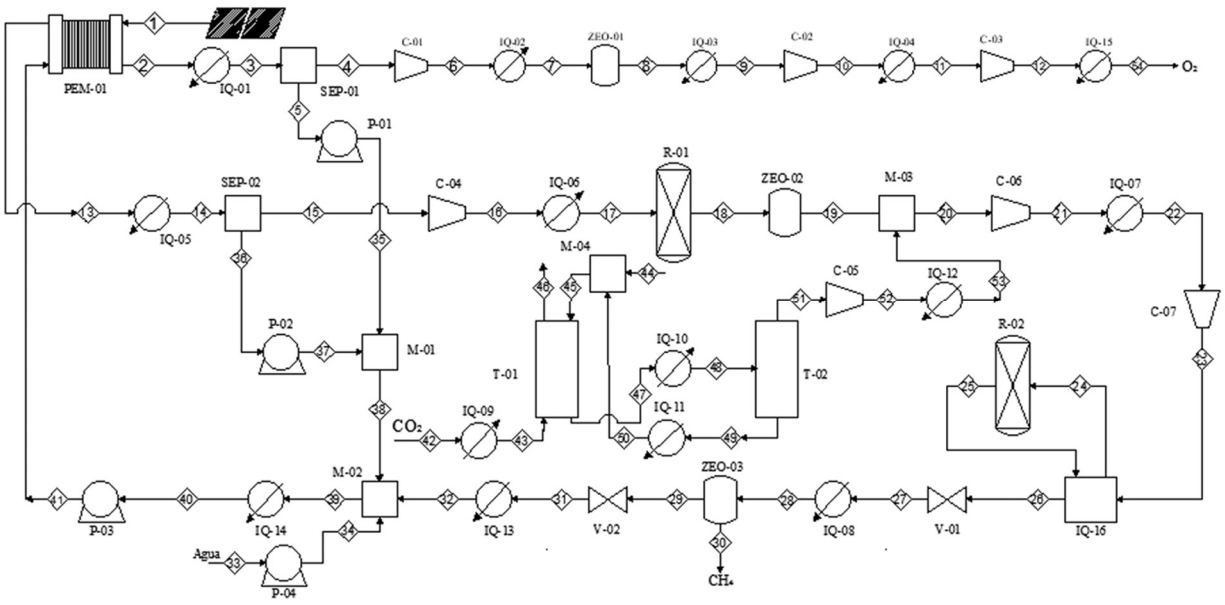

Fig. 1.: Process Block Diagram.

Following electrolysis, the oxygen stream undergoes deep dehydration using zeolites (removing 99.97% of residual moisture) and is compressed in three stages up to 125 atm for commercial storage. The hydrogen stream requires even more rigorous purification, as any trace of oxygen could pose severe safety hazards in the subsequent methanation reactor. To mitigate this risk, the hydrogen is passed through a deoxo reactor equipped

with a Pd/Al_2O_3 catalyst. Operating at 90 ºC and 5 atm, this reactor effectively converts residual oxygen into water with an efficiency of 99.7%.

Carbon dioxide is obtained as a byproduct from an existing ethylene oxide production plant, yielding a gas stream with nearly 100% purity. Despite this high initial purity, a chemical absorption unit utilizing a monoethanolamine (MEA) solution is incorporated into the design to guarantee the removal of any potential trace impurities prior to the catalytic reaction.

The core of the plant is the methanation stage, driven by the Sabatier reaction where hydrogen and carbon dioxide react to form methane and water. A fixed-bed reactor configuration was chosen due to its simplicity, reliable gas-catalyst contact, and lower capital costs compared to monolithic or membrane reactors. The catalytic bed uses nickel supported on alumina (Ni/Al_2O_3), highly valued for its excellent selectivity toward methane and cost-effectiveness. The reaction is highly exothermic and is favoured by low temperatures and high pressures. Thus, the reactor operates at an inlet temperature of 370 ºC and a pressure of 30 atm, achieving a remarkable CO_2 conversion rate of 96%.

To handle the process safely, the reactor design incorporates an advanced control system with two simultaneous loops. A pressure control loop regulates the internal pressure at 30 atm by manipulating the outlet gas flow, while a temperature control loop adjusts the flow of a cooling fluid to prevent catalyst damage from hot spots. From a mechanical standpoint, calculations based on the Langmuir-Hinshelwood-Hougen-Watson (LHHW) kinetic model determined a required catalytic bed volume of 13.24 m^3. Factoring in a 0.4 bed porosity and a 10% safety margin, the total reactor volume was dimensioned at 36.41 m^3, with a length of 8.8 m and a diameter of 2.2 m. Due to the harsh operational conditions, the vessel is designed with ellipsoidal heads and constructed from 310S stainless steel to resist high-temperature oxidation.

Tab. 1.: Key Reactor Design Parameters

L lecho (m)	6,46
D lecho (m)	1,62
V reactor (m^3)	36,41
D reactor (m)	2,2
L reactor (m)	8,8
t min (mm)	6,3

To assess the feasibility of the project, a comprehensive economic evaluation was conducted. Fixed capital costs (ISBL and OSBL), variable production costs (raw materials and utilities), and working capital were estimated. The total capital investment was calculated using empirical correlations based on the plant's production capacity.

Summary

The engineering and economic analyses confirm the technical viability of the proposed Power-to-Methane plant. By effectively combining renewable solar energy, industrial wastewater, and captured CO_2, the facility successfully yields 24,282 tons of synthetic methane annually. The strategic selection of PEM electrolysis coupled with a fixed-bed methanation reactor ensures an optimized, high-efficiency operational workflow.

From an economic perspective, the project demands a substantial initial layout. The Total Budget is evaluated at 143,898,847.46 €. The fixed capital investment amounts to 82,902,901.23 €. Meanwhile, operating variables, including utilities and raw materials, account for 24,397,039.23 € annually. Assuming a synthetic methane selling price of 3.86 €/kg, the plant projects annual sales revenues of 93.76 million €. This robust revenue stream yields an estimated gross profit of over 62.3 million € per year and promises a rapid investment payback period of just 1.75 years, underscoring the strong economic attractiveness of the venture.

However, an environmental assessment reveals a carbon footprint of 2.84 kg of CO2 equivalent per kg of product, primarily driven by indirect emissions related to external utility consumption. While the plant fulfils its role in integrating renewable energies and recycling CO_2, further sustainability optimizations regarding external energy dependencies are recommended to improve the overall environmental impact.

References

Bassano, C., Deiana, P., Lietti, L., & Visconti, C. G. (2019). P2G movable modular plant operation on synthetic methane production from CO2 and hydrogen from renewable sources. Fuel, 253, 1071-1079.

Davis, W., & Martín, M. (2014). Optimal year-round operation for methane production from CO2 and water using wind and/or solar energy. Journal of Cleaner Production, 80, 252-261.

De Paolis, R., Bernardini, V., Campana, L. G., Ermini, M. V., Verna, M., Raimondi, G., & Spazzafumo, G. (2024). Techno-economic and climate finance assessment of a methanation plant with green hydrogen production and CO2 recycling in Italy. International Journal of Hydrogen Energy.

Ghaib, K., & Ben-Fares, F.-Z. (2018). Power-to-Methane: A state-of-the-art review. Renewable and Sustainable Energy Reviews, 81, 433-446.

Computer Aided Process Engineering (CAPE)-Based Framework for Sustainability Assessment of Chemical Processes through Normalized indicators

Miguel Angel Peñaloza Rodriguez[a], Andrea Casas Gonzalez[a], Pierdomenico Biasi[b] and Juan García Serna[a]

[a]Pressure Technologies group, Bioeconomy Research Institute of the University of Valladolid, Department of Chemical Engineering and Environmental Technology, School of Industrial Engineering, University of Valladolid, 47011, Valladolid, Spain.
juan.garcia.serna@uva.es
[b]R&D Division, Casale SA, Lugano, Via Pocobelli 6, Lugano 6900, Switzerland.

Introduction

Chemical processes and industrial plants are increasingly required to satisfy technical, environmental and energy-related criteria simultaneously. In this context, sustainability assessment cannot be restricted to carbon footprint evaluation alone. In addition, the practical implementation of sustainability indicators is often limited by fragmented data handling, manual calculations and poor traceability between process simulation results and the final indicator values. This work presents a Computer-Aided Process Engineering (CAPE) web tool developed to calculate, normalize and visualize sustainability indicators for chemical processes using structured process data. The tool is designed to transform information obtained from process simulations, and in future stages from real plant data, into environmental, performance and energy indicators. To validate this tool, a simulated ammonia plant in Aspen Plus is used as a representative case study.

Experimental

The experimental section was defined as a computational methodology based on process simulation data. The development of the CAPE was structured around four main stages: process data extraction, data structuring, case definition and calculation and results display (according to Figure 1).

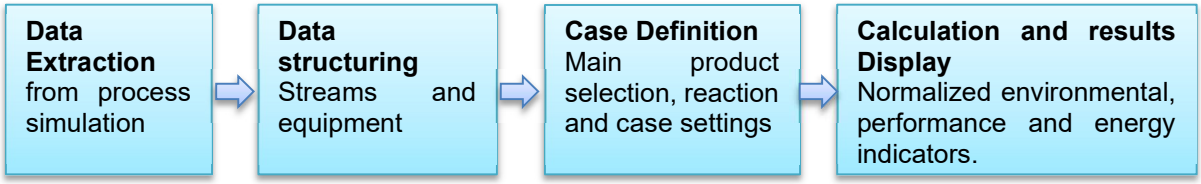

Figure 1. Workflow of the CAPE, from process data to normalized sustainability results

First, the tool processes simulation outputs containing stream and equipment information. For process streams, the CAPE identifies the main information blocks generated by the simulator. Within each block, the tool extracts molar flows, mass flows, molar fractions, mass fractions and thermodynamic properties (see Figure 2), preserving the distinction between global stream information and phase-specific information. This allows the original structure of the simulation output to be converted into organized datasets without losing the link with the source data. The same way the equipment information is extracted.

Figure 2. Thermodynamic properties extraction

Second, both equipment and stream data are structured to define the calculation basis of the tool. Equipment units are organized according to their type of operation: thermal units, such as heat exchangers, are associated with heat duties, whereas pumps, compressors, and electrolyzers are linked to energy requirements. In parallel, process and utility-related streams are classified according to their role in the process. All extracted values are standardized in compatible units and combined with user-defined classifications, such as equipment role, stream type and utility category, allowing the tool to connect mass and energy information with the corresponding sustainability indicators.

Third, a case definition stage is required to link the structured process data with the specific assessment objective. In this stage, the main product of interest is selected, the target reaction is defined, the relevant reactants and products are identified, and the case settings required for indicator calculation are established. These settings define the

reference basis for normalization, and process-dependent indicators. In addition, the case definition is complemented with auxiliary datasets required for environmental calculations. This configuration allows the CAPE to move from mass and energy accounting toward a process-specific and indicator-based sustainability assessment.

Finally, the calculation engine evaluates a set of sustainability indicators grouped into environmental, process-performance and energy dimensions. Each indicator is computed using the structured process data and is associated with methodological best-case and worst-case references (see Figure 3). These references allow the results to be normalized on a common scale, making it possible to compare different process alternatives under the same basis. The web interface then displays the normalized values together with detailed contribution analysis by compound, stream, equipment unit.

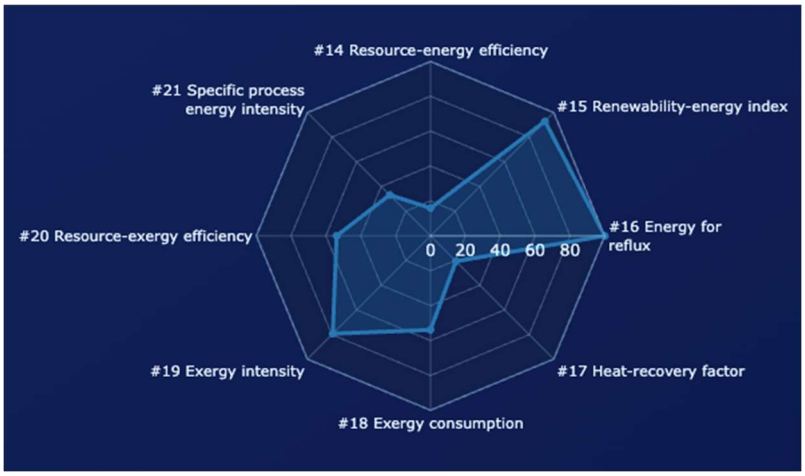

Figure 3. Energy indicators result for a validation case

Summary

The CAPE-based tool provides a structured bridge between process data and sustainability assessment. These input data can be obtained from process simulations, pilot-scale studies, industrial plant measurements, or other structured mass and energy balance datasets. Rather than generating only final indicator values, the tool makes it possible to identify which compounds, streams, equipment units or process variables are responsible for the main environmental, energy-related or process-performance contributions. This traceability is especially relevant for technical decision-making, since it helps determine whether a sustainability limitation arises from emissions, material losses, energy demand, low recovery, insufficient heat integration or other process inefficiencies. In this sense, the CAPE-based framework is proposed not only as a calculation tool, but also as a decision-support platform.

The current version of the tool evaluates 21 sustainability indicators distributed across three dimensions: environmental performance, process performance and energy.

References

[1] G.J. Ruiz-Mercado, R.L. Smith, M.A. Gonzalez, Sustainability indicators for chemical processes: I. Taxonomy, Ind. Eng. Chem. Res. 51 (2012) 2309–2328. https://doi.org/10.1021/ie200755k.

[2] G.J. Ruiz-Mercado, M.A. Gonzalez, R.L. Smith, Sustainability indicators for chemical processes: III. biodiesel case study, Ind. Eng. Chem. Res. 52 (2013) 6747–6760. https://doi.org/10.1021/ie302804x.

[3] G.J. Ruiz-Mercado, R.L. Smith, M.A. Gonzalez, Sustainability indicators for chemical processes: II. Data needs, Ind. Eng. Chem. Res. 51 (2012) 2329–2353. https://doi.org/10.1021/ie200755k.

Registered Teachers ERASMUS+ BIP ESS-HPT 2026

Country	University / Company	Name	Email
AT	Graz	Prof. Thomas Gamse	thomas.gamse@tugraz.at
AT	Natex	DI Martin Sova	m.sova@natex.at
AT	Natex	Dr. Eduard Lack	e.lack@natex.at
AT	INNOWELD	Maximilian Schrittwieser	m.schrittwieser@innoweld.at
CZ	Prag	Dr. Helena Sovova	helsov@seznam.cz
DE	Bochum	Prof. Marcus Petermann	petermann@fvt.ruhr-uni-bochum.de
DE	Bochum	Prof. Thomas Müller	thomas.mueller@ls-csc.ruhr-uni-bochum.de
DE	Darmstadt	Prof. Markus Busch	markus.busch@pre.tu-darmstadt.de
DE	Erlangen	Prof. Eberhard Schlücker	eberhard.schluecker@fau.de
DE	Erlangen	Dr. Detlef Freitag	detlef.freitag@fau.de
DE	Freising	Prof. Sabine Grüner	sabine.gruener@hswt.de
DE	Hamburg	Dr. Carsten Zetzl	zetzl@tuhh.de
DE	Hamburg	Prof. Pavel Gurikov	pavel.gurikov@tuhh.de
ES	Valladolid	Prof. Maria Cocero	mariajose.cocero.alonso@uva.es
ES	Valladolid	Prof. Angel Martin	angel.martin.martinez@uva.es
HR	Osijek	Prof. Stela Jokic	Stela.Jokic@ptfos.hr
HU	Budapest	Prof. Edit Szekely	edit.szekely@edu.bme.hu
HU	Budapest	Dr. Erika Vagi	vagierikamaria@gmail.com
IT	Bologna	Prof. Alessandro Zambon	alessandro.zambon2@unibo.it
PL	Wroclaw	Prof. Irena Zizovic	irena.zizovic@pwr.edu.pl
PT	Lisbon	Dr. Ana V.M. Nunes	avn07929@fct.unl.pt
RS	Belgrade	Prof. Marko Stamenic	stamena@tmf.bg.ac.rs
SI	Maribor	Prof. Urban Bren	urban.bren@um.si
SI	Maribor	Prof. Zeljko Knez	zeljko.knez@um.si
SI	Maribor	Prof. Maša Knez-Marevci	masa.knez@um.si
SI	Maribor	Dr. Amra Perva	amra.perva@um.si

Registered Participants ERASMUS+ BIP ESS-HPT 2026

	University / Company	First Name	Family Name	Sex	Nationality
AT	Graz	Manuel	Egger	m	Italy
AT	Graz	David Christian	Kühne	m	Germany
AT	Graz	Marlene	Metzler	f	Austria
AT	Graz	Ann Sophie	Mossauer	f	Austria
AT	Natex	Farimah	Heydari	f	Iran
AT	Natex	Christian	Mayer	m	Austria
AT	Natex	Anna	Michaelis	f	Austria
AT	Natex	Maryam S.	Mortazavi	f	Canada
DE	Bochum	Jan	Caputo	m	Germany
DE	Bochum	Tanmay	Tiwari	m	India
DE	Bochum	Jan Hendrik	Westerbarkei	m	Germany
DE	Darmstadt	Michelle	Becker	f	Germany
DE	Darmstadt	Jonas	Geider	m	Germany
DE	Darmstadt	Inka	Helmer	f	Germany
DE	Darmstadt	Xaver-Philipp Guido	Possehl	m	Germany
DE	Freising	Jörg	Schäffer	m	Germany
DE	Freising	Anna Lena	Schuhmacher	f	Germany
DE	Hamburg	Natalia	Gala	f	Poland
DE	Hamburg	Michel	Groth	m	Germany
DE	Hamburg	Mariem	Hamed	f	Tunesia
DE	Hamburg	Jesan	Joy	m	India
DE	Hamburg	Ushe	Mutamba	m	Zimbabwe
ES	Valladolid	Godwin	Aturagaba	m	Uganda
ES	Valladolid	Salvia	Frómesta Cuenca	f	Spain
ES	Valladolid	Irene	Ingelmo Flores	f	Spain
ES	Valladolid	Miguel Angel	Peñaloza Rodriguez	m	Bolivia
ES	Valladolid	Barbara	Ruiz Bolado	f	Spain
HR	Zagreb	Iva	Blažević	f	Croatia
HU	Budapest	Jose	Ruiz	m	Ecuador
HU	Budapest	Atád	Vészi	m	Hungary
IT	Bologna	Gaia	Lazzari	f	Italy
IT	Bologna	Lorenzo	Zamagni	m	Italy
PL	Wroclaw	Hira	Anwar	f	Pakistan
PL	Wroclaw	Maciej	Grabowski	m	Poland

Registered Participants ERASMUS+ BIP ESS-HPT 2026

	University / Company	First Name	Family Name	Sex	Nationality
PL	Wroclaw	Seyedabbas	Shahrtash	m	Iran
PL	Wroclaw	Zofia	Wolny	f	Poland
RS	Belgrade	Nevena	Djukic	f	Serbia
RS	Belgrade	Mihailo	Mladenović	m	Serbia
SI	Maribor	Kaja	Gajšt	f	Slovenia
SI	Maribor	Marko	Pavlović	m	Slovenia
SI	Maribor	Gašper	Vrečer	m	Slovenia